Emanuel Marc Lörtscher

Charge-Carrier Transport Measurements through Single Molecules

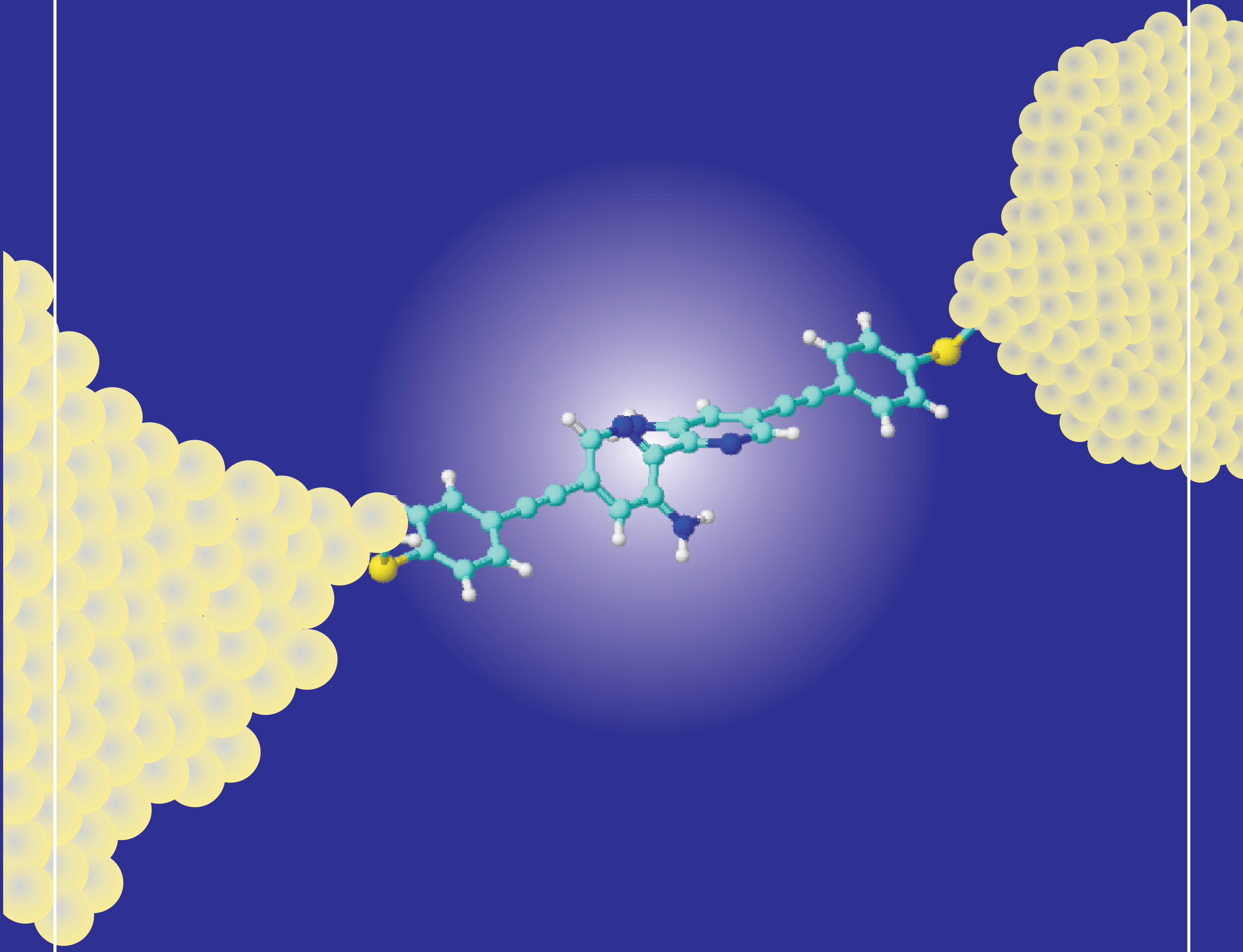

Cuvillier Verlag Göttingen

Charge-Carrier Transport Measurements through Single Molecules

Inauguraldissertation

zur
Erlangung der Würde eines Doktors der Philosophie
vorgelegt der
Philosophisch-Naturwissenschaftlichen Fakultät
der Universität Basel
von

Emanuel Marc Lörtscher
aus Wimmis (BE)

Basel, November 2006

Genehmigt von der Philosophisch-Naturwissenschaftlichen Fakultät
auf Antrag der Herren Professoren:

Prof. Dr. C. Schönenberger
Prof. Dr. J. M. van Ruitenbeek

Basel, 22. November 2006

Prof. Dr. H.-P. Hauri, Dekan

Bibliographische Information Der Deutschen Bibliothek

Die Deutsche Bibliothek verzeichnet diese Publikation in der Deutschen Nationalbiographie; detaillierte bibliographische Daten sind im Internet über http://dnb.ddb.de abrufbar.

1. Aufl. - Göttingen : Cuvillier, 2007
Zugl.: Basel, Univ., Diss., 2006
ISBN X-XXXXX-XXX-X

© CUVILLIER VERLAG, Göttingen 2007
Nonnenstieg 8, 37075 Göttingen
Telefon: 0551-54724-0
Telefax: 0551-54724-21
www.cuvillier.de

Alle Rechte vorbehalten. Ohne ausdrückliche Genehmigung des Verlages ist es nicht gestattet, das Buch oder Teile daraus auf fotomechanischem Weg (Fotokopie, Mikropie) zu vervielfältigen.
1. Auflage, 2007
Gedruckt auf säurefreiem Papier

ISBN X-XXXXX-XXX-X

Contents

Zusammenfassung **vii**

Summary **xiii**

Introduction **xix**

1 Theory of Molecular Conductance **1**

1.1 Theory of Metal–Metal Junctions 1

1.1.1 The Scattering Approach 4

1.1.2 Conductance Quantization 7

1.2 Theory of Metal–Molecule–Metal Junctions 10

1.2.1 Electron Hopping and Tunnelling Processes 10

1.2.2 Single-level Model 12

1.2.3 Broadening of Molecular Energy Levels 14

1.2.4 Charging Effects 15

1.2.5 Multi-level Generalization and Molecular Structure 17

1.2.6 Semi-Empirical and First-Principle Calculations 20

1.2.7 Inelastic Effects 21

2 Experimental Techniques **23**

2.1 Experimental Methods in Molecular Electronics 23

2.2 The Mechanically Controllable Break-Junction 29

2.2.1 Principle of Operation 29
2.2.2 Sample Fabrication 32
2.2.3 Sample Holder 33
2.2.4 Ultra-High Vacuum and Cryogenic Environment 38
2.2.5 Electrical and Controlling Setup 39

3 Properties of Metal–Metal Junctions 43
3.1 Temperature-Dependence without Bending 44
3.2 Transition from Direct Contact to Tunneling 46
3.3 Calibration of the Displacement Ratio 48
3.4 Stability and Resolution of the Electrode Pair 53
3.5 Conductance Quantization 57
3.6 Conditioning of the Electrodes 60
3.7 Conclusions 64

4 Statistical Measurement Approach 65
4.1 Molecules and their Application on the MCBJ 66
4.2 Contacting Procedure 67
4.3 Statistical Measurement Approach 70
4.3.1 Motivation 70
4.3.2 Principle of the Statistical Measurement Approach 71
4.3.3 An Illustrative Example: TPDT-DM at 300 K 74
4.4 Discussion on Single-Molecule Measurements 76
4.5 Conclusions 77

5 Properties of the Molecule–Metal Contact 79
5.1 Molecular Model Systems 80
5.2 Phenyl-1,4-Dithiol (PDT) 82
5.3 Phenyl-1,4-Diisocyanide (PDI) 87

5.4 Comparison of the Single-Ring Systems 89
5.5 Comparison of the Double-Ring Systems 93
5.6 Conclusions 98

6 Influence of the Intramolecular Structure on Transport 99

6.1 Molecular Model Systems 100
6.2 Charge-Carrier Transport Measurements 102
6.3 Conclusions 107

7 Molecules as Functional Building Blocks 109

7.1 Diode Behavior 109
7.2 Voltage-Induced Switching 117
7.3 Memory Operation 133
7.4 Conclusions 135

A Molecules 161

B List of Publications 165

C Acknowledgments 169

D Abbreviations 173

E Curriculum Vitae 179

Zusammenfassung

Ziel dieser Arbeit war die Kontaktierung und die elektrische Charakterisierung von einzelnen Molekülen mittels der Methode der mechanisch kontrollierbaren Bruchkontakte (*engl.* "mechanically controllable break-junction" (MCBJ)). Dieser experimentelle Ansatz erlaubt es, atomarfeine, sich gegenüberstehende Elektroden zu erzeugen, deren Abstand mit Pikometer-Auflösung kontrolliert werden kann. Diese Technik, welche von Moreland *et al.* 1985 entwickelt und von Müller *et al.* in den darauffolgenden Jahren weiter verbessert wurde um Quantenphänomene in Supraleitern zu studieren, zeichnet sich unter anderem durch eine hervorragende Stabilität der beiden Elektroden gegenüber externen Vibrationen aus. Dies wird durch eine rein mechanische Bewegungsausführung in einer Dreipunkt-Biegemechanik mit einem sehr kleinen Übersetzungsverhältnis zwischen der Stempelbewegung und der daraus resultierenden Separation der Elektroden in der Grössenordnung von 1×10^{-5} erzielt. Aufgrund der lateralen Stabilität und der sub-atomaren Spitzenpositionierbarkeit eignet sich das Elektrodenpaar ausgezeichnet für die Kontaktierung einzelner Moleküle.

Im Rahmen dieser Arbeit wurde ein Ultrahochvakuum-Messplatz mit einer Bruchkontaktmechanik konzipiert, aufgebaut, charakterisiert und kontinuierlich verbessert. Dieser Messplatz erlaubt es, ein einzelnes Molekül zu kontaktieren, und den Ladungstransport durch dieses molekulare System unter kontrollierten Bedingungen temperaturabhängig zu untersuchen. Die thermische Ankopplung zwischen dem Kryostaten und der Probe wurde dabei in mehreren Schritten verbessert, um schlussendlich einen Messbereich von 8 K bis 300 K zu erreichen. Ebenso wurde die Methode der Bruchkontakte in verschiedener Hinsicht massgeblich verbessert. Beispielsweise stellen zusätzliche Halterungsbolzen und ein dem Stempel gegenüberliegender elektrischer Messkopf sicher, dass das Substrat auch wieder zurückgebogen werden kann, sollte es einmal über den elastischen Bereich hinaus gedehnt worden sein (Biegeradius kleiner als 18 mm). Da-

durch kann der Bruchkontakt mehrere hundert Male geöffnet und geschlossen werden, ohne dass Ermüdungserscheinungen am Substrat auftreten. Des Weiteren wurde eine dauerhafte elektrische Kontaktierung der Probe mittels Federkontaktstiften realisiert, welche durch den Biegevorgang nicht beeinträchtigt wird. Mit Hilfe von Photo- und Elektronenstrahllithographie wurden mikrostrukturierte Proben mit einer 1 μm kurzen, zwischen 75 nm und 120 nm schmalen, freitragenden Brücke, hergestellt. In dieser Geometrie wird ein sehr grosser dynamischer Bewegungsbereich für das Öffnen und Schliessen des Kontaktes erreicht.

Im einführenden experimentellen Teil wurden die mittels der Bruchkontaktmethode hergestellten Metall-Metall-Kontakte bezüglich ihrer mechanischen und elektrischen Eigenschaften charakterisiert. Das Augenmerk wurde hier speziell auf diejenigen Untersuchungen gelegt, welche nachträglich die Handhabung der separierten Elektroden für die Kontaktierung von Molekülen erlauben. Dabei waren neben der Spitzengeometrie auch Positionierbarkeit und Stabilität wichtige Parameter. Als Elektrodenmaterial wurde ausschliesslich Gold (Au) verwendet, welches sich aufgrund der hohen Duktilität hervorragend eignet. Durch eine relative Abstandskalibrierung mittels Tunnelstrommessung zwischen den Elektroden wurde gezeigt, dass das theoretische Verhältnis zwischen der Stempelbewegung und der daraus resultierenden Elektrodenseparation (2.1×10^{-5}) gut mit dem experimentell gemessenen Wert (1.8×10^{-5}) übereinstimmt. Die Stabilität bei konstanter, tiefer Temperatur (z.B. $T = 30$ K) zwischen den Spitzen ist ausserordentlich gut, so kann beispielsweise ein Tunnelwiderstand von (15 ± 3) MΩ bei kleinen Messspannungen von 10 mV über mehrere Minuten konstant gehalten werden. Dies bedeutet, dass der Abstand zwischen den Elektroden innerhalb von weniger als 5 - 10 Pikometern variiert. Beim weiteren Zusammenfahren der Elektroden zeigte sich, dass der Abstand zwischen den Spitzen nicht beliebig klein eingestellt werden kann. So wurde für Tunnelwiderstände von weniger als 1 MΩ ein Einrastverhalten auf das Leitwertquant G_0 festgestellt. Die hervorragende Stabilität zwischen den Elektroden ändert sich grundlegend, wenn bei höheren Temperaturen ($T > 150$ K) gemessen wird. Dies lässt sich primär auf die erhöhte Beweglichkeit der Au-Atome zurückführen. Unabhängig von der Temperatur wurde bei langsamen Öffnungs- und Schliesszyklen (Geschwindigkeit $<$ 1 Pikometer/Sekunde) eine Quantisierung des Leitwertes in Einheiten des Leitwertquants G_0 beobachtet. Diese Quanteneffekte werden dann ersichtlich, wenn die Dimensionen des Punktkontaktes kleiner als die Fermi-Wellenlänge der Metallelektronen ($\lambda_F = 0.52$ nm) werden. Im Falle von Au bedeutet ein Leitwert von G_0 aufgrund des von der chemischen Valenz (s-Orbitale) beeinflussten Transportkanals, dass ein Einzelatomkontakt erzeugt wurde. Nach dem Auseinanderreissen eines solchen Kontaktes verfügen die separierten Elektroden über atomar-feine Spitzen. Da ein solch feines Elektrodenpaar für die Kontaktierung von Molekülen eine wichtige Voraussetzung darstellt, wurde eine Konditionierungsprozedur beschrieben, welche eine reproduzierbare, automatische Herstellung solcher Elektroden erlaubt.

Moleküle als funktionelle Bausteine stellen ein vielversprechendes Konzept für die Post-CMOS Epoche dar. Anfängliche euphorische Vorhersagen über den Einsatz von molekularen Bausteinen in der Informationstechnologie konnten bisher nicht eingehalten werden, bedingt vor allem durch die auftretenden Herstellungsvarianzen auf der Nanometerskala. Obwohl Moleküle durch chemische Synthese identisch hergestellt werden können, kann die variable Ankopplung der Moleküle an den Elektroden zu grossen Streuungen in den gemessenen Transporteigenschaften führen. Um diese Einflüsse zu quantifizieren, wurde in dieser Arbeit ein spezielles Augenmerk auf die Statistik gelegt. Hierfür wurde ein statistischer Mess- und Analyseansatz für die Bruchkontaktmethode entwickelt und implementiert, welcher es erlaubt, die Transporteigenschaften - allen voran Strom–Spannungs-Kennlinien - während der kontrollierten Manipulation des Molekül–Metall-Kontaktes von dessen Formierung bis zum Aufbrechen zu beobachten. Da dieser Messansatz aufgrund der Wahl der Kontrollparameter unabhängig vom Elektrodenabstand funktioniert, können damit auch temperaturabhängige Messungen durch Kompensation der thermischen Ausdehnung der Elektroden durchgeführt werden. Bei der Analyse mittels selbst entwickelter Software ist es nicht nur möglich, innerhalb grosser Datensätze die am häufigsten vorkommenden Transportkurven zu bestimmen, sondern auch die davon auftretenden Variationen. Unter anderem konnten beispielsweise die typischen stochastischen Fluktuationen in der Thiol-Au-Kopplung beobachtet und quantifiziert werden.

Für die Untersuchung des Ladungsträgertransportes durch einzelne Moleküle wurden gezielt molekulare Modellsysteme ausgewählt, die eine getrennte Untersuchung verschiedener Teilaspekte des Ladungsträgertransportes durch das System Metall–Molekül–Metall erlauben. Die Systeme wurden mittels des oben erwähnten statistischen Ansatzes elektrisch charakterisiert.

Ein erstes Ziel war es, den für das Leitverhalten äusserst wichtigen Molekül–Metall-Kontakt zu untersuchen. Dafür wurden speziell synthetisierte Moleküle eingesetzt, welche sich lediglich durch die funktionelle Endgruppe, nicht aber durch die eigentliche Molekülstruktur unterscheiden. Die gewählten Thiol- und Isocyanid-Endgruppen koppeln unterschiedlich stark an die Metallelektroden an. Eine stärkere Ankopplung vergrössert die Injektionsrate der Elektronen, wodurch sich deren Verweildauer auf dem entsprechenden Molekülorbital verkürzt und das entsprechende Niveau energetisch verbreitert wird. Durch die spektroskopische Analyse bei tiefen Temperaturen ($T = 50$ K), wo der Anteil der thermischen Linienverbreiterung an der Gesamtbreit vernachlässigbar wird, wurden thiol-gekoppelte Molekülsysteme (PDT, BPDT) mit isocyanid-gekoppelten Molekülsystemen (PDI, BPDI) verglichen. Beim PDT Molekül wurde eine Verbreiterung der Linie um rund 50% (oder 25 mV) im Vergleich zum PDI Molekül gemessen, wohingegen die Leitwertmaxima von 70 nS (PDT) respektive 95 nS (PDI) nahezu unverändert vorgefunden wurden. Die Isocyanid-Ankopplungsgruppe zeigte sich nicht nur in Bezug auf die Linienschärfe als vorteilhafter, es konnten auch Transporteigenschaften in der HOMO–LUMO-Lücke gemessen werden, die bei stärkerer Ankopplung nicht zu Tage traten. Des Weiteren erlaubt die Isocyanid-Ankopplung temperaturabhängige Messungen ohne dass dabei das kontaktierte Molekül verloren geht. Daraus ist zu folgern, dass die Isocyanid-Endgruppe eine grössere Oberflächenmobilität aufweist, welche es erlaubt, die thermisch-induzierten Abstandsänderungen im Elektrodenabstand zu kompensieren.

In den weiteren Untersuchungen wurde der Einfluss der molekülinternen Struktur auf den Ladungstransport bei gleicher Ankopplung evaluiert. Es wurden Oligophenylene mit einer ansteigenden Sulphur–Sulphur-Länge von 0.62 nm bis 1.97 nm hergestellt, bei denen eine durch Methyl-Gruppen erzielte sterische Abstossung der Phenylringe die gezielte Reduzierung der Längskonjugation des Moleküls bewirkt. Bei der elektrischen Charakterisierung zeigte sich, dass der Einfluss der Länge auf die Transporteigenschaften ganz erheblich ist. Während beim Benzol-Dithiol, dem kürzesten Molekül mit einem Ring und einer daraus resultierenden Elektrodendistanz von ungefähr 0.846 nm, nur ein resonantes Molekülorbital im stabilen Spannungsfenster lag, zeigten sich bei den längeren Molekülen mit zwei und mehr Benzolringen weitere Leitwert-Maxima. Diese sind charakteristisch für das jeweilige untersuchte Molekül.

Gleichzeitig vergrösserte sich der Spannungsbereich, ab dem der eigentliche Stromfluss durch resonante Molekülorbitale einsetzt, mit zunehmender Länge des Moleküls von 250 mV auf 580 mV. Dies lässt darauf schliessen, dass die externe Spannung für die Ladungsträgerinjektion über den Molekül–Metall-Kontakt auf das Molekül erhöht werden muss, weil sich auch der Spannungsabfall über der Tunnelbarriere durch die längere Moleküllänge entsprechend verändert hat.

Aufgrund der vorangegangenen Messungen und den daraus gewonnenen Erkenntnissen über die Ankopplung und den Einfluss der intramolekularen Struktur auf den Transport wurde das Transportverhalten von Molekülen untersucht, welche ein funktionelles Verhalten in ihrer internen Struktur beinhalten. Die Fragestellung, ob diese intrinsische Funktionalität eines Moleküls extern gesteuert werden kann und ob deren Einfluss sich auf den Ladungsträgertransport auswirkt, wurde anhand zweier Molekülarten angegangen: Gleichrichtende und spannungsinduziert schaltende Moleküle. Beim sogenannten SB-Dioden-Molekül wurde ein klar asymmetrisches Leitverhalten beobachtet, welches sich zudem als temperaturunabhängig herausstellte. Ein Gleichrichtungsverhältnis mit einem Faktor 10 wurde bei einer Spannung von 1.0 V gemessen. Aufgrund des Verhaltens des Stroms als Funktion der Spannung liess sich ein noch viel grösseres Verhältnis für höhere Spannungen extrapolieren. Allerdings verhinderte die Elektrodeninstabilität bei diesen hohen elektrischen Feldern Messungen über einen grösseren Spannungsbereich. Ein maximales Gleichrichtungsverhältnis von 15 konnte im stabilen Spannungbereich (von – 1.8 V bis + 1.8 V) gemessen werden.

Das spannungsinduzierte Schalten wurde an einem funktionellen Molekül, dem sogenannten BPDN-DT-Molekül, untersucht und mit einem Referenzmolekül, dem BP-DT-Molekül, verglichen, welches nicht über die internen funktionellen Nitro-Gruppen verfügt. Dieses Referenzmolekül zeigte kein Schaltverhalten und es konnten auch keine für thiol-gebundene Moleküle typischen stochastische Kontaktfluktuationen bei tiefen Temperaturen festgestellt werden. Hingegen liess sich das funktionelle Molekül mit einem Spannungspuls kontrolliert von einem schlechter leitenden "off"-Zustand in einen besser leitenden "on"-Zustand schalten. Durch den Vergleich mit dem Referenzsystem konnte eindeutig gezeigt werden, dass die internen funktionellen Nitro-Gruppen Ursache für das Schaltverhalten sind. Durch zeitabhängige Messungen wurde nachgewiesen, dass ein bistabiler Energiebereich von ungefähr 120 mV vorliegt, in dem beide Zustände mit unterschiedlichen Übergangswahrscheinlichkeiten vorherrschen.

Die gemessenen Schaltzeiten des Einzelmolekülsystems von weniger als 250 μs waren einzig durch den elektronischen Messaufbau limitiert. Des Weiteren zeigte die gemessene Hysterese in den Transportkurven ein anormales Verhalten, wenn auch der negative Spannungsbereich in die Betrachtungen einbezogen wurde. Es zeigte sich, dass der besser leitende Zustand für den positiven Spannungsbereich zum schlechter leitenden Zustand für den negativen Spannungsbereich (und umgekehrt) wird. Durch diese Erkenntnis liess sich das Molekül gezielt zwischen den zwei Zuständen hin- und herschalten. Dies wiederum erlaubte es, das Einzelmolekülsystem als reale Speicherzelle einzusetzen. Es wurde durch wiederholte Schreib-Lese-Lösch-Lese-Zyklen die grundsätzliche Speichermöglichkeit demonstriert und dabei eine Bit-Separation (Verhältnis zwischen “on“ und “off“ Zustand) zwischen 7 und 70 erzielt. Die Schaltpulse betrugen wenige Millisekunden und während der Auslesezeiten von mehreren Sekunden zeigte sich keine Zustandsänderung, wodurch ein zerstörungsfreies Auslesen des Speicherzustandes erreicht wurde. Über eine mehr als eineinhalbstündige Messzeit konnte keine Degradation des “on“ Zustands festgestellt werden. Dies lässt auf eine hervorragende Stabilität des molekularen Systems schliessen. Ebenso wurden mehr als 1500 aufeinanderfolgende Schaltzyklen gemessen, ohne dass sich dabei das Schaltverhalten des Einzelmolekülschalters veränderte.

Summary

The goal of this thesis was to establish and to characterize single-molecule junctions by means of the mechanically controllable break-junction (MCBJ) technique. Using this method, an electrode pair with atomic-sized tips can be created. These tips are located exactly opposite to each other and their distance can be adjusted with picometer accuracy. This technique was developed by Moreland *et al.* in 1985 and further improved by Muller *et al.* in the subsequent years to study quantum phenomena in superconductors. Mechanically controllable break-junctions are distinguished by an excellent stability of the two electrodes against external vibrations. The stability is achieved by a purely mechanical transaction in a three-point bending mechanism with a very low transmission ratio between the pushing-rod travel distance, and the electrode separation resulting therefrom (ratio of approximately 1×10^{-5}). This lateral stability combined with a sub-atomic spatial electrode positioning accuracy allow single molecules to be contacted.

In the framework of this thesis, an ultra-high vacuum system equipped with a MCBJ bending mechanism was designed, fabricated, characterized, and continuously improved. This experimental system can be used to establish a contact with a single molecule and to perform temperature-dependent investigations of its charge-carrier transport properties. The thermal coupling between the cryostat and the sample holder was improved in several ways to achieve a temperature range of 8 to 300 K. The bending mechanism of the break-junction was also modified considerably. For instance, additional supporting bolts and a proper head opposite to the pushing-rod ensure the back bending of the substrate should the bending force might have exceeded the elastic range of the metal (bending radii larger than 18 mm). As a result, the junction can be opened and closed several hundred times without any sign of fatigue. Moreover, a reliable electrical contact to the sample was implemented by means of spring-loaded contact pins. They provide a stable electrical connection between the measurement instrument and the

sample, which is not influenced by the bending procedure. The MCBJ samples were fabricated using a combination of optical and electron-beam lithography. These fabrication techniques allow 1 μm short, between 75 nm and 120 nm narrow, free-standing bridges to be manufactured. As a result of this geometry, the dynamic range for the opening and closing of the junction is excellent.

In the introductory experimental part, the metal–metal contacts as created via the MCBJ approach were characterized in terms of their mechanical and electrical properties. The attention was focussed especially on those investigations that are important for handling separated electrodes for contacting single molecules. The microscopic geometry of the electrode tips, their positioning accuracy, and the stability were found to be the essential parameters. Gold was used as an electrode material as it is very well suited because of its ductile response to deformation, therefore enabling the formation of atomic-sized tips. A relative distance calibration by means of tunnelling current measurements between the two electrodes revealed that the theoretical ratio between pushing-rod translation and the resulting electrode separation (2.1×10^{-5}) corresponds very well to the experimentally measured value (1.8×10^{-5}).

The stability of the electrodes at fixed, low temperature (e.g., $T = 30$ K) is extraordinary. For instance, a constant tunnelling resistance of (15 ± 3) MΩ can be maintained over many minutes. This means that the distance between the separated electrodes varies only within 5-10 picometers. Upon further closing of the junction, it was found that the electrodes cannot be approached arbitrarily close to each other. A "jump-to-contact" to the conductance quantum G_0 was observed for tunnelling resistances below 1 MΩ. The excellent stability between the electrodes changes fundamentally at higher temperatures ($T > 150$ K). Both resolution and the stability worsen at elevated temperatures, which is primarily due to the enhanced mobility of the gold atoms. In slow opening and closing cycles (velocity < 1 picometer/second), conductance quantization in units of G_0 was observed, independent of the temperature. These quantum effects become evident at the moment at which all dimensions of the point contact are smaller than the Fermi wavelength of the metal electrons ($\lambda_F = 0.52$ nm).

In the case of gold, a conductance value of G_0 signifies, by reason of the transmission which is influenced by the chemical valance of the atom (s-orbital), that a single-atom contact has been created. After the breaking of this point contact, the two electrodes possess atomic-sized tips. Such electrodes enable the contacting of single molecules. Hence, a conditioning procedure is described which allows electrode tips of this type to be fabricated automatically.

Molecules as functional building blocks are a promising concept for the post-CMOS era. Early prognoses about the use of molecular components were euphoric. In the meantime, these forecast had to be adjusted considerably, mainly because of the variances in manufacturing at the nanometer scale. Although molecules can be produced identical thanks to their chemical synthesis, their variable coupling to the electrodes causes large fluctuations in the measurement of the transport properties. To take this into account, special attention was paid to statistics in the experiments. For these reasons, a novel statistical measurement and analysis approach was developed. It facilitates the observation of transport properties, namely, the current-voltage curves, during the controlled manipulation from the formation to the breaking of the molecular junction. Because of the choice of the control parameters made, the measurement approach works independently of the distance of electrodes. Hence temperature ramps can be performed, while the influence of the thermal expansion of the electrode is being compensated. In the subsequent statistical analysis using the software tools developed, it was not only possible to determine the most probable transport characteristics occurring in huge data sets, but also to quantify the variations in the process. For instance, the stochastic fluctuations in the molecule–metal contact, an inherent feature of the thiol-metal bond, can be observed and quantified.

Based on this statistical approach, molecular model systems which allow a independent investigation of the different aspects of molecular transport were studied systematically. In the first part, the molecule–metal contact, which is an eminently important factor for the transport behavior, was studied. Various molecules were investigated, that differ only in their end groups but not in the molecular backbone. The functional end groups chosen, thiol and isocyanide termination, bond to the metal electrode in varying strengths.

In the case of strong coupling, the electron injection rate from the metal to the molecule increases; thus, the dwell time of the electrons on the molecular orbitals shortens. This causes the corresponding energy levels to broaden energetically. By the spectroscopic analysis at low temperatures ($T = 50$ K), where the influence of the thermal line broadening is negligible, thiol-coupled molecular systems (PDT and BPDT molecules) have been compared with isocyanide-coupled molecular systems (PDI and BPDI molecules). The line broadening caused by the coupling was found to be 50% larger (or 25 mV) in PDT than in PDI. In return, the conductance maxima were found to be slightly higher (95 nS) for PDI than for PDT (70 nS). The isocyanide end group turned out to be a better option, not only concerning the line sharpness, but also concerning the transport properties within the HOMO–LUMO gap, which could be measured in contrast to that in the corresponding thiol-coupled systems. Furthermore, the isocyanide-coupling allows temperature-dependent experiments because the molecule does not lose contact to the electrodes upon cooling. The results indicate that this type of end group possesses an enhanced surface mobility.

In further investigations, the influence of the intramolecular structure on transport at equal coupling was evaluated. Oligophenylenes of increasing length were studied. In the molecular backbone of these oligophenylenes, the electronic overlap of the conjugated subsystems, namely the phenyl rings, is reduced by means of steric hindrance between adjacent methyl groups attached to the phenyl rings. Thus, a selective breaking of the conjugation across the molecules was introduced. According to this idea, molecules with up to four phenyl rings were synthesized (sulphur–sulphur distances of 0.62 nm to 1.97 nm), individually addressed, and electrically characterized. The measurements revealed that the influence of the length of the molecular backbone on the transport properties is significant: For the phenyl-1,4-dithiol, the shortest molecule with one ring and a electrode gap distance of approximately 0.846 nm, only one resonant molecular orbital was lying within the voltage window available. For longer molecules possessing two or more phenyl rings, additional conductance peaks appeared and were found to be characteristic for the particular molecule under investigation. The so-called conductance gap increases from 250 to 580 mV with increasing length of the molecule. This means that the bias for charge-carrier injection has to be increased because the voltage drop across the molecule–metal tunnelling barrier changed according to the increased length of the molecule.

On the basis of the measurements addressing the coupling and the influence of the intramolecular structure on the transport, an attempt to investigate the transport behavior of molecules, which possess an intrinsic functionality, was made. The question of whether single molecules possess an intramolecular function that influences the electrical transport and could eventually be controlled externally was approached by investigating two types of functional molecules: rectifying and voltage-induced switching molecules. A clear diode behavior has been observed for the so-called SB-diode molecule. The behavior turned out to be temperature-independent, and a current rectification ratio of 10 was measured at a voltage of 1.0 V. On the basis of the functional behavior of the current as a function of voltage, even higher ratios could be expected. However, the instability inherent to the electrodes prevented investigations at higher electric-field strengths. Therefore, the maximum rectification ratio was determined to be 15 within the stable voltage window available (– 1.8 to + 1.8 V).

A voltage-induced switching was examined at a functional molecule, the so-called BPDN-DT molecule, and compared with a reference molecule which did not possess a functional internal structure. The reference molecule did not exhibit a switching behavior at low temperatures; in particular no stochastic contact fluctuations were found at low temperatures. In contrast, it was possible to switch the functional molecule in a controlled and reproducible way from a so-called “off” state to a higher conductive “on” state by applying a voltage pulse. By the comparison with the reference system it was proven that the internal functional nitro groups are truly the origin of the switching behavior. Through time-dependent experiments it was further demonstrated that a bistable energy range of approximately 120 mV exists, in which different switching times between the corresponding states occur. The switching times measured for the single-molecule system of 250 μs were only limited by the electronic instrumentation.

Furthermore, an anomalous hysteresis was found in the transport curves, if also the negative voltage branch was included in the inspections. It turned out that the higher conductive state for the positive voltage branch becomes the lower conductive state for the negative voltage branch. Exploring this knowledge, the molecule could be switched back and forth between the two distinct states in a very controlled and reproducible way.

This again enables the single-molecule system to be employed as a real memory cell. The potential to use single molecules as storage devices was demonstrated by repeated write–read–erase–read cycles and by achieving a bit-separation (ratio between “on” and “off” currents) between 7 and 70. The switching pulses used were in the range of milliseconds and during the readout times of several seconds, no change in both states were revealed. Hence, the bit read-out was found to occur non-destructively. Within the measurement time of more than one hour, no degradation of the “on” state was observed, which is an indication for an excellent stability of the molecular system. More than 1500 successive switching cycles were performed without any appearance of an altered switching behavior of the single-molecule switch.

Introduction

Small is beautiful. This is not a meaningless phrase in contemporary microelectronics. All electronic devices used in our daily life such as cellular phones, notebooks, digital cameras, digital assistants, and many more are getting smaller and smaller every year. The consumers of the entertainment and communication industry seem to have an insatiable desire for buying smaller, faster and more powerful devices. The semiconductor industry has made and still makes this performance possible by the continuous miniaturization process affecting all the different parts of electronic devices, from the core components, namely the transistors, to the user interfaces such as the display.

At dawn of information technology, computers were large, heavy objects filling entire rooms. Nowadays, portable computers have the size of one's hand, but possess thousand times higher processor power and memory capacity than the first models. Still, the basic building block of every electronic device is the integrated circuit (IC). In 1965, the very early days of ICs, only about 60 components were integrated on one chip. At this early stage, Gordon Moore, the later co-founder of Intel Corp., predicted that the number of transistors on one IC will double every year. Although Moore's empirical observation had to be re-formulated slightly after a few years (to become a doubling every 18 months), this rule has retained its validity up to now and is known as "Moore's Law". Today, one single processor has up to 55 million transistors (Intel Pentium IV generation). The increasing density of integration comes with a shrinking size of the fundamental building blocks. The miniaturization has reached today a minimal feature size of 90 nm (Intel Pentium IV generation) in mass-fabrication and is expected to shrink further to 30 nm within the next decade.

At the level of 30 nm, which corresponds to the length of approximately 100 atoms in one row, the entire semiconductor industry is supposed to encounter fundamental limitations because the physical concepts underlying the complementary metal–oxide–semiconductor (CMOS) devices will no longer work as quantum effects start to play an important role. Despite this, one should bear in mind that several limitations in CMOS scaling had been anticipated much earlier - and surpassed by sophisticated techniques. The technological skills the semiconductor industry had harnessed over the last 40 years to tackle and finally overcome various issues are numerous, e.g. gate oxides without pin holes, strained silicon, silicon on insulator and many more. There is and will continue to be in future a tremendous effort to push CMOS further and further. However, the ultimate limit of scaling lies on the order of molecules or even atoms. In these dimensions, interesting new physical phenomena appear. This field is called mesoscopic physics, and studies effects of quantum coherence in the properties of materials that are larger than the atomic scale but small compared with macroscopic dimensions. Conceptionally novel approaches are required for future nano-electronic devices tailored to the molecular or even atomic level. Possible candidates for this so-called post-CMOS era are carbon nanotubes, semiconducting nanowires, molecular electronics and, on a long-term perspective, also spintronics.

The first concepts of unimolecular electronics originated in the late 1960s when H. Kuhn introduced his vision of molecular engineering [36; 37]. Since then, it was often referred to as *Molecular Electronics*. H. Kuhn had the vision of performing electronic and logic operations based on molecular structures. Today, the field of molecular electronics is aimed at the use of small ensembles or even individual molecules as functional building blocks in electronic circuitry. The size of a single molecule lies in the range of 0.5 - 3 nm, and therefore as basic building block, it is at least one order of magnitude smaller than current transistors. Thus, single-molecule devices seem to be ideal candidates for future nano-electronics, as they possess the potential for creating high-density devices with low power consumption. Moreover, molecules are well-defined building blocks. Thanks to the chemical synthesis, they are identical and amenable for low-cost production. Molecular mechanisms are very fast and may provide novel intrinsic functionality not known in today’s silicon-based technology. If molecular devices took advantage of self-assembly processes, however, they could also achieve low manufacturing costs.

While on the one hand, molecular electronics has been referred to as a way to uphold the on-going miniaturization, it also possesses a significant challenge, namely, to establish contact to single molecules in a reliable and reproducible way. Understanding the underlying physical concepts of transport through single molecules is the basis for designing and creating molecular electronic devices and circuits. In chemistry, intramolecular functionality is mostly performed in liquids. Therefore, one major challenge is to demonstrate functionality on the single-molecule level in vacuum or another well-defined environment. Accordingly, the research effort was focused on the investigation of charge-carrier transport through single-molecule junctions in order to correlate chemical structure and device functionality.

The experimental investigations of these phenomena require tools for manipulation and characterization at the atomic scale. The mechanically-controllable break-junction technique provides a reliable test geometry for probing the electrical properties of an individual or a small ensemble of molecules. Using this technique, the distance between two electrodes can be controlled in a very precise way, down to picometer resolution to match the length of a single molecule, which can then be placed in between these electrodes, and characterized. This method enables for a reliable and resilient electrical contacting of various molecules, such as molecular insulators, wires, diodes, and molecular switches.

Outline

This thesis discusses electronic transport studies through single-molecule junctions under ultra-high vacuum conditions and at various temperatures. The mechanical controllable break-junction (MCBJ) is chosen as the primary measurement tool. The experiments investigate metal–metal junctions which are later employed as a separated electrode pair for contacting single molecules. These molecules are chosen in such a way that different aspects of transport can be monitored independently. These aspects are the coupling of the molecule to the electrodes and the influence of the internal molecular structure on transport. Very simple molecules act as benchmark systems and enable investigations of more complicated molecular systems. The ultimate goal was to demonstrate intrinsic molecular functionality, namely voltage-induced switching, and logic operation on a singe-molecule level.

The thesis is organized in the following way:

- The **first Chapter** presents the basic theoretical background of mesoscopic physics for understanding charge-carrier transport through metal–metal and metal–molecule–metal junctions.
- An overview on the current status of experimental methods in the field of molecular electronics is given in the **second Chapter**. Furthermore, it introduces the mechanically controllable break-junction technique and other experimental tools used in this thesis.
- Results on the mechanical and electrical properties of metal–metal junctions which are used subsequently as atomic-sized electrodes for contacting single-molecules are presented in the **third Chapter**.

- The large influence of contact effects on the transport properties of molecular junctions is addressed by the development of a statistical measurement approach, described in **Chapter 4**. In this approach, the transport properties are studied simultaneously during the repeated formation and breaking of a molecular junction.

- In **Chapter 5**, the molecule–metal contact is studied by investigating charge-carrier transport through molecules having the same molecular back-bone but different linker groups to the electrode. Thiol-coupled molecules are compared with cyano-coupled molecules.

- To study the influence of the intramolecular structure on the transport properties, a series of oligophenylenes with increasing length and interrupted π-conjugation are electrically characterized in **Chapter 6**.

- The experience gathered in these investigations enables the demonstration of intrinsic molecular functionality in **Chapter 7**: A unimolecular diode and a unimolecular voltage-induced switch are presented. In addition, memory operation on a single-molecule level is demonstrated.

Chapter 1

Theory of Molecular Conductance

In this chapter, a brief introduction to theoretical concepts of mesoscopic physics will be given. It covers the theory of charge-carrier transport through metal–metal and metal–molecule–metal junctions. A metallic junction is present upon bending, breaking, and closing of the metal bridge on the MCBJ sample, whereas metal–molecule–metal junctions are formed when the bridge has broken and molecules are bridging the gap between the two metallic electrodes.

1.1 Theory of Metal–Metal Junctions

The conductance of a macroscopic conductor with dimensions of more than 1 mm [14] is described by the well-known Ohm's law [56]. For these dimensions, the conductance, G, is directly proportional to its cross-sectional area, A, and inversely proportional to its length, l:

$$G = \sigma \cdot \frac{A}{l} , \tag{1.1}$$

where the conductivity, σ, is a material property of the sample independent of its dimensions. Smaller conductors whose dimensions are intermediate between the macroscopic (meaning dimensions larger than 1 μm) and the microscopic (dimensions smaller than 1 nm for metals, or 10 nm for semiconductors) are called mesoscopic. When entering the mesoscopic regime, the wave character of electrons becomes essential for electronic processes, therefore the macroscopic description of transport represented by Ohm's law is no longer valid. Quantum effects will start to play an important role when one or more spatial dimensions of a sample, e.g. its length, l, or width, w, are in the range of one of the following three characteristic length scales

[14]: (1) The phase-coherence length, L_φ, which measures the distance over which quantum coherence is preserved. A typical value for crystalline Au at T = 1 K is around 1 μm [31]. Inelastic electron–electron and electron-phonon collisions can destroy phase coherence. (2) The elastic mean free path, L_{mf}, which roughly measures the distance between elastic collisions of charge-carriers at static impurities, and (3), the de Broglie wavelength, L_{dB}, which is related to the kinetic energy of the electrons: $L_{dB} = h/p$, where h is the Planck's constant and p the momentum of the electron.

Electrons moving through a conductor are scattered at impurities, defects, or by the atoms composing the medium. According to the characteristic length scales, two regimes can be identified for a quasi-1D conductor of length l (see Figure 1.1):

- **Diffusive regime**: Conductor length $l >> L_{mf}$
  Electrons incident to the transport channel are scattered at impurities (Figure 1.1(A)). The resulting electron motion is a random walk with an average step size l_{mf} among the impurities.

- **Ballistic regime**: Conductor length $l << L_{mf}$
  Electrons are not scattered at impurities within the conductor (Figure 1.1(B)). The electron motion is therefore constant, only limited by scattering at the boundaries of the sample.

An overview on the sample dimension (length scale) and corresponding transport mechanisms including the theoretical frameworks is given in Table 1.1. A quantum point contact (QPC) is a point-like constriction between two electrically-conducting regions. In order to study quantum mechanical effects, the size of this constriction has to be comparable to the particular electron wave length and must be much smaller than the mean free path for impurity scattering (see Figure 1.1(C)). It is therefore material-dependent: For semiconductor materials with an electron Fermi wavelength much longer than the order of magnitude for the atomic separation, it is a mesoscopic object (constriction some dozens of nm). Whereas for metals with an electron Fermi wave length in the order of atoms, its size is microscopic (constriction 1 nanometer or smaller). A travelling electron is therefore not scattered at impurities within the QPC, and ballistic transport takes place.

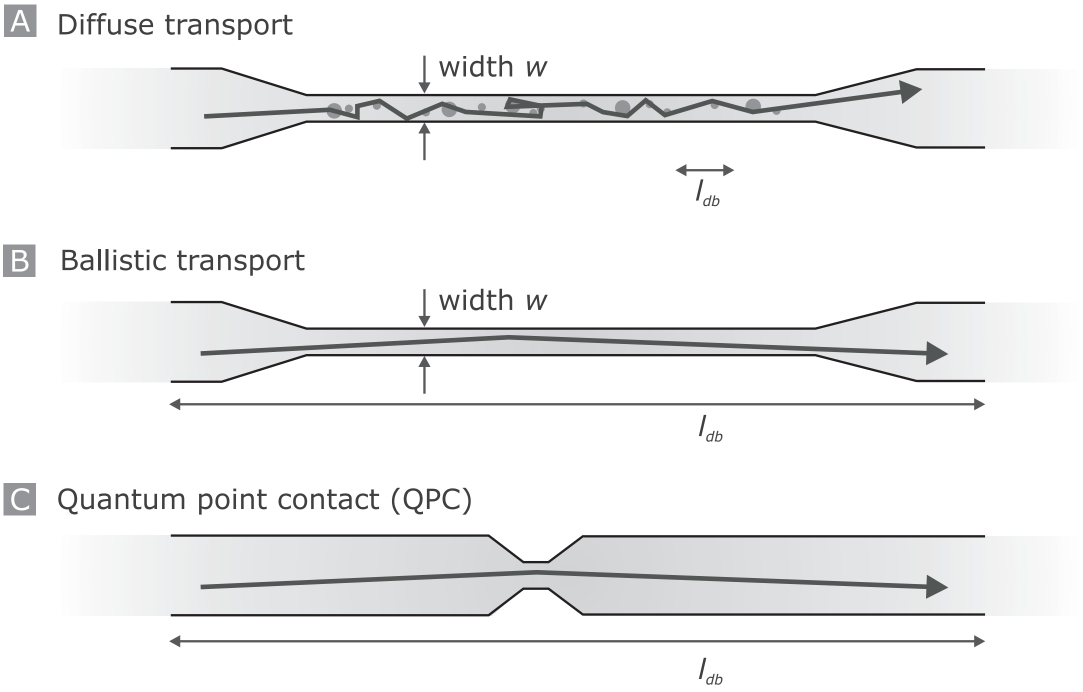
A
Diffuse transport
width w
l_db
B
Ballistic transport
width w
l_db
C
Quantum point contact (QPC)
l_db

Figure 1.1: *Three different types of transport regimes in a mesoscopic, quasi-1D conductor: (A) Diffusive transport due to scattering occurring within the transport channel. (B) Ballistic transport without scattering due to the absence of scattering centers within the channel. (C) Ballistic transport through a Quantum Point Contact (QPC). In QPCs, the width,* w*, and the length,* l*, are both smaller than the characteristic length scale, e.g. the elastic mean free path,* L_{mf}*.*

The contact region of a metal–metal junction in the MCBJ (see following Chapters 2 and 3) can be as small as a single atom. Therefore the contact width, w, and length, l, are both in the order of a metal atom (atom radius, e.g., for Au, approximately 0.288 nm). This geometry is spatially smaller than the Fermi wavelength λ_F of metals, e.g., 0.5 nm for Au. Therefore one enters the full quantum limit.

Length scale	Transport mechanism	Theoretical framework
$\gg 1\mu$m	diffuse	Ohm's Law [56]
$\leq$ 100 nm	quasi-ballistic	Non-equilibrium Boltzman
$\leq$ 10 nm	ballistic + semiclassic	Sharvin [69]
$\leq$ 1 nm	ballistic + quantum	Landauer [38]

Table 1.1: *Length scales ranging from objects much larger than 1 μm down to sub-nm with corresponding transport mechanisms and theoretical frameworks.*

One way to describe ballistic quantum transport processes is to use the Landauer scattering approach [38] (see Table 1.1). This theoretical framework turned out to be particularly powerful for the understanding of various transport properties of mesoscopic conductors, but also for various transport phenomena occurring in other areas of physics, like, e.g. shot-noise power, superconductor–metal heterojunctions and Josephson junctions. The theoretical concept will be described in the next section.

1.1.1 The Scattering Approach

The theoretical concept was proposed by Landauer and Büttiker in 1957 [38]. The idea of this scattering approach is to relate the transport properties of a conductor with the quantum mechanical transmission and reflection probabilities of propagating modes for carriers incident on the sample. Figure 1.2 shows a conductor which consists of a scatterer, S, which is connected via two ballistic leads to a left and a right reservoir of electrons.

Electrons can travel from one reservoir to the other reservoir via the leads and the scatterer. For simplicity, no scattering is assumed to occur in the left and right leads, thus, transport is purely ballistic in these perfect leads. Thus, scattering occurs only within the scatterer, S. In addition, the scattering processes are assumed to be purely elastic and the scattered electrons

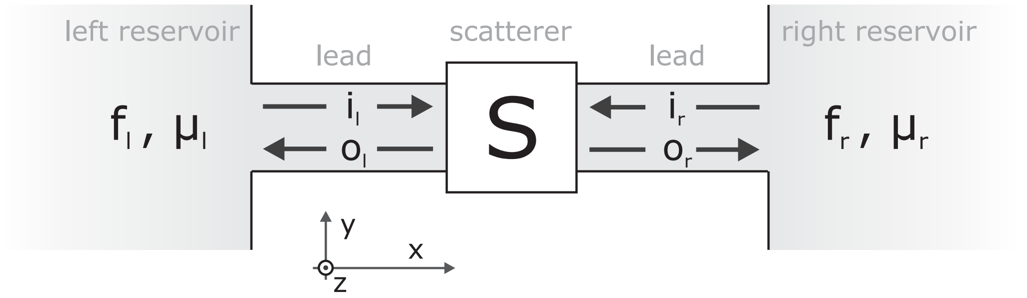

Figure 1.2: *A conductor consisting of a coherent scatterer (S) connected via two ballistic leads to a left and a right reservoir of electrons. The lead direction is labelled x.*

maintain their coherence as a consequence. Inelastic processes occur only in the two reservoirs. The electron distributions in the left and right reservoirs are defined via their Fermi functions:

$$f(E,\mu_\alpha) = \left[exp\left(\frac{E-\mu_\alpha}{k_B T_\alpha}\right)+1\right]^{-1} \ , \ \alpha = l,r, \tag{1.2}$$

where $\mu_{l,r}$ denotes the chemical potential and $T_{l,r}$ the temperature of the left and right reservoir. When applying a potential, electrons are moving from the left to the right reservoir, or vice versa, depending on the bias direction. Due to the transversal confinement of the transport channel perpendicular (y and z direction) to the lead orientation x, the charge-carrier trajectory modes can be described by a plain-wave expression in x and a transverse wave function $\chi_i(y,z)$ in y and z direction:

$$\Psi_i^{l,r} \propto e^{\pm i k_i x}\chi_i(y,z)\,, \tag{1.3}$$

where i = 1,...,N denotes the mode or channel index, l,r an index corresponding to a plain wave moving to the left and to the right, respectively (see Figure 1.2).

The wave vectors for the plane wave expression are k_i. The transverse wave functions $\chi_i(y,z)$ are solutions of the time-independent Schrödinger equation in a confining potential $V(y,z)$:

$$\left[-\frac{\hbar^2}{2m}\left(\frac{d^2}{dy^2}+\frac{d^2}{dz^2}\right)+V(y,z)\right]\chi_i(y,z) = E_i\chi_i(y,z)\,. \tag{1.4}$$

The confining potential is related to the electrostatic potential of the conductor, e.g. in case of a cylindrical wire it is a also a cylindrical potential. The confinement yields in a quantization in the energy spectrum of the electrons in the leads due to transversal confinement perpendicular to the lead orientation. The energy dispersion relation $E_i(k_i)$ in the i-th sub-band is

$$E_i(k_i) = E_i^0 + \frac{\hbar^2 k_i^2}{2m^*} \,, \tag{1.5}$$

with $\hbar$ the reduced Planck constant, and m^* being the effective mass of the charge-carriers. A net current will arise from the imbalance between the population of the modes moving from left to right and the population of the modes moving in the opposite direction. The current, I, is the product of the number of charge carriers multiplied by their charge and travelling velocity. Hence, I, is given by

$$I = \frac{e}{\pi}\int dk\nu_k(f(\epsilon_k, \mu_l) - f(\epsilon_k, \mu_r)) \,. \tag{1.6}$$

In the one-dimensional system of a QPC, the density of states is DOS(ϵ) = $(1/\nu_k)\cdot\hbar$ [2] for one channel and the current can then be simply written as

$$I = \frac{2e}{h}\int d\epsilon(f(\epsilon, \mu_l) - f(\epsilon, \mu_r)) \,. \tag{1.7}$$

For T = 0 K, the Fermi function $f(\epsilon, \mu_\alpha)$ is a step function, equal to 1 for energies below ϵ + eV/2, and ϵ - eV/2 respectively, and equal to 0 above these values. Hence, equation (1.7) reduces to

$$I = \frac{2e^2}{h} \cdot V = G \cdot V \,, \tag{1.8}$$

with G = $2e^2$/h. As a consequence, a perfect mesoscopic single-mode conductor has a non-vanishing resistance, given by h/$2e^2$ ≈ 12.9 kΩ.

More modes are taken into account in the Landauer scattering approach: All the incoming modes form a 2N vector (i_l, i_r) with N being the number of channels. The incoming modes are connected to the outgoing modes (o_l, o_r) via energy dependent scattering matrix **s**:

$$\begin{pmatrix} o_l \\ o_r \end{pmatrix} = \mathbf{s}\begin{pmatrix} i_l \\ i_r \end{pmatrix}, \qquad \mathbf{s} = \begin{pmatrix} s_{11} & s_{12} \\ s_{21} & s_{22} \end{pmatrix} = \begin{pmatrix} r & t' \\ t & r' \end{pmatrix}. \tag{1.9}$$

r and t, as well as r' and t', are the reflection and transmission matrices for incoming as well as out-coming waves, respectively. If a voltage, V, is applied to the left reservoir in respect to the right one, the states in the reservoirs are filled up to the energy $\mu_l = E_F + eV/2$ and $\mu_l = E_F - eV/2$, with E_F being the Fermi energy of the reservoirs. Since the product between the group velocity $\nu_i = (1/\hbar) \cdot (dE_i/dk)$ and the density of states of a sub-band $\sigma_i = (1/\pi) \cdot (dE_i/dk)^{-1}$ is independent on energy, the total current is partitioned in equal parts among the modes, each carrying the universal current of $2e/h$ per unit energy. A fraction $(1/N)\sum_n |t_{nm}|^2$ of all incoming modes is transmitted to the right. Only states with energies between $E_F < \epsilon_k < E_F + eV$ contribute to the net current, I:

$$I = \frac{2e}{h} \sum_{n,m=1}^{N} \int_{E_F}^{E_F+eV} dE |t_{n,m}|^2 \; . \tag{1.10}$$

With $G = I/V$, the Landauer formula is obtained for $eV \to 0$:

$$G = \frac{2e^2}{h} \sum_{n,m=1}^{N} |t_{n,m}|^2 = \frac{2e^2}{h} Tr(\mathbf{tt}^\dagger) = G_0 \cdot Tr(\mathbf{tt}^\dagger) \; , \tag{1.11}$$

with $G_0 := 2e^2/\mathrm{h}$ and $\mathrm{Tr}(\mathbf{tt}^\dagger)$ the trace of a diagonalized matrix $\mathbf{tt}^\dagger$.

1.1.2 Conductance Quantization

Due to the quantum mechanical nature of the electron waves, the resistance of the ballistic conductor without scattering is not equal to zero. If no backscattering takes place inside the conductor, all modes have unit transmission probability and $\sum_{n,m=1}^{N} |t_{n,m}|^2$ becomes an integer number. Thus, the conductance G of a conductor in the ballistic regime is ideally observed in units of $G_0 := 2e^2/h \simeq 1/12.9\ \mathrm{k\Omega}$.

The Fermi wavelength, λ_F, is a hundred times larger in a two-dimensional electron gas of a semiconductor (e.g. GaAs: 200 nm) than in a metal (e.g. Au: 0.52 nm). Therefore, the first experimental observation of conductance quantization was found in GaAs–AlGaAs semiconductor heterojunction devices [79; 85; 80]. In these experiments, the 2D electron gas is confined at the GaAs–AlGaAs interface and a point contact of adjustable width is created using an electrical field (voltage gate) in order to deplete the electron gas beneath it. Figure 1.3(A) shows the conductance of such a constriction as a function of its width which was varied by means of the voltage on the gate. The resulting conductance steps are smeared-out when the thermal energy becomes comparable to the energy separation of the modes. This is due to the mode splitting, given by [79; 85; 80; 1]:

$$\Delta_{Mode} = \frac{\pi^2 \hbar^2}{2m\lambda_F^2}, \tag{1.12}$$

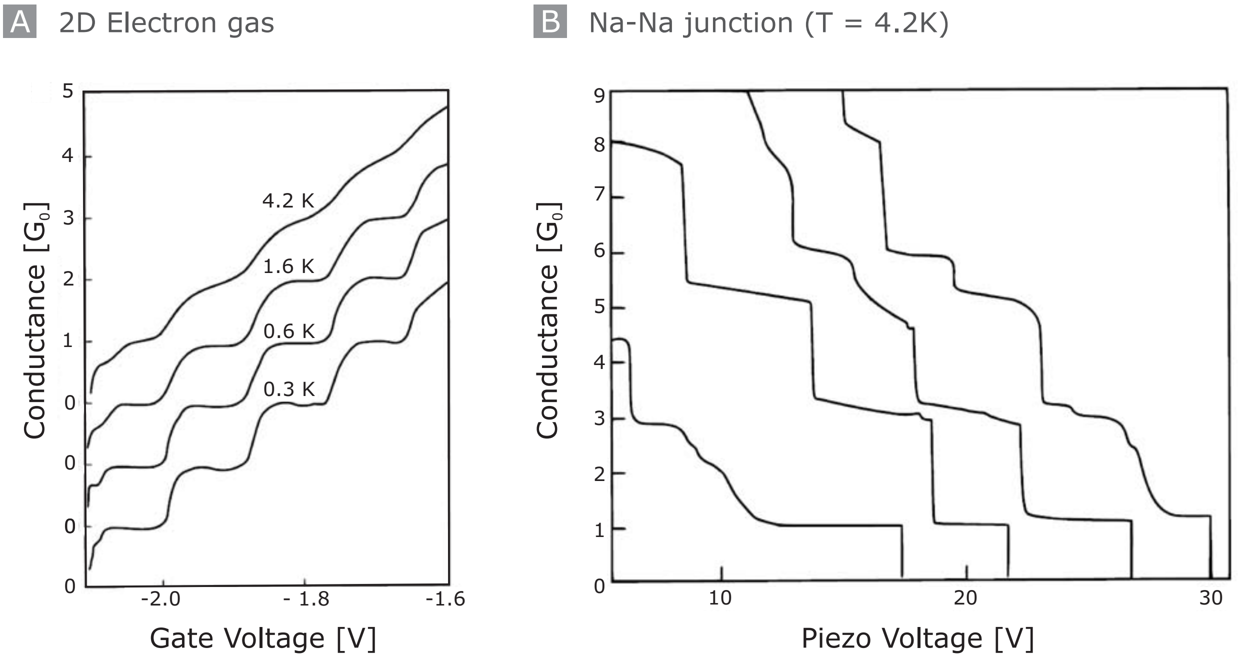

A 2D Electron gas

B Na-Na junction (T = 4.2K)

Figure 1.3: *First experimental observations of conductance quantization: (A) 2D electron gas in a GaAs–AlGaAs heterojunction (reproduced from [82]). (B) Na-Na break-junction (reproduced from [34]). The channel separation of the transverse modes is different due to different Fermi wavelengths in semiconductors and metals: The distinct steps are smeared-out in (A) when the thermal energy becomes comparable to the mode separation, whereas in (B), conductance quantization can even be observed at room temperature.*

Therefore, the order of magnitude for the separation of the modes in a 2D electron gas in semiconductor materials is $\Delta_{Mode,Semiconductor} \approx 1$ meV, which requires cooling to liquid helium temperatures (4.2 K) or below to resolve the splitting, as shown in Figure 1.3(A).

Due to the much smaller Fermi wavelength of metals, e.g $\lambda_{Au} = 0.52$ nm, the size of a metal–metal QPC has therefore necessarily to be of atomic dimensions in order to have quantized conductance. In contrast to 2D electron gas devices, the mode separation in metals is much larger, $\Delta_{Mode,Metal} \approx 1$ eV, sufficiently high to allow the observation of quantized conductance at room temperature.

A relationship between conductance and spatial cross-section of the ballistic contact can be estimated using the semiclassical approximation, the Sharvin formalisms [69]. The total conductance is given by the contact radius, a, and the Fermi wave vector, k_F:

$$G_S = \frac{2e^2}{h}\left(\frac{k_F a}{2}\right)^2 , \tag{1.13}$$

Using this formula, the number of relevant conductance channels $(k_F \cdot a/2)^2$ in a single-atom contact can be estimated. In case of Au, this value is 0.83 and close to 1 [1]. Therefore, a single conductance channel corresponds to a single-atom contact. In other words, the appearance of conductance quantization in metal–metal junctions signals the formation of a few- or even a single-atom contact [32; 78; 1]. Figure 1.3(B) shows the conductance quantization of a Na-Na junction, measured with the MCBJ technique (see following chapter 2). In contrast to semiconductor devices, the conductance channel is varied via spatial elongation of the wire and not via depletion due to the gate voltage. Due to the mode separation, the quantization can also be observed at room temperature as it will be reported in the following Chapter 3.

The atomic-sized contact is described by the geometrical arrangement of the atoms. If the cross-section reduces further to the size of a single atom, the transport properties are determined by the chemical nature of this atom: The number of conductance channels is then determined by the number of valence orbitals of the atom, as directly measured in superconducting contacts by Scheer *et al.* [67; 66]. The theoretical picture developed by Cuevas *et al.* [13] can be understood as a very simple concept: The number of conductance channels is determined by the number of valence orbitals of the atom.

1.2 Theory of Metal–Molecule–Metal Junctions

The above described metal–metal quantum point contacts represent ideal electrodes after their separation for contacting a single-molecule. A prerequisite is that the molecule is equipped with functional end groups which allows to bond chemically to both electrodes (see Chapter 4). Since the molecule has a typical length of a few nanometers, it cannot be regarded as an isolated system itself. For example, the coupling of the molecule to the metal has a strong influence on the energy spectrum of the molecule and therefore also on the transport properties of this molecular system. If the two molecule–metal couplings are both weak, the molecule represents a quantum dot of at least one order of magnitude smaller in size compared to semiconducting quantum dot devices. This enables mesoscopic and many-body effects to be studied at much higher temperatures compared to semiconductor quantum dots.

The theoretical framework of charge-carrier transport through molecular structures involves classical electrostatics and quantum mechanics. Realistic transport models are very complex, therefore only simple models will be discussed in the following sections. Nevertheless, even these simple concepts help to illustrate the general principles of charge-carrier transport through molecular structures.

1.2.1 Electron Hopping and Tunnelling Processes

A molecule bridging the gap between two metallic or semiconducting electrodes acts primarily as a barrier for incoming electrons (and holes) (see Figure 1.4(A)). This situation can be described by the fundamental Landauer approach considering "conduction as scattering". This concept can be generalized to molecular junction structures. Depending primarily on the length of the molecule, either incoherent hopping (long molecules) or coherent quantum tunnelling (short molecules) is the predominant transport process. Figure 1.4(B) shows illustratively a molecule with the coherent quantum tunnelling channel and the hopping channel. In the hopping regime, the electron dwells on several molecular orbitals and transport is therefore incoherent. In the quantum tunnelling regime, the electron passes through the molecule without scattering, therefore transport is coherent.

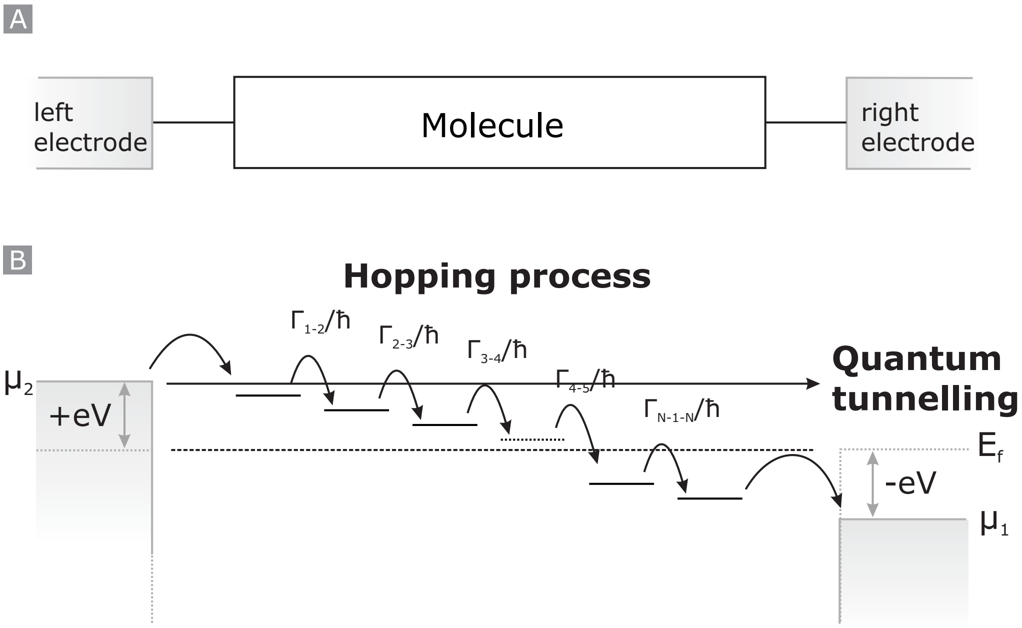

Figure 1.4: *(A) Schematic illustration of a molecule connected to two electrodes. (B) Energetic situation under a small bias V. Inherent hopping process (red) versus coherent quantum tunnelling process (blue).*

Charge-carrier transport through a molecule is in principal a non-equilibrium process and can therefore be regarded as a “balancing act”. In the equilibrium energy level diagram, current flow involves a non-equilibrium situation where the left and right electrodes have different electrochemical potentials, $\mu_{l,r}$ (see Figure 1.5). For instance, if a positive voltage V is applied externally between left and right electrode, then the electrochemical potentials are increased in case of the left electrode, $\mu_l = E_f + eV/2$, or lowered in case of the right electrode, $\mu_r = E_f - eV/2$ (the voltage drop does not necessarily have to be symmetric). The left and right electrodes thus have different Fermi functions and each seeks to bring the active device into equilibrium with itself. The left electrode keeps pumping electrons into the molecule hoping to establish equilibrium. But equilibrium is never achieved as the right electrode keeps pulling electrons out in its bid to establish its own equilibrium. The system thus enters into a continuous process between the two reservoirs. To describe this balancing process, we need a kinetic equation that keeps track of the in- and out-flow of electrons from the reservoirs.

1.2.2 Single-level Model

The conductance through a simple molecule represented by one energy level and sandwiched between the two metallic electrodes can be calculated analytically. This single, discrete molecular level has an energy, ε, in respect to the Fermi energy of the metal contacts. The charge-carrier transport can be described using kinetic equations. The total number of electrons located on the molecular level, N, can be calculated in equilibrium using the number of electrons being injected from the left reservoir, $N_l = 2f(\varepsilon, \mu_l)$, and from the right reservoir, $N_r = 2f(\varepsilon, \mu_r)$, respectively (the factor 2 comes from the spin degeneracy). The resulting current injected from left and right can be expressed as follows:

$$\begin{aligned} I_l &= e\frac{\Gamma_l}{\hbar}[N_l - N] \,, \\ I_r &= e\frac{\Gamma_r}{\hbar}[N - N_r] \,, \end{aligned} \tag{1.14}$$

with $\Gamma_{l,r}$ being the injection (and escape) rates from left or right electrode onto the molecule.

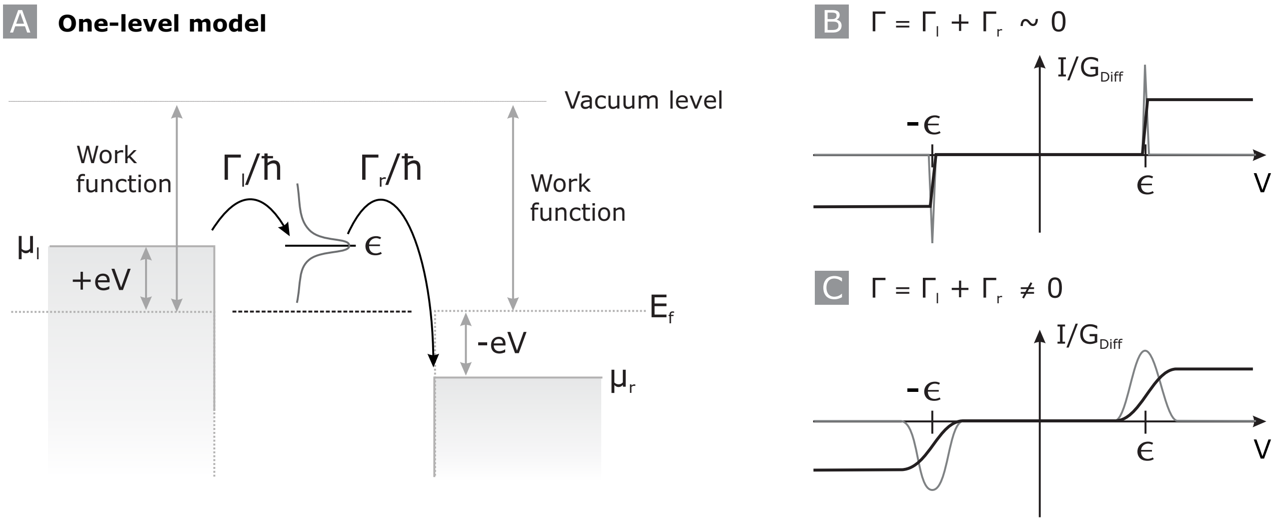

Figure 1.5: *(A) Simple one-level model of a molecule represented by one molecular orbital with hopping rates $\Gamma_l/\hbar$ and $\Gamma_r/\hbar$ to left and right electrodes. (B) Corresponding I–V and G_{Diff}–V data without broadening, and (C) with broadening of the molecular level due to coupling.*

Under equilibrium, I_l must be equal to I_r, defining the number of electrons on the molecule

$$N = \frac{\Gamma_l N_l + \Gamma_r N_r}{\Gamma_l + \Gamma_r} . \tag{1.15}$$

The net current is then obtained by using equation (1.14) to be:

$$I = \frac{2e}{\hbar} \frac{\Gamma_l \Gamma_r}{\Gamma_l + \Gamma_r} [f(\varepsilon, \mu_l) - f(\varepsilon, \mu_r)] . \tag{1.16}$$

This single molecular orbital affects the transport properties as it can be seen in the behavior of the corresponding current-voltage, I–V curves as illustrated in Figure 1.5(B): For small voltages, $V < V_\varepsilon$, the current is zero because both μ_l and μ_r are below the energy level, ε (see Figure 1.5(A)). When increasing the bias further to the voltage V_ε, the chemical potential of the left (or right) electrode, μ_l, (or μ_r, respectively) is aligned with the molecular energy level in resonance, ε. The current increases instantaneously to I_{max}, which is the maximum current that can flow through this particular level. It is obtained from equation (1.15) by setting $f(\varepsilon, \mu_l) = 1$ and $f(\varepsilon, \mu_r) = 0$:

$$I_{max} = \frac{2e}{\hbar} \frac{\Gamma_l \Gamma_r}{\Gamma_l + \Gamma_r} . \tag{1.17}$$

When increasing the voltage further, μ_l lies above the energy level but the current cannot increase further because no additional energy level can contribute to the transmission. As a consequence, the I–V curve shows a step at $|V| = E_f - \varepsilon$. Therefore, the energetic position of the molecular orbital involved in transport can be determined in respect to the Fermi energy of the metal from the step in the transport characteristics measured.

This single-level model represents an ideal picture of molecular transport. In reality, the situation is more complicated since the molecular orbital is not a delta function but broadened, as it will be shown in the next section.

1.2.3 Broadening of Molecular Energy Levels

In the inherent hopping regime, a finite dwell time of the electrons on the molecular orbital arises from the coupling of the molecule to the contacts. The injection rate, Γ_i, is thus related to the broadening of the molecular levels caused by the coupling of the molecule to the contacts. The total broadening of the single energy level is the sum of left and right broadening: $\Gamma = \Gamma_l + \Gamma_l$. The resonant level broadening can be described by a Breit-Wigner or Lorentzian distribution [7; 6]:

$$D(E) = \frac{\Gamma/2\pi}{(E-\varepsilon)^2 + (\Gamma/2)^2} \,. \tag{1.18}$$

The Breit-Wigner distribution can be implemented into Equation (1.16), which now becomes an integral over energy in order to consider all contributions caused by the broadened energy level:

$$I = \frac{2e}{\hbar} \int_{-\infty}^{\infty} dE D(E) \frac{\Gamma_l \Gamma_r}{\Gamma_l + \Gamma_r} [f_l(E, \mu_l) - f_r(E, \mu_r)] \,. \tag{1.19}$$

Compared to equation (1.16), the step-like increase in the I–V plot at $|V| = E_f - \varepsilon$ is now smeared-out and no longer squared (Figure 1.5(C)). The G_{Diff}–V plot has changed from a delta function to a broad peak located at $|V| = E_F - \varepsilon$. However, the energetic position of the molecular orbital in respect to the Fermi energy can still be determined from the I–V data.

The level broadening arising from coupling is only one effect which illustrates that the energetic properties of the metal–molecule–metal system clearly differs from the one of the corresponding isolated molecule in vacuum. Another effect of the chemical coupling of the molecule to the electrodes is the charge-transfer upon establishing contact between a molecule and a metal reservoir as it will be discussed in the next section.

1.2.4 Charging Effects

In the previous section it has been shown that the discrete energy levels of an isolated molecule are broadened due to the finite dwell time of electrons on the molecule. Here, it will be demonstrated that the molecular levels are additionally shifted in respect to the vacuum level when coupling the molecule to metallic leads.

HOMO and LUMO are acronyms for the Highest Occupied Molecular Orbital and the Lowest Unoccupied Molecular Orbital, respectively. The HOMO level is to organic molecules what the valence band is to inorganic semiconductors, and the LUMO to the conductance band, respectively. The Fermi-level of the metal used as electrode material lies somewhere in the so-called HOMO-LUMO gap, where the charge-neutral level of the molecule is positioned.

The location of the Fermi energy relative to the HOMO and LUMO levels is probably the most important factor in determining the *I–V* characteristics of molecular conductors. Typical values for work functions of metals are $\Phi_{Au} = 5.3$ eV, $\Phi_{Al} = 4.3$ eV, $\Phi_{Pt} = 5.3$ eV, and $\Phi_{Ag} = 4.3$ eV [2].

When a molecule is coupled chemically to the metal, a partial charge-transfer takes place (without having applied an external bias). Therefore, the number of electrons on the molecule differs from the vacuum equilibrium value of an isolated molecule. The additional potential caused by these charges has to be considered in the calculations, representing electrons lost or gained by the molecule upon coupling to the leads. The charging energy, $U_{charging}$, describes how the molecular levels are shifted in energy by a contact potential due to changes in the intramolecular electrostatic potential.

$$U_{charging} = U(N - 2f^0) \, , \tag{1.20}$$

with $f^0 = f(\varepsilon_0, E_f)$ being the equilibrium Fermi distribution.

Regime	Γ_l	Γ_r	Comparison	Charge transport
Coulomb blockade	weak	weak	$\Gamma_{l,r} \ll U_{charging}$	Integer values of e
Self-consistent field	weak or strong	strong or weak	$\Gamma_{l,r} \ll U_{charging}$ or $\Gamma_{l,r} \sim U_{charging}$	Fractional values of e
Self-consistent field	strong	strong	$\Gamma_{l,r} \geq U_{charging}$	Fractional values of e

Table 1.2: *Different charge-carrier transport properties for the three distinct regimes of coupling.*

The charging potential shifts each molecular level ε_i equivalently:

$$\varepsilon_i = \varepsilon_i^0 + U_{charging} \ , \tag{1.21}$$

with ε_i^0 being the energy level of the isolated molecule. This modified energy can be inserted into equation (1.18) to express the density of states including charging effects:

$$D(E) = \frac{\Gamma/2\pi}{(E - \varepsilon - U_{charging})^2 + (\Gamma/2)^2} \ . \tag{1.22}$$

The coupling term, Γ, generally depends on the energy, $\Gamma = \Gamma(E)$, therefore, $D(E)$ can deviate significantly from the ideal shape of the Lorentzian distribution. Depending on the relative magnitude of $\Gamma_{l,r}$ in respect to $U_{charging}$, different transport regimes have to be considered, as displayed in Table 1.2: If a molecule is weakly coupled to the leads, e.g., a molecule physisorbed to two contacts, Coulomb blockade is present and charge-carrier transport occurs in integer values of the charge quantum e. Strong coupling occurs due to hybridization between molecular orbitals and the delocalized wave functions of the electrodes (e.g. a molecule chemisorbed between two contacts). Fractional charge-carrier transport is then observed and the regime is so-called self-consistent field.

1.2.5 Multi-level Generalization and Molecular Structure

Using the above described single-level model, charge carrier transport through a single molecule can be described taking into account the two molecule-metal coupling terms, the resulting energy level broadening, and charging effects. The molecule itself, however, is a much more complicated three-dimensional object than represented by a single molecular energy level. A more satisfactory description can be achieved when more molecular levels are included in the calculations and the transmission is described by the density of states (DOS). The DOS quantifies how closely packed the molecular energy levels are. By the thermal line-broadening, the DOS changes from a superposition of delta functions to a continuous function. Assuming the charge transfer upon coupling a molecule to leads (see section 1.2.4), it is obvious that the vacuum DOS is only a rough estimation for describing the transmission through an individual molecule coupled to leads. Thus, the generalization of multiple single levels by the DOS does not sufficiently describe the three-dimensionality of molecular structures.

Molecules are not flat and formless but have well-defined spatial arrangements that are determined by the length and the orientation of their chemical bonds. Since electrons and nuclei are charged particles, electrical forces of attraction and repulsion determine the bonding and the spatial arrangements. This again defines an atomic orbital for each electron surrounding a nucleus which is related to its quantum mechanical probability of finding an electron in a particular volume in a given distance and direction from the nucleus ($1s$; $2s$, $2p$; $3s$, $3p$, $3d$; $4s$...). The electronic structure of the entire molecule is then a linear combination of the individual atomic orbitals, which defines the molecular orbitals of the molecule. A perfect example to illustrate this principle is the benzene molecule, consisting of six carbon atoms hexagonally arranged with an H atom adjacent to each C atom (molecular formula: C_6H_6). Figure 1.6 shows the molecular structure with the different representations (A), and an illustration of the molecular orbitals (B).

A covalent bond between two atoms involves sharing a pair of electrons; one from each atom. Two overlapping atomic orbitals can be considered to combine in either a low-energy bonding or a high-energy antibonding molecular orbital. The first case is called a σ-bond, the latter one a σ^*-bond. Sidewise overlap of p-orbitals is called π-bond. The π-bond differs from the

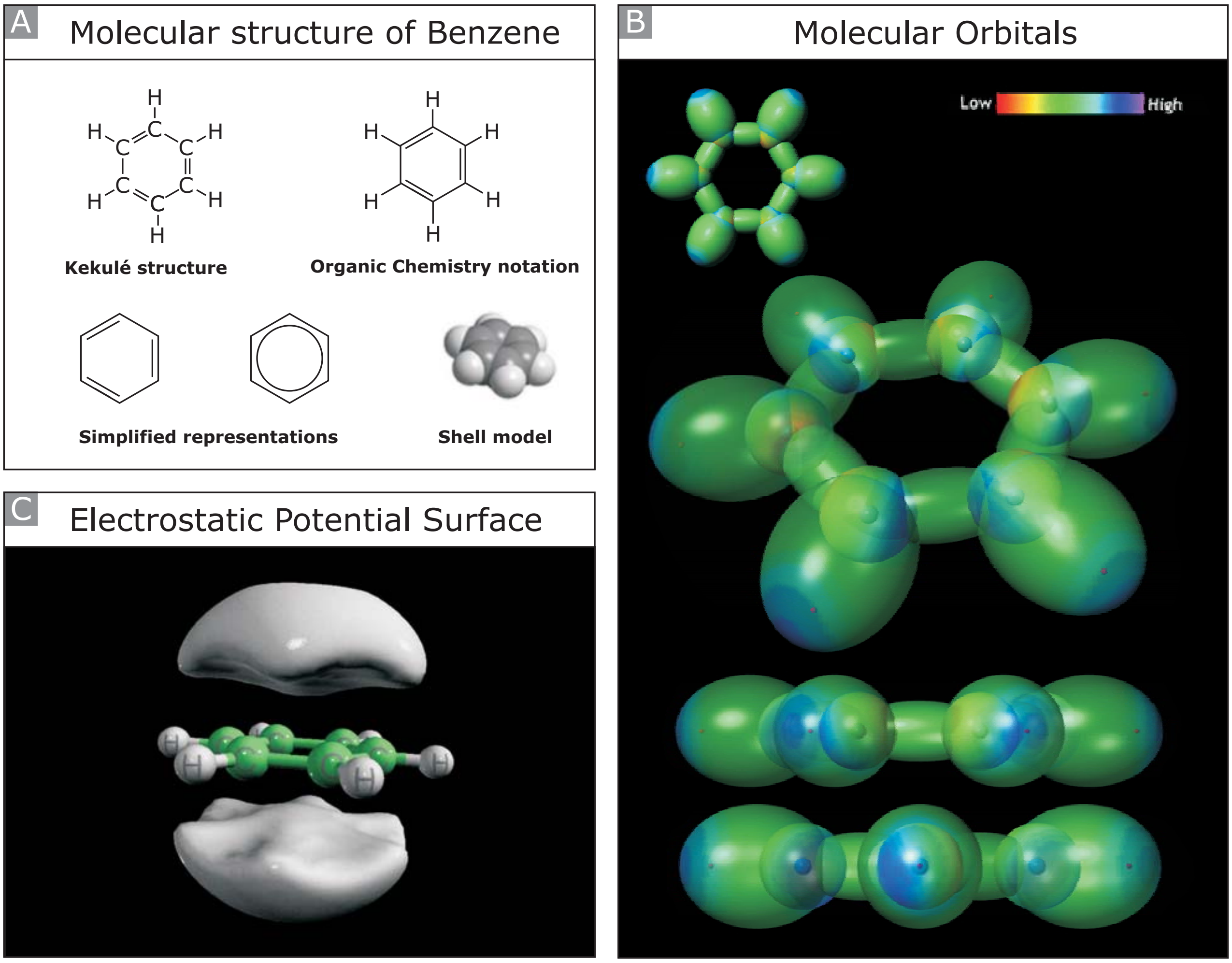
A
Molecular structure of Benzene
Kekulé structure
Organic Chemistry notation
Simplified representations
Shell model
B
Molecular Orbitals
Low
High
C
Electrostatic Potential Surface

Figure 1.6: *(A) Molecular structure of Benzene (C_6H_6) in different representations. Kekulé and organic chemistry notation, simplified non-resonant and resonant structure, as well as the shell model. (B) The linear combination of the atomic orbitals define the molecular orbitals (reproduced from Blacklight Power Inc., www.blacklightpower.com). (C) Delocalized π orbitals illustrated with the electrostatic potential surface (gray color-code).*

σ-bond in that electron density is concentrated in the regions above and below the bond axis rather than along the bond axis. The benzene ring is comprised of alternating single–double carbon–carbon bonds. The π-electrons are perfectly paired all around the ring and form continuous π-bonds above and below the carbons atoms in the ring.

Figure 1.6(C) shows the delocalized π-bonds, defining the aromatic benzene system. The carbon–carbon system is called a conjugated system, since the individual orbitals are hybridized and the probability of finding an electron is equal all over the ring.

The relatively simple benzene ring already suggests that the electronic structure of a molecule can be fairly complicated. However, the electro-dynamical and chemical interactions between different orbitals, their varying degree of conjugation, and the possibility of adding (reduction) or loosing (oxidation) charges are the causes of various intramolecular electron transfer reactions. Molecular electronics takes advantage of this intrinsic functionality since the different conjugation paths across the molecule can be varied dynamically in such a way that they are affecting the charge-carrier transport properties through the functional molecule.

1.2.6 Semi-Empirical and First-Principle Calculations

A number of theoretical concepts with the goal to explain and even predict the electronic behavior of molecular devices has been developed. The different approaches mainly differ in the way they take into account the electronic levels of the molecule, the modification by the coupling to the leads, and the change of electrostatic potential due to bias. Semi-empirical methods [15; 44; 22] as well as first principle calculations [68; 72; 74] are used, the latter being restricted to systems of moderate size.

Since $U_{charging}$ depends on the number of electrons on the molecular system, calculations in the self-consistent field regime are performed iteratively. First, the charging potential, U, is calculated using equation (1.20) assuming that a certain number of electrons is preserved in the molecular orbital from the start. This enables to calculate the electron distributions in both reservoirs, as well as the number of electrons according to equations (1.15), and (1.16) using an iterative process.

Common to all the theoretical results is the sensitivity in the positioning of the molecular orbitals in respect to the Fermi energy, E_F, of the metals. This is due to the low DOS in the HOMO-LUMO gap of molecules. Depending on the energetic situation, charge-carrier transport occurs either through the LUMO (n-type conduction, E_F closer to LUMO) or through the HOMO (p-type conduction, E_F closer to HOMO). More complicated models take further into account the potential profile across the molecule by solving the Poisson equation for the potential between the two electrodes.

$$\nabla \cdot (\varepsilon \nabla U_{applied}) = 0 \, , \tag{1.23}$$

and taking charging effects into account

$$\nabla \cdot (\varepsilon \nabla (U_{applied} - U_{charging})) = 0 \, , \tag{1.24}$$

All calculations revealed that the orientation of the atoms belonging to the molecule and to the contacts, the different binding sites, and the surface reconstruction (with different work functions) are crucial parameters. In general, independent on the different models, all calculations predict the current several orders of magnitudes too high compared to the experimental findings. The calculations predict typically several micro-Amps at 1 V, whereas the experimental results report only on a few to tens of nano-Amps at 1 V, i.e., the typical resistance of a molecule is in the order of some MΩ to GΩ.

A satisfactory understanding of molecular transport has not yet been achieved, as it is discussed in more details in a recent review on molecular transport models given by reference [55]. Some of the problems with the theoretical transport calculations in molecular structures are supposed to be the missing band structure of molecules, the lacking effective mass of charge-carriers, the presence of a real 3D problem (without the possibility of a transformation in the k-space), a soft matter structure with variable bond lengths, and open boundary conditions.

1.2.7 Inelastic Effects

The internal vibrational and rotational modes of a molecule can be excited electronically by electron and hole injection from both electrodes. Electrons can thereby undergo inelastic processes while tunnelling or hopping through a molecule. The so-called inelastic electron tunnelling spectroscopy (IETS) therefore provides a powerful technique to study individual molecules and their corresponding vibrational excitations.

Figure 1.7 shows schematically a metal–molecule–metal system where the molecule is represented by one energy level for simplicity. It is assumed that there is a strong coupling between the electrons and the vibrational states. As the bias voltage, V, reaches the first molecular orbital, purely elastic tunnelling through this particular molecular orbital takes place (Figure 1.7(A)). Therefore, no energy is dissipated within the molecule. The total transmission, σ, consists only of an elastic channel, σ_e. Increasing the bias voltage further, the energy reaches the threshold level for exciting a molecular vibration ($eV > h\nu$). Therefore, an additional channel for inelastic electron tunnelling, σ_{ie}, opens up (Figure 1.7(B)). Thus, the energy is transferred to the molecular system, exciting vibrational and rotational modes of the molecule. The transmission has now an additional inelastic contribution $\sigma = \sigma_e + \sigma_{ie}$.

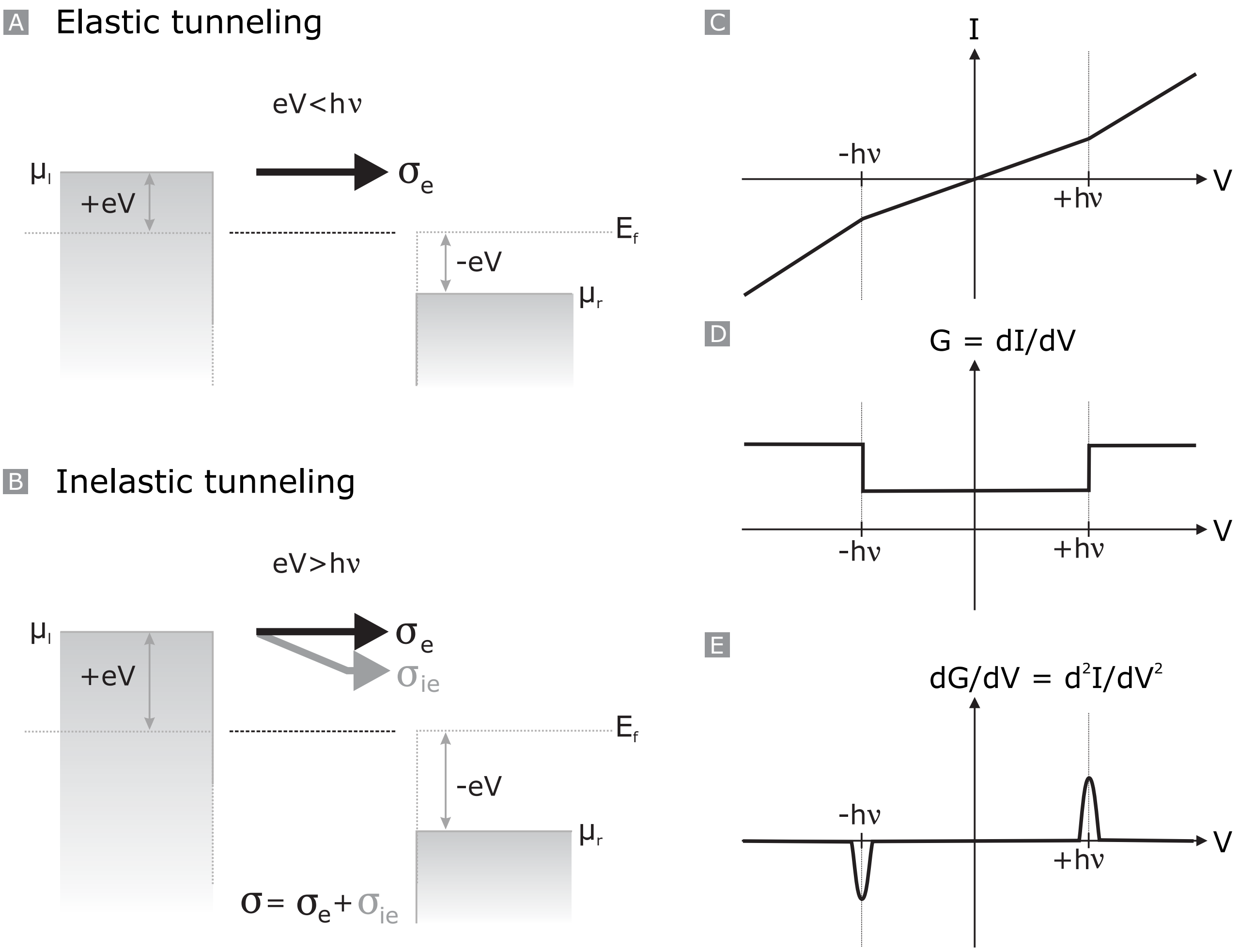
A
Elastic tunneling
eV<hν
μl
+eV
σe
Ef
-eV
μr
B
Inelastic tunneling
eV>hν
μl
+eV
σe
σie
Ef
-eV
μr
σ= σe+σie
C
I
-hν
+hν
V
D
G = dI/dV
-hν
+hν
V
E
dG/dV = d²I/dV²
-hν
+hν
V

Figure 1.7: *Schematic Illustration of (A) elastic electron tunnelling, and (B) inelastic electron tunnelling. An Additional inelastic channel gives rise to (C) two kinks in the I–V, (D) two steps in the* G_{Diff}*–V, and (E) two peaks in the* dG_{Diff}/dV*–V plot.*

This additional channel can be observed in the current–voltage (I–V) plot as two kinks (Figure 1.7(C)), located at $-h\nu$, and $+h\nu$, respectively. These kinks evolve as steps in the differential conductance–voltage, $G_{Diff} = (dI/dV)$–V, (Figure 1.7(D)) and peaks in the (dG_{Diff}/dV)–V plot (Figure 1.7(E)). The positions of these peaks are characteristic for the molecular vibration excited, being, e.g., C–H bond.

Chapter 2

Experimental Techniques

2.1 Experimental Methods in Molecular Electronics

The investigation of charge-carrier transport through molecular structures has attracted both scientific and technological interest during the past thirty years. The motivation for the various research activities at the molecular or even atomic scale has already been illustrated in the introductory chapter. In general, Molecular Electronics is aimed at the use of small ensembles or even individual molecules as functional building blocks in electronic circuits. The molecules of interest have a typical length in the order of 0.5 – 5 nm. General requirements for making contact to such small objects are a pair of atomic-sized electrodes, an accurate control of their distance in the sub-atomic range, an appropriate mechanical stability, and a chemical coupling between the molecule and the electrodes causing the confinement of the molecule between the electrodes.

The understanding of electronic transport through a single molecule has been a scientific key challenge, which became experimentally feasible only very recently. Experimental realizations of the early theoretical concepts and predictions, e.g. the unimolecular rectifier proposed by A. Aviram and M. Ratner in 1974 [61], were impossible to demonstrate experimentally due to the general impracticality to manipulate single atoms and molecules. In 1981, more than ten years after H. Kuhn's vision, the Scanning Tunneling Microscope (STM), was invented by G. Binnig and H. Rohrer [4]. It was the first technique to create atomic-sized contacts.

Today, feature sizes down to about 50 nm can be fabricated in mass-production using optical lithography. Electron-beam lithography opens the way to manufacture even 10 nm feature sizes. Nevertheless, there is still a large discrepancy of at least one order of magnitude in the manufacturing capability for making contact to a single-molecule using optical or electron-beam lithography techniques. Until lithography can achieve the feature size of 1 nm, conceptual novel approaches are required for making contact to a single-molecule.

In that respect, contacting an ensemble of molecules seems to be an easier and more practical method in terms of electrode fabrication. Therefore, the first molecular transport studies employed molecular multi- [36; 37] and monolayer [24; 48] architectures based on the Langmuir-Blodgett technique to create a self-assembled monolayer (SAM) of molecules (see Figure 2.1(A)). The formation of SAMs onto metals is nowadays well-known with the most widely studied systems being alkanethiols on Au [77]. In this experiment, the second contact is usually established by evaporation of a thin metal layer on top of the molecular film. This enables a huge ensemble of molecules, in the order of 10^4 to 10^{12}, to make contact to the top metal layer and to conduct electrical characterization. However, the evaporation process at hot temperatures is detrimental for the molecules.

Less destructive techniques for the molecules can be applied instead of evaporating the second electrode at high temperature. For instance, the Mercury drop technique, which does not require a hot process step. In Figure 2.1(F) a two-terminal junction is shown, where one electrode is formed by a Mercury drop making contact to a SAM grown previously on a metallic substrate. Due to the high surface tension of Mercury, no meniscus is formed and a very small and controllable contact area to the SAM is established. The droplet can also be removed in order to repeat the measurement. Further progress towards the single-molecule level was made by shrinking the two electrode surface areas: In the so-called crossed-wire technique shown in Figure 2.1(E), a wire is covered with a SAM whereas another wire is deflected in a magnetic field $\vec{B}$ by passing a current through the wire. Due to the induced magnetic field, the deflection wire can be approached to the static wire under the Lorentz force. The active contact area is hence much smaller than in conventional SAM devices and even the gap distance can roughly be adjusted.

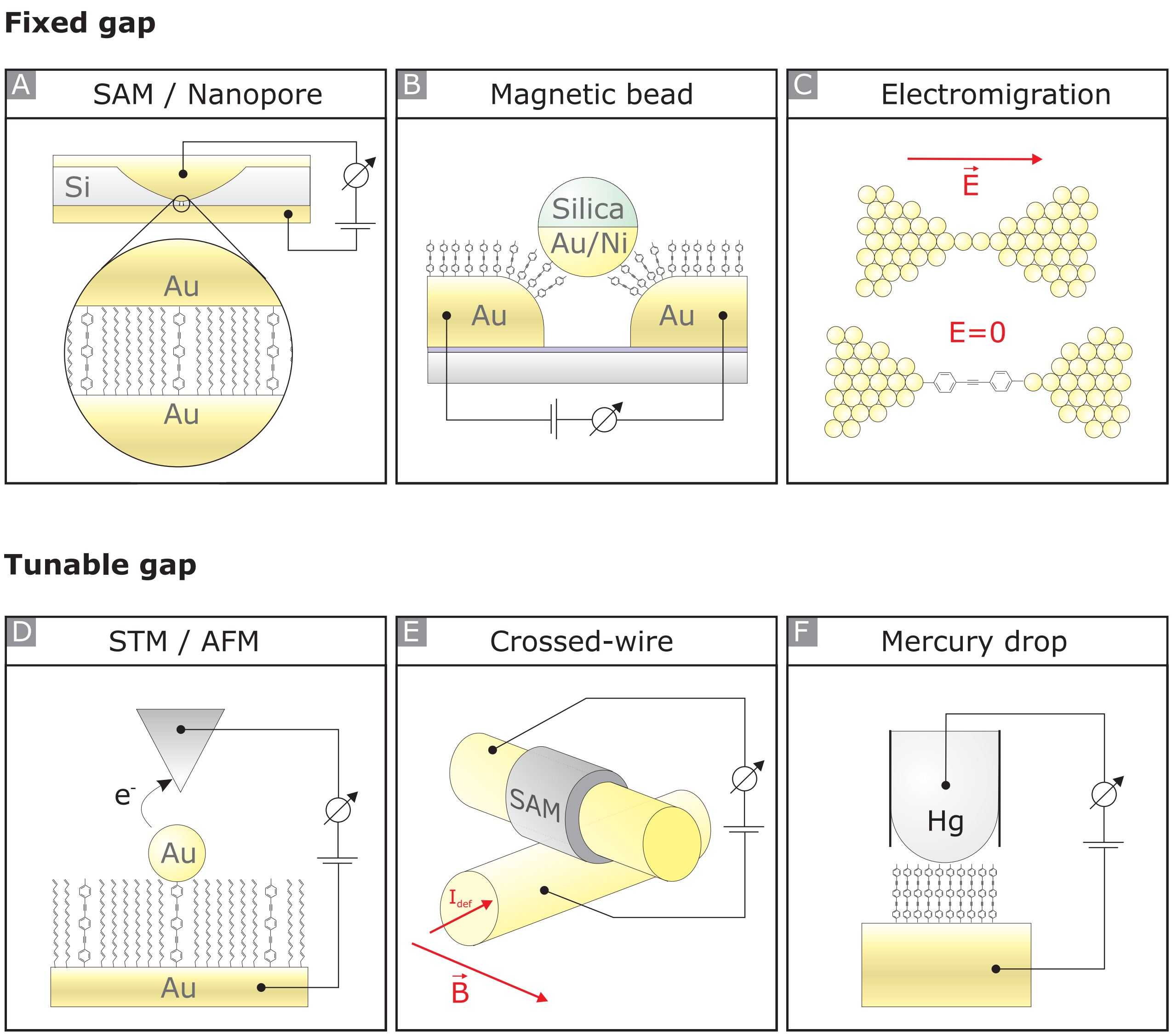
Fixed gap
A
SAM / Nanopore
Si
Au
Au
B
Magnetic bead
Silica
Au/Ni
Au
Au
C
Electromigration
$\vec{E}$
E=0
Tunable gap
D
STM / AFM
e-
Au
Au
E
Crossed-wire
SAM
I_{def}
$\vec{B}$
F
Mercury drop
Hg

Figure 2.1: *Schematic illustration of various selected experimental approaches used for contacting molecules: The upper row shows approaches with a fixed gap. (A) Self-assembled monolayer (SAM) and Nanopore architectures, (B) magnetic bead junction, and (C) electromigration techniques. The lower row shows techniques which offer a tunable gap: (D) STM/AFM technique allowing for direct or indirect (via Au cluster) contact to the molecules embedded in a supporting insulating SAM of other molecules. (E) Crossed-wire junction where one wire is covered with a SAM whereas the other one is deflected by the Lorentz force in a magnetic field* $\vec{B}$ *by passing a deflection current through the wire. (F) Mercury drop technique making use of the high surface tension of Mercury without formation of a meniscus creating therefore a defined contact area.*

Using optical lithography techniques, the contact areas sandwiching a SAM were further shrunk and so-called cross-bar structures were developed. In these structures, an array of molecular junctions with many thousands of molecules contacted in parallel have been fabricated. The use of different metals or different deposition techniques yields in an inherently asymmetric device architecture, thus, mostly asymmetric transport behaviors were observed. This device architecture enabled first molecular memory devices to be presented [12; 35]. Despite of this progress, the stacking and mixing of metallic and molecular layers makes it impossible to clearly differentiate between contact effects (e.g. metallic filaments penetrating the almost insulating molecular layer) and intrinsic molecular functionality [12; 35].

However, for a fundamental understanding of transport at the molecular level, and also for studying intrinsic molecular functionality, it is important to investigate charge-carrier transport through individually contacted and addressed molecules. A prerequisite for such investigations is a set of appropriate electrodes. First, the electrodes need to have a geometrical shape which allows single molecules to be individually probed. Secondly, the distance between the electrodes should be controlled with atomic (1 Å$= 10^{-10}$ m) or even sub-atomic accuracy ($1 \text{ pm} = 10^{-12}$ m).

In 1981, the invention of the STM [4] triggered enormous progress in nanoscale science and technology. In particular, the ability to manipulate single atoms and molecules opened up numerous scientific opportunities. It was the first technique to create atomic-sized contacts: Owing to the ductile response of Au to deformation, a STM tip which was crashed into the surface can be withdrawn from the surface and forms thereby a neck and finally a bridge of individual atoms. Using the Transmission Electron Microscope (TEM), Ohnishi *et al.* [57] were able to observe directly the shrinking of a Au contact upon stretching. Figure 2.2(A) shows a TEM picture of a Au bridge consisting of four Au atoms suspended between the STM tip and the surface. In the same Figure 2.2(B)–(D), the contact formation using a STM tip was calculated and schematically illustrated. Hence, the STM technique fulfills the first prerequisite of atomic sized electrodes.

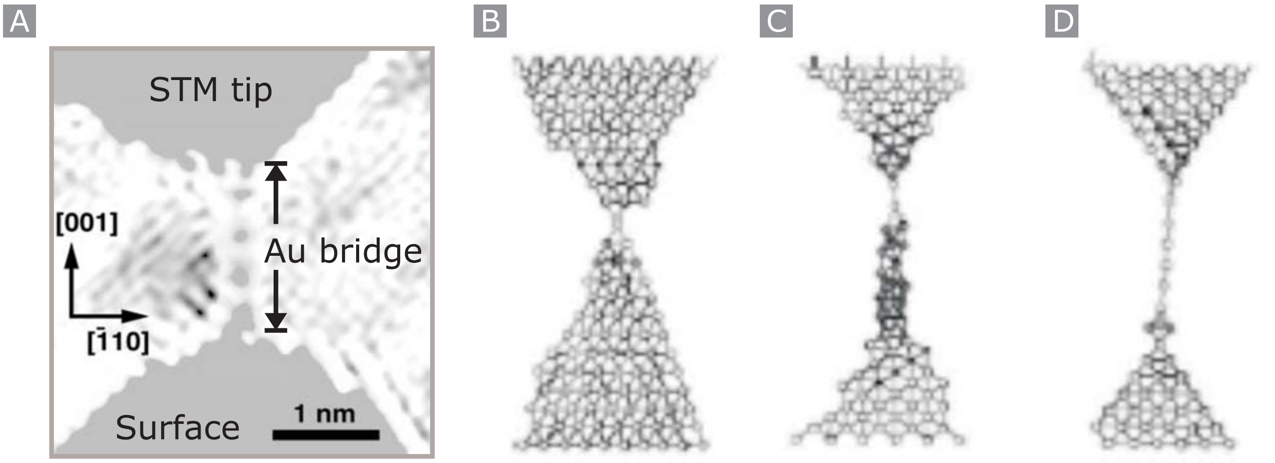

Figure 2.2: *(A) TEM image of a Au bridge consisting of 4 Au atoms between a STM tip and the surface consisting of 4 Au atoms (reproduced from [58]). (B) Calculation of an atomic contact formation using a STM (reproduced from [73]).*

For transport investigations, the molecules of interest are often embedded in an insulating and supporting matrix (e.g. C12 alkanethiolate) in order to compensate the relative low lateral stability between the STM tip and the substrate (see Figure 2.1(D)). The measurements are then performed in constant current mode without establishing a chemical contact to the molecule. An additional Au cluster can be attached to the second linker group of the molecule. This clusters provides a covalent bond to the molecule and allows better contacting. In other experiments, the tip–sample distance is varied resulting in a different number of molecules being captured in the junction [87; 86].

The scanning-probe techniques have two major advantages: First, they provide the ability to image the molecules on the substrate. Second, the tip can be moved very fast in perpendicular direction to the substrate due to piezo control. This allows many thousands of junctions to be repeatedly formed and broken in order to create conductance histograms therefrom. A disadvantage of the scanning probe technique is an inherent lateral drift since the tip and the substrate are mounted at different positions inside the chamber with a large distance between the supporting points.

Compared to STM, the MCBJ technique, which was introduced by Moreland *et al.*, [51], offers improved lateral and vertical stability. Moreland and coworkers used a thin wire of a superconductor mounted on top of a glass substrate to study the tunneling characteristics of superconductors. Further development was made by Muller *et al.* [52], who also introduced the term "Mechanically Controllable Break-Junction". Due to the high stability achieved by a purely mechanical operation principle, e.g. the elastic properties of Au have been monitored [89]. STM and MCBJ experiments are typically performed under ultra-high vacuum (UHV) conditions in order to preserve the integrity of the molecular system from unwanted effects such as oxidation or contamination. Both techniques offer a tunable gap between the two electrodes. Alternatively, techniques with a fixed gap offer long-term stability. Nanopore systems (see Figure 2.1(A)) [90; 9; 10] have been created using Si_3N_4 etching, and nanogaps have been fabricated by shadow mask evaporation [33; 34]. Another approach made use of electro-migration for creating nanometer-sized gaps [58; 49]. In this experiment, high current densities flowing through a thin metal wire were used to cause migration of metal atoms due to the momentum transferred from the electrons [45] (see Figure 2.1(C)). For this to work, it is crucial to stop the fast migration process at a certain distance. A novel robust concept for creating many molecular junctions in a 2D nanoparticle array was realized by a colloidal network of interlinked molecular junctions [42].

However, in all the techniques mentioned above, contact to an ensemble of molecules is established due to reduced control over the gap distance. Hence, single-molecule resolution gets lost. As a consequence, the transport properties measured are a statistical ensemble averaging over many junctions. One advantage of these approaches is that the electrical properties are robust in that sense that experiments are less sensitive to the typical fluctuations inherent to single-molecule junctions. However, many of the very fine molecular transport properties, e.g. the small features of intrinsic molecular functionality, may get lost in return. In conclusion, for fundamental research, STM and MCBJ are the experimental techniques of choice. Nevertheless, also in these techniques, the control over details of the specific molecule–metal coupling remains a desirable parameter. In very recent experiments [64], promising results for controlling the specific binding site of the molecule to the metal were reported.

The MCBJ technique will be discussed in details in the next section.

2.2 The Mechanically Controllable Break-Junction

2.2.1 Principle of Operation

The main idea of the MCBJ technique is to reduce the spatial degrees of freedom of the two electrodes to one dimension by minimizing the distance between the two supporting carriers. This in combination with a purely mechanical operation drastically improves the stability of the instrument. The working principle is illustrated in Figure 2.3: A thin freestanding metal bridge with a central lateral constriction is fabricated on top of a flexible substrate. Such a sample is mounted in a three point bending mechanism (Figure 2.3(A)). A bending force is then applied to the sample by pushing a rod to the bottom of the substrate. This introduces surface extension elongating the metal bridge which finally breaks at its smallest constriction, creating two separated electrodes with clean surface (Figure 2.3(B)). After the initial breaking, the distance between the electrodes can be controlled in both the opening and closing direction with high accuracy by either bending or relaxing the sample. The ratio r between pushing-rod translation, Δh, and resulting electrode separation, Δd, is given by [82]:

$$r = \frac{\Delta d}{\Delta h} = \frac{6 \cdot t \cdot s}{L^2} \, , \tag{2.1}$$

where t is the sample thickness, s the length of the freestanding bridge, and L the distance between the two bolts in the three-point bending mechanism (see Figure 2.3).

Equation (2.1) is based on assumptions of engineering mechanics, and is derived by the elastic deformation of a twofold-supported beam. The transmission ratio, r, depends primarily on the length of the freestanding bridge, s, and a low value ensures an inherently stable junction and less influence by external vibrations coupling in through the sample mounting.

In the pioneering break-junction experiments by Muller *et al.* and van Ruitenbeek *et al.* [52; 78], a manually notched wire was aligned in parallel to the edges on a flexible substrate covered by an insulating Kapton foil (Figure 2.4(A)). Four Stycast epoxy droplets provided mechanical fixation to the wire at its ends and close to the notch, resulting in a s of approximately 1 mm (see inset of Figure 2.4(B)).

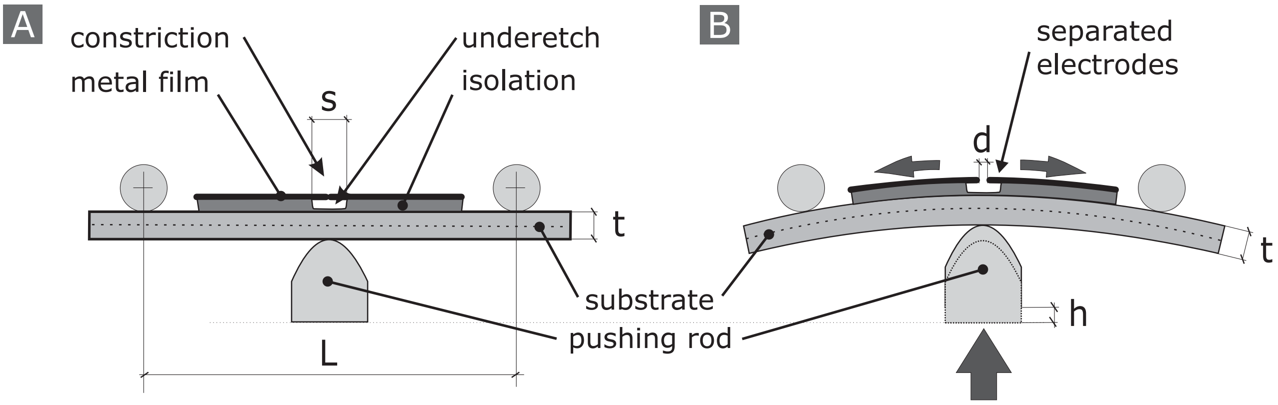

Figure 2.3: *Principle of operation of a MCBJ: (A) A freestanding metal bridge with a central lateral constriction is fabricated on top of a flexible substrate and mounted into a three-point bending mechanism. (B) The bending force applied to the bottom of the substrate introduces surface extension which finally breaks the metal bridge at its smallest constriction, creating two separated electrodes which can be controlled thereafter with picometer accuracy in both the opening and closing direction.*

Electrical contacts were created using silver paste droplets connecting thin copper wires to the external instruments (Figure 2.4(B)), enabling a four-point measurement to compensate the contact resistance.

For optimal stability of the atomic-sized junctions, it is favorable to have a small displacement ratio, r. Therefore, in this work, micro-fabrication tools have been used to fabricate break-junction samples with a much smaller s in the order of 1 μm, compared to the manually notched samples.

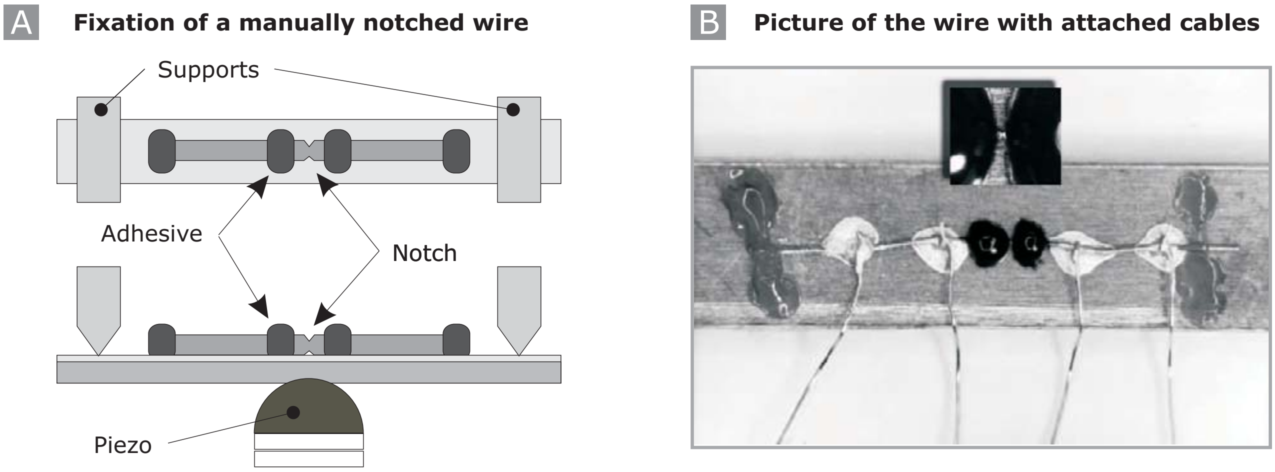

A Fixation of a manually notched wire

B Picture of the wire with attached cables

Figure 2.4: *(A) Schematic top and side view of the mounting of a MCBJ as used in the pioneering work by Muller et al. and van Ruitenbeek et al., displaying the notched wire, four fixed counter supports, drops of epoxy adhesive and the stacked piezo element. (B) Top view of a manually notched Au wire. The substrate is 4.5 mm wide and the wire has a diameter of 0.1 mm. The inset shows an enlargement of the wire with the notch between the two drops of epoxy (s is approximately 1 mm). On each side of the notch, four wires make contact to the sample wire using silver paint. Reproduced from [Agrait2003].*

For the breaking process, both the bridge length and the width play important roles. On the one hand, the smaller the width of the bridge, the less bending is necessary in order to break the bridge into two separated parts. On the other hand, if the bridge breaks too early (at low bending radii), the dynamic range available in order to close the bridge completely is too small (a hysteresis is present upon closing of the bridge, see the following Chapter 3). In case of Au, a bridge having a width of 50 nm up to 100 nm and a thickness of 50 nm provides an adequate dynamic range, a non-fatiguing substrate assumed. The entire process to fabricate the MCBJ samples will be described in the next section.

2.2.2 Sample Fabrication

The goal of fabricating break-junction samples is to create a freestanding metal bridge on top of an insulating and flexible substrate. As discussed, the bridge width ranges between 50 and 100 nm. Therefore, electron-beam lithography is employed to fabricate such small features. The different process steps are described in the following list:

1. A metal substrate (e.g. Phosphorous Bronze, PhBr, Beryllium Copper, BeCu, or stainless steel) with a thickness of 200 - 250 μm and a size of 100 mm x 100 mm is polished and cleaned with Aceton and Isopropanol. Polyimide (PI) is spin-coated to achieve an insulating layer with a thickness of 4-6 μm. In the first heating step on the hot plate at 90° C for 3 min, the solvents are removed and the PI surface becomes smooth. Cross-linking of the PI chains is carried out in an oven at the temperature of 400° C for 30 min. The PI is then solvent-free and lyophobic for all the solvents used later on.

2. The large structures such as the contact pads and the wide connector lines (see Figure 2.8), are patterned using UV photo-lithography in order to reduce electron-beam lithography writing time. A standard photolithography resist (AZ6612) is spin-coated on the metal substrate to obtain a layer thickness of 1.2 μm. UV light is then irradiated through a Chromium/glass mask in order to expose the large structures (Figure 2.6(A) shows the layout of the UV mask). During development, the exposed photoresist is removed and the unexposed geometric pattern, which is determined by the mask, remains on the sample.

3. A thin Ti adhesion layer (2 nm) followed by a 100 nm thick Au layer is then sputtered in a high-vacuum (HV) system at a base pressure of $5 \cdot 10^{-7}$ mbar. Evaporation rates are 0.15 nm/s for Ti and 0.5 nm/s for Au, respectively. The metallic structure is uncovered in a lift-off step using acetone.

4. In order to fabricate the small metal bridge, standard electron-beam lithography is used, as explained in Figure 2.5. A double-layer resist system consisting of polymethylmethacrylate (PMMA) of different molecular weights (200 K and 950 K) is spin-coated subsequently (layer thickness around 150 nm). After each coating step, the PMMA layer is cured in an oven at 160° C for 30 min. The patterning of the second mask for the metal bridge is done by using a Raith e-line lithography system with a dose of 190 μC/cm^2. The

exposure with electrons breaks the PMMA chains apart, which are then dissolved into an isobutylmethylketone (MIBK) isopropanol mixture (1:3). The resulting PMMA mask exhibits an undercut (see Figure 2.5(A)) due to the lower molecular weight of the bottom PMMA layer (Figure 2.5(A)). This undercut creates sharper metal edges during metal evaporation and facilitates the lift-off of the excess material.

5. A thin Ti adhesion layer (2 nm) followed by a 50-nm-thick Au layer is sputtered in the same evaporation system under the same evaporation conditions (Figure 2.5(B)). The unexposed PMMA with the excess metal on top is dissolved in a second lift-off step using Aceton leading to the desired structure (Figure 2.5(C)). The width of the metal bridge is between 75 nm (steel substrate) and 120 nm (BeCu substrate). The inset in Figure 2.6(B) shows a SEM picture of a junction.

6. With the design developed, 40 samples are fabricated in parallel on one metal plate with a size of 100 mm x 100 mm (Figure 2.6(A)). These samples are then laser-cut into pieces of 5 mm x 18 mm, still kept into the embedding frame via pull-linkage (Figure 2.6(B)).

7. In order to achieve a freestanding bridge, the PI is partially removed in the last fabrication step using isotropic reactive ion etching ($s \approx$ 1-2 μm) (Figure 2.5(D)). The samples can then be pulled out of the frame and mounted into the three-point bending mechanism.

Using this fabrication procedure, MCBJ samples can be manufactured on large metal plates with very low sample-to-sample variations.

2.2.3 Sample Holder

Besides the MCBJ samples described in the previous section, the working principle of the MCBJ requires a second, mechanical part: the three-point bending mechanism consisting basically of two bolts fixing the sample and a pushing-rod by which the bending force can be applied to the bottom of the sample. Figure 2.7 shows a Computer-Aided Design (CAD) image (A) and an actual picture (B) of the sample holder which was developed during this thesis to realize the MCBJ principle. The sample holder has to fulfill several tasks: first, it has to provide a stable and reproducible mechanical fixation of the sample on the pushing-rod, which allows a controlled bending without sliding of the sample. Second, it has to establish electrical

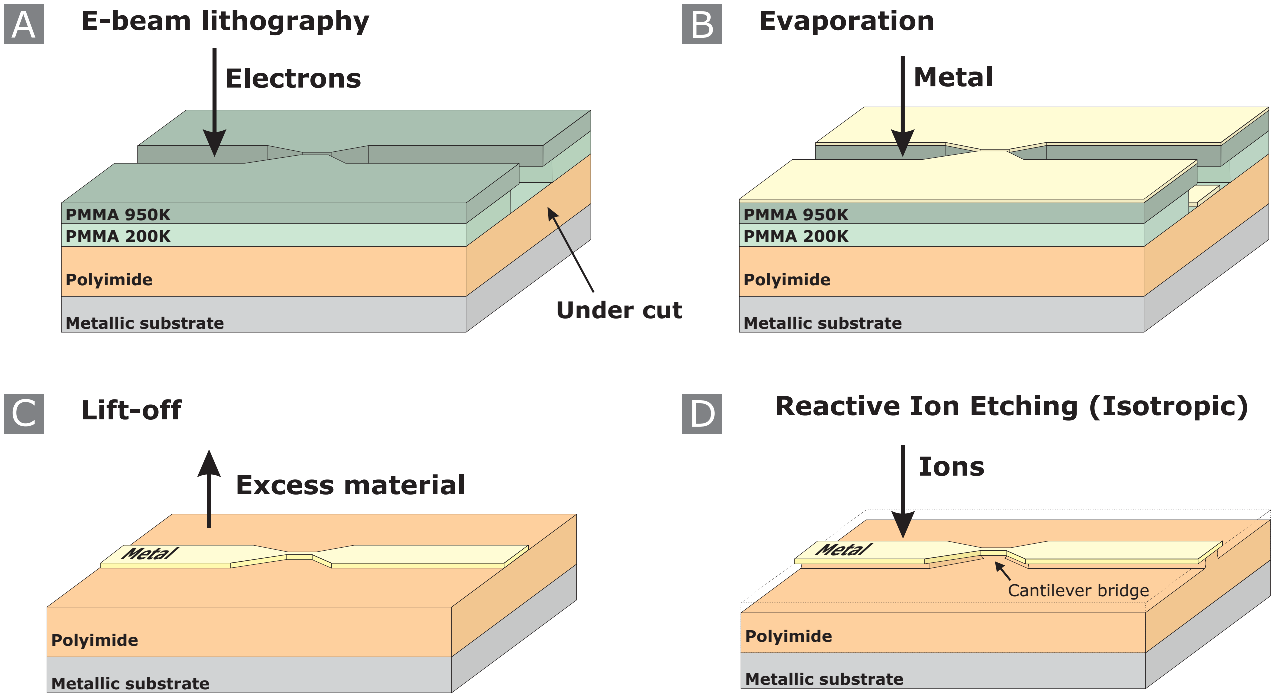
A
E-beam lithography
Electrons
PMMA 950K
PMMA 200K
Polyimide
Metallic substrate
Under cut
B
Evaporation
Metal
PMMA 950K
PMMA 200K
Polyimide
Metallic substrate
C
Lift-off
Excess material
Metal
Polyimide
Metallic substrate
D
Reactive Ion Etching (Isotropic)
Ions
Metal
Cantilever bridge
Polyimide
Metallic substrate

Figure 2.5: *Electron-beam lithography process steps used for the fabrication of the small metal bridge on a MCBJ sample: (A) Exposure of a double layer resist system to an electron beam, creating an undercut due to different molecular weights. (B) Evaporation of Au after development. The structure is uncovered in a lift-off step (C) removing the PMMA and the excess material. (D) Reactive ion etching is used to partially remove the PI and in order to achieve a freestanding, cantilevered bridge.*

contact between the sample and the instrumentation attached. Another issue which has to be considered for the design as well, is that, although s is rather small (approximately 1-2 μm) due to e-beam lithography used, the dynamic range during bending may sometimes exceed the elastic regime of the metal substrate. Hence, the sample cannot be bent back and remains buckled, consequently, the junction cannot be closed again.

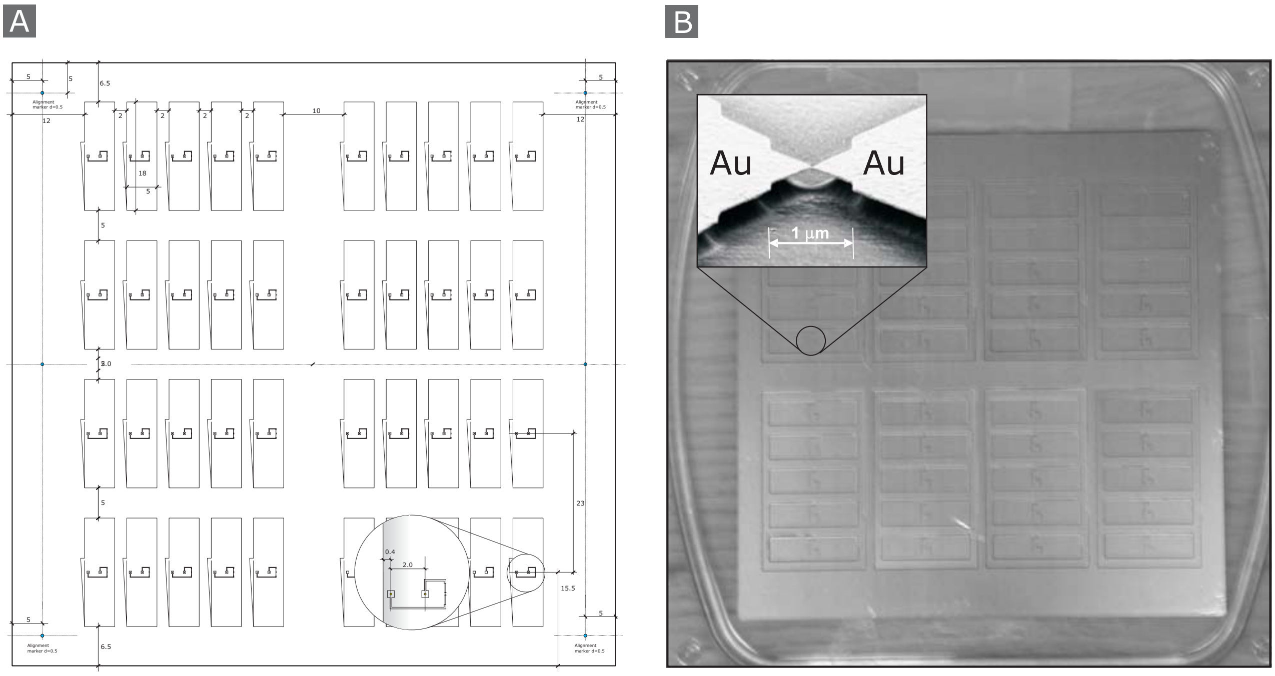
A
B
5
6.5
Alignment marker d=0.5
12
10
2
18
5
3.0
23
0.4
2.0
15.5
Au
Au
1 µm

Figure 2.6: *(A) Sample design for a 100 mm × 100 mm plate containing 40 samples, and (B) a processed sample plate. The samples are laser-cut and still kept into the embedding frame via pull linkage. The inset shows a SEM picture of the freestanding metal bridge.*

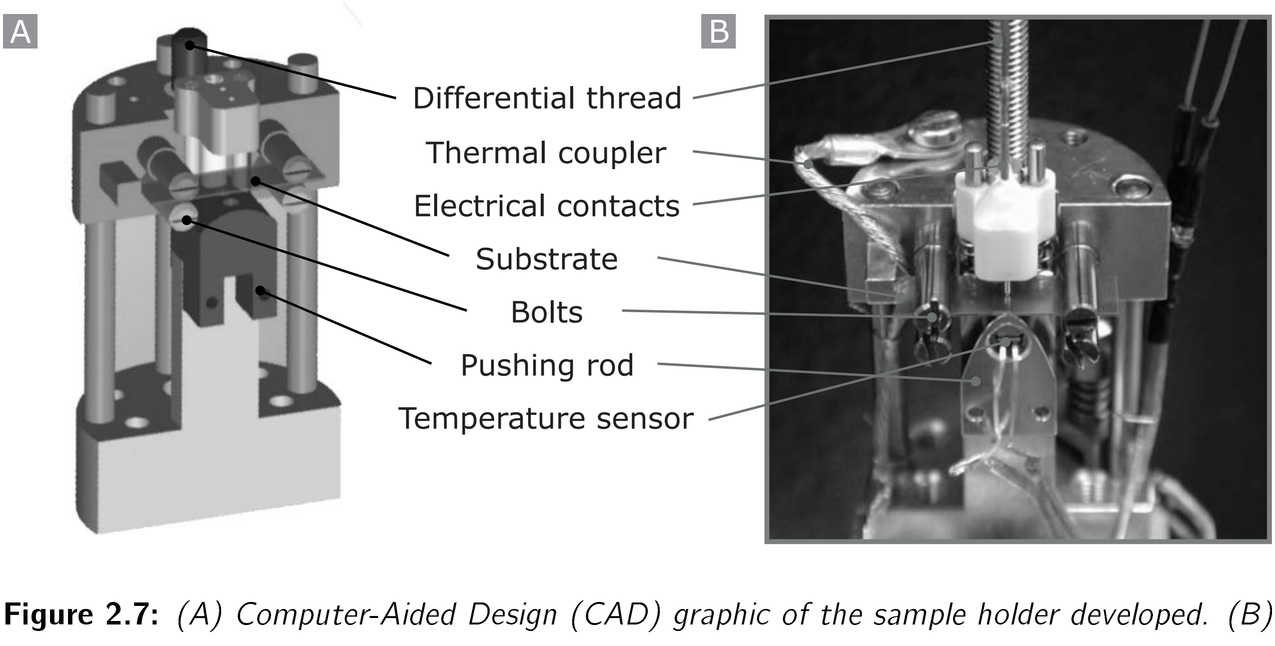
A
B
Differential thread
Thermal coupler
Electrical contacts
Substrate
Bolts
Pushing rod
Temperature sensor

Figure 2.7: *(A) Computer-Aided Design (CAD) graphic of the sample holder developed. (B) A picture showing various details of the sample holder.*

The issue of back-bending was resolved by attaching four instead of two bolts only to the sample holder. Figure 2.8 shows an illustration of the sample mounted in the three-point bending mechanism. These additional bolts in combination with the spring-loaded contacts enable back-bending of the substrate in case the bending has exceeded the elastic range of the metal. Both upper bolts have a flange in order to allow for a reproducible sample positioning (see Figure 2.8). In this mechanical configuration, the MCBJ samples can be bent many hundred times without any indication of fatigue.

Reliable electrical contact to the sample contact pads was achieved by using spring-loaded contacts (see Figure 2.8) which ensure a stable electrical connection during bending. The spring travel distance is around 2 mm and both contacts are casted in a highly insulating UHV-compatible ceramic. The electrical insulation between the two contacts and between the contacts and the ground is better than 10 TΩ at 40 V (see Figure 2.7). The contacts are probing the sample at a position in the neutral bending zone (located over the pushing-rod) where the sample is not sliding upon bending, see Figure 2.8. This ensures a stable electrical connection to the sample.

The ratio r between pushing-rod translation, Δh, and resulting electrode separation, Δd, given by Equation (2.1) can be calculated: Taking the geometry of the bridge ($s \approx 2$ μm) and the geometry of the three-point bending mechanism into account ($L = 11.8$ mm), a ratio r of 2.1×10^{-5} is achieved. This very low transmission ratio ensures an inherently stable junction where external influence are suppressed. Back-bending of the substrate allows for the controlled approaching of the electrodes with subatomic ($\sim 10^{-12}$ m) resolution due to a high-precision rotary motor (Newport SR50 CC with an angular resolution of 0.001°, see Figure 2.9(B)) in combination with a differential thread (1:10).

In addition, the sample holder can be equipped with a liquid cell for measurements in solution. This cell is built by filling polydimethylsiloxane (PDMS) into a casting mold. Due to the elastic properties of the elastomer, the liquid cell can adjust to the bending of the sample and ensures a leak-proof encapsulation. The cell is mounted into the probing head where the spring contacts are embedded. In this part, both the liquid supply and outlet for purging are built-in.

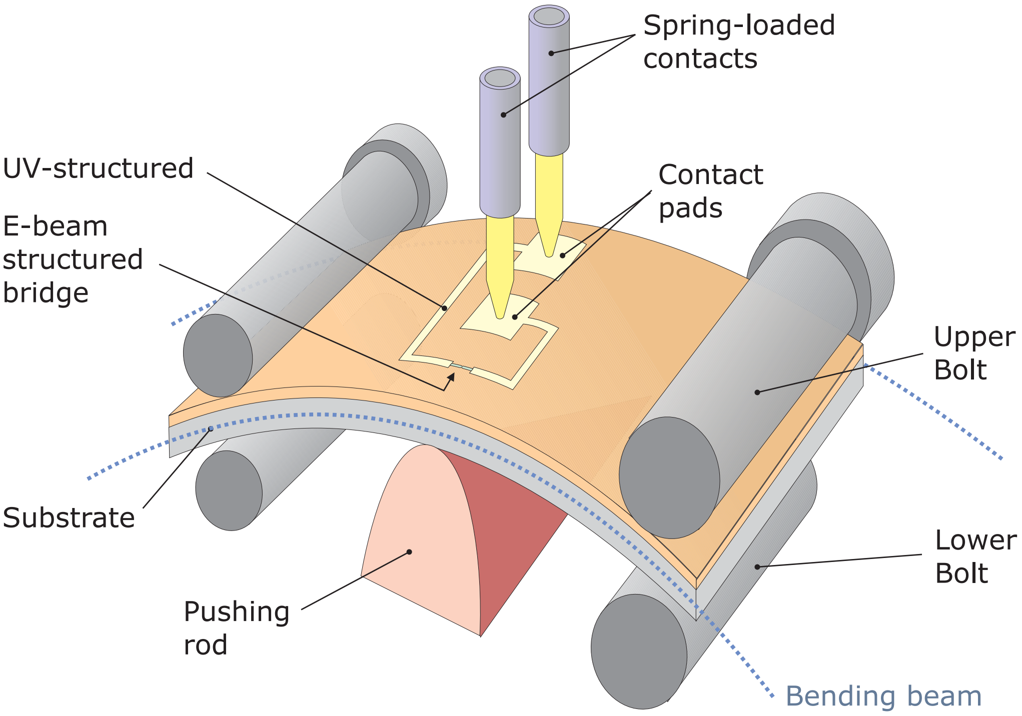
Spring-loaded contacts
UV-structured
Contact pads
E-beam structured bridge
Upper Bolt
Substrate
Lower Bolt
Pushing rod
Bending beam

Figure 2.8: *Illustration of the technical realization of the sample holder: A stable fixation of the sample in the three-point bending mechanism is achieved by using bolts with flanges. The additional lower bolts support the back-bending of the sample in case the bending exceeded the elastic range of the metal substrate. Stable electrical contact to the sample is ensured using spring-loaded contacts.*

Another add-on to the standard MCBJ sample holder is the mounting of a glass fibre enabling optical excitation. The glass fiber (single-mode, transmission between 180 nm and 1200 nm) is connected to the UHV system by a on optical feed-through (Caburn, FFT-UV600-C40). It is also attached to the probing head and ensures therefore a stable and reproducible alignment and also coarse focusing of the light spot onto the molecular junction. Various light sources can be attached, e.g. a Hamamatsu UV source (200 W power, spectrum between 240 and 400 nm).

2.2.4 Ultra-High Vacuum and Cryogenic Environment

Figure 2.9 shows an overview of the entire setup, consisting of two MCBJ mechanics (setup 1 and setup 2) operated in a UHV chamber with a base pressure of 2×10^{-9} mbar, and attached instruments. The chamber is divided into two sub-chambers comprising each a MCBJ mechanics. They can be separated by a gate valve. This allows both MCBJ systems to be evacuated, flooded, and opened independently. After every opening of the system, e.g. for loading and unloading of a sample or for application of molecules, the subsequent evacuation of the chamber is performed in two steps: First, the forepump evacuates the chamber to 5×10^{-2} mbar within 5 minutes. Second, the valves to the turbo molecular pump are opened and the system is pumped down further. After 30 minutes, a base pressure of 1×10^{-7} mbar, after 5 hours 1×10^{-8} mbar and after 15 hours a final base pressure of 2×10^{-9} mbar is reached. An even lower pressure is reached when the system is heated (at 400 K) or cooled down to liquid He temperature. The pressure achieved is then below the measurement range of the sensor used ($p < 1 \cdot 10^{-10}$ mbar).

Setup 1 is equipped with a He flow cryostat (Cryovac) to enable temperature-dependent measurement in the the range of 5 to 400 K. The determination of the exact temperature of the substrate is crucial. Therefore, the thermal coupling and the temperature measurement, which is normally performed by a temperature sensor built in the cryostat, have to be optimized. Tests of the cooling properties revealed a weak thermal coupling between the cooling finger of the cryostat and the bending mechanism. Figure 2.10 shows how the temperature measured by the sensor embedded in the pushing-rod (see Figure 2.7) deviates from the temperature measured in the cryostat (set point). If a temperature of 4 K is measured in the cryostat, the final temperature on the substrate reaches only 47 K (blue curve in Figure 2.10). After covering the entire bending mechanism with a thin Au layer, attaching copper cables between cooling finger and bending mechanism, and carefully removing all weakly coupled thermal reservoirs from the sample holder (see Figure 2.7(B)), the thermal coupling was improved and a final temperature in the pushing-rod of 9.5 K was achieved (gray curve in Figure 2.10). The temperature reaches here 6.5 K after a waiting time of 15 min. To minimize the effect of the described temperature differences between cryostat and sample, the sensing and driving temperature sensor was embedded in the pushing-rod, located very close to the sample. Therefore, all the temperatures reported in the experiments later on, refer to the temperature of the pushing-rod.

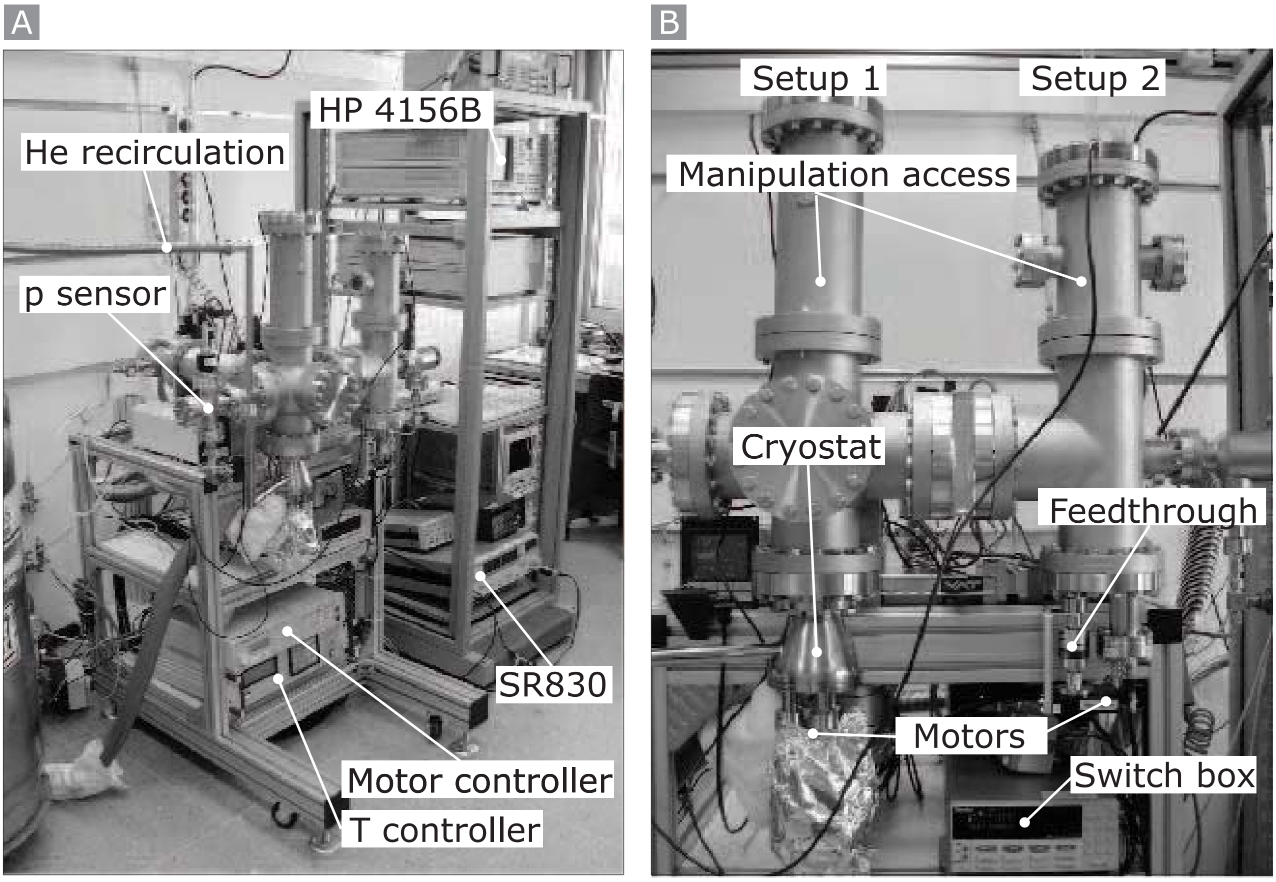
A
HP 4156B
He recirculation
p sensor
SR830
Motor controller
T controller
B
Setup 1
Setup 2
Manipulation access
Cryostat
Feedthrough
Motors
Switch box

Figure 2.9: *(A) Overview of the entire setup: UHV chamber on the left hand side, rack with instruments on the right hand side. (B) The picture shows the two MCBJ systems of the setup. The left one is equipped with a He flow cryostat enabling temperature-dependent measurements, the right one is restricted to room temperature measurements.*

2.2.5 Electrical and Controlling Setup

The electrical characterization of the metal–metal and metal–molecule–metal junctions is performed using an Hewlett-Packard 4156B Semiconductor Parameter Analyzer. This instrument has four source measure units (SMU) with high resolution in voltage (2 μV) and current (1 fA). It is dedicated to perform fast current–voltage, I–V, sweeps in direct current (DC) measurements. Figure 2.11(A) shows the DC measurement principle. In addition, a Stanford Research SR 830 lock-in amplifier is attached to the MCBJ. This instruments measures phase-sensitively the response of the device-under-test (DUT) to an alternating current (AC) signal which is

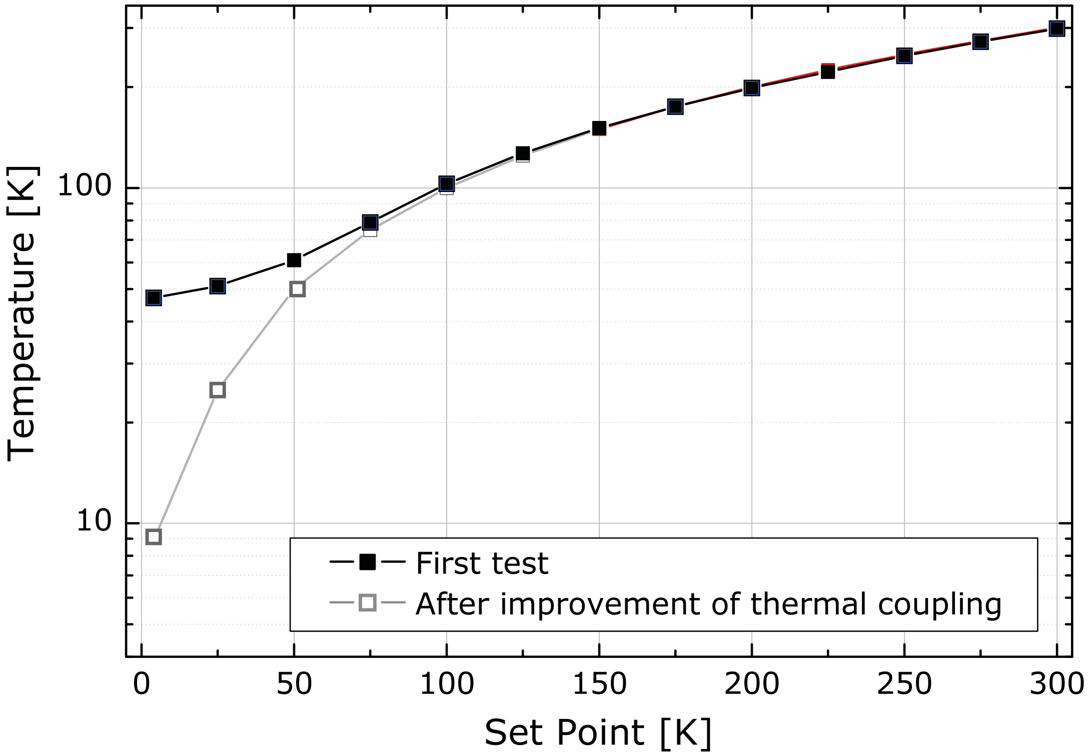

Figure 2.10: *Temperature measured in the pushing-rod (y-axis) versus temperature measured in the He cryostat (x-axis, set point). Before (black curve) and after improvement (gray curve) of the thermal contact between cooling finger of the He cryostat and the sample holder. The temperature of the sample reaches finally 6.5 K, instead of 47 K before improvement.*

superimposed to the DC working voltage. Figure 2.11(B) shows the AC measurement principle. Both electrical signal paths (ground and signal) can be switched to one of these instruments via a Keithley 7001 switch box (equipped with two Keithley 7152 8 x 12 multiplexer cards).

Figure 2.11 shows the cabling between the DUT and the two (or more) instruments connected to the switch box. In measurements on molecular junctions reported later on, it turned out that the switching method with sequential guarding of the individual channels does not affect the sensitive junction. Therefore switching between DC and AC characterization can be performed *in-situ*.

In addition to the instruments, the MCBJ experiment consists of several more hardware parts.

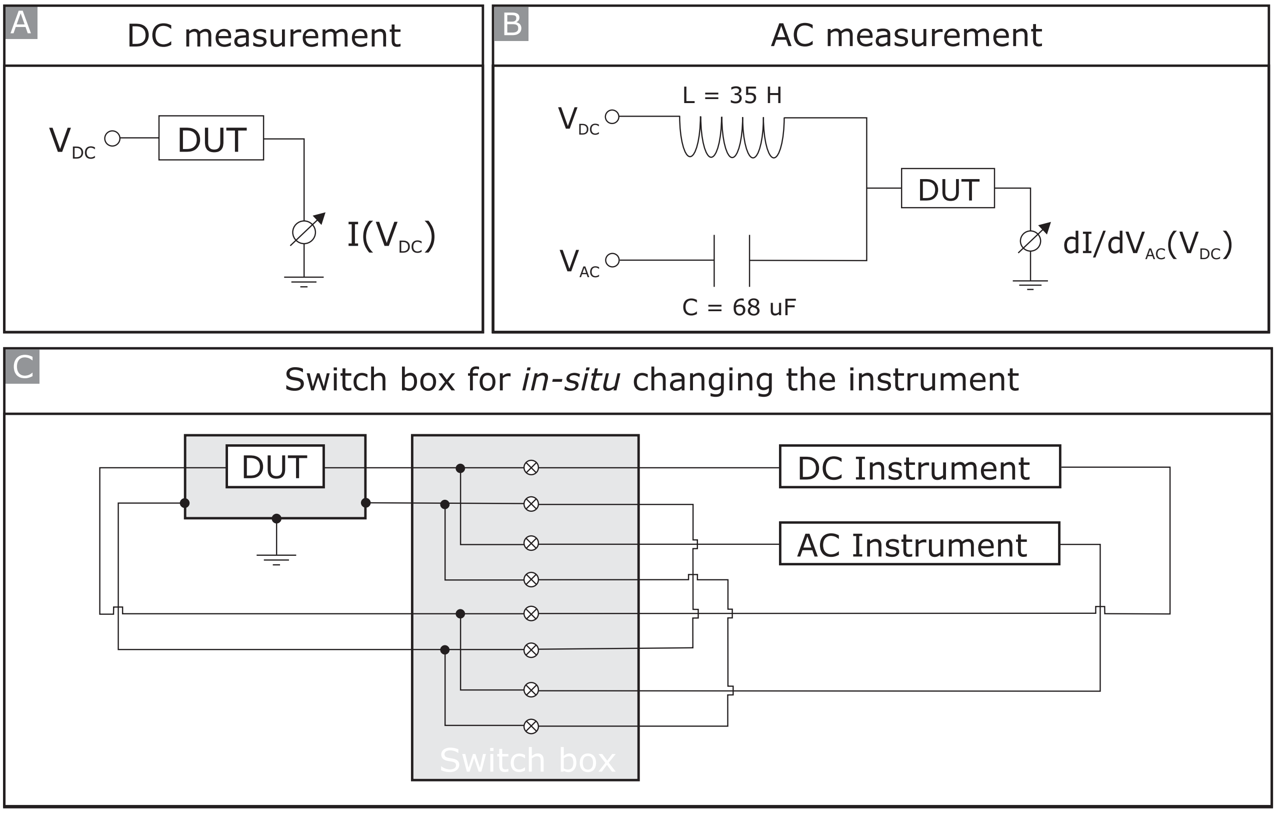
A
DC measurement
V_DC
DUT
I(V_DC)
B
AC measurement
V_DC
L = 35 H
DUT
dI/dV_AC(V_DC)
V_AC
C = 68 uF
C
Switch box for in-situ changing the instrument
DUT
DC Instrument
AC Instrument
Switch box

Figure 2.11: *A) DC measurement type, B) Differential AC resistance measurement by analog superposition of the DC working voltage to an AC amplitude. C) The cabling of the DUT to the instruments using a switch box. Signal and ground are guided and switched separately. This enables in-situ changing the different instruments without affecting the molecular junction.*

The goal was to achieve a fully automated control of the instruments for repeated long-term measurements. Therefore all the instruments have to communicate to the controlling computer. All the instruments (HP4156B, SR 830, Keithley 7001), as well as the rotary motors driven over a Newport ESP300 controlling unit, can be controlled over the General Purpose Interface Bus (GPIB) (IEEE488 Standard). The croyvac temperature controller can also be addressed over this bus type.

The entire measurement system is controlled over LabView© [1] Virtual Instruments (VIs), all developed within the time frame of this thesis. Based on this graphical programming environment, various experimental modules and tools have been developed during this thesis, wherefrom a selection is listed below:

Program	Feature	Main control parameters	Typical values
Cond	Initial breaking and conditioning of electrodes by repeated opening and closing of the junction	R_{closed} R_{open} V_{bias}	$\leq$ 12.9 kΩ $\geq$ 1 TΩ 2 mV
IV(d)	Repeated opening and closing of electrodes during simultaneous I-V data acquisition	I_{closed} I_{open} Sweeps / position	1 μA @ 1 V 10 pA @ 1 V 5
Hist	Repeated opening and closing of electrodes by repeated measuring the resistance of the junction	R_{closed} R_{open} V_{bias}	$\leq$ 12.9 kΩ $\geq$ 1 TΩ 5 mV
Statistical Tool	Displaying and analyzing huge data sets of I–V	Peak detection Building histograms	

Controlling all instruments automatically by software tools and a computer has not only the advantage of being user-independent and comfortable, it also introduces some kind of impartiality to the experiments, since the controlling and the analysis are based on objective parameters measured.

---

[1] LabView© (short for Laboratory Virtual Instrumentation Engineering Workbench) is a platform and development environment for a visual programming language. LabVIEW is a proprietary product of National Instruments (http://www.ni.com).

Chapter 3

Properties of Metal–Metal Junctions

In this chapter, the electrical and mechanical properties of metal–metal junctions as formed in the MCBJ method will be discussed. Thereby, it will be shown that this relatively simple experimental technique enables the creation of atomic-sized contacts. As explained in Chapter 2, the MCBJ sample is mounted in a three-point bending mechanism and a bending force is applied. Starting from a wire-like geometry with bulk properties, extension is induced on the substrate which results in a stretching of the freestanding metal bridge. Its cross-section is decreasing further and further upon bending. At the last stage, just before the bridge breaks, single atoms can be pulled out of the bulk to create a chain of individual atoms. The electrical transport properties are then mainly determined by the nature of the atoms composing the quantum point contact. Since the diameter of such a constriction is approximately equal to the diameter of the atom (e.g. for Au 0.288 nm), it is smaller than the corresponding Fermi wavelength of the metal (e.g. $\lambda_{Au} = 0.52$ nm) and quantum effects can be observed. Compared to two-dimensional electron gas semiconductor devices, where quantized conductance is exhibited only at very low temperature (in the range of 50 mK up to 4.2 K, see Chapter 7.1), these phenomena are present at much higher temperatures in case of metal-metal QPCs, and can be observed even at room temperature.

In the following sections, the transition from direct contact to tunneling in the initial stretching and breaking process, the calibration of the displacement ratio via tunneling current measurements, the electrode stability, and, finally, the conductance quantization as a strong indication for the presence of atomic-sized electrodes will be described. Since the two metal tips will be employed later on as a separated electrode pair to contact single molecules and to perform charge-carrier transport studies through these molecular junctions, the main focus in the experiments here is set to the investigations of properties concerning the controlling ability of the electrode pair. Because Au electrodes have the suitable properties for the following experiments with molecules, no other electrode material was hence investigated. A complete review article on the quantum properties of atomic-sized conductors consisting of different materials is given by reference [1].

The MCBJ technique was introduced in 1985 to study atomic-sized junctions [52; 78]. Microscopic manipulations upon stretching of the bridge and of the two separated electrodes created by breaking the bridge, can be monitored in great detail due to the superior mechanical stability. This is achieved by a purely mechanical working principle with a low transmission ratio between pushing-rod translation and resulting electrode separation. Of special importance is the transition from direct contact to tunneling and vice versa. By investigating the electrical transport characteristics, information about the channel cross-section can be extracted.

3.1 Temperature-Dependence without Bending

The MCBJ samples fabricated by e-beam lithography have a typical initial bridge cross-section of 50 nm x 100 nm, as explained in the fabrication procedure in Chapter 2. The resistances of the virtual bridges vary between 95 and 150 Ω. The total electrical resistance of the metal bridge connected via the leads to the metal pads is a function of temperature and the cross-section of the bridge, which can be varied by means of sample bending (see Chapter 2).

Figure 3.1 shows the resistance of a sample without bending force applied measured in the temperature range between 300 K and 25 K (5 mV bias applied). The linear fit reveals a good agreement of the experimental data to a linear behavior. The offset extrapolated to 0 K is around 60 Ω.

The specific resistance of a metal is generally determined by electron–phonon interaction which describes the scattering of the charge-carriers at lattice vibrations, e.g. phonons. Additional

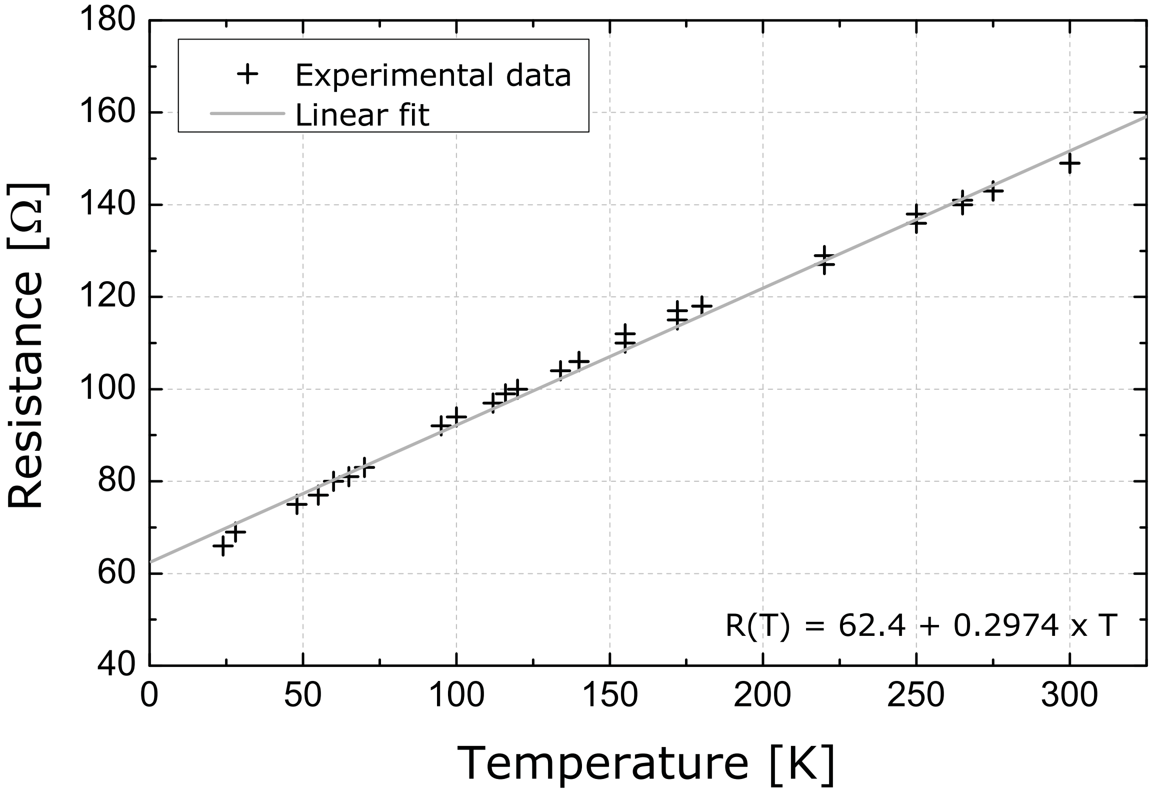

Figure 3.1: *Temperature dependence of the resistance of the Au bridge and the connector lines, measured under a small bias of 5 mV in the temperature range between 300 K and 25 K. An expected almost linear decrease of the resistance with lowering temperature is observed. The extrapolated offset at low temperatures indicates scattering at defect and impurity locations within the amorphous evaporated film.*

sources of scattering are defects and impurities. The specific electrical resistance can therefore be described by a temperature-dependent component of the pure metal and a temperature-independent component due to scattering at defect and impurity locations, known as the rule of Matthiessen [2]:

$$\sigma(T) = \sigma(T_0)(1 + \alpha \cdot (T - T_0)), \tag{3.1}$$

where T denotes the temperature, α the linear temperature coefficient, and $\sigma(T_0)$ a known specific resistance, e.g. measured at $T_0 = 300$ K. For pure metals, the specific resistance decreases linearly with decreasing temperature. In equation (3.1), it has been assumed that the channel dimensions are constant. This assumption is also justified for MCBJ samples due to the compensation of the thermal expansions in the fully symmetric design of the connectors. Thus, the electrical resistance, R, is directly proportional to the specific electrical resistance, σ. The linear fit of the data in Figure 3.1 reveals an α of $1.98 \cdot 10^{-3}$ K^{-1}. For a pure Au film, σ_0 is typically $2.44 \cdot 10^{-8}$ Ω m at $T = 300$ K, and α is reported to be $3.9 \cdot 10^{-3}$ K^{-1}, almost twice the measured value [83]. The large offset of the fit at $T = 0$ K in the order of 60 Ω, might indicate that the metal film is rather amorphous than pure crystalline.

3.2 Transition from Direct Contact to Tunneling

In this section, the resistance of the bridge is investigated during stretching at a constant temperature. Now, the electrical resistance of the junction varies due to spatial changes of the transport channel across the metal bridge and not due to altered material properties as reported before.

Figure 3.2 shows the typical behavior of a Au junction upon slowly stretching (with a rotary speed of only 0.05°/s) at room temperature: The electrical resistance increases almost linearly from 120 Ω to approximately 250 Ω at pushing-rod position 1200°. Above this value, the resistance increases rather irregularly in steps than monotonously. The point where the metal–metal bridge breaks is located at pushing-rod position 2400°, corresponding to a pushing-rod travel of 0.70 mm.

The functional behavior of the resistance upon bending can be understood as follows: In general, if mechanical bending is induced, the transport channel's cross-section shrinks due to stretching of the metal bridge. Since the cross-section is rather large at the beginning (approximately 50 nm x 100 nm), the first regime follows an almost linear behavior. When the channel's cross-section is further decreased, more stepwise features in the resistance appear. They are related to distinct microscopic changes in the transport channel (see following section 3.5), which appear now in the transport signature because the channel's cross-section has finally shrunk to microscopic dimensions.

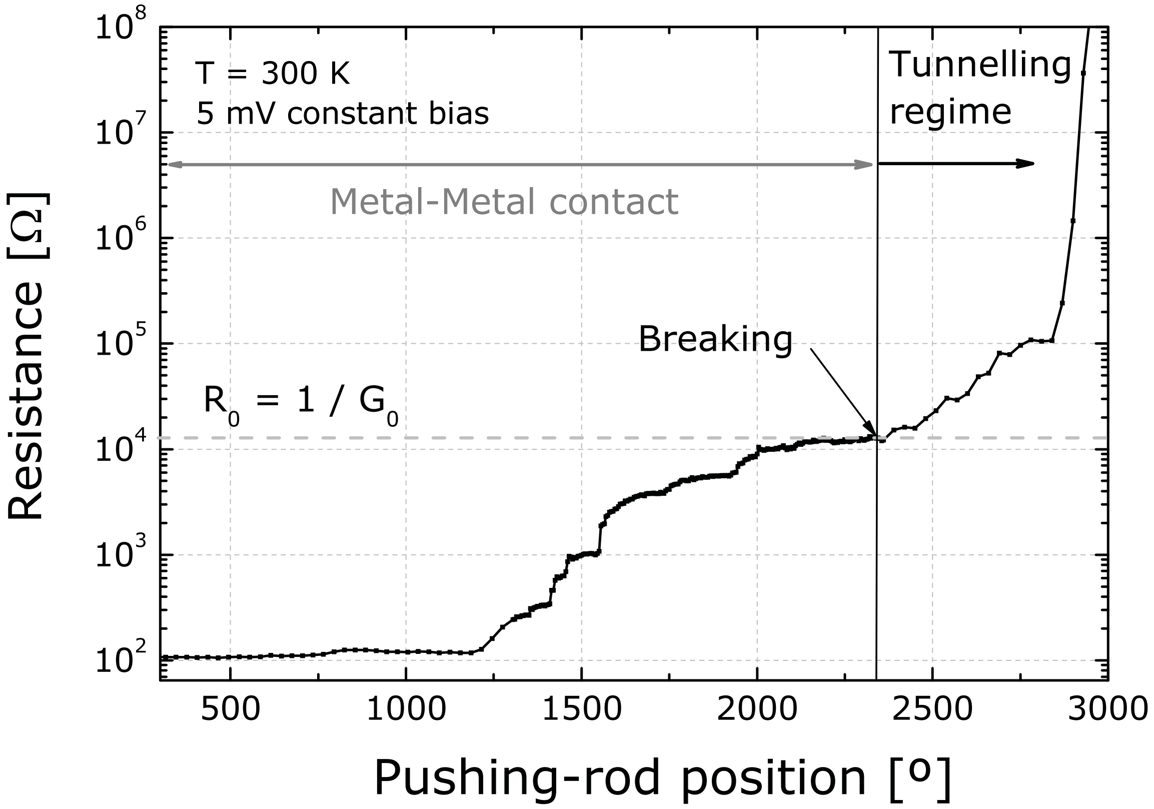

Figure 3.2: *Initial breaking of a junction during simultaneous measurement of its electrical resistance (bias of 5 mV applied). The initial resistance of approximately 150 Ω increases first almost linearly to 250 Ω (for pushing-rod positions smaller than 1200°), then in irregular steps. This behavior is due to the transition from bulk properties to smaller, microscopic dimensions. Finally, the breaking of the Au–Au QPC at a resistance of approximately 12.9 k Ω at pushing-rod position 2300°, indicates the transition from direct contact to tunneling (blue arrow).*

After breaking of the metal bridge (at pushing-rod positions 2300° in Figure 3.2), a change of four orders of magnitude in the tunneling resistance is achieved within approximately 450°. This gives a preliminary displacement ratio of 1 pm $\equiv$ 4.5° assuming a normal tunneling behavior. However, dynamic effects have also to be considered. Although the velocity of the rotary motor and the sampling rate are kept constant, the data points are obviously much more separated in Figure 3.2 for the tunneling regime than for the direct metal–metal contact (for pushing-rod positions smaller than 2300°). This indicates, that the electrodes possess an additional driving force in their movement than only introduced by the bending force. Remaining tension in the contacts can be assumed as being the origin of this behavior, causing the separated electrode to be withdrawn. This assumption is also based on the large hysteresis which is observed between breaking and closing points (see following section 3.6). Due to this strain, a precise calibration is not possible in the tunneling regime of the initial breaking process.

For the repeated breaking and closing of the junction, as well as for the contacting of molecules, it may sometimes be necessary to know the precise distance between the two electrodes. In the above discussed initial breaking process, a significant amount of tension is released and the bridge breaks up in an uncontrolled way. A much better calibration is expected to be possible during the repeated opening and closing cycles following the initial breaking. In addition, at low temperatures, the electrodes are expected to be more stable due to the reduced mobility of Au surface atoms. Hence, the calibration can much better be performed at low temperatures in the subsequent closing or opening cycles after breaking. These measurements will be demonstrated in the next section.

3.3 Calibration of the Displacement Ratio

The goal of these measurements is to obtain the transmission ratio between pushing-rod displacement and resulting electrode separation. In principle, this ratio is given by equation (2.1). However, many of the assumptions considered for the calculation of equation (2.1) are not fulfilled in the MCBJ geometry. First, the bending beam (see Figure 2.8), which is an imaginary line across the sample monitoring the area which is neither stretched nor compressed, is not uniform. This is because the distance between the carriers of the bridge is finite (1 - 2 μm), which causes a inhomogeneous bending of the bridge. Second, the dynamic region for the substrate bending may exceed its elastic range. In this case, the bending procedure is rather a kinking than a homogenous bending. In addition, the distance between the carriers of the bridge, s, may differ due to variations in the fabrication process of the samples, in particular the polyimide etching step.

Moreover, microscopic changes of the tip geometries prevent an absolute distance calibration due to the ductile response of metal to deformation for the entire temperature range.

For all these reasons, an absolute calibration of the ratio between pushing-rod displacement and resulting electrode separation is not possible and a relative calibration has to be performed instead. This is done in the simplest approach by tunneling current measurements between the two electrodes. Due to the aforementioned microscopic variations in the contacts and the fabrication fluctuations, it is necessary to make such a relative calibration for each new sample if required.

In the tunneling regime, the tunneling current, I, depends exponentially on the electrode distance, d, which is again proportional to the pushing-rod translation, Δh:

$$I(d) \propto exp(-\sqrt{8m_e\Phi_{Au}}d/\hbar), \tag{3.2}$$

where m_e is the electron mass, Φ_{Au} the work function of Au and $\hbar$ the reduced Planck's constant [76]. Figure 3.3 (A) illustrates the situation of an ideal tunneling barrier. A more generalized theory of tunneling between two electrodes consisting of the same material through thin insulating films was proposed by J. G. Simmons [70] (see Figure 3.3 (B)). The current density, J (in A cm^{-2}), for small bias voltages, V, is expressed by:

$$J = 3.16 \cdot 10^{10}\sqrt{\overline{\phi}}\frac{V}{\Delta d}exp\Big(-0.125\Delta d\sqrt{\overline{\phi}}\Big), \tag{3.3}$$

with $\overline{\phi}$ being the average barrier height, and Δd the effective length of the barrier. The average barrier height is calculated as follows:

$$\overline{\phi} = \frac{1}{\Delta d}\int_{d_1}^{d_2}\phi(x)dx, \tag{3.4}$$

with $\phi(x)$ the local barrier height.

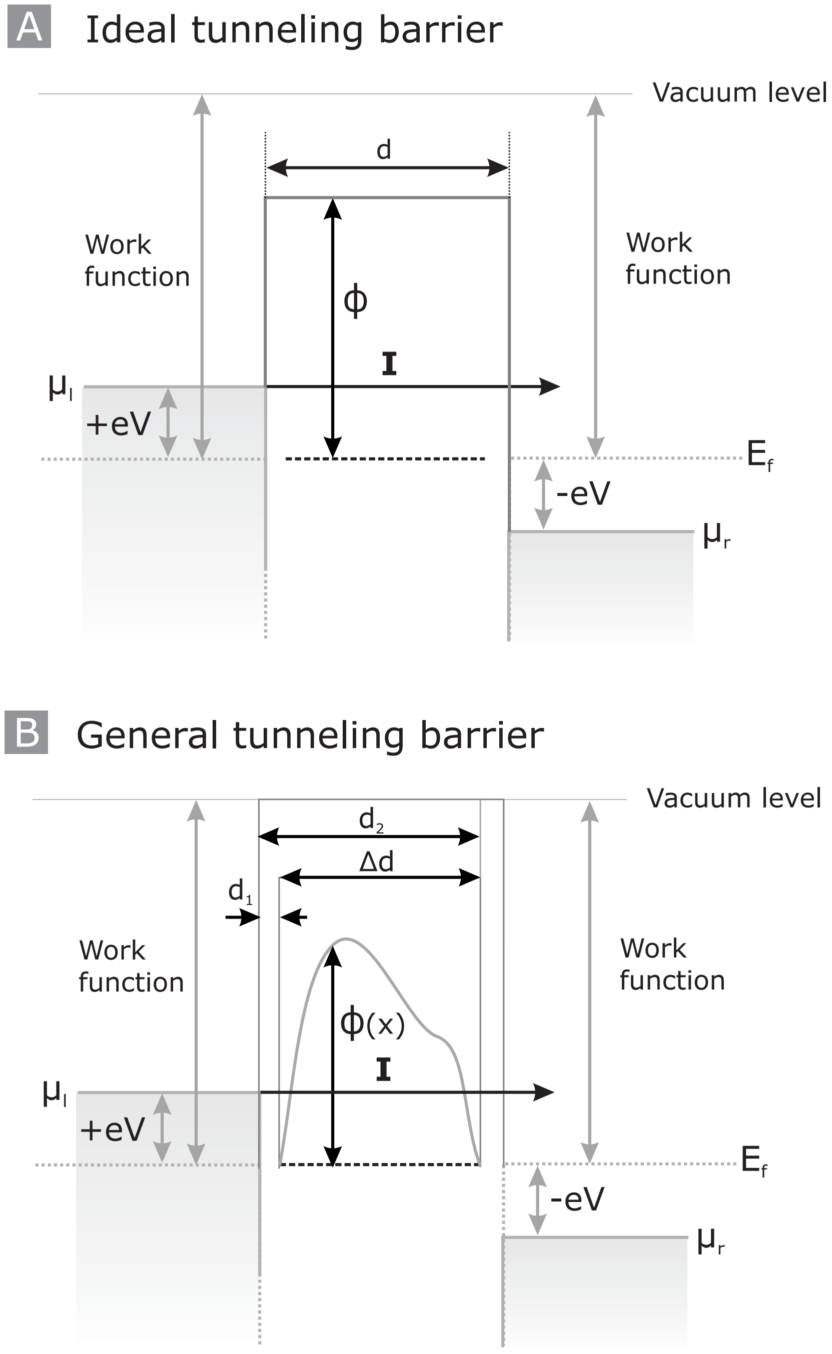
A
Ideal tunneling barrier
Vacuum level
d
Work function
Work function
ϕ
I
μ_l
+eV
E_f
-eV
μ_r
B
General tunneling barrier
Vacuum level
d_2
Δd
d_1
Work function
Work function
ϕ(x)
I
μ_l
+eV
E_f
-eV
μ_r

Figure 3.3: *(A) Ideal tunneling barrier with a constant barrier height, and (B) a generalized tunneling barrier.*

Figure 3.4 shows the tunneling resistance of a Au–Au junction as a function of the pushing-rod displacement in a semi-logarithmic representation. The two electrodes were approached very slowly with a speed of 0.05°/s at a temperature of 30 K. The sampling rate was set to be one point upon a distance change of 0.1°/s. In general, the resistance exhibits a linear functional behavior in the semi-logarithmic representation, indicating tunneling between the electrodes. Within 40°, the resistance decreases three orders of magnitude and shows a sudden drop at a pushing-rod position of 3280° to a value of 12.9 kΩ ($= 1/G_0$) within three measurement points. This value indicates a metal–metal QPC and is maintained upon further closing.

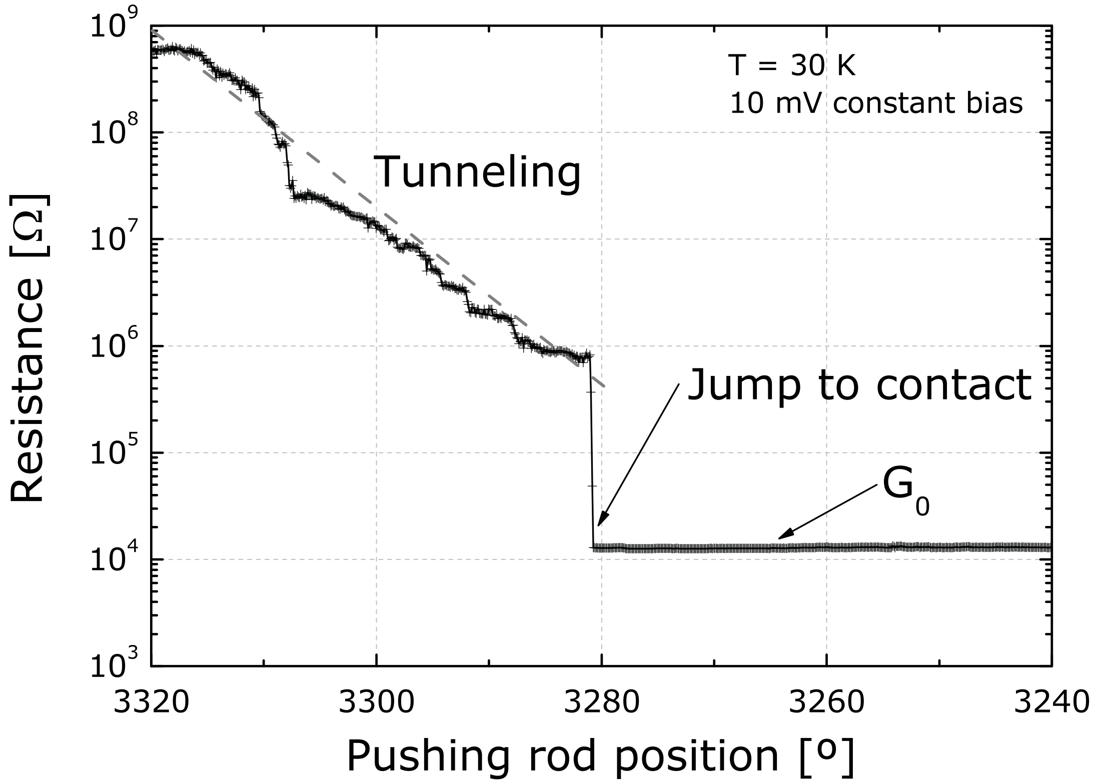

Figure 3.4: *Tunneling resistance measured at 30 K with small bias of 10 mV applied during simultaneous closing of the junction. The closing direction is from left to right. The resistance decays exponentially and suddenly drops to a closed metal-metal QPC ("jump-to-contact") with a resistance of* $R_0 = 1/G_0$. *This value is maintained upon further closing.*

The pushing-rod is controlled with a rotary motor using a differential thread with a ratio of 1:10 as described in Chapter 2. Therefore, one rotation of 360° results in a pushing-rod travel change, Δs, of 100 μm. Hence 1° corresponds to a Δs of 0.28 μm.

Using the mechanical formula in equation (2.1), it can be derived that 1° results in a distance change between the electrodes of 5.5 pm. This extreme theoretical resolution is reduced in the experiment due to the surface mobility of Au atoms. Under an applied electric field, they can move towards the gap, thus gradually reducing the gap between the electrodes. Since the mobility of the Au surface atoms decreases with lowering temperatures, the experiments are performed at low temperatures.

A fit according to equation (3.2) with $\Phi_{Au} = 5.3$ eV yields a transmission ratio, r, of 1.875 $\times$ 10^{-5}, in good agreement with equation (2.1). Therefore, a change of the rotary motor of 1° yields a distance change between the electrodes of 5.2 pm. Other micro-fabricated samples were also calibrated in this setup and showed transmission ratios of 1.65 - 2.1 $\times$ 10^{-5}.

No reliable calibration data can be conducted when the sample had exceeded its elastic range which is indicated by a kinking of the substrate when returning to the initial position. However, an uncertainty exists in the calibration because Φ_{Au} depends on the exact microscopic surface lattice structure of the tip which is not known ($\Phi_{Au} = 5.1 - 5.47$ eV (100)) [43]. The uncertainty due to the sample fabrication variations may result in an altered s in the order of 5 - 20 %, mostly because of anisotropic RIE etching of the polyimide. If necessary, the relative distance calibration enables the individual value of r of each sample to be determined.

The transmission ratios found are in good agreement with calibrations [16] performed with the setup developed at the Forschungszentrum Karlsruhe (FZK). Di Leo found a transmission ratio, r, of 1.25 $\times$ 10^{-5}, hence a ratio between rotation and electrode separation of 1 ° $\equiv$ 3 pm [16].

In conclusion, the following calibration data can be given for the setup and the samples used:

- Transmission ratio: $r = (1.8 \pm 0.3) \times 10^{-5}$,
- Rotation–electrode distance change: $1\ ^\circ \equiv (4.5 \pm 0.9)$ pm.

In Figure 3.4, the tunneling regime ends abruptly, when the resistance "jumps-to-contact" and values of 12.9 kΩ are measured upon further closing. This discontinuity indicates that the electrodes cannot be approached arbitrarily close to each other in a controlled way. Even at low temperatures, e.g. 30 K, the Au atoms possess sufficient mobility to move towards the gap under the applied electric field. This makes the distance between the electrodes smaller and smaller, hence the electric field is increasing drastically. The entire migration process accelerates thereby and the closing cannot be stopped. This behavior is important for the subsequent measurements on molecules reported in the next chapters.

3.4 Stability and Resolution of the Electrode Pair

The tunnelling current is studied at low temperature to test the stability and the resolution of the electrodes. As shown in Figure 3.4, at very low tunneling resistances, the electrodes cannot be kept in an arbitrary small distance opposite to each other. Therefore, the stability has to be measured at a larger electrode separation and a higher corresponding tunneling resistances.

Figure 3.5 shows the tunneling resistance of a junction as a function of time at a fixed electrode distance. The distance and the voltage are chosen in a way that the Au atoms are stable and not driving towards the gap. In this case, the tunneling resistance is approximately 15 MΩ and away from the "jump to contact" distance, as displayed in Figure 3.4. The signal remains constant during the time measured of 25 minutes (1500 s) at a constant low temperature of 30 K. The resistance shows an almost constant signal of 15.8 MΩ and fluctuations between 10.8 and 18.5 MΩ. The distribution of the resistance values is shown in Figure 3.6. Obviously, the tunneling resistance is maintained with very low fluctuations when the pushing-rod is immobilized. From the tunneling resistance, it can be deduced that a constant distance can be maintained within 5-10 pm in the tunneling regime above 10 MΩ and at low temperatures and small bias (10 mV).

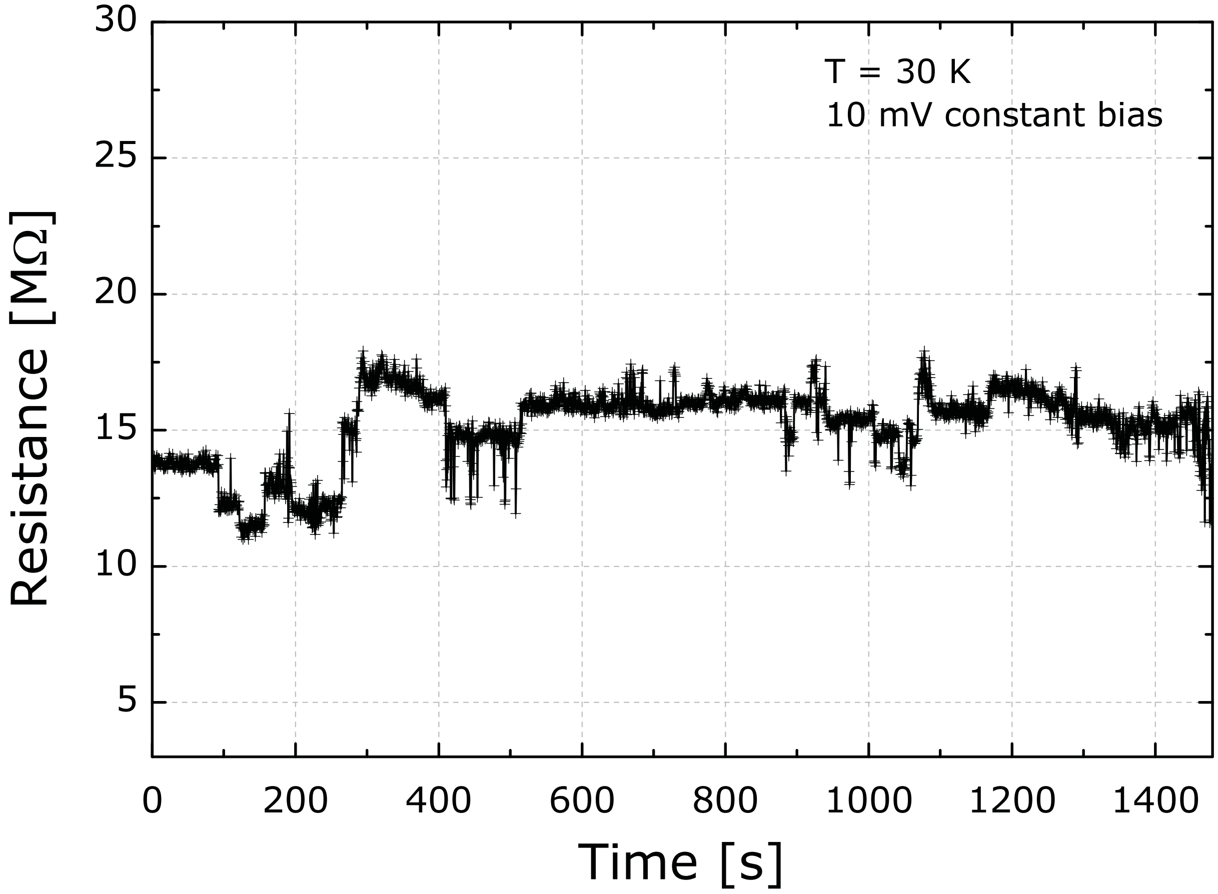

Figure 3.5: *Tunneling resistance measured at a bias of 10 mV applied for times up to 1500 s (25 min). The electrode motion was stopped at a distance that the tunneling resistance yields a value of approximately 15 MΩ, far away from "jumping-to-contact".*

This steady state situation changes drastically at higher temperature when the mobility of the Au atoms increases. Due to the non-planar arrangement of the electrodes in respect to the substrate, the thermal expansion is expected to be rather non-linear.

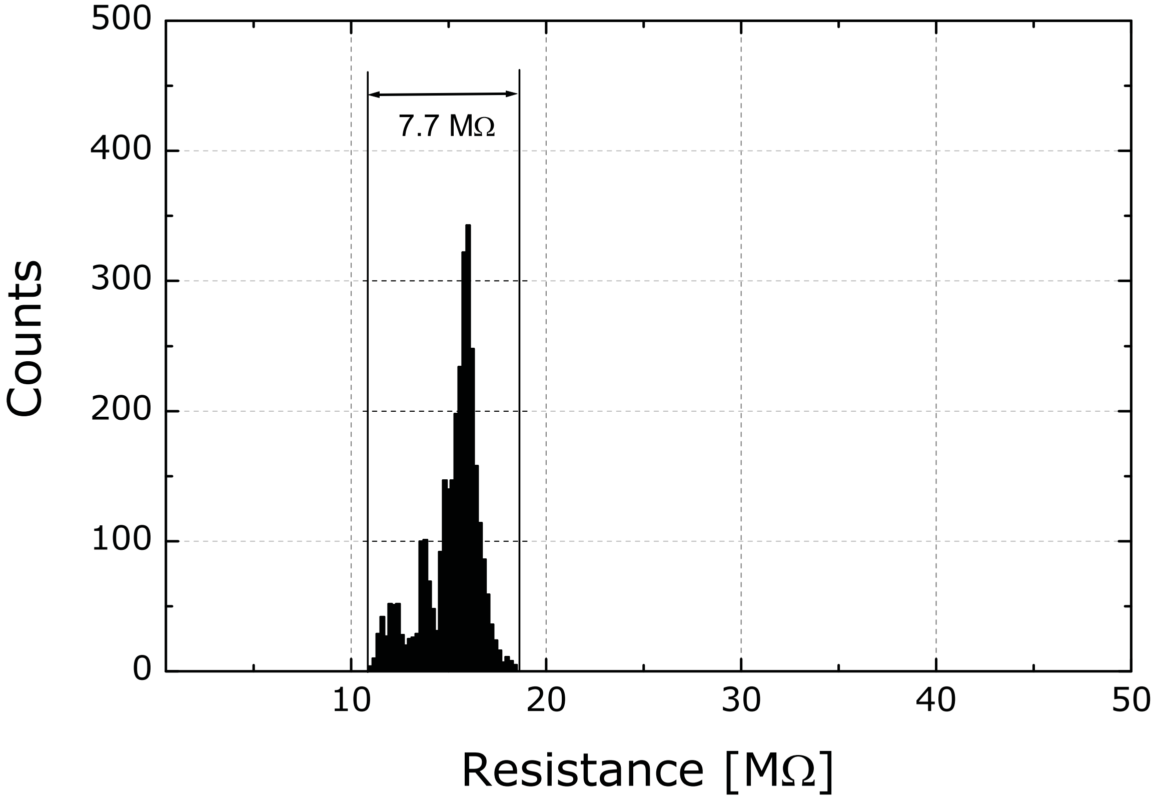

Figure 3.6: *Statistical distribution of the tunneling signal recorded in Fig. 3.5. The distribution reveals a sharp peak at 15.8 MΩ with very low fluctuations, indicating a very constant gap distance.*

Figure 3.7 shows that the electrode distance has to be corrected strongly in order to maintain a tunneling resistance of approximately 1 MΩ during cooling of the junction. Two regimes are observable with different correction dynamics (slopes S_{HT} and S_{LT}).

The temperature-dependence of the gap separation is difficult to analyze. The non-planar arrangement of the electrode during bending of the substrate causes a non-linear temperature vs. gap distance relation. Furthermore, the slopes displayed in Figure 3.7 also varies among different samples, indicating microscopic variations in the tips. At temperatures below 100 K, the system reacts too fast to be able to manually adapt the gap distance over the mechanics in order to keep the resistance constant. This is due to the low thermal capacitance of the entire sample holder at low temperatures.

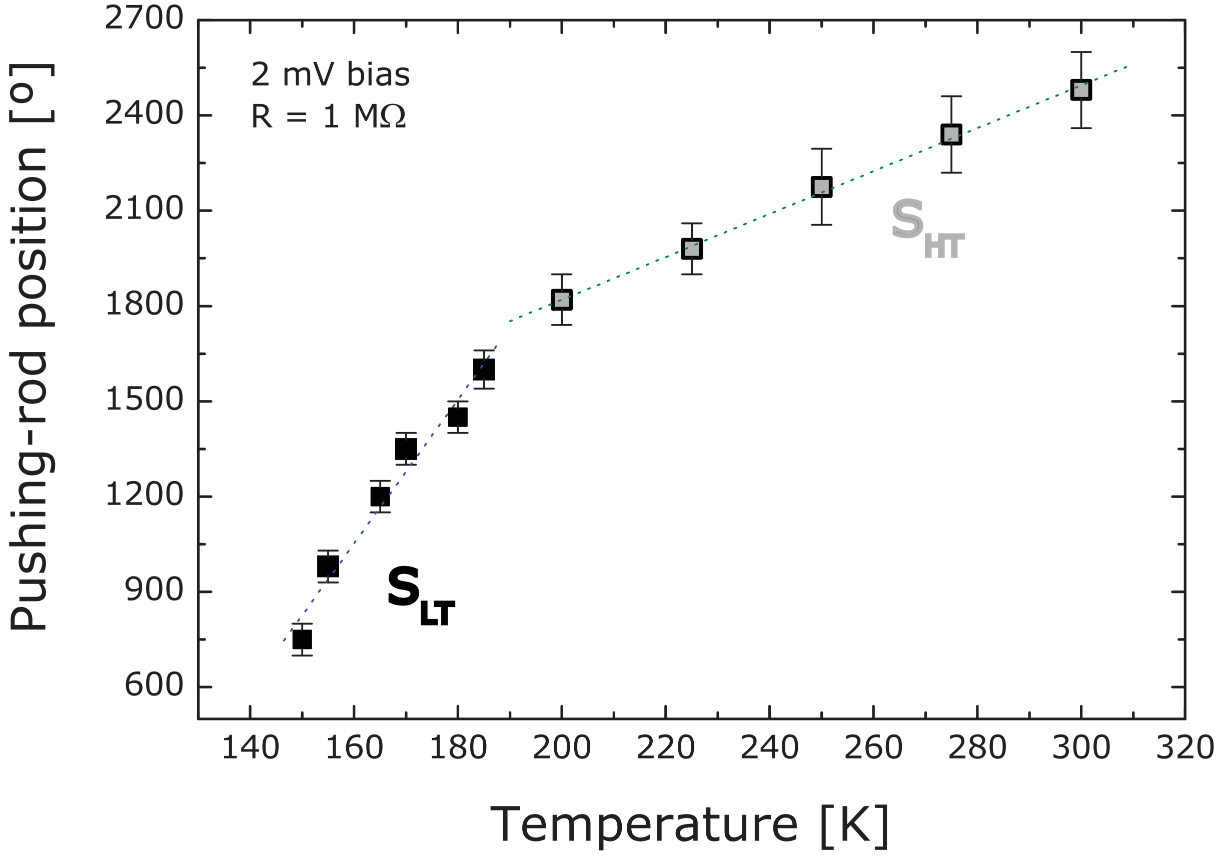

Figure 3.7: *The electrode distance correction is adjusted manually by moving the pushing-rod upon cooling in order to maintain a constant tunneling resistance of approximately 1 MΩ. The correction values follow an almost linear behavior for high temperatures (S_{HT} for $T > 200$ K) and change the slope for low temperatures (S_{LT} for $T < 200$ K). At lower temperatures than 100 K, the system reacts too fast to be able to manually adjust the gap distance over the mechanics. This is due to the low thermal capacitance.*

In summary, the stability of the MCBJ setup at low temperatures is excellent. Temperature sweeps are crucial to perform since the electrode distance changes rather non-linear with temperatures. This renders any correction mechanisms extremely difficult in order to maintain a constant gap distance. This has to be kept in mind for later investigations of transport through molecules.

3.5 Conductance Quantization

In the previous chapters, it has been shown that the last resistance value before breaking as well as the first value when closing the electrode pair are mostly found to be located very closely to a resistance of 12.9 kΩ. This value is well-known in mesoscopic physics as the inverse of the conductance quantum G_0 (see Chapter 7.1). The study of atomic-sized contacts was first conducted [26] after the invention of the STM. Values around 20 kΩ were measured in Ir by Dürig *et al.* [20]. Shortly afterwards, the conductance quantization was measured in two-dimensional electron gas devices [79]. The MCBJ technique, which was invented in 1985 [51; 52; 78], was dedicated to study these phenomena. Using this approach, quantum point contacts (QPCs) can be created relatively simple to investigate their electrical properties. As explained in Chapter 7.1, a QPC is represented by two metal reservoirs which are connected over a channel of the same material which has a spatial constriction in the dimension of the Fermi wavelength, λ_F. Due to excellent stability of the MCBJ, QPC's can be created by slowly breaking and closing the metallic junction.

Figure 3.8 shows the conductance, G, of a metal–metal junction as a function of the pushing-rod position during the opening procedure. The conductance is measured for various temperatures at a constant voltage of 5 mV. Distinct step-like features are present at multiple integer values of G_0. These steps are generally more pronounced for smaller multiple integers of G_0. The total pushing-rod travel distance during this step-like decrease of conductance, e.g. from $G \simeq 10 \cdot G_0$ to $G \simeq 1 \cdot G_0$ varies for different temperatures. At 150 K, this range is almost four times longer than at room temperatures due to the formation of longer plateaus. The last plateau value at 150 K is found to be slightly higher than G_0. This is often observed at low temperatures.

The appearance of conductance quantization with a fundamental value of G_0 indicates that the transport channel is narrower than the characteristic dimension, e.g. λ_{Au}, and no scattering occurs and electrons travel ballistically. However, the resistance of this channel is not equal to zero but limited by G_0. This is due to the quantum mechanical nature of electron waves which has to be invoked (the mean free path of electrons in bulk Au is 42 nm [2]) and which yields in a reduced transmission (see Chapter 7.1).

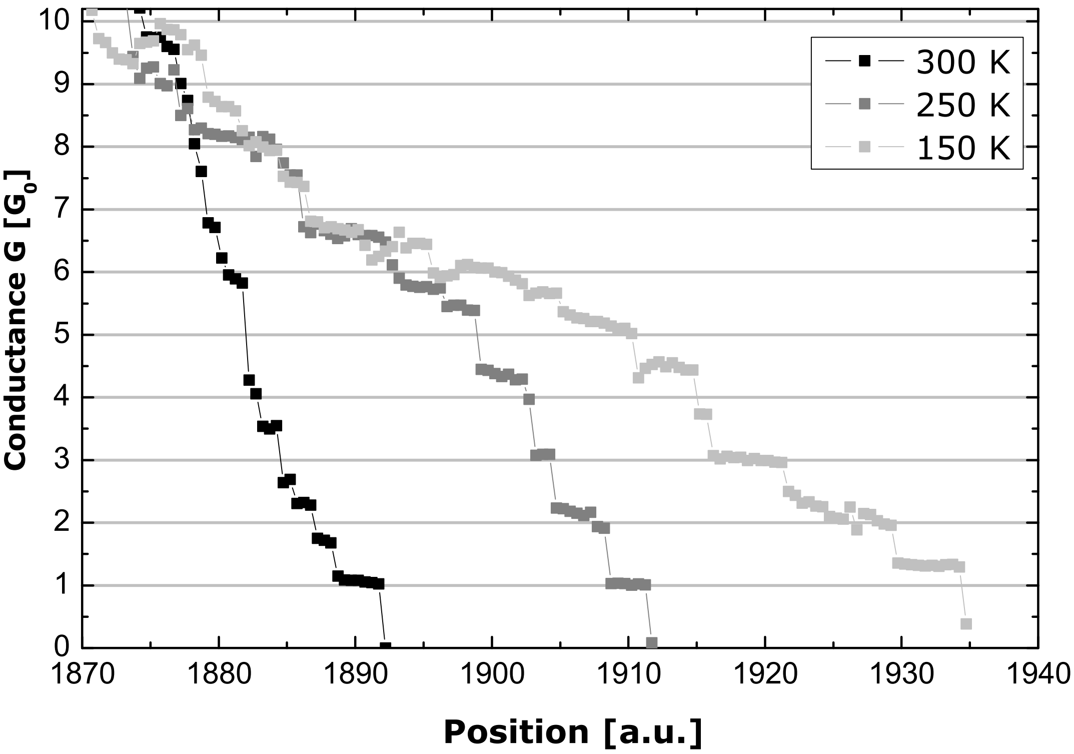

Figure 3.8: *Conductance measured during opening at 300 K, 250 K and 150 K of a Au-Au contact. The signal shows distinct steps, close to integer values of* G_0.

The atomic structure of the contacts can be quite complicated, as indicated by the behavior at higher conductance values (5 - 20 $\cdot$ G_0). However, if the contact reduces to a few atoms, the complexity is removed and clearer features are observed. Although no huge data set is presented here, which would allow histograms to be built, conductance values near 1 - 4 $\cdot$ G_0 are consistently observed. Especially G_0 is always very pronounced and the conductance quantization recorded under different temperatures and samples seems to reproduce. The energy scales involved are so large, that quantized conductance is visible even at room temperature (see Chapter 7.1).

Using the calibration described in section 3.3, the length of the plateaus can be calculated. Compared to the previously reported plateau lengths on manually notched Au wires [89], the plateau lengths in Figure 3.8 are much smaller, 20 - 30 pm, compared to 300 - 2500 pm. Taking the radius of a Au atom (approximately 288 pm) into account, it seems rather unlikely that these short plateaus correspond to the formation of mono-atomic chains. It is more likely that atomic-sized contacts are created.

The temperature-dependence of the mobility of a Au atom on the surface yields a different dynamic behavior in the neck formation at different temperatures. The mobility decreases at lower temperatures, and as a result, longer plateaus appear. The mobility has not only an influence on the formation of atomic-sized contacts but also on the diffusion of these atoms into the bulk.

Au as an inert electrode material has a low reactivity and its surface can easily be cleaned, e.g. by crashing the two contacts into each other. The chemical nature of Au plays an important role. The last value of the plateau at low temperatures deviates from G_0 (approximately $1.3 \times G_0$). This behavior is still present when the two tips have been cleaned by crashing them gently into each other. In order to understand this effect in more detail, further studies are required, such as creating histograms of conductance values with a large number ($\gg 1000$) of individual conductance curves [1]. But this was beyond the scope of this work. Moreover, no piezo element was used which would allow faster sampling rates with its higher bending speed. However, one can speculate that at low temperatures, even under UHV conditions, adsorption of impurities onto the junction may take place. This can create scattering centers which affect the transport properties of the channel and it becomes difficult to reach the theoretical value G_0.

3.6 Conditioning of the Electrodes

In the previous sections, it has been demonstrated that single-atom contacts can be created by the MCBJ method. In order to create atomic-sized electrode tips which are a prerequisite for facilitating the contacting of single molecules, a conditioning procedure is necessary and will be described in this section. This process conditions the tip of the electrodes in such a way that it yields atomic-sized electrodes. Since this conditioning is performed for every sample prior to the application of the molecules, it is necessary to have an computer-automated routine. Using very simple objective electrode driving parameters, it is possible to routinely create atomic-sized electrodes. This procedure is very important because the sharper the tips, the more likely it is to contact an individual molecule.

Due to the uniform initial channel dimensions defined by e-beam lithography, the first breaking point of the metal bridge is located at almost equal position for all samples on the wafer when using the same preparation parameters, like, e.g., the temperature, pressure, velocity, and bias voltage. In the initial breaking process, the breaking points of the bridges are usually located at $(4200 \pm 200)^\circ$ for BeCu substrates and at $(3600 \pm 300)^\circ$ for PhBr substrates, respectively. This slight variation is due to an altered width of the initial metal bridge. The bending velocity of the rotary motor is set to be rather fast, 5°/s, in the breaking procedure, since high-resolution is not required; this is in contrast to the measurements in section 3.2 where velocity was set to be slow, 0.05°/s. Therefore, when the junction breaks, the resistance jumps immediately to the TΩ regime. Hence, the tunneling regime cannot be studied in detail. The bending velocity has a direct influence on the tension release within the Au film, therefore the initial breaking point depends on the stretching velocity. If the velocity of the rotary motor is in the range of 5°/s, the tension induced in the bridge cannot be compensated, thus causing the bridge to break immediately and the electrodes to be withdrawn.

After initial breaking of the electrodes, the ductile response of metal to deformation and the possibility of forming QPCs under an applied electric field are used to create atomic-sized tips [89; 57]. Figure 3.9(A) shows 30 subsequent opening and closing cycles of one specific sample measured at room temperature. The threshold for changing the direction of movement of the pushing-rod were resistance values lower than 100 kΩ and higher than 100 GΩ. The velocity

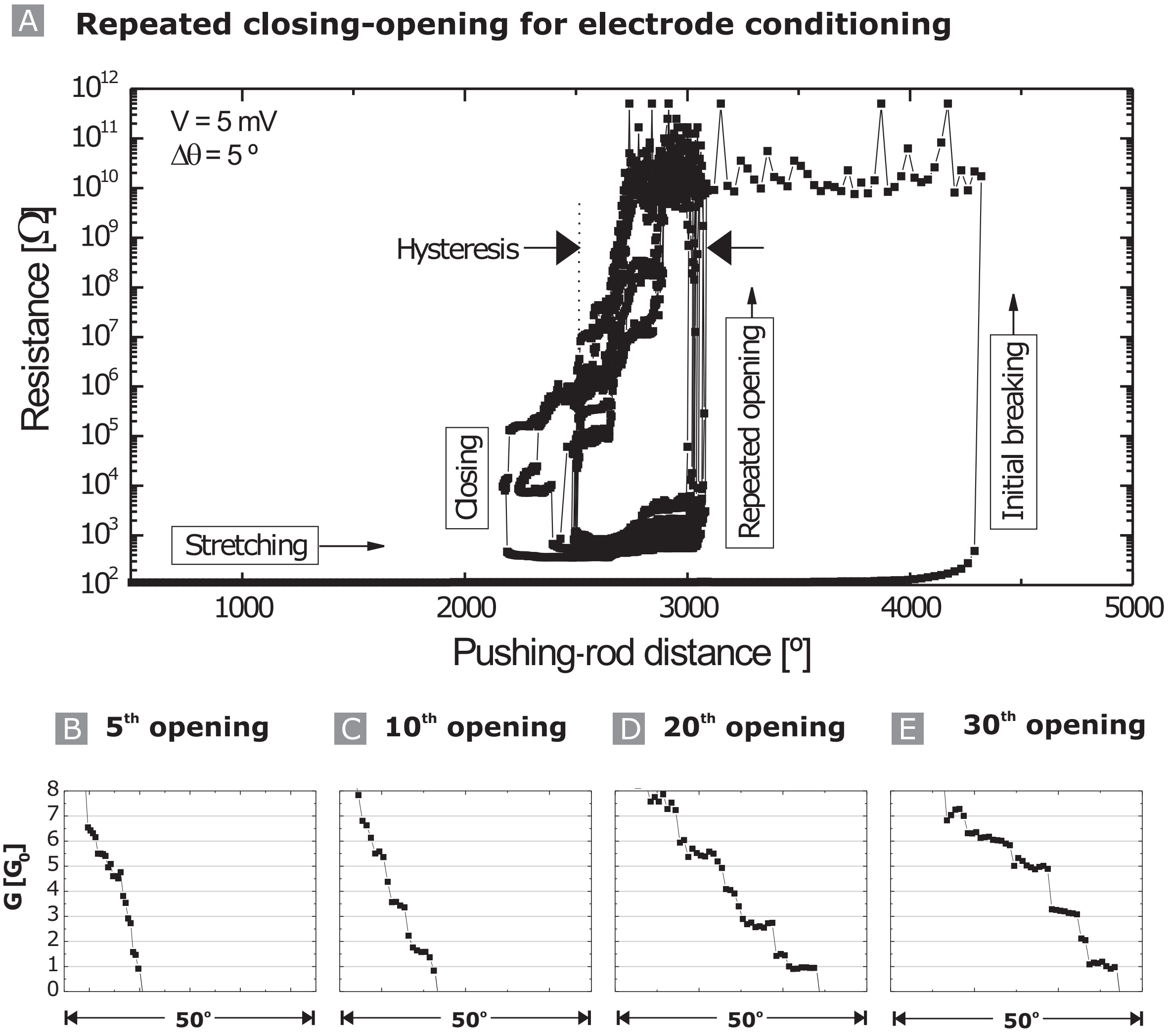

Figure 3.9: *(A) Repeated breaking and closing of the junction under a small bias of 5 mV. (B)-(E) Pronounced steps close to multiple integer values of* G_0 *appear in the conductance versus distance plot, indicating formation of atomic-sized electrode tips.*

was kept constant at 1°/s. The initial breaking occurs at pushing-rod position 4300°, and the initial closing at position 2100°. All subsequent openings occur at position 3100°, and the closings between 2100° and 2500°. This creates a hysteresis between the opening and the closing point of about 500°.

An open junction exhibits a resistance of 10^{10} to 10^{12} Ω. With increasing number of opening and closing cycles, the conductance quantization becomes more and more pronounced, as shown in Figure 3.9(B)-(E). This sequence illustrates how the conductance quantization evolves with increasing number of opening cycles.

In addition to more pronounced steps, the dynamics during the opening of the contacts changes as well: From 15° to 40°, or 68 to 180 pm, between the 5th (Figure 3.9(B)) and the 30th closing cycle (Figure 3.9(E)). This indicates that the transport channels are becoming more pronounced and that at the end, a single-atom contact is present and defines the microscopic shape of both electrodes.

The hysteresis displayed in Figure 3.9(A) changes as a function of the temperature. Figure 3.10 shows that the opening positions change only slightly when ramping the temperature (Δd = 200°, from 3700° to 3500°), compared to the closing positions which are more affected by the temperature change (Δd = 700°, from 3500° to 2800°). The overall hysteresis increases from 200° at 300 K to 700° extrapolated to 0 K. This temperature-dependence indicates that the mobility of the Au atoms under an applied electric field is reduced with decreasing temperature: the electrodes needs to compress further compared to room temperature in order to establish a direct metal–metal contact. The atoms can no longer be aligned and easily being moved under the electric field due to the reduced mobility.

After the initial breaking, the largest amount of tension induced by the bending has to be released and therefore the two electrodes created are withdrawn. This causes a hysteresis to appear in the subsequent closing procedure. All subsequent opening positions are located at pushing-rod position 3100°. This can be explained by the limited reservoir of atoms participating in the junction formation: most other atoms remain in the bulky part of the electrodes unaffected by the mechanical manipulation.

In addition to the tension release discussed, the mechanical influence from the three-point bending mechanism can play a role. Because the pushing-rod is controlled by threads which are connected to a rotary motor, the possibility of a backlash cannot be fully excluded. How-

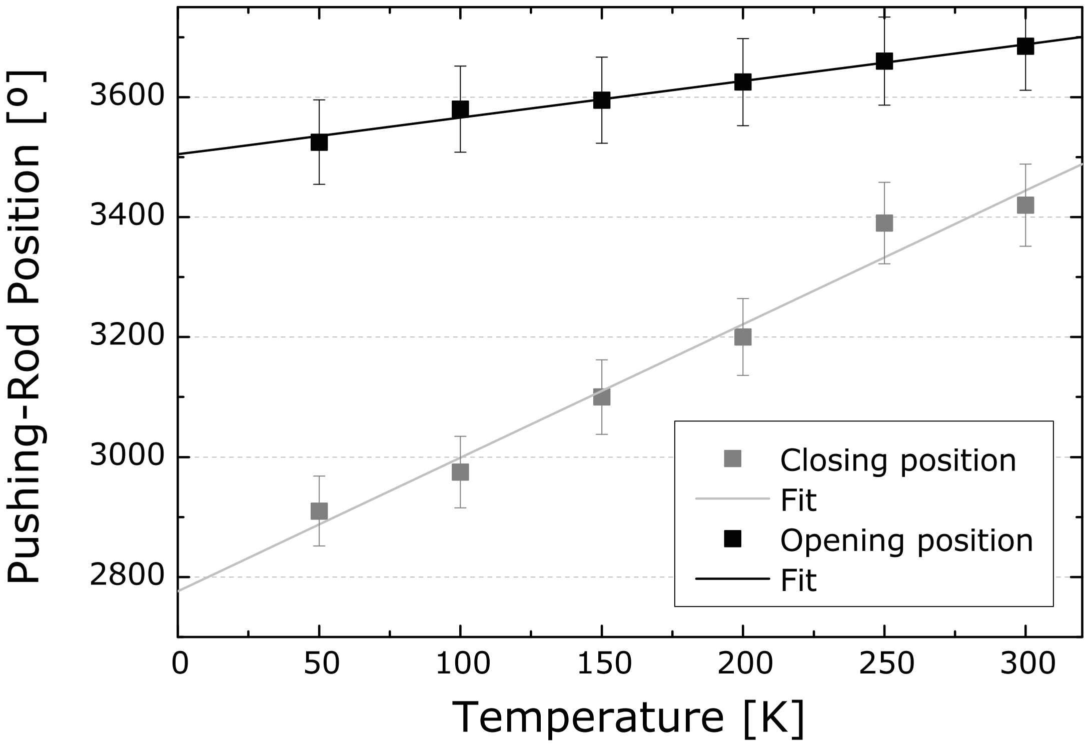

Figure 3.10: *Temperature dependence of the hysteresis occurring between opening and closing positions. The opening positions remain almost constant whereas the closing positions are shifting. The hysteresis increases with decreasing temperatures. This is due to a decreasing surface mobility of the Au atoms which needs to be compensated by a larger mechanical movement in order to close the junction again.*

ever, since the order of magnitude for the hysteresis varies from sample to sample, it is more likely that the hysteresis is caused by the tension release and the rearrangement of atoms than by mechanical effects originating in the bending mechanism. If the mechanical backlash was causing this effect, the hysteresis would always have the same value.

The automated electrode conditioning procedure is stopped when pronounced steps in the conductance vs. pushing-rod position plot are observed, e.g., like displayed in Figure 3.9(E). The entire procedure takes around two hours. The appearance of conductance quantization indicates the formation of single atomic-sized electrode tips.

3.7 Conclusions

The experiments on metal–metal junctions reported in this chapter show that atomic-sized contacts can be created using relatively simple and purely mechanical techniques. The stability of the MCBJ setup is excellent, allowing the electrodes to be manipulated with picometer resolution. This is mainly due to the immunity of the mechanical operating principle to vibrations and drifts. At low temperatures, the distance between the electrodes can be kept constant over minutes or even hours within 10 picometers. At elevated temperatures, the resolution and stability is drastically reduced due to increased mobility of Au atoms. However, even at room temperature quantum effects such as quantized conduction can be observed, indicating stable channel dimensions smaller than the characteristic parameters like the Fermi wavelength and mean free path. In conclusions, these atomic-sized contacts turned out to be very suitable for contacting single molecules, as it will be reported in the next chapters.

Chapter 4

Statistical Measurement Approach

In the previous chapter on the electrical and mechanical properties of metal–metal junctions, it has been demonstrated that the MCBJ electrodes possess excellent stability. In addition to having a positioning accuracy in the picometer range, these atomic-sized electrodes meet the basic requirements for contacting single molecules. In this chapter, the process of contacting single molecules between the electrodes will be explained.

The measurements on molecular transport have to be conducted at low temperatures to stabilize the electrodes (see previous chapter). Here, consistent transport measurements can be taken routinely and repeatedly. However, the solution containing the organic molecules of interest needs to be applied to the junction at room temperature. As mentioned in the previous chapter, temperature-dependent measurements are challenging due to the thermal electrode elongation. Therefore, experiments in the MCBJ geometry have to get rid of the thermally induced distance variations upon cooling or heating.

Once a molecule is contacted to both electrodes, contact effects have to be considered. Due to small size of the molecules, which is in the order of the surface roughness of the electrodes, various microscopic contact configurations are possible. The corresponding transport properties may vary due to their sensitivity to different bonding sites, the voltage drop across the molecule and the corresponding charge transfer (see Chapter 7.1).

Due to the different microscopic electrode geometry, various bonding sites are available for the linker group on the metal surface. In case of the hexagonal packed Au, the coupling can result in a top-side or a hollow-side contact. So far, the control over such details is not under experimental control.

For all these reasons, only statistical measurements and analysis can adequately address the distance variations and the contact effects. Therefore, a statistical measurement and analysis approach was developed within the framework of this thesis. It fulfills several of the aforementioned requirements: First, it is almost independent on distance changes between the two electrodes opposite to each other. Second, it manipulates the coupling of the molecule to the two contacts in a statistical way. This enables the entire conductance spectrum of a molecular junction during formation and breaking to be monitored at a certain temperature.

Furthermore, the most probable curves and the fluctuations can truly be identified during the subsequent statistical analysis. Due to the lack of experimental control over precise atomic arrangement of the molecule in respect to the contacts, a statistical approach is, the only available way to get an understanding of the various transport phenomena at the molecular scale.

4.1 Molecules and their Application on the MCBJ

Charge-carrier transport through individual organic molecules will be preformed in this thesis under UHV conditions and at different temperatures. This necessitates the molecules to be attached to metallic or semiconducting materials over so-called "alligator-clips". These functional end groups bind the molecule chemically to the electrode material (see following Chapter 5) which allows the experiments to be conducted outside of solution. Measurements under UHV conditions facilitate a more accurate investigation of charge-carrier transport experiments through such systems, since the complicated interaction with the ambient solvent is no longer present and the molecular system can be regarded as being perfectly isolated.

The functional end groups of all molecules are protected using protection groups in order to avoid agglomeration of the molecules within the solution. These protection groups are either removed ("deprotected") actively by adding aqueous NH_4OH (in case of the acetate moieties) prior to the application onto the junction, or deprotected *in-situ* when the molecule gets in contact with the Au surface (being the case when using acetyl protection groups).

After having created two atomic-sized electrodes by using the conditioning procedure described in Chapter 3, the distance between the leads is set to be slightly longer than the molecule to be studied. This can be achieved despite of the hysteresis discussed in Chapter 3.6 because the closing events remain at fixed positions for a constant temperature. Then, the UHV-system is flooded with nitrogen and subsequently opened, so that a small droplet of the solvent containing the molecules can be placed on the junction. The dome of the system is nitrogen-flooded and will be closed immediately after the application. Within a few second, the solvent is evaporated and the system is pumped and evacuated again (see Chapter 2).

4.2 Contacting Procedure

Measurements are conducted after reaching a chamber pressure below $8 \cdot 10^{-8}$ mbar. Under a small bias, typically 1-20 mV, the junction is slowly closed and the resistance is measured simultaneously. Figure 4.1 shows a typical contacting curve. Starting from an open junction with TΩ resistance, a sudden drop in resistance over at least four orders of magnitude is observed at pushing-rod position 2462° (Figure 4.1(A)). The first contact with a resistance below 1 TΩ is usually shifted by approximately 300 - 900°, compared to the closing positions in the conditioning procedure. During further closing, the signal is maintained and its trace forms a stable plateau, approximately (42 ± 5) pm long (Figure 4.1(B)). The resistance drops again over two orders of magnitude at pushing-rod position 2452°, and values below the inverse of the conductance quantum ($R_0 = 1/G_0 = 12.9$ kΩ) are measured (Figure 4.1(C)). A subsequent opening cycle exhibits a similar behavior, again with a plateau. The length of this plateau is in the picometer range, e.g., in Figure 4.1(B) it is approximately (42 ± 5) pm. In general, the length depends on the molecule captured in the junction.

If the junction is closed further (Figure 4.1(C)), the resistance drops again over two orders of magnitude and a value below the inverse of the conductance quantum ($R_0 = 1/G_0 = \pi\hbar/e^2 =$ 12.9 kΩ) is measured, indicating a closed metal–metal contact.

The formation of a plateau in both the closing and the opening direction strongly differs from the tunneling characteristic between the metallic electrodes observed during the conditioning procedure in absence of molecules. Therefore, the region where the junction resistance creates a plateau as a function of electrode distance can be attributed to the formation of a molecular junction in which at least one molecule bridges the gap between the electrodes. Within this region, the characteristic transport properties of the particular metal–molecule–metal junction can be investigated.

The resistance plateau does not always appear in every closing cycle. Statistically, approximately every second junction shows a formation of a plateau. The functional behavior upon closing is the same as described in the electrode conditioning procedure, apart from the shift mentioned. This shift can be attributed to an additional withdrawal of the electrodes due to solvent treatment of the surface. The solvent–surface interaction releases tension within the electrodes. Due to this withdrawal, the pushing-rod has to be lowered further in order to close the junction again.

In the case where no plateau is formed, no molecule is located at the very end of one of the tips. During closing, since no molecule is bridging the gap, a metal–metal junction is formed directly. Therefore, the closing curve looks similar to that of metal–metal junctions. The 50 % success rate for creating a molecular junction seems to be rather low. However, the concentration of molecules in the solution is crucial and in principal a trade-off between having molecules at all at the very end of the tips and creating a high surface coverage on the electrodes. A higher concentration would increase the surface coverage and hence also the contacting probability. However, the concentration is not increased because the goal is to contact an individual molecule.

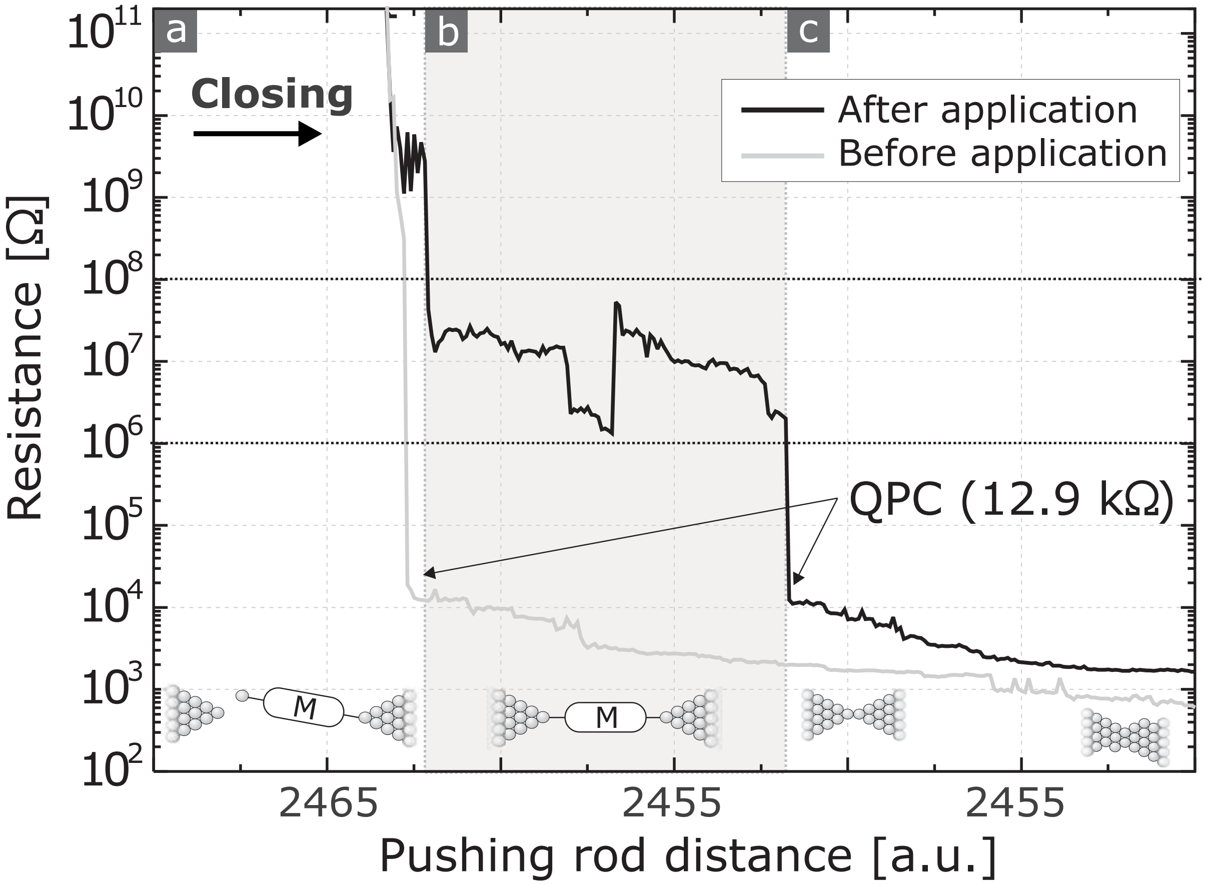

Figure 4.1: *Closing of a junction with molecules applied under a small bias of 2 mV (closing from left to right): (A) Starting from an open junction with TΩ resistance, a sudden drop in resistance over three orders of magnitude is observed at pushing-rod position 2462°. (B) During further closing, the signal is maintained and its trace forms a stable plateau approximately (42 ± 5) pm long. (C) The resistance drops again over two orders of magnitude at pushing-rod position 2452°, and values below the inverse of the conductance quantum ($R_0 = 1/G_0 = 12.9$ kΩ) are measured, indicating a closed metal–metal contact. The gray curve shows the closing behavior prior to the application of molecules.*

4.3 Statistical Measurement Approach

4.3.1 Motivation

In Figure 4.1, the formation of a plateau in the conductance versus pushing-rod position plot indicates the formation of a molecular junction. The resistance values of the plateau are not exactly constant during closing, when this data was recorded, as well as during opening, but are fluctuating even under a fixed bias. This can be explained by the inherent property of the molecular system, and the general sensitivity to microscopic details of the contact. These contacts are continuously manipulated during closing and opening procedure of the junction. Figure 4.2(A)+(B) gives two extreme illustrations of how the molecular junctions are supposed to look like. The molecule in this illustration is chosen to be the famous benzene-1,4-dithiol. Its length of 0.846 nm is in the same order as the size of a Au atom with a diameter of 0.288 nm. In the ideal picture, Figure 4.2(A), the molecule is symmetrically coupled to the same bonding sites on the metal, the microscopic shape of the two electrodes are equal, thus, the voltage drop across the molecule is homogenous. In the more realistic situation, as illustrated in Figure 4.2(B), the molecule couples at different bonding sites on the metal, hence the coupling is not symmetric. In addition, the microscopic shapes of the electrodes are not perfectly symmetric, which causes a more complicated electric field distribution and therefore a non-homogenous voltage drop across the molecule. These are only a few examples of all the possible factors a molecular system can be affected by.

Since the microscopic details of the contacts, including the different bonding sites of the molecule to the metal are not fully under experimental control, a statistical measurement approach is required. However, not only in terms of technology, the variations have to be quantified, analyzed, and resolved in the future. At the early stage of molecular electronics, research underestimated the issue of reproducibility and promised working molecular memory devices by the year 2005, which obviously did not happen yet. The large and, to a certain extent uncontrolled, fluctuations are doubtlessly a key challenge for a possible success of molecular electronics as a post-CMOS technology in the future. Since these fluctuations are caused primarily by the metal–molecule contact, a statistical approach to understand the behavior of the molecular contact to the metal has been developed and is described in the following.

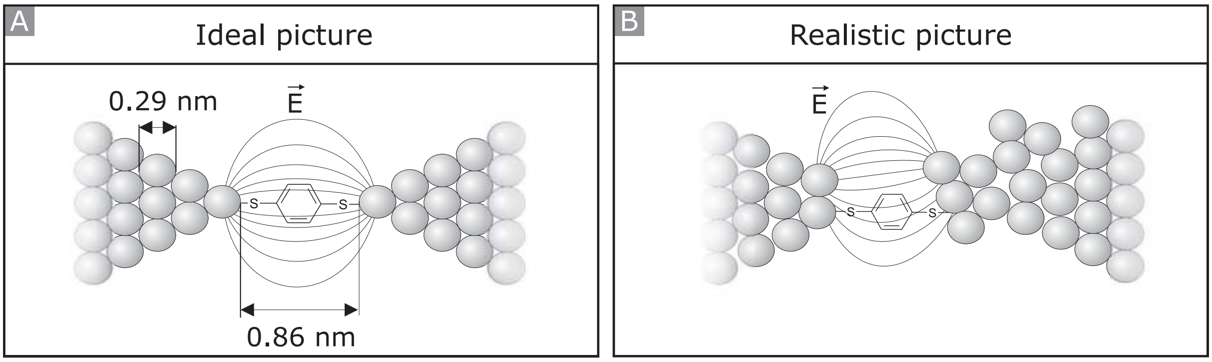

Figure 4.2: *Ideal and more realistic illustration of a simple molecular junction. The phenyl-1,4-dithiol molecule (PDT) can bond on different sites to the metal, providing a different work function. Moreover, the geometrical shapes of the two electrodes can differ on the microscopic level, causing a different voltage drop across the molecule.*

4.3.2 Principle of the Statistical Measurement Approach

In terms of charge-carrier transport investigations, it is necessary to study the functional behavior of the current as a function of voltage in a large voltage window (typically 0.5 – 3.0 V) in which the first molecular orbitals can be probed. Conventional measurements can determine the conductance of a molecule only at one specific bias value by applying fixed voltage [71; 86]. Therefore, in the approach presented here, current–voltage, *I*–*V*, curves of the molecular junction are simultaneously acquired during stepwise closing and opening. Only *I*–*V* curves provide the information on the non-linear transport properties. The *I*–*V* curves can also not be constructed by acquiring different conductance values at different voltage points.

The incremental change of the electrode distance is chosen to be typically between 1 and 5°, depending on the length of the molecule under investigation. The electrode motion is completely stopped at each position, and several *I*–*V* curves (typically 3 - 5) are recorded to study the reproducibility of the data and the dynamic effects in the electrode motion as well. Since the molecule is attached to both electrodes, the bending is not only meant to create a larger gap but also results in a change of the microscopic electrode tip geometry. This assumption is justified since the Au interbulk forces are weaker compared to the sulphur-gold bond, and also compared to the intramolecular forces.

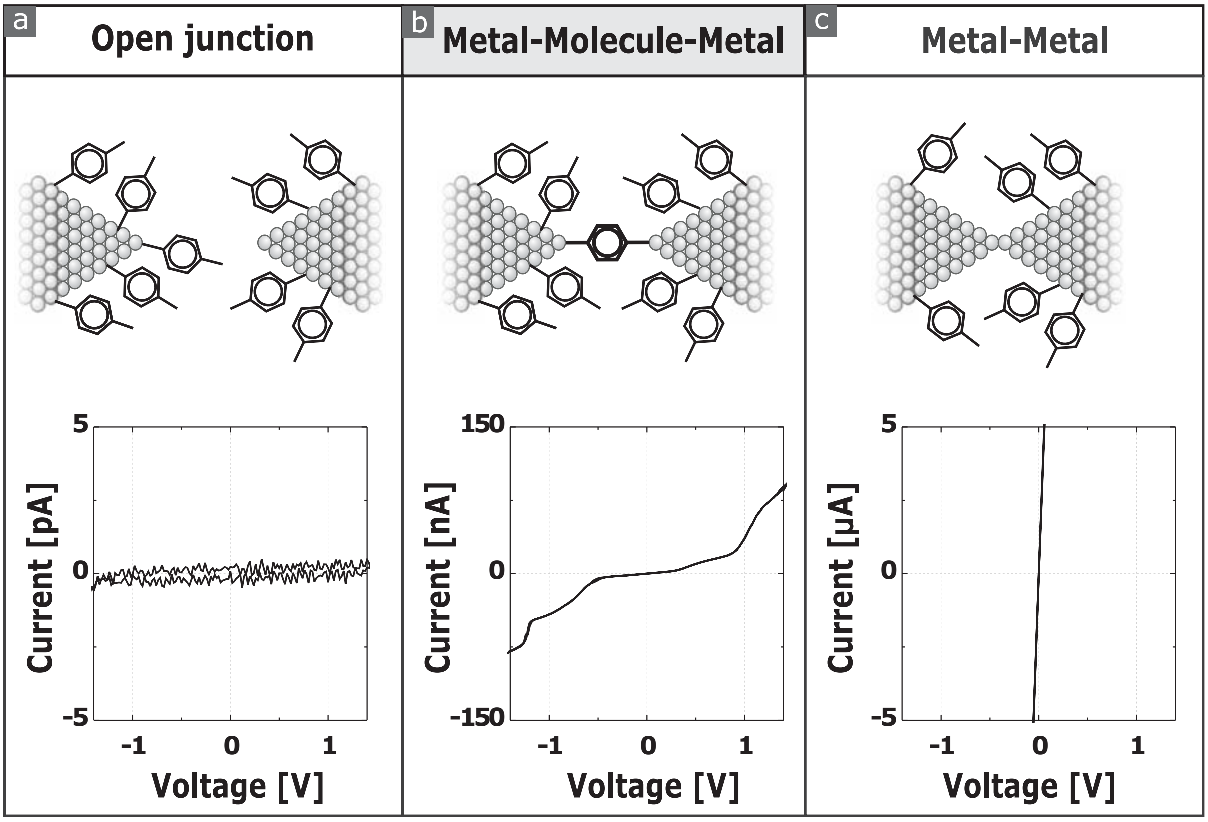

Figure 4.3: *Illustration of the different situations assumed in the junction: Distance variation from (A) an open junction with molecules attached so far only to one electrode, to (B) a metal–molecule–metal contact, and (C) a closed metal–metal contact. Corresponding I–V measurements (experimental data) reveal (A) a noisy signal in the sub-pA range, (B) stable I–V curves with features characteristic of the particular metal–molecule–metal system under investigation (currents typically in the nA range), and (C) an ohmic behavior with currents in the μA range.*

Therefore, the stretching of the metal–molecule–metal junction, primarily manipulates the electrodes. Hence, the statistical approach creates different microscopic configurations of the junction.

Starting from an open junction with the molecules attached only on one electrode (Figure 4.3(A)), a signal with currents in the sub pico-Ampere (pA) range is measured, which are dominated by the electronic noise level of the setup. When decreasing the distance between the electrodes, an abrupt jump to a stable and reproducible *I–V* curve is observed, in a good agreement with the jump in resistance under fixed bias as already described in Figure 4.1. Now, the current flow is in the nano-Ampere (nA) range and the *I–V* curves exhibit a non-linear behavior (Fig. 4.3(B)), which can be attributed to the characteristic signature of the particular metal–molecule–metal system under investigation. During further closing, the *I–V* characteristic is maintained over a range which is also in a good agreement with the plateau length observed during closing or opening under a constant bias (as described in Figure 4.1(B)). Beyond this region, a sudden jump to much higher currents in the micro-Ampere (μA) range occurs where the *I–V* data is characterized by a linear curve, indicating a closed metal–metal junction (Figure 4.3(C)). At this point, the direction of electrode motion is reversed and a subsequent opening cycle is performed accordingly, which also results in the formation of a plateau. From the formation of a plateau in the opening direction, it can be deduced that the second linker of the molecule is indeed chemically attached to the second electrode. Because the molecular backbone is rigid and the thiol-gold linkage is not broken, the mechanical stretching must be counterbalanced by a ductile deformation of the gold electrodes. Further bending finally breaks the metal–molecule–metal junction, creating again an open junction with TΩ resistance at 1 V. This closing–opening procedure is automatically repeated between 10 and several hundred times and the huge data set acquired is statistically analyzed using software tools developed.

Owing to the aforementioned ductility-induced drifts in the electrodes, the controlling of the junction is accomplished via the resistance measured rather than via the pushing-rod distance. Typical threshold parameters are given by a closed metallic contact with a resistance below $R_0 = 1/G_0 = 12.9$ kΩ and an open junction of at least 1 TΩ at 1 V. Using these parameters, drifts of the electrodes due to thermal expansion during temperature-dependent investigations can be compensated, even by means of a computer-controlled routine. This automated measurement procedure provides objectivity to the investigations, and the entity of all data acquired represents a solid basis for statistical analysis. To determine, for example, the number of molecules captured in the junction, conductance histograms at any arbitrary voltage can be extracted automatically from huge data sets. In these histograms, peaks at equidistant current values provided information about the number of molecules contacted [86]. Using the statistical approach described, not only conductance histograms can be extracted, but also the most probable *I–V* curves in the ensemble of all measured curves can be identified. Each *I–V* curve measured represents one specific microscopic configuration of the metal–molecule–metal system. In addition, the evolution in the formation of a molecular junction can also be observed.

4.3.3 An Illustrative Example: TPDT-DM at 300 K

The principal advantage of the statistical measurement approach becomes apparent in the following example, where a huge measurement dataset is displayed and analyzed exemplarily. An extended data set consisting of more than 1000 *I–V* individual and unfiltered raw data will be presented. In particular, the overview and the comparison of all transport characteristics acquired allows the individual transport curves to be understood in detail.

Figure 4.4(A) shows an extensive dataset of 1500 *I–V* double-sweep curves starting from – 1.0 V to + 1.0 V, measured at 300 K. For this measurement, 4,4”-bis(acetylthiol)-2,2’,5’,2”-tetramethyl-[1,1’;4’,1”] terphenyl (TPDT-DM, see inset of Figure 4.4(A) and following Chapter 6 for details on the molecular structure) was chosen. In this case, the free sulphur of the linker group creates two covalent bond on each side of the molecule to the gold electrodes. The acetyl protection group is released when establishing contact to the Au surface. This mechanism traps the molecule between the electrodes and allows for reproducible transport measurements. The dataset shown contains 25 opening and closing cycles, acquired over more than 14 h. Curves with linear behavior in the micro-Ampere range are excluded from the plot as they can doubtlessly be attributed to a closed metal–metal contact without molecules.

Figure 4.4(A) shows that three distinct branches of *I–V* curves are observed: A set S1 of curves carrying currents below 5 nA at +0.4 V and two sets, S2 and S3, of curves with currents above 5 nA at +0.4 V and below –5 nA at –0.4 V, respectively. The current histograms extracted at ± 0.4 *V* (Figure 4.4(B)) indicate that the majority of *I–V* curves is located in set S1. Figure 4.4(C) shows a subset of S1 in which the electrode distance was varied incrementally (7.5 pm).

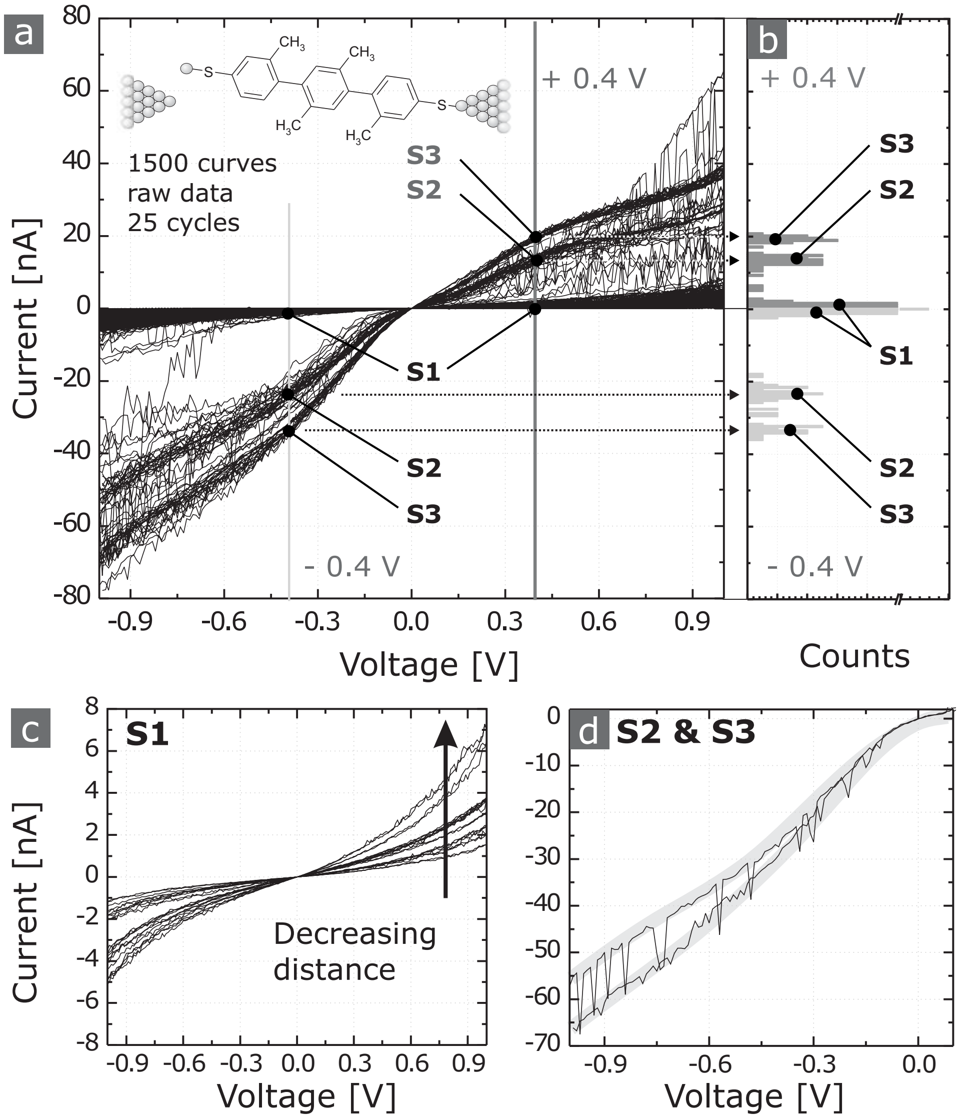

Figure 4.4: *(A) 1500 I–V curves acquired at 300 K for 4,4"-Bis(acetylthiol)-2,2',5',2"-tetramethyl-[1,1';4',1"] terphenyl (TPDT-DM) using the statistical measurement approach. (B) Current spectrum extracted at ±0.4 V displaying three sets of curves: (C) distance-dependent exponential curves indicating tunneling (S1) - the arrow indicates decreasing electrode distance. (D) Two sets (S2 and S3) containing a few curves with stochastic switching between the two distinct curves. The two envelopes according to the fluctuations in the dataset (A) are drawn in the background in light gray.*

The current depends exponentially on the distance between the electrodes, and increases by 1 nA with decreasing electrode distance of approximately 0.06 nm. Set S1 can be attributed to direct tunneling between the two electrodes. By contrast, the sets S2 and S3 can be attributed to a metal–molecule–metal junction (Figure 4.4(A)). Within these sets, a few special *I*–*V* curves can be observed that exhibit a bistable behavior where the current signal switches stochastically between two traces as shown in Figure 4.4(D). This type of stochastic switching has already been observed [60] and can be explained by different coupling of the thiol to gold, which leads to changes in the current flow through the molecule [84]. As shown, stochastic switching can very well be measured in *I*–*V* sweeps. In conventional conductance measurement under a fixed bias, these phenomena are very difficult to be measured.

Using the statistical measurement approach, the entire spectrum of *I*–*V* curves during the formation and breaking of a molecular junction can be monitored and the most probable transport characteristics can be objectively identified.

4.4 Discussion on Single-Molecule Measurements

In general, the MCBJ technique lacks proper imaging instrumentations. Therefore, analysis can only be based on the interpretation of mechanical and electrical properties of the molecular junctions. In this last and concluding section, the various indications for single-molecule measurements in the above and subsequently performed measurements using the MCBJ technique and the statistical measurement approach will be discussed.

There are several experimental observations which indicate single-molecule measurements:

1. As reported in Chapter 3, atomic-sized electrodes are formed during the conditioning procedure performed prior to the application of molecules. In combination with the very low concentration of molecules in the solvent, only in half of the cases a molecule is caught in the junction. This indicates that a very low surface coverage is present. A pronounced snap-in and an abrupt closing behavior is observed. The electric field assists the formation of a molecular junction, since the molecules can align to the gradient of the electric field applied

2. The plateau length is very short and scales approximately with the length of the molecule under investigation. This indicates that no molecules are lined up in one row.
3. Jumps to conductance values of twice the value can only be stochastically bserved. However, these are single events and generally, no distinct higher integer multiples in the current are found either.
4. Asymmetry in the *I*–*V* curves is a generic feature and typical for single-molecular junctions. If more than one molecule were participating in the molecular junction, the asymmetry would be smeared-out and hence not be observable.
5. Quantitative conductance values are found to be similar for similar molecular systems.
6. Upon closing of a junction, there is a sharp transition from the molecular range, indicated by non-linear transport properties, and the metal–metal range. No intermediate range is observed.
7. The switching molecules reported later on show only two distinct states. More than these two states would be present if two or more molecules were contacted.
8. The best way to get information, however, is to perform statistical analysis and to create histograms therefrom. If many thousand data show only a few distinct bundles, than single-molecule measurements were doubtlessly performed.

This discussion provides the argumentation for the interpretation of single-molecule transport results reported later on.

4.5 Conclusions

A statistical measurement approach was described in this chapter which allows the non-linear charge-carrier transport properties of molecular junctions to be studied in detail. The simultaneous acquisition of current–voltage characteristics upon the controlled manipulation of the molecular junction provides the entire conductance spectrum. Based on this data, the most probable transport properties as well as their fluctuations can be determined.

The statistical approach was described and illustrated in this chapter. It will be used for all measurements reported in the next chapters. Thereby, the measurement approach will demonstrate its importance.

Chapter 5

Properties of the Molecule–Metal Contact

The goal of this chapter is to study the influence of the chemical nature of the molecule–metal contact on the transport properties. Molecules with two different end groups will be discussed as examples. The first group is chosen to be the mostly used thiol (-SH) termination, providing a covalent bond to the metal. The second group is the isocyanide (-NC) termination forming a weaker covalent bond.

Investigating the charge-carrier transport properties of single-molecules necessitates the molecules to be attached to metallic or semiconducting electrodes via so-called "alligator-clips", the terminal linker part of the molecule. These functional end groups bind the molecule chemically to the electrode which facilitates measurements of charge-carrier transport through these systems under well-defined experimental conditions, e.g. under UHV conditions. Thus, the metal–molecule–metal system can be regarded as being perfectly isolated.

In the last chapter, in which a novel statistical measurement approach was introduced, it has already been mentioned that large contact effects due to different microscopic configurations of the electrodes have to be considered. In addition, the type of the chemical bond in the two molecule–metal contacts plays an important role in terms of transport as well. The metal-molecule coupling has thereby different tasks: First, it should provide mechanical and chemical stability to the system by making the molecule stick to the metal. It is generally more desired to have rather chemisorbed than physisorbed molecules on the metal. Second, the linker group should enable electrons to be injected from the electrodes to the molecule either by a small tunneling barrier or an almost ohmic contact. In the latter case, a good electrical contact and therefore a strong coupling is possible by the hybridization of molecular and metal wave functions, where the electron waves extend over the entire molecule–metal contact.

The choice of an appropriate metal and a corresponding chemical linker group is an empirical tradeoff between having an excellent contact, which in return may influence or dominate the transport properties of the entire molecular junction, or a bad contact, which may cause an instable molecular junction but does not disturb the intrinsic transport properties.

5.1 Molecular Model Systems

In order to study directly the influence of the chemical linker group on the transport properties of the single-molecule system, specially designed molecules are required. Small molecules enable a clear investigation of the different aspects of transport and can therefore be regarded as benchmark systems for more extended molecular systems. The molecular backbone of the molecules to be investigated and compared with must be the same whereas only the linker group should differ. Figure 5.1 shows the four molecules that were chosen to be investigated for this particular task: 1,4-phenyl-dithiol (PDT), 1,4-phenyl-diisocyanide (PDI), 4,4'-Bis(acetylthio)-biphenyl-dithiol (BPDT), and 4,4'-biphenyl-diisocyanide (BPDI).

The most prominent molecule among all four displayed is the 1,4-phenyl-dithiol (PDT), shown in Figure 5.1(A). It consists of a fully conjugated system, the benzene ring (see section 1.2.5 in the previous Chapter 7.1). This system is coupled to metallic leads by establishing a covalent bond (-SH). The 4,4'-Bis(acetylthio)-biphenyl-dithiol (BPDT), shown in Figure 5.1(B) uses the same linker group but has a different molecular backbone which consists of two instead of one phenyl rings.

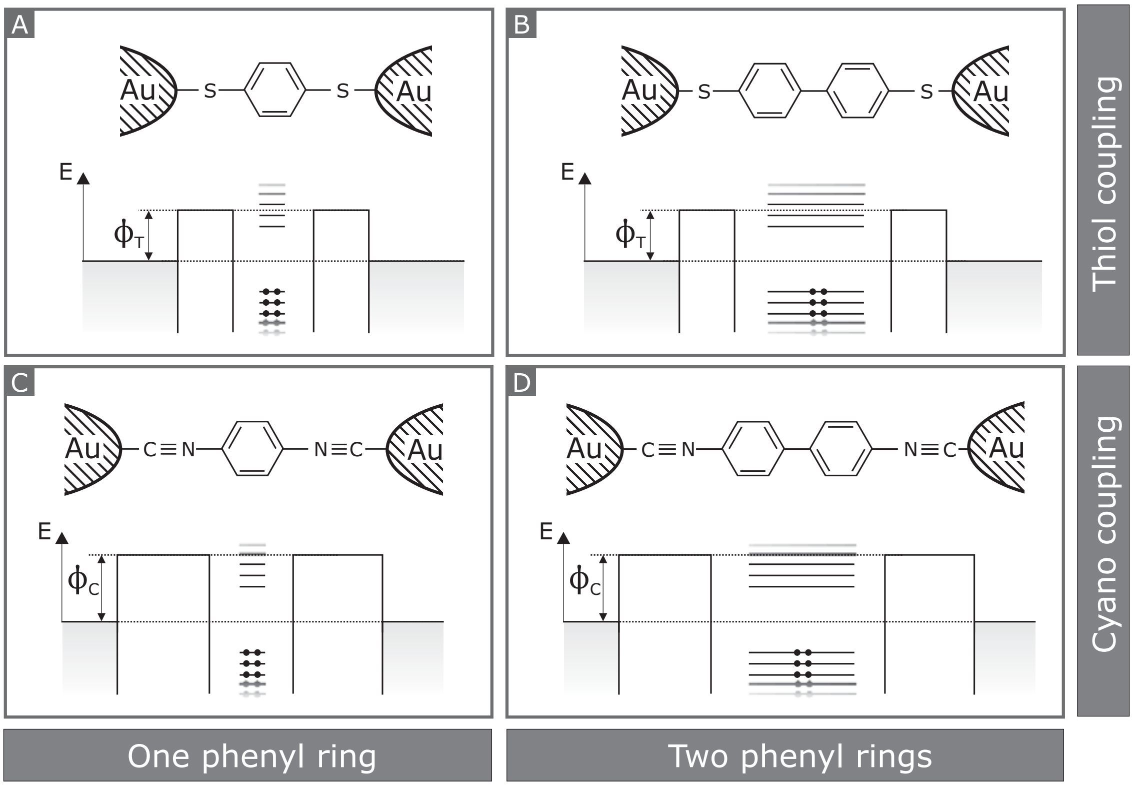

Figure 5.1: *-NC and -SH coupled single- and double-phenyl-ring systems with their corresponding energy diagrams: (A) 1,4-phenyl-dithiol (PDT), (B) 4,4'-Bis(acetylthio)-biphenyl-dithiol (BPDT), (V) 1,4-phenyl-diisocyanide (PDI), and (D) 4,4'-biphenyl-diisocyanide (BPDI)*

The conjugation between the two phenyl rings depends on the tilting of the rings relative to each other. The conjugation is assumed to be almost interrupted if the two rings are aligned perpendicular to each other, or in the other extreme case, it is assumed to be enhanced if the rings are lying in the same plane. The PDT and BPDT represent the two thiol-coupled systems. The isocyanide coupled systems consist of two analog molecules. The 1,4-phenyl-diisocyanide (PDI) (Figure 5.1(C)) represents a fully conjugated, single-ring system which is coupled to the leads using isocyanide (-NC) end group. Compared to the thiol linker group, this group forms a weaker, but still covalent, coordinate bond over the carbon atom which binds to the Au. The 4,4'-biphenyl-diisocyanide (BPDI) (Figure 5.1(D)) is the analogue to the BPDT, consisting of two sub-systems of phenyl rings. The conjugation between the two sub-systems in the BPDT and the BPDI is assumed to be equal for simplicity.

Also shown in Figure 5.1 are the corresponding, simplified energy diagrams of the molecules. The different molecule–metal coupling strengths were simplified and represented by an injection tunneling barrier of different heights between the electrode and the molecule. Φ_T denotes the tunneling barrier for the thiol termination, Φ_C the one for the isocyanide termination, respectively. The single- and double-ring systems differ in the molecular level spacing. Assuming a simple potential-well for the molecular system, the double-ring systems have a larger width but the same depth compared to the single-ring systems. This causes the density of states to increase, as illustrated by more molecular orbitals being present in the energy diagram of BPDT and BPDI, than in case of the PDT and PDI.

5.2 Phenyl-1,4-Dithiol (PDT)

The PDT is a molecule of fundamental interest because it represents one of the simplest molecules consisting of a conjugated system that is coupled via two tunneling barriers (sulphur linkers) to metallic leads. Therefore, charge-carrier-transport is mostly influenced by the molecule–metal coupling, because the electrons have to be injected over a tunneling barrier. This barrier defines the highest resistance of the metal–PDT–metal system. Thus, PDT is often considered as an ideal system to study the temperature-dependence of the metal–molecule coupling on charge-carrier transport. First measurements of this system were performed as early as 1997 by Reed *et al.* [63], using a similar MCBJ method.

Results

Figure 5.2(A) shows a set of five I–V and G_{Diff}–V raw data curves for PDT taken at 250 K. This data represents several dozens of curves acquired at different electrode positions during the closing and the opening cycle of the statistical measurement approach (see section 4.3 of the previous Chapter 4). Figure 5.2(B) shows the transport properties of PDT taken at 50 K. Both data sets at 250 and 50 K reveal two peaks in the differential conductance. At 250 K, the peaks are located at approximately $-$ 0.5 V and + 0.4 V, defining a conductance gap $2 \cdot \Delta_{\mathrm{cond}}$ of 0.9 V. At 50 K, $2 \cdot \Delta_{\mathrm{cond}}$ is slightly smaller, on the order of 0.6 V. In the temperature range between 100 and 250 K, the molecular junction can be opened and re-formed for many cycles. This is not the case at lower temperature. For instance, at 50 K, data acquisition is only possible for a few cycles at each position, because the junction becomes unstable and finally a closed metal–metal junction is formed.

In contrast to Reed's work [63], no stable and reproducible *I*–*V* characteristics could be measured for the Au–Single-PDT–Au system at room temperature, despite of extensive attempts (more than 30 samples tested). However, for much smaller voltages than 0.5 V, resistance histograms can be acquired even at room temperature. Figure 5.3 shows two resistance histograms measured at a voltage of 5 mV in the absence of molecules (Figure 5.3(A)) and the presence of PDT molecules (Figure 5.3(B)). In both cases, the junction was opened and closed 100 times, lasting 5 days in total for each measurement (no piezo is attached which would allow for a faster sampling). For creating histograms, all the curves measured during opening and closing cycles were taken into account and no artificial selection of curves exhibiting plateau formation was made. Figure 5.3(A) shows the resistance histogram in the MΩ region with an almost exponential behavior, indicating direct tunneling between the electrodes. In contrast, a peak in the resistance spectrum around 260 MΩ appears after the application of PDT molecules to the junction, as displayed in Figure 5.3(B).

Discussion

The most striking feature in the transport behavior of PDT is the appearance of a conductance gap, Δ_{cond}. For voltages within this gap, charge-carrier transport is only based on direct tunneling between the electrodes. If the voltage aligns with the first molecular orbital, the current increases. This molecular orbital can either be the LUMO or the HOMO, depending on the charge transfer occurring upon coupling (see Chapter 7.1). The energetic position of the molecular orbital involved in respect to the Fermi energy of the leads is represented by a peak in the G_{Diff}–V plot. Therefore, the size of Δ_{cond} is directly related to the energy difference between the molecular energy levels and the Fermi energy of the metal [59]. A shift in Δ_{cond} of 150 mV due to a temperature change of 200 K (as observed in Figure 5.2) cannot solely be explained by excitation of vibrational modes. Instead, manipulation of a junction during cooling can induce surface reconstruction of both electrodes, which may change the molecule–metal coupling and therefore results in the shift of the the conductance peaks with energy. An altered

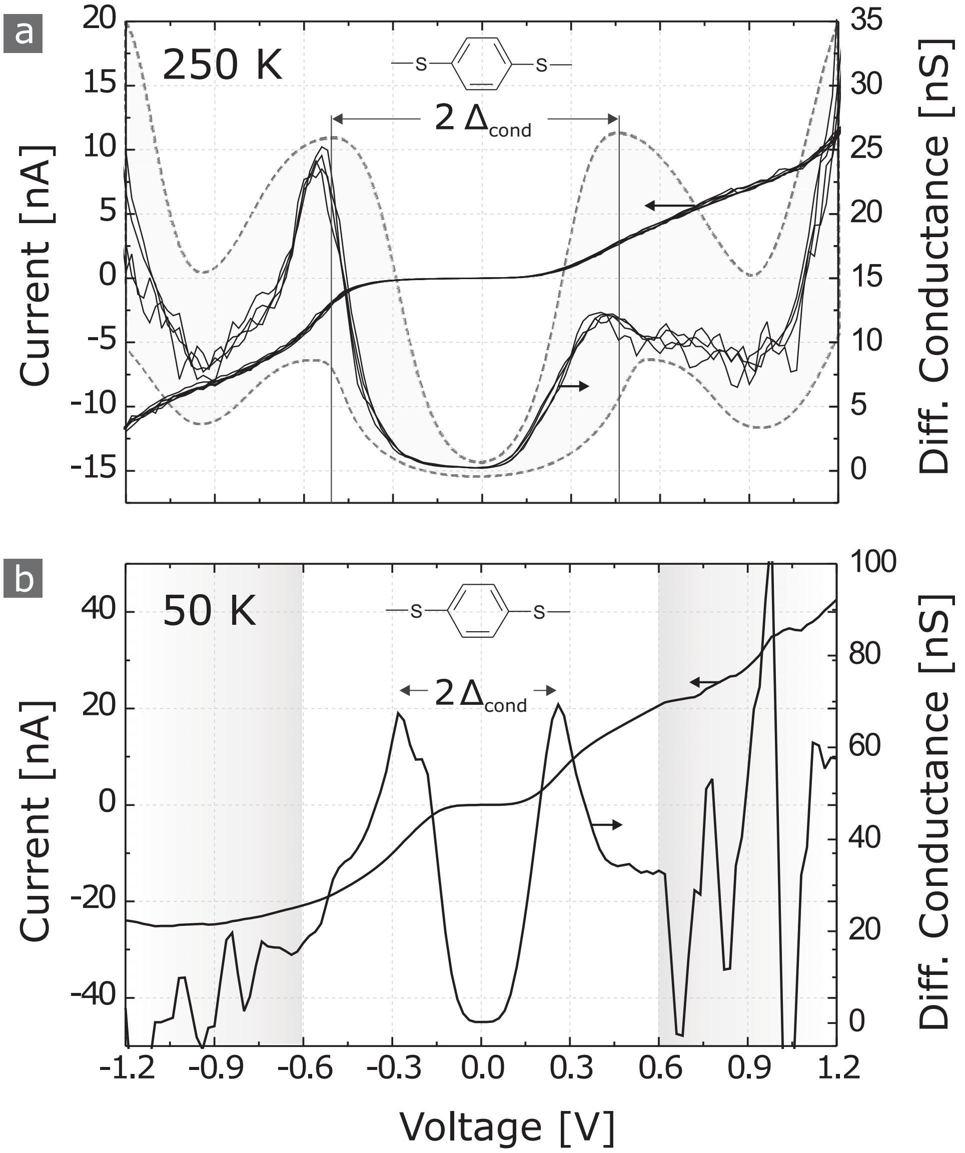

Figure 5.2: *Current–voltage, I–V, and differential conductance–voltage, G_{Diff}–V, characteristics of phenyl-1,4-dithiol (PDT) measured at (A) 250 K and (B) 50 K. The conductance gap, $2{\cdot}\Delta_{cond}$, decreases from 0.9 V at 250 K to 0.6 V at 50 K. At 50 K, an instability occurs for voltages larger than 0.6 V. This feature is inherent to the molecular system and cannot be attributed to the noise of the setup.*

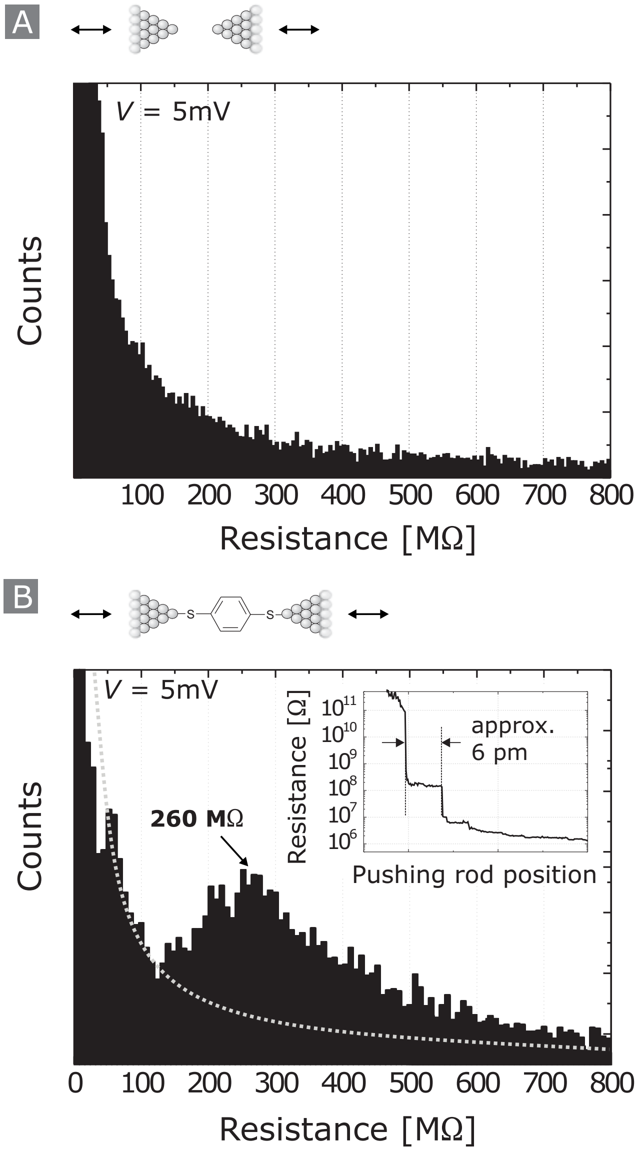

Figure 5.3: *Resistance histograms of 100 closing and opening cycles: (A) In the absence of molecules, and (B) the presence of PDT molecules (the gray dotted line in (B) represents approximately the envelope of the data in (A)). The measurements were taken at 300 K under constant bias (5 mV). The inset shows one representative contacting curve with a plateau length of only (6 ± 2) pm.*

charge transfer to or from the molecule at the different temperatures is plausible. The zero bias conductance at 50 K is 0.24 nS and relatively similar to 0.28 nS at 250 K, indicating the low density of states at energies close to the Fermi energy of the metal [59]. However, the zero bias conductance is very difficult to determine, since the signal level is only slightly above the noise level of the setup (some 100 fA at 300 K).

In Figure 5.2(B), the current signal above +0.6 V and below –0.6 V reveals significantly more noise than below ± 0.6 V. This feature is inherent to the metal–single-PDT–metal system and cannot be attributed to the instrumental setup. Interestingly, these features are also present in the work of Reed *et al.* [63]. In contrast to the results presented here, Reed *et al.* [63] used a MCBJ system with a manually notched wire completely covered by a SAM of PDT molecules. Voltages up to ±5.5 V were applied and a conductance gap of $2\ \Delta_{\mathrm{cond}} = 2.4$ V was found, which is much larger than measured in this work. Here, the two peaks in the conductance-voltage curve appear at significantly lower voltages for both temperatures. In addition, this metal–PDT–metal junction would not sustain voltages higher than ± 2.0 V, even at low temperatures. At room temperature, it was not even possible to establish a metal–single-PDT–metal junction prior to a metal–metal contact when performing *I*–*V* curves from –1.5 V to + 1.5 V, even on samples that formed molecular junctions at lower temperatures. This could be due to the ductile response to deformation of the Au electrodes, which is more pronounced at higher temperatures and the instability of the Au electrodes under the high electric fields in the order of $1 \cdot 10^9$ V/m (see Chapter 3).

The appearance of a peak in the conductance histogram for very small bias differs from the one without molecules. Therefore, the presence of the peak indicates the formation of a molecular junction. The peak is relatively broad because of variations in the microscopic details of the molecular junction due to repeated opening and closing. For example, the possible adsorption sites of the thiol group on the Au electrode and/or the orientation of the molecule with respect to the two Au electrodes (see Figure 4.2) may lead to different metal–molecule coupling and therefore broaden the peak in the histogram.

Since the applied voltage of 5 mV is very small and thus the electron energy is far away from any molecular orbital, the value of 260 MΩ is difficult to interpret. Basically, it illustrates the low density of states in the conductance gap. In contrast to [87; 86], no second peak was revealed, even when plotting the conductance instead of the resistance.

5.3 Phenyl-1,4-Diisocyanide (PDI)

In lieu of the thiol as linker group, isocyanides have been suggested as another possible “alligator clips” for single-molecule devices [68]. Compared to the famous PDT, the isocyanide-terminated PDI has only rarely been experimentally investigated, especially on a single-molecule level. Measurements on SAMs using isocyanide linkers have already been conducted [8; 19; 3; 41]. When studying the SAM device architecture, intermolecular reactions or variations in the contact geometry have to be taken into account. Measurements on a single-molecule level using STM techniques have been reported in [28]. In general, this fact is surprising, because the molecular structure of PDI provides in principle the same basis for fundamental investigations of transport through a very simple molecular system as the PDT represents. It will be shown in this section that isocyanide-terminated molecules can be contacted in the MCBJ geometry as well. Moreover, it will be demonstrated that the isocyanide linker group offers many advantages in terms of transport investigations on a single-molecule level compared to the “traditional” thiol linkers.

Results

As a first surprising result in the I–V characteristics of PDI, the weakly coupled PDI could be measured not only at low temperatures but even at room temperature. This is in contrast to the PDT which has approximately the same molecule length (approximately 0.85 nm length) and is thus exposed to the almost same electric field. Figure 5.4 shows several I–V and G–V sweeps taken at 50 K. This data represents several dozens of curves acquired at different electrode positions during the closing and the opening cycle. Compared to the PDT, the reproducibility of the data on different samples is much better, and for the entire temperature range, data acquisition is possible for many opening and closing cycles. At 50 K, no instability for voltages above ± 0.6 V is present, contrary to the PDT. In addition, the transport properties can be measured in many reproducible sweeps. Very similar to the PDT, a conductance peak appears. Its width is slightly smaller, as it will be compared and discussed in the next section.

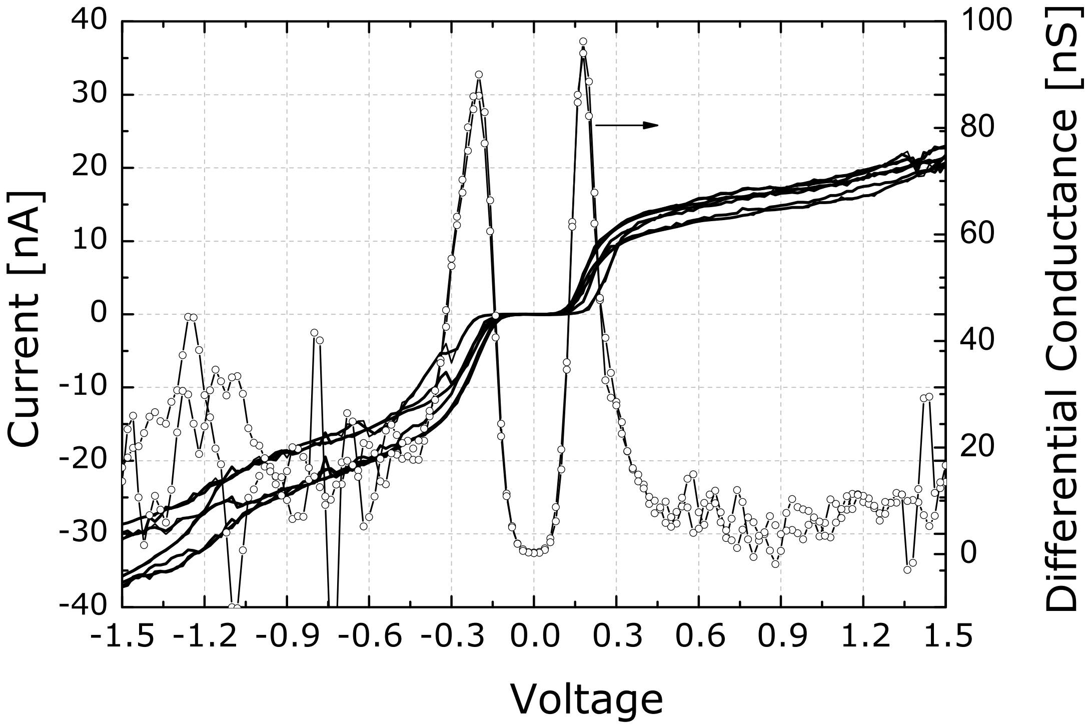

Figure 5.4: *Transport properties of PDI: Several I–V and G_{Diff}–V sweeps taken at 50 K. The conductance gap $2{\cdot}\Delta_{cond}$ is around 0.4 V, slightly smaller than in case of PDT. No instability is observed for voltages above ± 0.6 V, in contrast to the thiol coupled PDT.*

Discussion

It has been demonstrated that the isocyanide-coupled PDI can be contacted in the MCBJ geometry in a very reproducible and reliable way. In general, the discussion on the PDI results follows the one of the PDT. As already discussed, the position of the conductance peak signals the energetic location of the molecular orbital nearest to the Fermi energy of the metal. Compared to the PDT, the CN-coupling of the PDI results in a much better reproducibility, in the possibility of performing measurements at room temperature, and in the absence of any instability inherent to the molecular system at low temperatures. A more detailed comparison of the distinct differences between strongly and weakly coupled single-dot systems will be carried out in the next section.

5.4 Comparison of the Single-Ring Systems

The transport properties of PDT and PDI at 50 K are compared in Figure 5.5. The current amplitudes are very similar for both molecules, which is an indication that single molecules have been contacted. In the G_{Diff}–V plot of the PDT as well as for the PDI, no second peak is observed within the voltage window available. Furthermore, the symmetry of the differential conductance versus voltage plot for the positive and the negative voltage branch is consistent with the symmetric molecular structure of both molecules. This indicates that the coupling of the molecule to both Au electrodes is identical for this particular microscopic configuration. An empirical observation that holds especially for higher temperatures, shows that the coupling can also be rather asymmetric, as shown in Figure 5.2(A).

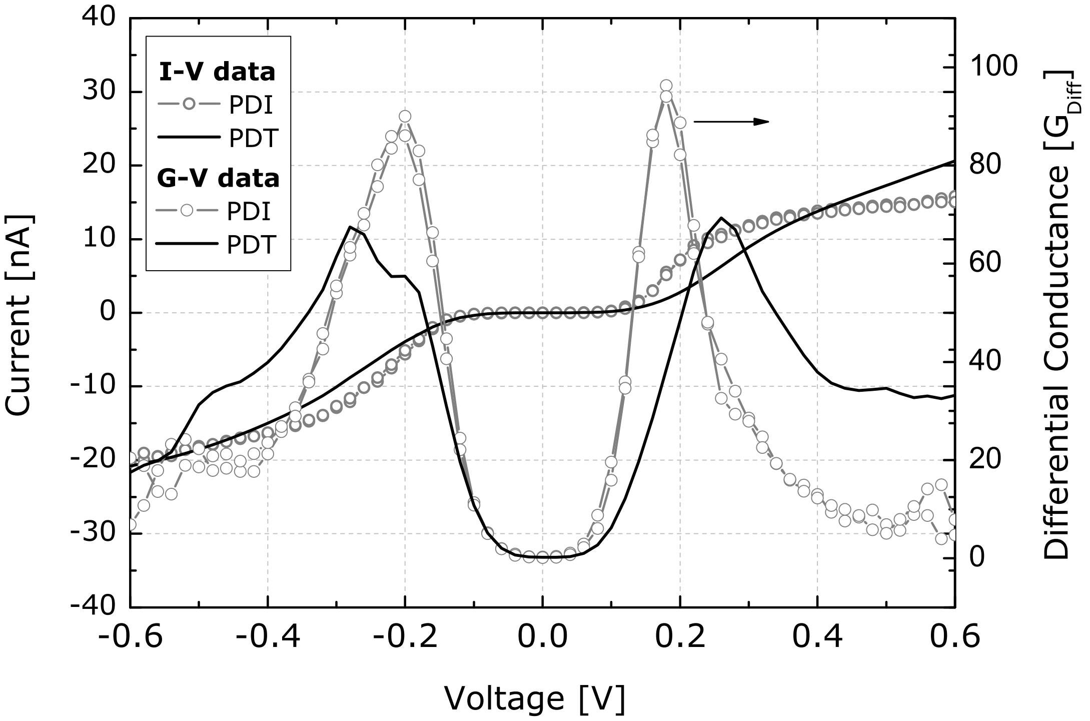

Figure 5.5: *Comparison of I–V and G_{Diff}–V data, measured for PDI and PDT at 50 K.*

Table 5.1 shows the conductance values at the peak position, the conductance gap resulting thereof, the conductance peak position, ϵ, in respect to the Fermi energy of the Au electrode, and the level broadening, Γ. The molecular level position, ϵ, was found to be $\epsilon_{PDT} = (266 \pm 5)$ meV for PDT, and $\epsilon_{PDI} = (197 \pm 5)$ meV for PDI, respectively. Hence, the conductance gap is around 140 mV smaller in case of PDI. In return, the conductance of the peak for the PDI is 35 % higher compared to PDT. The Fermi level of the metallic contact does not energetically line up with either the HOMO or LUMO levels in the molecule [15], as illustrated in Figure 5.1. The shift of about 69 meV between the two linker groups can be explained by different charging energies, U, for the two linker groups. If the conductance occurs through the HOMO, then charging energy of the isocyanide end group, U_C, would be smaller than the one of the thiol end group, U_T. If the conductance occurs through the LUMO, then the situation would be the opposite: $U_C > U_T$.

Molecule	Conductance / nS	ϵ / mV	Δ_{cond} / mV	Γ / mV
PDT	70 ± 10	266 ± 5	530 ± 5	137 ± 10
PDI	95 ± 10	197 ± 5	390 ± 5	93 ± 10
Relative	0.74 ±10	+ 69	1.35 ± 5	1.47 ± 10

Table 5.1: *Fitting results of the width of the peak, Γ, in the experimental data of PDT and PDI, according to a Breit-Wigner distribution. Also given are the conductance values of the first peak in resonance, the level positions, ϵ, and the resulting conductance gap, Δ_{cond}.*

Hong *et al.* conducted investigations on the same class of molecules using scanning tunneling microscopy (STM) [28]. They concluded that the isocyanide molecules reveal a shift in the Fermi level of the molecule as a function of phenyl ring number that is opposite to that observed for the thiol-terminated molecules. However, for the molecules containing one phenyl ring, they found $\epsilon_{PDT} = (980 \pm 100)$ meV, $\epsilon_{PDI} = (380 \pm 100)$ meV, which shows the same trend as the results achieved here using two symmetric electrodes.

As described in Chapter 1, the electron injection rate $\Gamma_i/\hbar$ from the electrode onto the molecule can be derived from the maximal current flowing through the molecular orbital involved (equation (1.17)). Due to the symmetry in the *I–V* data, the injection rate can be assumed to be equal to the escape rate, hence, $\Gamma_l = \Gamma_r$. Equation (1.17) simplifies therefore to:

$$I_{max} = \frac{2e}{\hbar}\frac{\Gamma_l\Gamma_r}{\Gamma_l+\Gamma_r} = \frac{e\Gamma}{\hbar} \,. \tag{5.1}$$

From the peak currents, $I_{max,PDT} = 7.7$ nA at 0.28 V, and $I_{max,PDI} = 5.1$ nA at 0.18 V, displayed in Figure 5.5, the injection rates, Γ_i, for the PDT and the PDI molecules can be derived to be $\Gamma_{PDT} = 3.16 \cdot 10^{-2}$ meV, and $\Gamma_{PDI} = 2.10 \cdot 10^{-2}$ meV. These very low injection rates indicate, the contact to the Au electrodes is rather weak and that a high tunneling barrier is present for both molecules. Due to the high injection and escape rates, the electrons are supposed to dwell for a relatively short time on the molecular orbital. This causes the particular level to be broadened energetically. As described in Chapter 1, the total level broadening of one single orbital is the sum of left and right coupling $\Gamma = \Gamma_{left} + \Gamma_{right}$ and can be described by a Breit-Wigner distribution:

$$D(E) = \frac{\Gamma/2\pi}{(E-\varepsilon)^2 + (\Gamma/2)^2} \, . \tag{5.2}$$

From the experimental results in Figure 5.5, the level position (in respect to E_F), ε, and the level broadening, Γ can be extracted, according to equation (5.2). Since the measurements were taken at 50 K, the thermal broadening, $\Gamma_T = \mathrm{k}_B\mathrm{T} \simeq 0.4$ meV, can be neglected. Table 5.1 displays the numerical results of a fitting procedure of the experimental data to a Breit-Wigner distribution, as shown in Figure 5.6. The level broadening due to coupling was found to be approximately 50 % higher (or 25 mV larger) in case of thiol compared to isocyanide coupling. This means that the influence of these particular chemical linker groups on the transport properties in general and on the level broadening in particular are very small.

Up to now, the work by Reed *et al.* [63], has never been reproduced on a single-molecule level. Nevertheless, it triggered many theoretical concepts for a fundamental understanding of charge-carrier transport through this relatively simple molecule. Depending on the different approximations and models, the simulated conductances [65; 88; 17; 27; 29; 74] often differ from the experimental data [86; 81]. For instance, N. Lang and Ph. Avouris have calculated the conductance and peak positions for PDI and PDT molecules contacted to Au leads [17; 39]. The results of the calculations are shown in Table 5.2. The conductance for the PDT is theoretically found to be 2.5 times higher than for the PDI. This trend is not found in the experimental data presented here. The typical discrepancy between theory and experiment, which is given in the conductance values, can be explained by the sensitivity of the calculations to the exact configuration of the contacts.

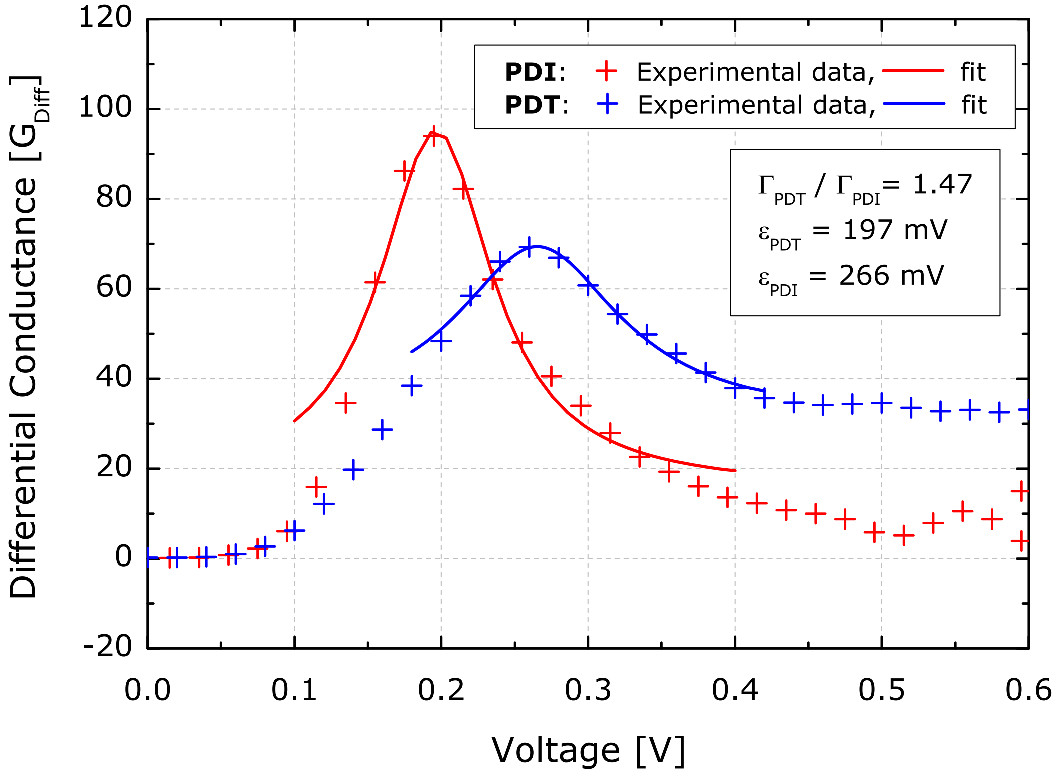

Figure 5.6: *Experimental G–V data for PDI and PDT, fitted to a Lorentzian distribution using equation (5.2). The parameters achieved are given in the inset.*

5.5 Comparison of the Double-Ring Systems

In this section, the two double-phenyl-ring systems, the BPDT and the BPDI molecule, will be electrically characterized. The influence of the longer molecular backbone on the electron injection rate from the metal electrodes onto the molecule, as well as on their transport properties will be studied.

Molecule	Conductance / ($2e^2/h$)	Length / nm	DOS / meV
PDT	0.21	0.78	730
PDI	0.08	1.03	110
Relative	2.6	0.75	6.6

Table 5.2: *Density Functional Theory (DFT) calculations performed for PDT and PDI, reproduced from Lang et al. [18; 41].*

Results

Figure 5.7 shows *I–V* and *G–V* sweeps starting from 0 V to 1.0 V taken at 50 K for BPDT and BPDI. The isocyanide-coupled double-ring system BPDI has a lower onset in current compared to the thiol-coupled BPDT, in agreement with the PDT and the PDI. A first peak is observed at 210 mV for BPDI, whereas for BPDT, it is located at around 340 mV. For voltages higher than 0.3 V, the conductance of BPDT is more than a factor of two higher compared to the BPDI.

Beyond the first conductance peak, both molecules reveal several reproducible peaks for higher voltages. BPDI has a second peak at around 0.45 V and a third at 0.72 V. BPDT has a pronounced peak at 0.62 V. The third peaks are smeared-out for both systems. For voltages higher than 1.0 V, the current increases for both systems linearly to values above 100 nA. Features in this regime are not distinct and also not reproducible.

The difference in transport of the thiol- compared to the isocyanide-coupling are not so much apparent in the double-dot systems. However, there are other remarkably different behaviors, for instance, the temperature-dependence. In principle, temperature-dependent measurements are desirable for the investigation of the charging energies, barrier heights, and conduction mechanisms. However, in the MCBJ geometry, temperature-dependent measurements are crucial due to thermal expansion of the two electrodes and reduced stability (see Chapter 3). Using thiol linkers, temperature-dependent measurements on single-molecule junctions

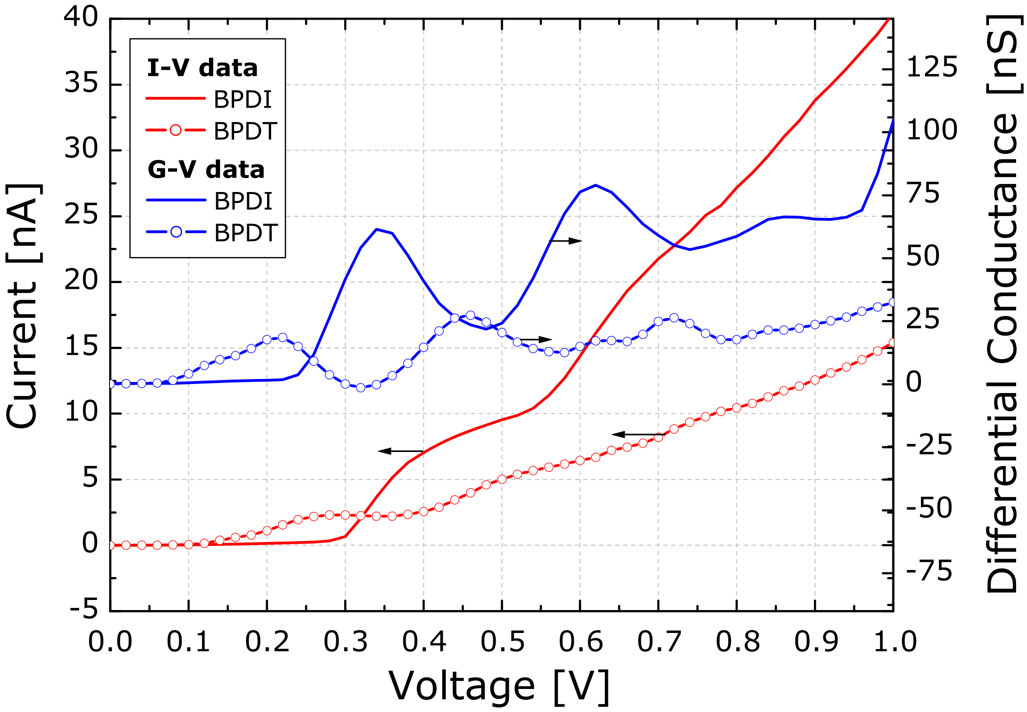

Figure 5.7: *Transport behavior for BPDT and BPDI: I–V and G–V sweeps taken at 50 K. In agreement with the measurements on PDT and PDI, the CN-coupled BPDI reveals a lower onset in current than the BPDT.*

mostly end up with undesired closing or breaking of the molecular junction. This is due to temperature-induced drifts of the electrodes caused by thermal elongation of the metallic electrodes. However, weaker coupled molecules have a larger degree of freedom and can arrange in the junction with only marginal external adjustment of the electrode distance: Figure 5.8(A) shows a temperature ramp using BPDI. The inset shows the electrode position correction necessary for not breaking the molecular junction due to electrode withdrawing (the measurement was started at room temperature). The correction values are in the order of 1-2 nm required for the compensation of thermal elongation during a temperature change of 300 K. The *I–V* characteristics reflect the typical behavior of single-molecule junctions during temperature ramps: The transition from a more diffuse transport signature, where the current depends almost exponentially on the voltage, to more pronounced features, such as, i.e. conductance peaks.

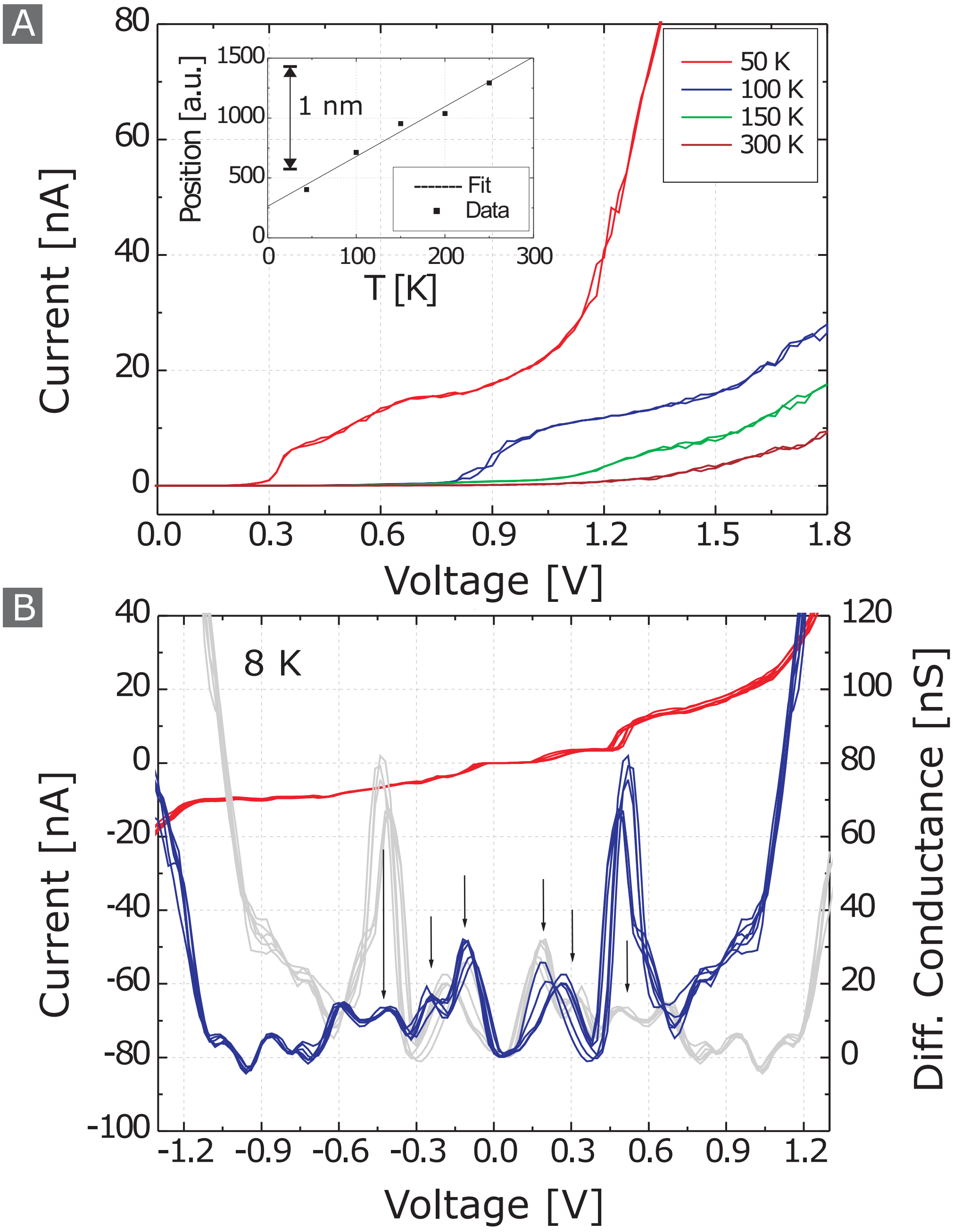

Figure 5.8: *(A) Temperature-dependence of the transport properties of BPDI: Decreasing conductance gap with increasing molecular signature. (B) Low temperature (8 K) measurements for the same molecule revealing a rich conductance spectra.*

More structure within the measured conductance curve for the molecule with two isocyanide groups can be observed compared to measurements with molecules terminated by thiols. For instance, the longer of the weakly coupled molecules, the BPDI, reveals a conductance spectrum at 8 K exhibiting many features. Even without using phase-sensitive AC techniques, but only using DC measurements, man peaks in the G_{Diff}–V plot were clearly observable. Figure 5.8(B) shows the conductance spectra taken at 8 K. The peaks are not symmetric (the light gray curve is the blue curve mirrored at zero voltage as a guide for the eye.) If the curves are shifted by 80 meV, most peaks coincident, providing a better symmetry.

Discussion

In contrast to the single-ring systems, the double-ring systems reveal more than one conductance peak. The influence of the coupling strength on the transport properties was also identified in case of BPDT and BPDI. For instance, the conductance gap was also found to be lower for isocyanide coupling. The double-phenyl-ring systems provide a large spectra of molecular structure on the transport properties. Whereas in case of the single-dot systems, only one molecular orbital was revealed within the voltage window available, the BPDT and BPDI exhibit many characteristic peaks in the conductance versus voltage plot. The most remarkable influence of the coupling strength, however, was found upon cooling or heating, whereby the BPDI did not loose contact to the thermally elongated or withdrawn electrodes. The isocyanide coupling seems to provide enhanced degrees of freedom for the molecular backbone, resulting in more surface mobility of the molecule–metal linker.

Remarkable was the rich spectrum of features at very low temperatures that was found in the BPDI data at 8K. On a single molecule level, the additional features can be explained by the enhanced degrees of freedom of the molecular backbone. Other groups have experimentally observed more structure within the measured conductance curve for molecule terminated by two isocyanide groups, compared to measurements with molecules having thiol end groups [28; 19]. IR data in [75] showed that the molecules have a high degree of alignment perpendicular to the interface in a SAM. The additional features were interpreted theoretically only by a monolayer with additional molecules perturbing the periodicity. It is conjectured that the weaker coupling to Au of isocyanide groups compared to thiol groups might be responsible for such perturbations. J. Lee *et al.* manufactured devices using SAM of PDT, PDI, BPDT, and BPDI sandwiched between two Au electrode [41]. They found a conductance gap of 0.5 - 0.6 V at 4.2 K for BPDT. In agreement with the results presented here, much more pronounced peaks were found for the double-ring systems BPDT compared to the single-ring system PDT. Measurements here were restricted to Au only. Future investigations should include other metals, such as Pt, Pd, Al.

5.6 Conclusions

In summary, the influence of the end group of the molecule on the transport properties was studied using two different terminal groups, namely thiol coupling and isocyanide coupling. Single- and double-phenyl-ring systems with thiol and isocyanide termination were studied and compared at low temperature.

The molecular level broadening was found to be 50 % higher in case of PDT compared to PDI. The isocyanide coupled molecule showed more pronounced peaks, whereas in case of thiol-coupling, they were more smeared-out. The quantitative conductance at these peak positions, however, were found to be on the same order. This indicates that transport is not predominantly determined by the chemical coupling. The conductance gap was found to be increased by SH-coupling, a fact that can be explained by a different charge transfer from the electrode to the molecule upon coupling. The double-ring systems provided more molecular signature, namely the appearance of conductance peaks.

In general, the thiol-Au coupling is very sensitive to specific details of the surface reconstruction. This can be observed by the typical stochastic fluctuations in the thiol-Au contact. The isocyanide-Au coupling group is suggested to be the better choice since it possesses a higher degree of freedom on the electrode surface. To a certain extend, it can equalize surface effects and simultaneously establish a similar coupling to the metal without lowering the conductance. From a general point of view, the molecule–metal coupling should be decoupled from a possible intramolecular functionality.

Chapter 6

Influence of the Intramolecular Structure on Transport

In the last chapter it has been demonstrated that the molecule–metal contact has a direct influence on the transport properties. However, the coupling has rather an influence on the width of the conductance peaks than on the absolute conductance. Whereas both single-phenyl-ring systems revealed only one peak in the conductance within the voltage window available, the double-phenyl-ring systems exhibited various peaks, characteristic for the molecule under investigation. This fact raises the question whether the intramolecular structure provides signature in the transport properties.

The molecular backbone, the part of the molecule which is not involved in the coupling to the electrode, may possess various functionality: Simple insulating or rectifying behavior, a structure that provides non-linear transport properties, or even logic functionality enabling switching for memory applications (see following Chapter 7). In principle, obtaining a correlation between molecular structure and corresponding transport properties is of fundamental importance for the understanding of transport at the molecular scale. It is a key for the successful development of molecular electronics, in particular for the design of tailored molecules as functional building blocks with well-defined transport properties.

In this chapter, the influence of the intramolecular structure on transport will be systematically studied by molecules with a well-defined structured length.

6.1 Molecular Model Systems

A family of oligophenylenes with increasing length and controlled intramolecular structure will be investigated in order to obtain a relationship between molecular structure and corresponding transport properties.

Figure 6.1 shows the four molecules studied for this issue: The PDT has already been discussed in the previous Chapter 5. 4,4-Bis(acetylthio)-2,2-dimethyl-biphenyl (**2**) is similar to the BPDT already investigated, but has additional methyl groups attached to the central phenyl rings to cause an interruption of the π-system by rotation of the phenyl-rings out of plane due to steric strain. Three phenyl rings are present in 4,4-Bis(acetylthio)-2,2,5,2-tetramethyl-[1,1;4,1]-terphenyl (**3**), and finally, four rings are found in the quaterphenyl (**4**).

The synthesis and the subsequent chemical analysis was performed by the group of Prof. Dr. Marcel Mayor (see Appendix A). The identity of all molecules has been proven by ^{1}H-, ^{13}C-NMR, mass spectrometry using either EI-MS or MALDI-TOF-MS and by elemental analysis. Single crystals of the molecules **2** and **3** were grown for x-ray analysis. Thereby, the phenyl rings are rotated with respect to each other by an angle of 79.7° in case of molecule **2**, and 71.6° for molecule **3**, respectively. The outer phenyl-rings are rotated by an angle of 71.6° with respect to the central phenyl ring.

In general, an angle of rotation between 70 - 80° suggests that the overlap between the p_z-orbitals is greatly reduced. Hence, molecule **2** can be regarded as a structure consisting of two almost separated π-systems that are interrupted between the two phenyl rings. Presumably, **3** consists of three (almost) separate π-systems due to two conjugation breaking elements. Although no crystal structure of molecule **4** has been obtained in the analysis of the synthesis, probably similar conclusions hold for this compound, that is the quaterphenyl comprises four distinct π-systems that are separated by three conjugation breaking elements.

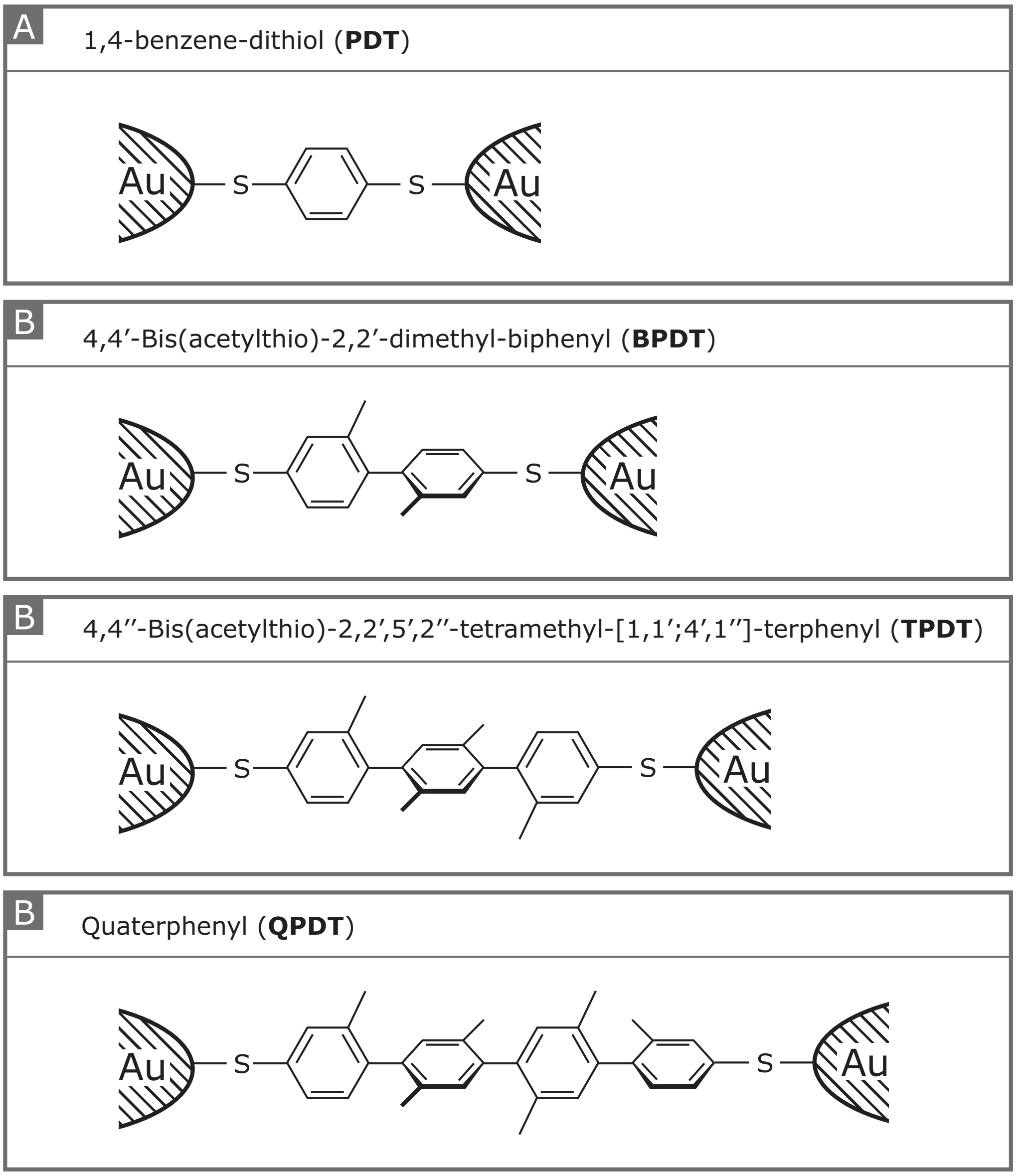

1,4-benzene-dithiol (**PDT**)

4,4′-Bis(acetylthio)-2,2′-dimethyl-biphenyl (**BPDT**)

4,4′′-Bis(acetylthio)-2,2′,5′,2′′-tetramethyl-[1,1′;4′,1′′]-terphenyl (**TPDT**)

Quaterphenyl (**QPDT**)

Figure 6.1: *Molecular structures of PDT,* **2**, **3** *and* **4**. *The acetyl protection groups (-COCH$_3$) were already removed upon coupling to the metal. The length of the molecules increases from 0.846 nm for the PDT, to 2.189 nm for the molecule* **4**.

In conclusion, the interruption of the π-system by rotation of the phenyl-rings out of plane due to steric strain has been proven by chemical analysis and found to reach values between 70 - 80°. These values were derived from the crystalline state and cannot directly be taken as the values for the isolated single molecule. In the next section, it will be investigated, whether this intramolecular structure has a measurable influence on the transport properties of each molecule.

6.2 Charge-Carrier Transport Measurements

All the molecules were successively tested on different samples and at various temperatures in order to obtain a large dataset for performing statistical analysis.

Results

Figure 6.2 shows the statistical overview gained of the transport properties of all four oligophenylenes investigated. Various measurements using in total more than 50 samples (at least 5 samples for each molecule) have been conducted. The most pronounced transport properties were revealed at low temperatures, e.g. at 50 K. The curves are only drawn within their stable and reproducible voltage window. For the PDT, the stability range is limited to ± 0.6 V, as already discussed in Chapter 5). For the longer molecules, the voltage range is extended to almost ± 1.5 V, or even beyond that range (for the molecules **2** and **3**).

The data reveals that the onset of electronic transport is increasing with increasing number of phenyl-rings. In addition to the conductance gap, other peaks appear for the molecules **2**, **3**, and **4**. The location of these peaks varies only slightly. Its relative and absolute amplitudes, however, are affected by the coupling and the thermal line broadening. Thus, they are much more affected by the various microscopic configurations of the junctions, giving rise to the fluctuations. These fluctuations have a different influence on the *I*–*V* characteristics. For instance, it can happen that one peaks is only hardly observable or completely suppressed. In 20 % of all the data, the first peak is not revealed and the current onset occurs at the second peak.

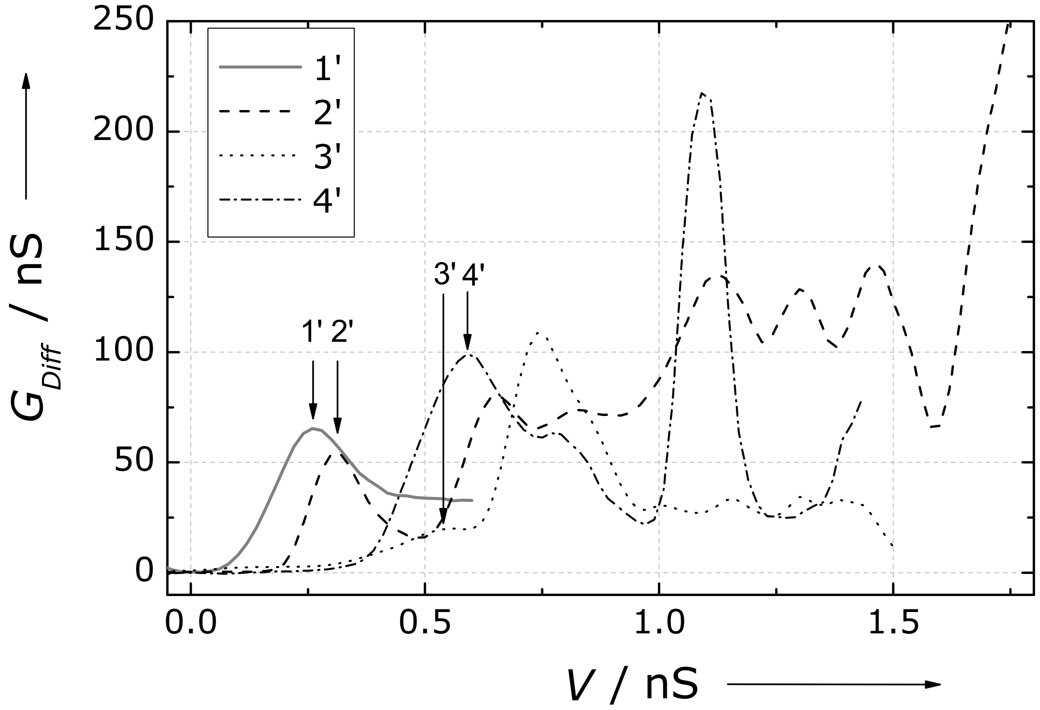

Figure 6.2: *Transport properties of the oligophenylenes, PDT (***1***),* **2***,* **3** *and* **4***. The double-sweep I–V characteristics were taken at 50 K. The curves drawn are restricted to their stable and reproducible voltage window. The data represents the statistically most probably curves found within a huge data set, measured on more than 50 samples. The arrows indicate the locations of the first peak, defining the conductance gap.*

At room temperature, the molecular signature is rather diffusive due to the thermal line broadening the molecular vibrations excited. In particular, no high fields can be applied due to the lack of electrode stability. Therefore, histograms are the only way for acquiring any molecular signature at room temperature without destroying the junction irreversibly. The voltages which are applied for acquiring histograms are very small and located therefore within the conductance gap. The conductance values for a small fixed bias were determined by the repeated formation of a molecular junction and the subsequent analysis of the conductance histograms, an approach very similar to one reported in reference [87] using a STM. For creating the histograms, no data selection was performed.

Molecule	Resistance / MΩ	Bias/ mV
PDT	260	5
2	2.3	10
3	3.8	10
4	1.9	20

Table 6.1: *Low bias resistances of PDT, molecules* **2**, **3**, *and* **4** *determined statistically by histograms over 100 opening and closing cycles under a fixed small bias.*

The results for PDT have already been shown in section 5.2 of Chapter 5. For the other molecules, lower resistance values were found and given in Table 6.1. The bias voltage was increased for the longer molecules in order to achieve an improved current measurement accuracy in the pA range. In contrast to the short PDT molecule with a resistance of 260 MΩ, the resistances for **2**, **3** and **4** are found to be lower, between 1.9 and 3.8 MΩ.

Discussion

The different conductance gaps for the series of molecules have been extracted from the data presented in Figure 6.2 and are plotted as a function of the number of phenyl rings in Figure 6.3. The data comprises the values from all samples measured (error bars). An obvious increase in the conductance gap comes along with an increase in the molecule length, being the number of phenyl rings.

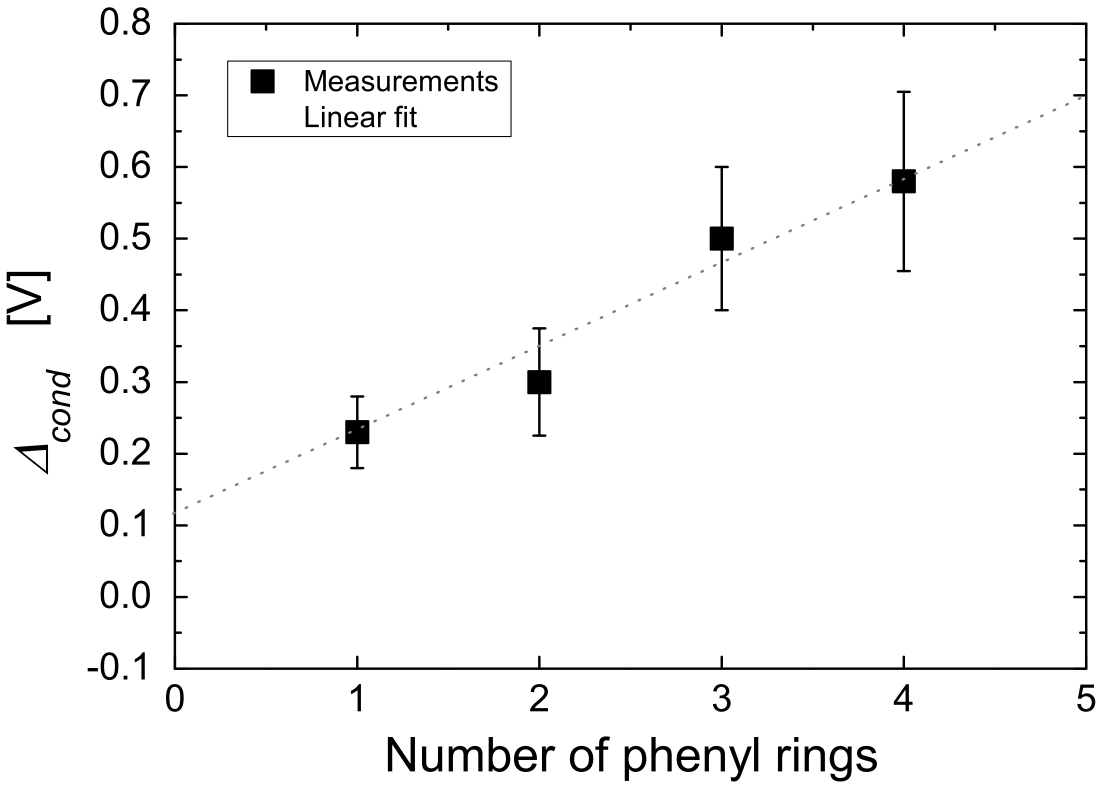

Figure 6.3: *Increasing values of the conductance gap with increasing number of phenyl rings (left axis). The experimental data is based on several samples measured (error bars). The length of the molecules increases linearly with the number of phenyl rings (right axis).*

Table 6.2 gives an overview on the estimated lengths of the molecules investigated.

Assuming a constant injection barrier height, the longer molecular backbone results in a different voltage drop across the molecule. In a very simple picture, the onset in current signals current flow trough the molecule. This means that the voltage has reached an energy which permits the electrons from one electrode to pass the tunneling barrier of the molecule–metal contact and to be injected onto the molecule. If one assumes a constant voltage drop between the two electrodes and two identical tunneling barriers between molecule and metal, than the resulting onset in current becomes a function of the molecule length.

Molecule	Sulphur–Sulphur distance / nm	Electrode distance / nm
PDT	0.627	0.846
2	1.0526	1.271
3	1.495	1.714
4	1.971	2.189

Table 6.2: *Overview on the length of the oligophenylenes investigated. PDT reveals a sulphur-sulphur distance below 1 nm, whereas the four rings in* **4** *yield a sulphur-sulphur distance of almost 2 nm.*

As illustrated in Chapter 5, the longer molecular backbone has also an influence on the energetic distribution of molecular orbitals within the voltage window available. In principle, the various peaks for the molecules **2**, **3**, and **4**, represent those molecular orbitals. In a simple transport picture the frontier orbitals of the π-system are assumed to be dominating for electronic transport properties. However, it is very difficult to assign these conductance peaks to the molecular orbitals involved, due to charge transfer, charging effects and broadening. However, the results clearly show that the intramolecular structure has an influence on the transport properties and the measurements performed allow for more detailed investigations in future single-molecule spectroscopy.

In contrast to the conductance gap, the conductance values acquired statistically under a small fixed bias do not show a clear trend as a function of the length of the various molecules. This highlights the issue of determining conductance or resistance values of molecules at small voltages in the conductance gap. In general, the molecules have a very low density of states in the HOMO-LUMO gap. Therefore, all the measurements are very sensitive to the bias applied and vary therefore largely in the results reported in literature. However, at room temperature, it is so far the only way to determine the resistance of a molecule due to the reduced electrode stability mentioned.

Since charge-carrier transport through molecules is a fairly non-linear process, it is therefore very difficult to establish a relationship between the low bias conductance values and the measured I–V characteristics at low temperatures.

6.3 Conclusions

The question whether the intramolecular structure has an influence on transport has clearly been answered: the intramolecular structure is reflected by characteristic peaks in the G_{Diff}–V plot. The reproducibility was good in terms of the energetic positioning of the energetic position. The relative and absolute conductance peak amplitudes, however, vary significantly among different samples.

The so-called conductance gap increases from 250 mV to 580 mV with increasing length of the molecule. This means that the external bias for charge-carrier injection from the electrodes onto the molecule has to be increased since the voltage drop across the molecule–metal tunneling barrier has changed according to the increased length of the molecules.

Much more experimental and theoretical efforts are required to assign the conductance spectrum to the molecular properties and therefore by finally establish a correlation between molecular structure and corresponding transport properties.

Chapter 7

Molecules as Functional Building Blocks

Based on the systematic studies of the molecule–metal contact and on the intramolecular structure on the transport properties reported previously, it will be shown in this chapter that single molecules can have intramolecular functionalities. This property can make the individual molecules work as functional building blocks in electric circuits. The investigation of the functional behavior of single-molecules is the fundamental driving force for research at the molecular scale. The building blocks which can be imagined are as numerous as the various chemical processes which molecules offer. The two intramolecular functions investigated in this chapter are current rectification behavior and voltage-induced resistance switching. Moreover, memory operation will be demonstrated as a potential application.

7.1 Diode Behavior

Concepts of Uni-Molecular Current Rectification

For molecular electronics to be attractive for future applications, it is imperative to develop a molecular building block mimicking the rectifying behavior of a p-n junction. In 1974, A. Aviram and M. Ratner made a theoretical proposal for an intrinsic uni-molecular rectifier, a unimolecular diode [61]. The theoretical construction is based on the use of a single organic molecule consisting of a donor π-system and an acceptor π-system separated by a sigma-bonded tunneling bridge (see Chapter), which needs to be almost insulating. Figure 7.1(A) shows the molecular structure proposed in this seminal paper [61]. The donor and acceptor systems have different threshold voltages for resonant transport through molecular orbitals, which causes rectification of the current in respect to the bias voltage (Figure 7.1(B)-(D)).

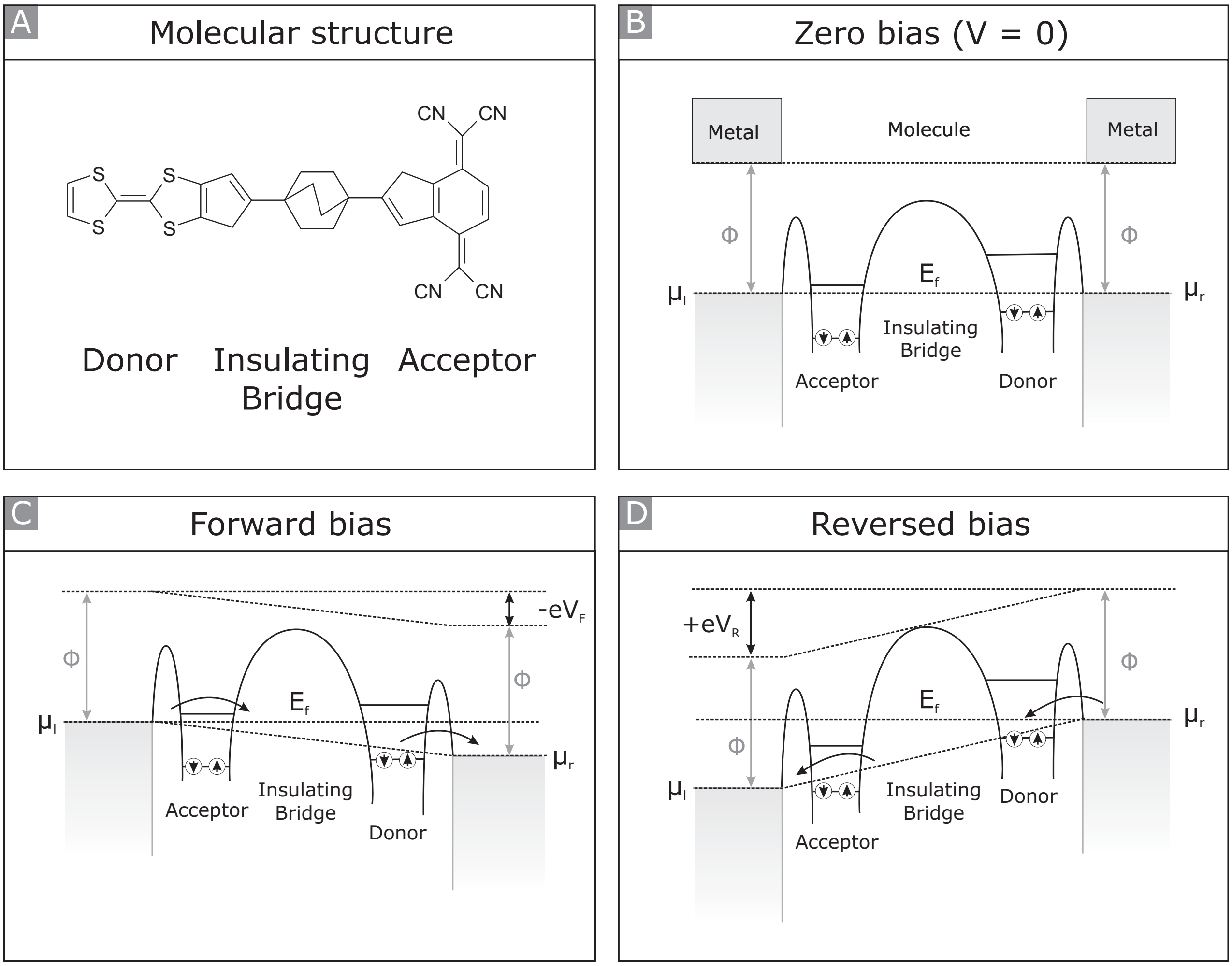
A
Molecular structure
S
S
S
S
CN
CN
CN
CN
Donor
Insulating Bridge
Acceptor
B
Zero bias (V = 0)
Metal
Molecule
Metal
Φ
Φ
E_f
μ_l
μ_r
Insulating Bridge
Acceptor
Donor
C
Forward bias
$-eV_F$
Φ
Φ
μ_l
E_f
μ_r
Acceptor
Insulating Bridge
Donor
D
Reversed bias
$+eV_R$
Φ
Φ
E_f
μ_r
μ_l
Insulating Bridge
Donor
Acceptor

Figure 7.1: *Molecular diode as proposed by A. Aviram and M. Ratner [63]: (A) Molecular structure consisting of a donor and an acceptor part, spaced via an insulating bridge. (B) Zero bias energy diagram. (C) Forward and (D) reversed bias situation giving rise to different current flow in the two directions.*

In 1974, this visionary concept was experimentally far away from realization. The progress in manipulating and controlling single molecules and atoms enabled several experiments which showed molecular rectification: In 1997, R. Metzger *et al.* demonstrated that a Langmuir-Blodget monolayer of zwitterionic hexadecylquinolinium tricyanoquinodimethanide sandwiched between the two Au electrodes reveals unimolecular rectification behavior [47; 3]. The top Au electrode was deposited using a technique called "cold evaporation". Very recently, M. Elbing *et al.* reported on a single-molecule diode in the MCBJ geometry [21]. The control experiment using a non-rectifying molecule showed that the rectification behavior observed has a truly molecular origin.

All organic rectifiers or molecular diodes are asymmetric organic molecules in which charge-carriers flow preferentially in one direction [46], according to the Aviram-Ratner proposal [61]. In this section, a relatively simple molecule was studied in terms of its rectification behavior on a single-molecule level. Figure 7.2 shows the molecular structure of the so-called SB diode molecule [50]. It consists of a bipyrimidinyl moiety which is connected to a biphenyl group. The dipyrimidinyl group is an electron acceptor which acts as an electron-withdrawing part.

The molecule was especially designed for use in self-assembly structures [50]. Therefore, it has two different thiol-protecting groups in order to enable oriented sequential growth of the film in respect to the substrate (see Appendix A). The cyanoethyl protecting group can be cleaved *in-situ* by sodium ethoxide (NaOEt) in ethanol to form the free thiol. In the SAM approach, the SB diode molecules are then co-assembled with dodecanethiol in a 1:500 ratio on a Au(111) substrate [50]. Finally, the trimethylsilylethyl groups on top of the molecule are cleaved with a solution of tetrabutylammonium fluoride (TBAF) in THF.

However, in the MCBJ geometry, both electrodes consist of the same material, eliminating the need for an oriented alignment via sequential deprotection of the terminal groups. Hence, the deprotection was carried out simultaneously on both ends of the molecule, using a solution of tetrabutylammonium fluoride (TBAF) in tetrahydrofuran (THF) [50].

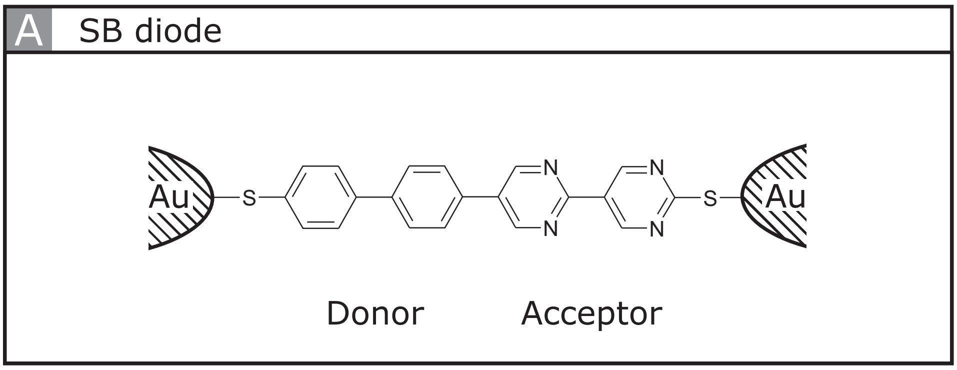

Figure 7.2: *Molecular structure of the SB diode molecule coupled symmetrically to Au electrodes over thiol linkers. The asymmetric cyanoethyl and trimethylsilylethyl thiol protecting groups are already deprotected, and thus not drawn.*

Results

Immediately after deprotection of the end groups, a droplet of molecules was deposited onto an opened MBCJ sample that has been conditioned. *I–V* sweeps have been measured at 300 K at a pressure of $8 \cdot 10^{-9}$ mbar. Figure 7.3 shows the typical rectification behavior of the Au–single-SB-diode–Au junction. For negative voltages, the current is remarkably low for such high fields applied, e.g. the current is still below 5 nA at – 1.5 V. This is a relatively low current compared to other systems studied in the previous chapters. For positive voltages below 0.9 V, the current is also below 10 nA. For higher voltages than 1.0 V, the current increases strongly in an almost linear way. The inset shows the corresponding rectification ratio of approximately 10 for voltages above 1.2 V.

Figure 7.4 shows the temperature-dependence of the current rectification. The representative *I–V* curves were taken at 300, 200 and 150 K. All data shown is raw data and no filter was applied. When the temperature is decreased, the rectification behavior is maintained and does not change quantitatively. However, the onset in current is shifted towards + 1.2 V.

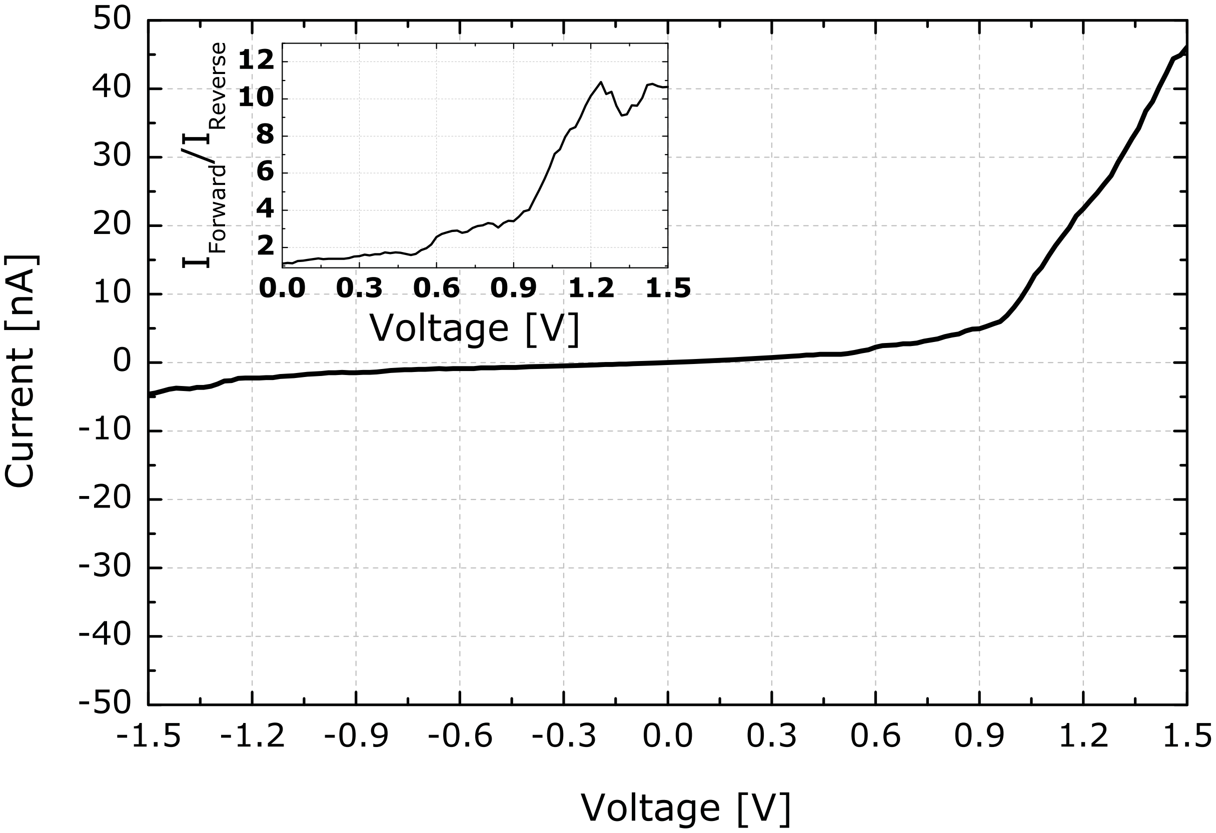

Figure 7.3: *I–V characteristics of the SB-diode molecule taken at 300 K. The inset shows the rectification ratio of approximately 10 at 1.2 V. The onset in current is around + 1.0 V.*

Regarding the steep increase in current for higher voltages, one might expect a much higher rectification ratio for higher fields. With that in mind, the measurement is performed at 100 K to improve the electrode stability. This extends the voltage window available to ± 1.8 V. The first measurement sweep (1st run), shown in Figure 7.5, reveals a current of –32 nA at –1.8 V and almost 500 nA at +1.8 V, respectively.

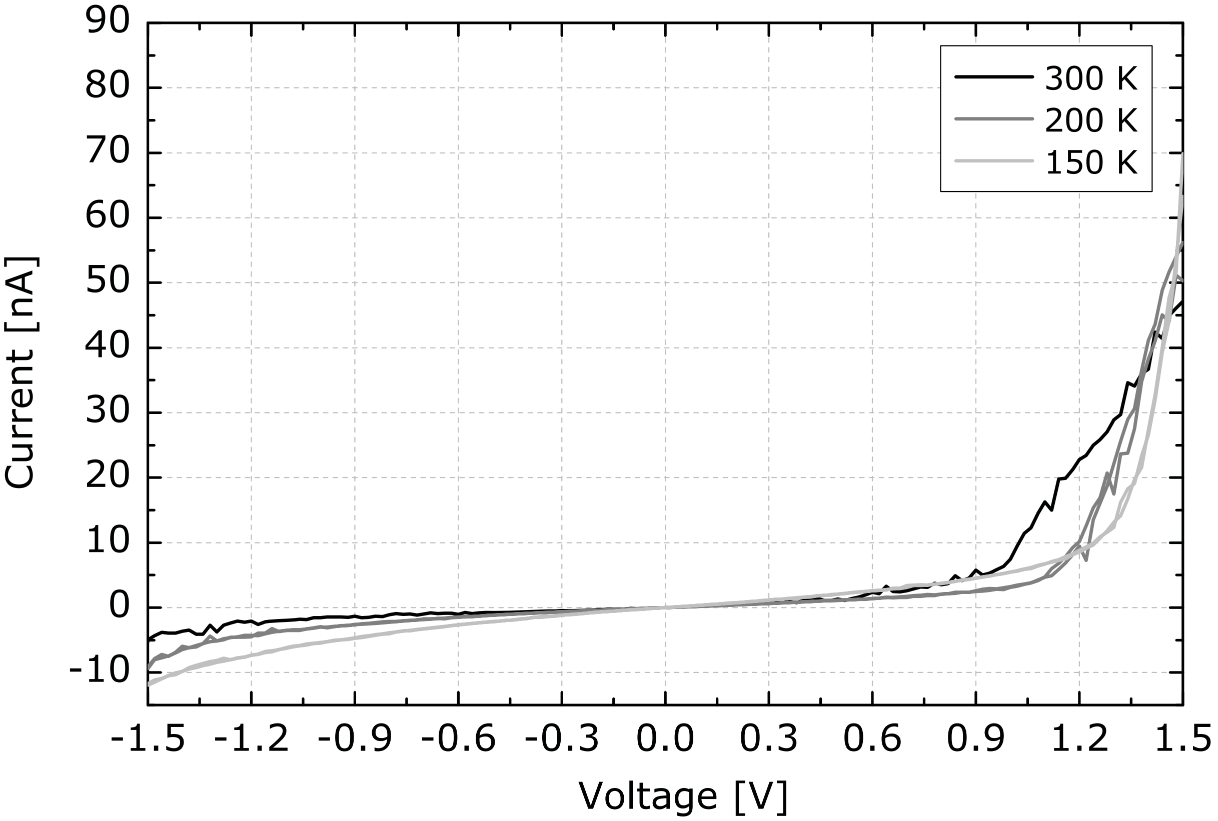

Figure 7.4: *The I–V characteristics show the transport properties of the SB-diode molecule taken at various temperatures. The rectification behavior is maintained upon temperature changes. The current onset is shifted from + 1.0 V towards + 1.2 V with decreasing temperature.*

This gives a rectification ratio of 15 at ± 1.8 V. Unfortunately, the junction cannot endure such high electric field strengths, even at 100 K. The closing of the junction under the high fields is reflected by an unstable *I–V* curve in the second sweep and an increasing current for voltages below −1.0 V due to a direct tunnelling channel superimposed to the molecular channel. The third sweep shows already an almost symmetric behavior where rectification has disappeared. Now, the functional behavior is more exponential. Finally, a closed metal–metal bridge is formed, without any molecular signature and very high currents in the order of some μA.

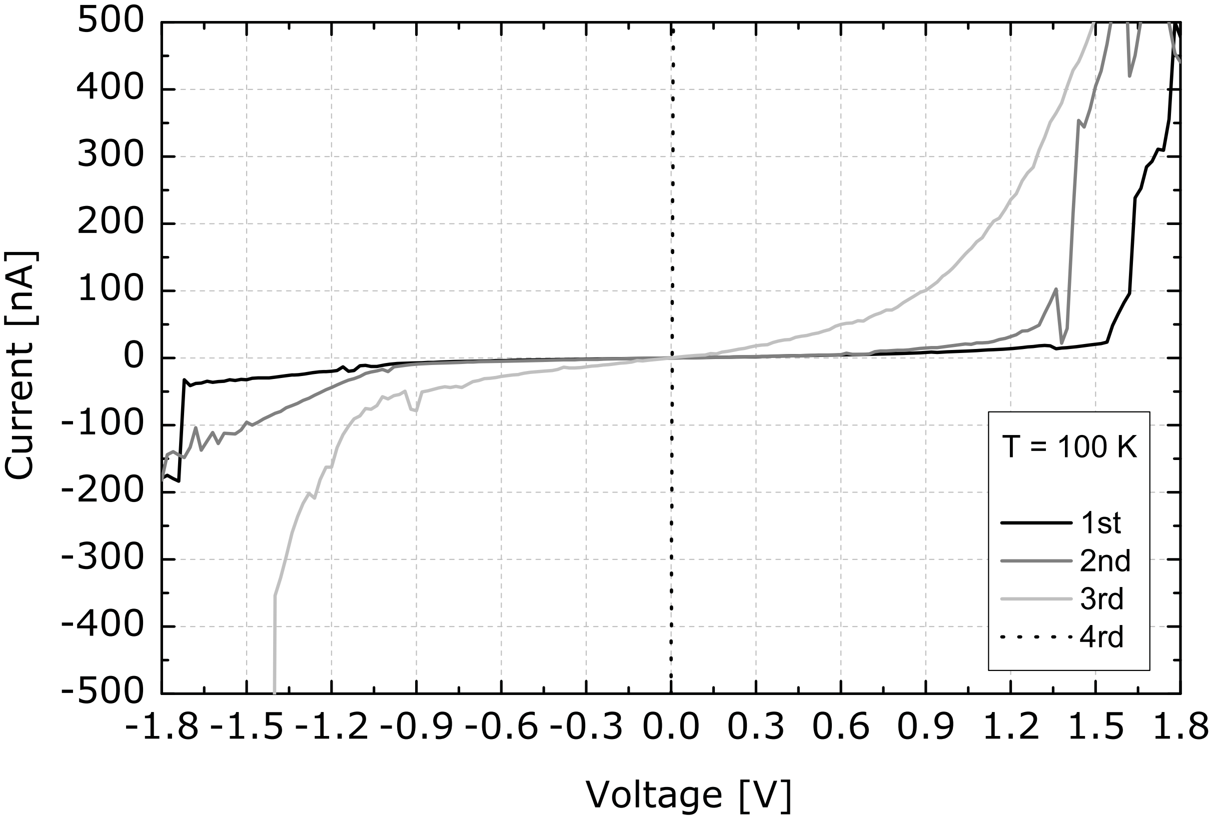

Figure 7.5: *Subsequently measured I–V sweeps (raw data) for the SB-diode in a larger voltage window from −1.8 V to +1.8 V. The high-field conditions lead to irreversible changes of the molecular junction destroying first the rectification behavior (2nd and 3rd sweep), and finally the molecular junction itself (4th sweep), forming a closed Au–Au junction.*

Discussion

The measurement demonstrate that the SB-diode molecule is able to rectify current. Furthermore, the rectification ratio is 10 at 1.5 V, and increases to 15 at 1.8 V. The functional behavior of the rectification is found to be almost independent of the temperature.

In principle, asymmetric *I–V* curves can also be obtained if the molecule–metal coupling is asymmetric. However, in comparison to the previous experiments, an asymmetry in the order of 10 arising from coupling has never been observed. These effects are in the order of 50 %. In addition, the rectification found in the SB-diode molecule is rather due to an unimolecular behavior than different metal–molecule coupling situation, because the branches in the *I*–*V* possess distinct features and not a purely exponential behavior. Especially the kink at the onset position is a strong indication that the rectification functionality has a molecular origin.

Results from very similar molecules [53; 54] suggests that the rectification effect can be increased by the dipole moment of the molecules. With that in mind, the SB-diode molecules have been designed and synthesized. Scanning tunneling microscopy (STM) and STS studies revealed that the molecules not only have a more pronounced rectifying behavior but also exhibit in addition a sensitivity to protonation on the nitrogen atoms by strong acids, which can reversibly alter the rectifying direction completely [50]. The work of Morales *et al.* is the first example where the effect of protonation on charge transport through a molecule was observed. However, under UHV conditions, protonation effects can be excluded. Thus, the observed rectification behavior must be caused by different molecular level spacing in the donor and acceptor unit of the molecule as proposed by Aviram and Ratner [61].

7.2 Voltage-Induced Switching

Conductance switching in devices based on molecules [62; 11] has been reported in recent years. The device architectures utilizes included SAMs of molecules sandwiched between two metallic electrodes. This enables huge ensembles of molecules, in the order of 10^4 to 10^{12}, to be contacted. In similar cross-bar structures, first molecular memory devices have already been presented [12; 35]. However, due to critical manufacturing processes, it is controversial whether the molecules would survive, e.g. during the "hot" metal evaporation step of the counter electrode fabrication and whether the molecules are really responsible for the conductance switching observed.

From a microscopic point of view, the device architecture makes it very difficult to differentiate between contact effects (e.g. metallic filaments penetrating the almost insulating molecular layer) and intrinsic molecular functionality measured in all of these devices.

Hence, the origin of switching is controversial and was therefore excessively discussed. Recent experiments aiming to identify the fundamental mechanisms indicate that the generic mechanism is dominated by the electrode properties or the molecule–metal interfaces, rather than by the behavior inherent to the molecule [73; 40].

In general, the investigation of intrinsic molecular functionality is difficult in these device architectures employing thousands of molecules in parallel because contact effects and collective phenomena can not be excluded. Another type of switching often observed is stochastic switching [18]. It is caused by statistical fluctuations in the molecule itself or the molecule–metal contact. The lack of control over this type of switching makes it essentially undesirable for any technological application.

In this section, it will be demonstrated that a single molecule connected to two symmetric leads in a simple two terminal configuration can be reversibly and controllably switched between two stable states in response to an external trigger, namely a simple voltage pulse. In the MCBJ geometry and under the very controlled UHV environment, the formation of metal filaments can be excluded and investigations can be performed on a single-molecule level.

Results

Charge-carrier transport through a single bipyridyl-dinitro oligo-phenylene-ethynylene dithiol (BPDN-DT) molecule [23] and bipyridyl oligo-phenylene-ethynylene dithiol (BP-DT) molecule was investigated. The molecular structures are shown in Figure 7.6(A)+(B). The BP-DT molecule without the nitro groups acts as a reference molecule. The rigid rod-like molecules are designed such that the BP-DT can attain a more planar arrangement due to its minimal steric interactions in the central bipyridyl unit compared with the significant juxtaposed nitro interactions in the BPDN-DT. The molecules are dissolved in tetrahydrofuran (THF) (concentration of 10^{-4} mol L^{-1}) and the acetate moieties are removed with aqueous NH_4OH during assembly to the Au leads via the free thiols.

Figure 7.6(C) displays I–V sweeps starting from –1.2 V to +1.2 V, and back again to –1.2 V (double sweep) for BPDN-DT (blue) and BP-DT (red) at 100 K. All data presented is raw data and no filter was applied. Both molecules reveal a symmetric I–V curve with a conductance gap $2 \cdot \Delta_{cond}$ of approximately 1 V. Within the conductance gap, charge-carrier transport is based only on direct tunneling between the electrodes [59]. In the case of BP-DT, the current increases for voltages above 0.5 V and reaches ±(20-30) nA at ±1.2 V. For BPDN-DT, the currents above + 0.6 V and below –0.6 V are approximately six times lower than for BP-DT.

What is noticeable, in the I–V curve of BPDN-DT is the appearance of a hysteresis at about ±0.9 V, which is highlighted in Figure 7.6(C) by the gray rings. In Figure 7.6(D), the G_{diff}–V is plotted. The conductance of BP-DT reveals two pronounced peaks symmetrically located at around ± 0.6 and ± 1.0 V. These two peaks result from the maximum current flowing through the two molecular orbitals nearest to the Fermi level E_{F} [59]. For BPDN-DT the G_{diff}–V plot reveals that the hysteresis exhibits a discontinuity at – 1.0 V and + 0.8 V. The curves shown for BPDN-DT and BP-DT represent the statistically most probable characteristics out of several hundreds acquired which all reveal the features described. For every molecule, seven different MCBJ samples have been used and several hundreds of characteristics were measured with each sample. As the molecules are deposited from a very diluted solution onto the junction, a molecule is only successfully contacted in 50 % of the MCBJ samples.

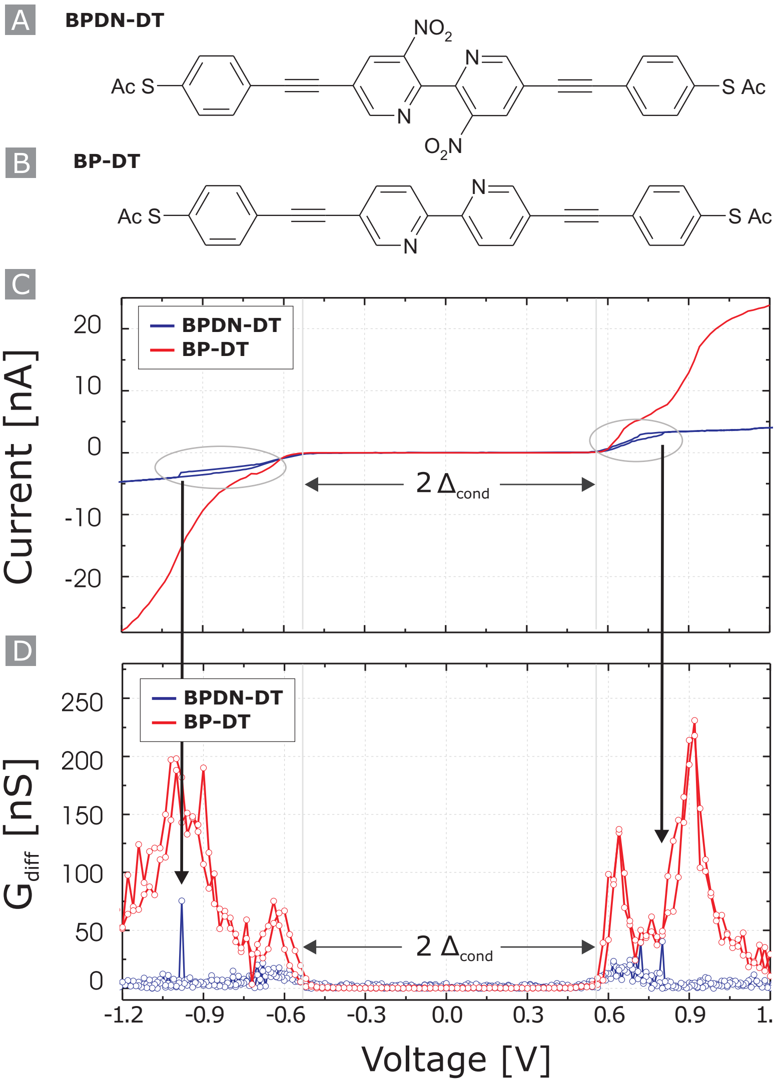

Figure 7.6: *Molecular structures of the two molecules under investigation: (A) BPDN-DT and (B) BP-DT. Charge-carrier transport characteristics of single BPDN-DT (blue) and BP-DT (red) molecules acquired at 100 K: (C) Statistically representative I–V curves (double sweep) based on several hundreds of sweeps acquired. An approximately six times higher current is observed for the BP-DT molecule compared to the BPDN-DT molecule (all raw data). A reversible hysteresis in the BPDN-DT signal is highlighted with gray rings. (D)* G_{diff}*–V data reveals a similar conductance gap for both molecules of approximately 1.0 V. Black arrows indicate the discontinuity in the BPDN-DT curve.*

For all the samples with BPDN-DT applied, the measurements always revealed hysteresis with switching. By contrast, the BP-DT exhibited exclusively monotonic traces without any switching.

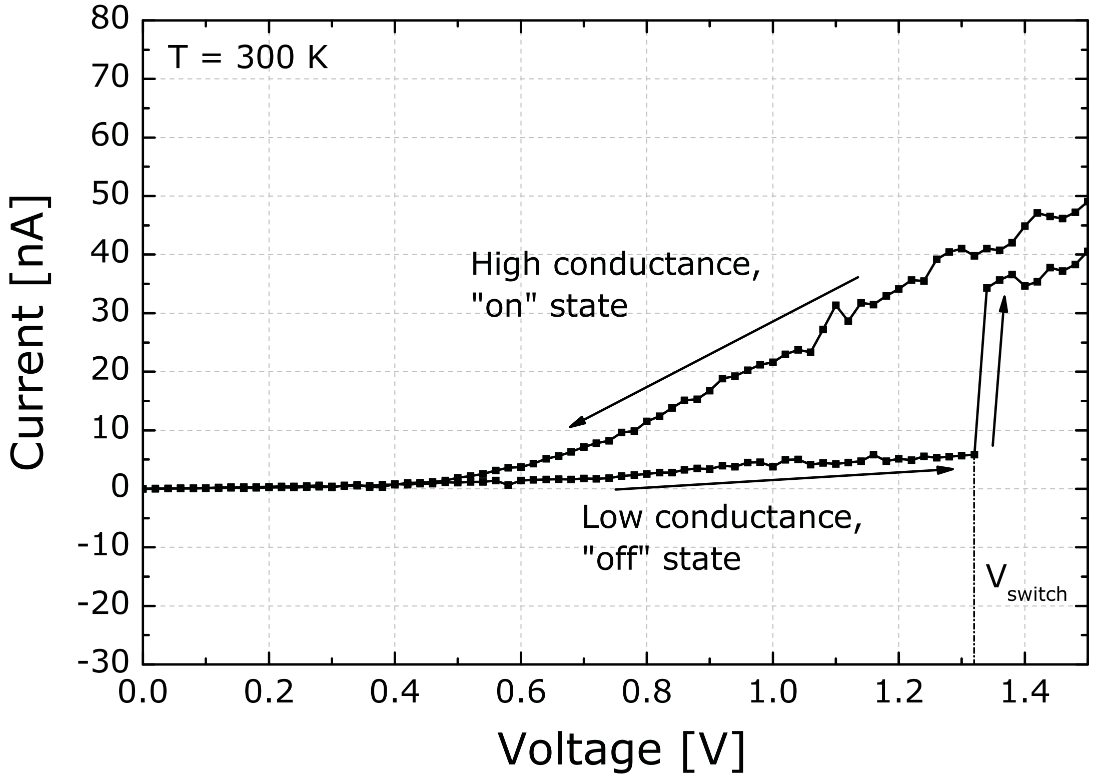

Figure 7.7: *Switching behavior measured at room temperature: The Au–single-BPDN-DT–Au system switches at slightly higher voltages compared to 100 K at 1.3 V to a higher conductive state. The sweep from higher voltages to zero volt shows an additional shift and again a hysteresis.*

Switching can be observed at room temperature as well; however, the junction becomes unstable after measuring a few switching events and a closed metal–metal contact is finally formed. This is due to increased mobility of the Au atoms of the electrodes at elevated temperatures which affects the stability of the junction when applying high electrical fields of more than 1.5×10^7 V cm^{-1}.

Figure 7.7 shows the switching behavior at a voltage of 1.3 V for a voltage sweep from 0 V to 1.8 V. The reproducibility at 300 K is not as good as at low temperatures. In addition, the curves show slight variations, as indicated in the shift of the “on” state trace compared to the “off” state trace at high voltages in Figure 7.7.

At low temperatures, e.g. 100 K, the stability is much higher compared to room temperature. Hence, more detailed experiments are possible to perform. Figure 7.8 shows the I–V characteristics when the end point for the voltage sweep is continuously increased starting always from 0.0 V to 0.7, 0.8 V, and finally to 0.9 V (and back again). First, the current follows a monotonous trace in forward and backward direction (double sweep), as displayed in (A) and (B). For 0.9 V, the system switches to the higher conductive “on” state. Upon decreasing the end point for the sweep from 0.9 V to 0.7 V, the “on” state is maintained, as shown in (D)-(F).

Figure 7.9 shows the hysteresis appearing in the I–V curve of BPDN-DT in more detail. Starting the measurement from 0 V, the current signal increases monotonically until the voltage exceeds $V_{\mathrm{Switch,pos}}$. The current signal suddenly jumps from a low conductive curve, called the “off” trace, at approximately +0.8 V, to a high current curve, called the “on” trace. For even higher voltages, the current continues to increase. Sweeping the voltage back from +1.5 to 0 V, one observes a hysteresis. The current decreases monotonically without a signal jump, exhibiting higher current values than the initial upwards sweep between 0.55 and 0.8 V. In addition, the conductance gap is now slightly reduced.

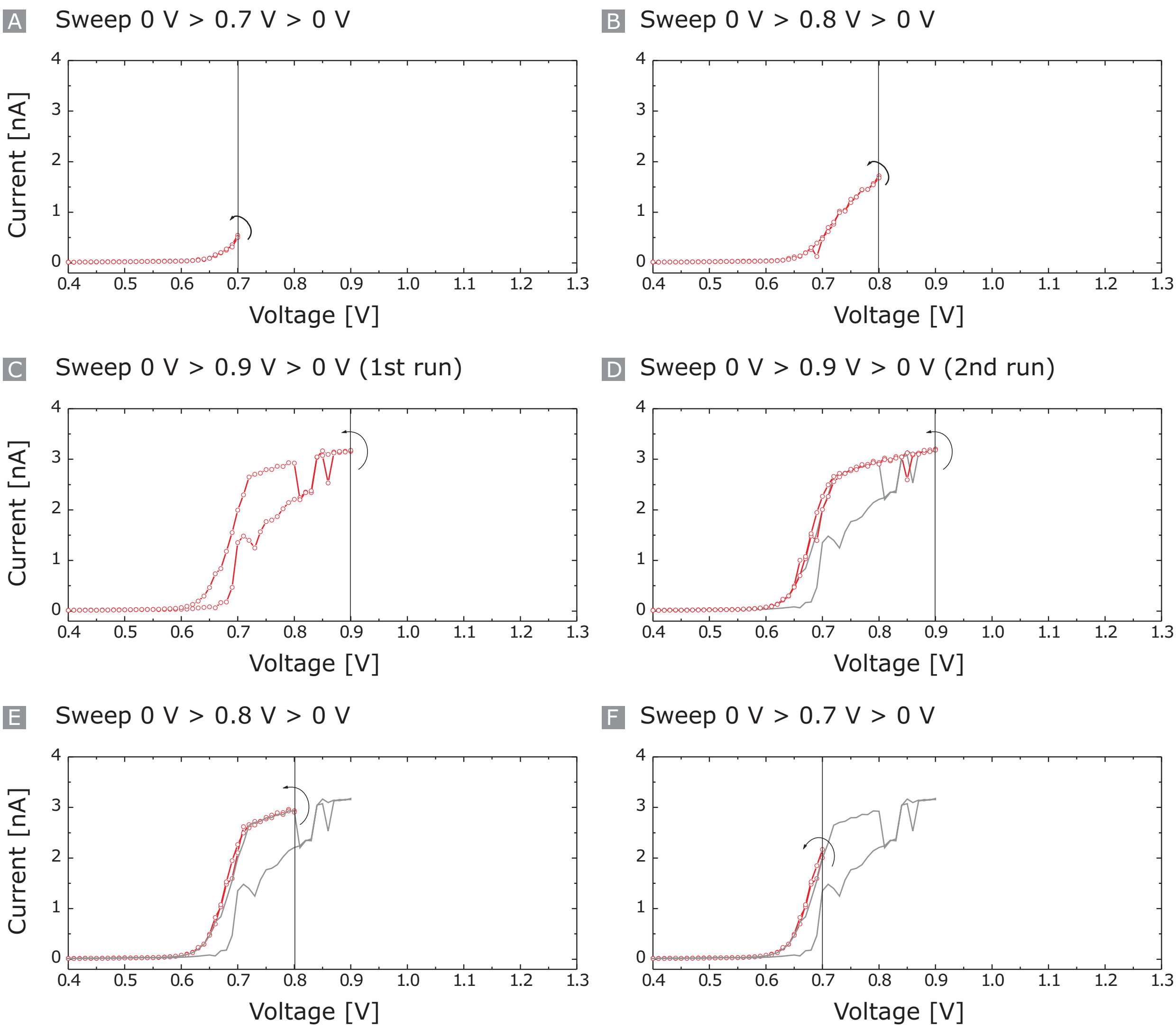

Figure 7.8: *Stepwise increase of the maximum voltage of the I–V double sweep of the Au–single-BPDN-DT–Au system. The system switches if 0.9 V are approached. The initial "off" state is no longer accessible when the voltage has exceeded the positive voltage threshold and the system stays in the "on" state even after decreasing the maximum voltage again. The gray curve shows the switching sweep displayed in (C) again for the guidance in (D)-(E).*

After this first switching sweep, when operating only at voltages above $V_{\text{Switch,neg}}$, the initial "off" state is no longer accessible and the metal-molecule-metal system remains in the higher conductive "on" state during all subsequent positive sweeps. Performing a negative voltage sweep from 0 to –1.5 V, a similar switching behavior at around –1.0 V is observed. Sweeping

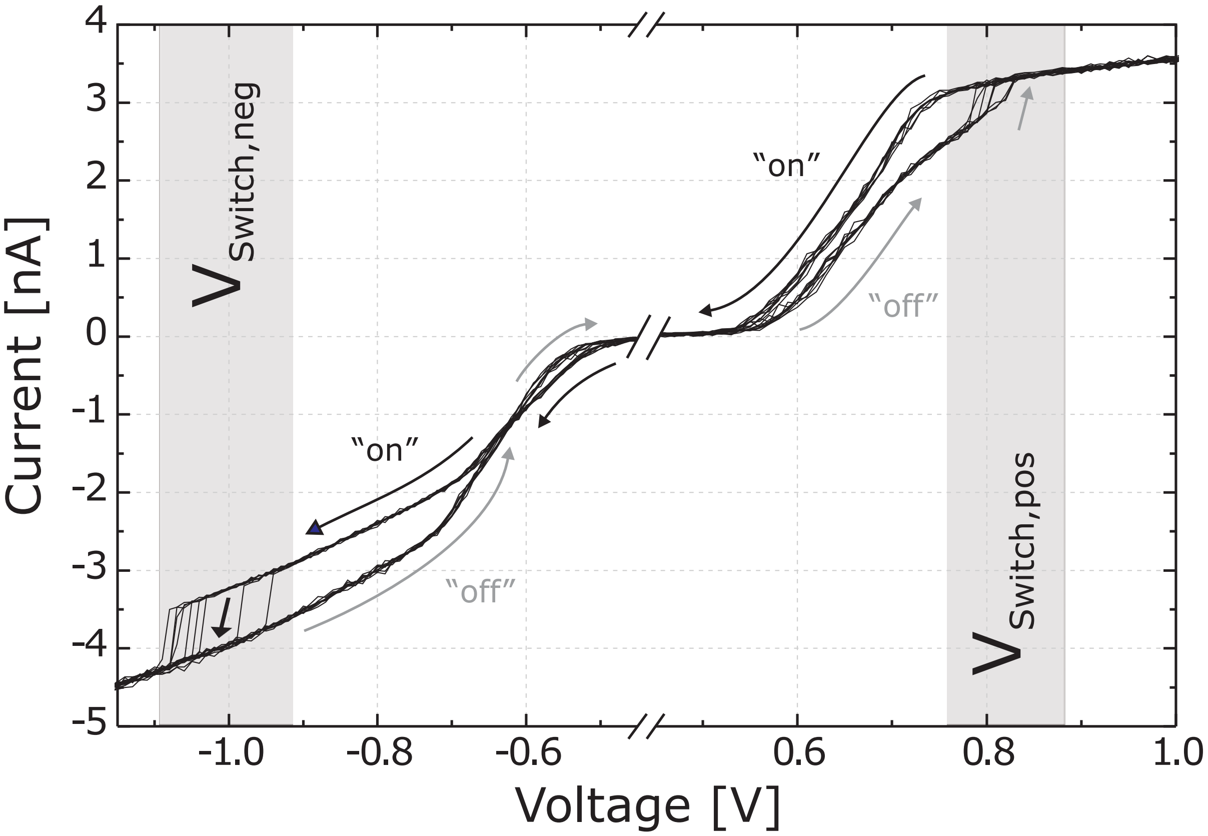

Figure 7.9: *Several repeated switching cycles of the BPDN-DT: If the voltage applied to the Au–single-BPDN-DT–Au junction exceeds a certain positive threshold value ($V_{\text{Switch,pos}}$), the system switches from the initial "off" state to the "on" state. This state is maintained when operating only at voltages above $V_{\text{Switch,neg}}$. A negative voltage sweep or a pulse below the negative threshold value ($V_{\text{Switch,neg}}$) resets the molecule again to the initial "off" state.*

back from –1.5 to 0 V, the current signal follows again a monotonous trace.

There is an intersection of the two signals at –0.62 V. This feature can appear on the positive or on the positive and negative voltage axis. Figure 7.10 shows the case where the intersection of the two current traces appears on the positive as well as on the negative voltage axis, measured at 100 K. Within the huge data sets measured, there are also curves which show no intersection.

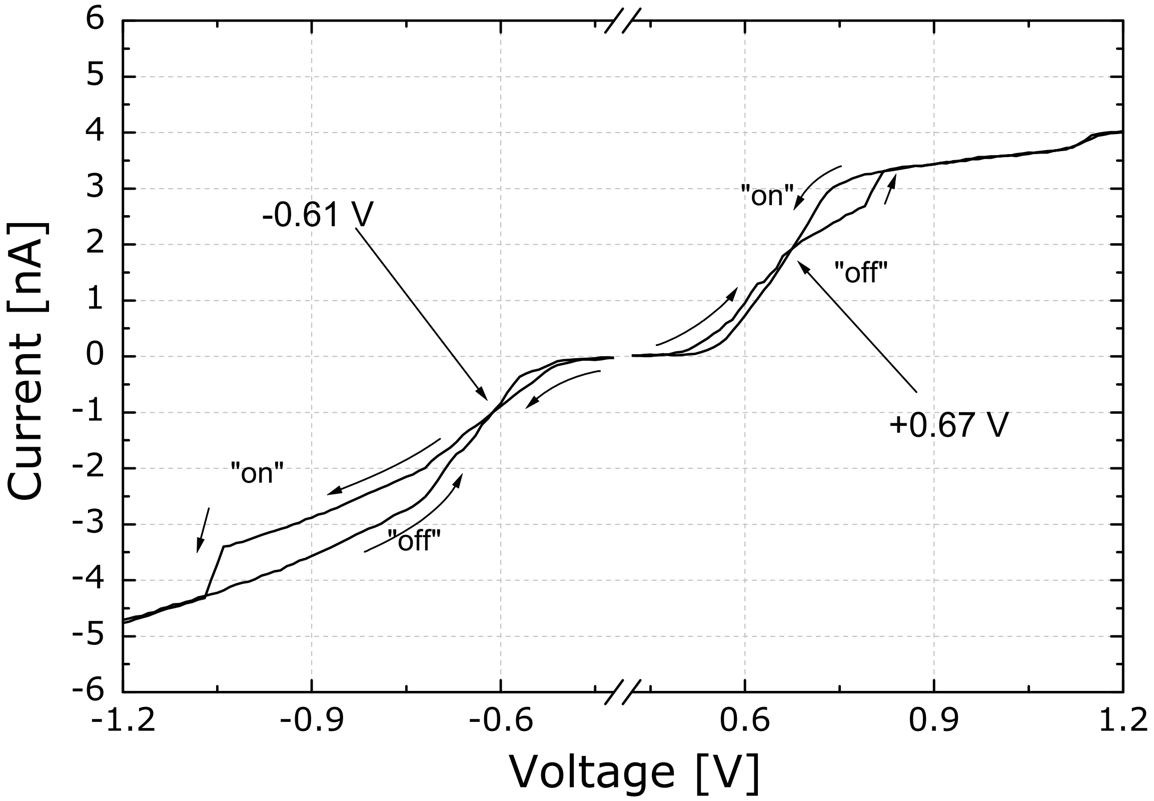

Figure 7.10: *The intersection of the two current traces on the positive and negative voltage axis, measured at 100 K.*

The negative sweep with a voltage range below $V_{\text{Switch,neg}}$ resets the system to the "off" state, which is verified by a subsequent positive sweep that again exhibits a lower current and reveals again a switching to the "on" state at approximately +0.8 V. In all the samples measured, the "off" state was always reconfigurable by applying a negative voltage pulse below a certain threshold voltage ($V < V_{\text{Switch,neg}}$). $V_{\text{Switch,pos}}$ varies between +0.7 V and +1.4 V, and $V_{\text{Switch,neg}}$ between –0.7 V and –1.4 V, respectively.

Even after several hours of measurement and performing more than 1500 positive and negative sweeps iteratively, the hysteresis effect is maintained and the system retains its ability to switch. A remarkable result for a single-molecule system.

Further insight into the switching mechanism was gained by studying the temporal behavior of the switching process. Therefore, measurements at different integration times were performed. Using a long current measurement integration time of $t_{int,long}$ = 320 ms per data point, compared to a short integration time of $t_{int,short}$ = 0.64 ms per data point used previously, the current signal reveals a bistable behavior in the range of approximately $+0.7$ to $+0.82$ V for increasing voltage (Figure 7.11(A)). In this particular voltage range, the system switches back and forth between the competing "on" and "off" state. For higher voltages, which means also higher electrical fields across the molecule, the current signal follows again a single trace, indicating that the "on" state is energetically more favorable. Upon decreasing the voltage from $+1.0$ to 0 V (Figure 7.11(B)), the signal follows a monotonic trace and starts to switch again in the above-mentioned bistable voltage range. Measuring with $t_{int,long}$, the "on" state is not maintained, and the molecule relaxes to the "off" state for lower voltages. Measuring with $t_{int,short}$, the system switches to the "on" state for increasing voltages and remains in the "on" state, in contrast to $t_{int,long}$ (Figure 7.11(C)).

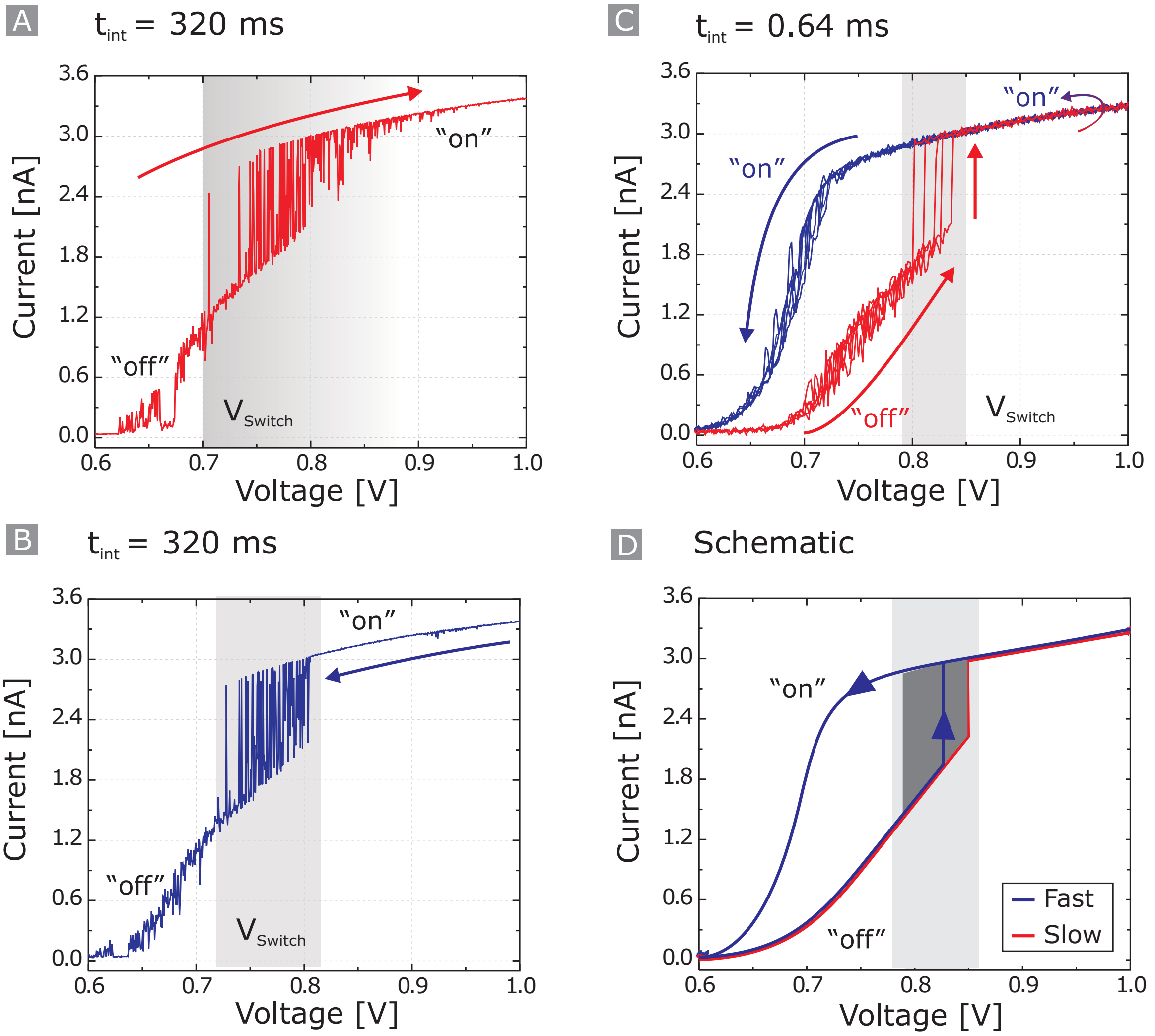

Figure 7.11: *Dynamics of the switching mechanism: (A) Upon increasing the current measurement integration time significantly ($t_{int,long}$ = 320 ms per data point), the current signal becomes bistable for increasing voltages within a certain range, finally switching to the "on" state for higher voltages. (B) When lowering the voltage with $t_{int,long}$, fluctuations can be observed in a certain voltage range, after which the "on" state finally relaxes into the "off" state for $V < V_{\text{Switch}}$. (C) For short integration time ($t_{int,short}$ = 0.64 ms per data point) a sudden switching to a high conductive "on" state occurs. The system maintains the "on" state even upon decreasing the voltage. The gray area represents the region of V_{Switch}. (D) Schematic illustration of the switching response for slow and fast voltage sweeps.*

Discussion

Single BPDN-DT and BP-DT molecules have been contacted by two symmetric leads using the MCBJ technique. It has been demonstrated that the Au–single-BPDN-DT–Au system can be controlled and reversibly switched between two distinct states using the aforementioned control principle. Two other groups have also investigated the switching properties of the BPDN-DT molecules [5; 30]. They found a unipolar voltage-triggered conductance switching of an ensemble of BPDN-DT molecules, using three different techniques [5]. Since the molecule–metal coupling is equal in both molecules in the measurements reported here, the lower current flow in BPDN-DT can be explained by the reduced conjugation due to its more twisted molecular structure.

In addition, stochastic switching [18] is absent for both molecular systems. This can be explained by the low temperatures where the measurements have been performed. Consequently, the mechanisms causing the observed switching in BPDN-DT is obviously not a stochastic one. In the experiments mentioned above, even after performing more than 1500 positive and negative sweeps iteratively, the BPDN-DT system retained its ability to switch. In contrast, the BP-DT molecule without nitro groups did not exhibit any switching feature, not even of a stochastic type [18]. In the MCBJ measurements discussed here, collective phenomena can be excluded. In contrast, the conductance switching reported in the inherently asymmetric crossbar structures [62; 11; 73; 40], can be attributed to filamentary current flow. If metal-metal contacts were formed in the MCBJ approach, much higher currents would be measured with resistances below 12.9 kΩ, as described in Chapter 3. However, the conductance changes are much smaller. This further substantiates that the switching found in the BPDN-DT has a truly molecular origin. Comparing the molecular structures of BPDN-DT and BP-DT, obviously the nitro groups are responsible for the switching behavior of the BPDN-DT.

In Figure 7.9, it can be observed that the threshold for the switching varies between 0.8 V and 1.1 V. This can be attributed to microscopic changes in the molecule–metal coupling causing a change in the voltage drop across the molecule. As a consequence, the positive and negative threshold can be slightly asymmetric. Despite of these small variations in the switching threshold, both states of the system are remarkably stable.

Further insight into the switching dynamics was gained via time-dependent measurements (see Figure 7.11). This behavior can be an important step to verify the applicability of the different theoretical models. Figure 7.12 illustrates the switching principle found by the experiments. The “on” state can be relaxed by either performing a negative voltage sweep exceeding the negative switching voltage (see Figure 7.12(B)), by applying a negative voltage pulse also exceeding the negative switching voltage (see Figure 7.12(C)) or by slowly decreasing the voltage over the positive bistable switching range (see Figure 7.12(A)). Although expected to be very slow in operation, the latter case is technologically very interesting, since only positive voltages are required to fully execute the controlled switching.

Within the bistable regime, the two states are energetically accessible. Within the data displayed in Figure 7.11(A) and (B), it can be seen that for smaller voltages, the probability to switch from the “off” state to the higher conductive “on” state is not as high as for higher voltages within the bistable voltage window. This bistability may be explained by a double-potential picture with a bias voltage dependent tunneling barrier in between. The switching time is faster than the integration time of 640 μs. Within this sampling time, the HP4156B averages over 3 measurement points, therefore, the switching must be faster than 215 μs.

Compared to other mesoscopic conductance switching phenomena, e.g. resistance switching in thin films, the hysteresis in the BPDN-DT molecule is anomalous. An induced intramolecular asymmetry causes the positive “on” (the higher conductive) state to become the negative “off” (the lower conductive) state. By comparison with the reference molecule BP-DT, the nitro groups are supposed to be the origin of switching. This groups cause a steric hindrance and a tilting of the molecule between the two pyridine units of approximately 60 degrees. Possible reasons for switching are conformational change, trapping of charges on the molecule or tilting. Recently, polaronic transport [25] has been suggested to cause hysteresis effects in I–V curves very similar to the characteristics shown in Figure 7.11(C).

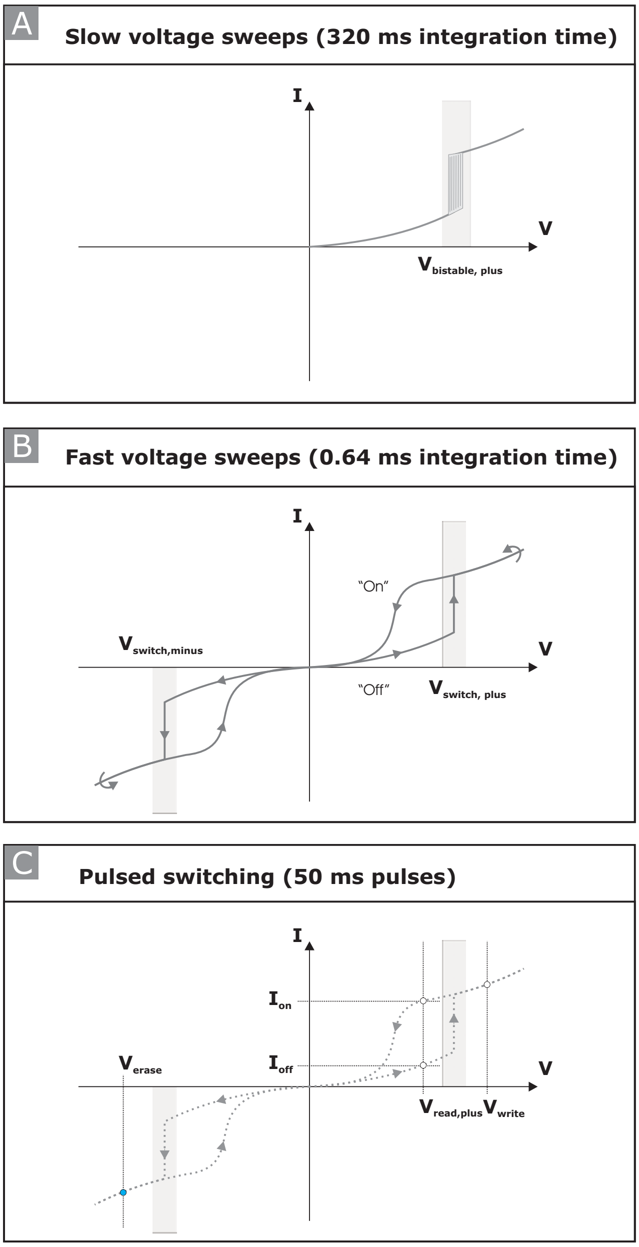
A Slow voltage sweeps (320 ms integration time)

B Fast voltage sweeps (0.64 ms integration time)

C Pulsed switching (50 ms pulses)

I
V
V bistable, plus
I
"On"
V switch,minus
V
"Off"
V switch, plus
I
I on
V erase
I off
V
V read,plus
V write

Figure 7.12: *Schematic of the switching behavior: (A) Sweeping the voltage slowly, the system switches after passing a bistable region to the "on" state. However, for voltages below the bistable region, the "off" state relaxes. Only by using fast integration times (B), a hysteresis is observed. Instead of sweeps, voltage pulses can be applied instead (C) to control and detect the state of the molecular system.*

The theory group of Dr. Ferdinand Evers at the Institute for Nanotechnology (INT) at the Research Center Karlsruhe (FZK) (Dr. V. Meded, Dr. A. Bagrets, A. Arnold) has performed Density Functional Theory (DFT) calculations on the BP-DT and BPDN-DT molecule. The work is still ongoing, however, a few preliminary results are allowed to be presented here.

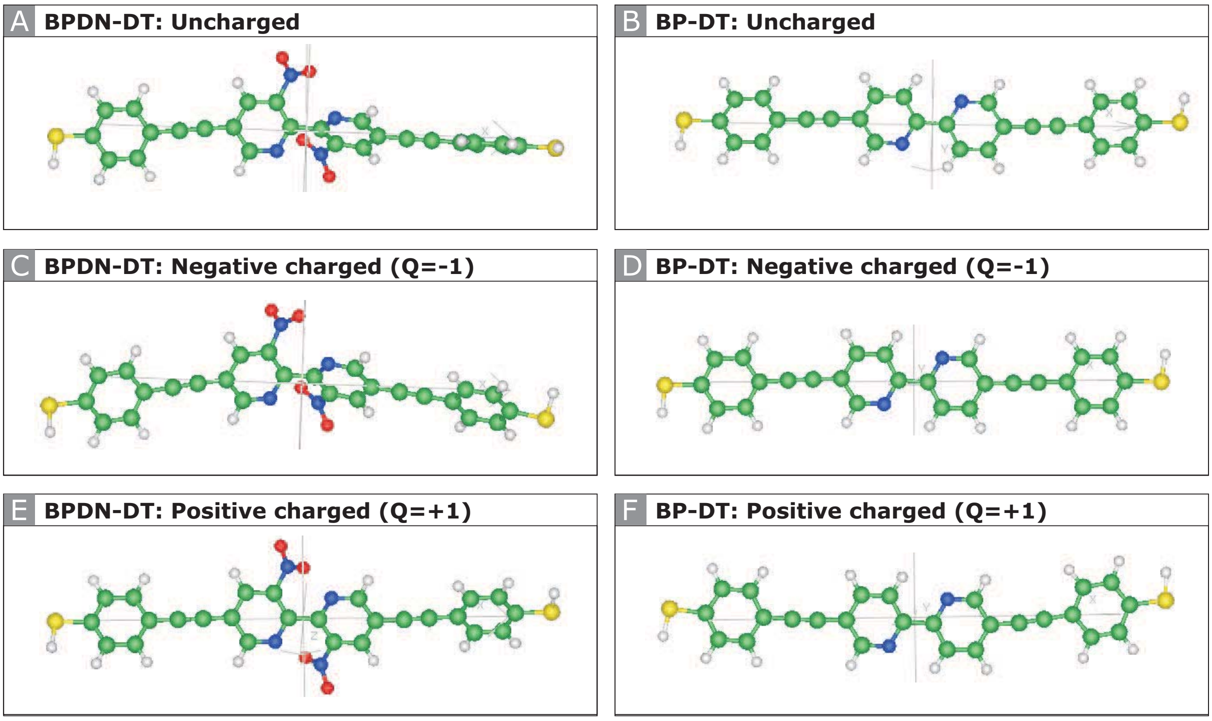
A BPDN-DT: Uncharged
B BP-DT: Uncharged
C BPDN-DT: Negative charged (Q=-1)
D BP-DT: Negative charged (Q=-1)
E BPDN-DT: Positive charged (Q=+1)
F BP-DT: Positive charged (Q=+1)

Figure 7.13: *Density Functional Theory (DFT) calculations performed for the BPDN-DT and BP-DT molecules: Molecular structures show (A)+(B) the uncharged, (C)+(D) the positively charged, and (E)+(F) negatively charged molecules. The BPDN-DT shows a tilting between the two pyridil units of approximately 60°, which is only slightly affected by the positive or negative charging. BP-DT reveals always a planar structure which is not affected by the charging.*

For the calculations, it has to be kept in mind that the hysteresis must be bias voltage controllable, hence a static asymmetry is not sufficient. Evers and his group concluded that there is a dipole moment present in the BPDN-DT which is not present in the test molecule, the BP-DT. But the direction of the dipole moment is not pointing along the molecule and has no interaction with the electric field applied.

Hence, an obvious asymmetry was not found (see Figure 7.13). In addition, all molecular orbitals calculated were lying above -5 eV or the Fermi energy of bulk Au (see Figure 7.14). Hence it is not likely that the molecule BPDN-DT gets charged, although it would be easier compared to the BP-DT.

In conclusion, the DFT calculations could so far not explain the switching mechanism found experimentally in the BPDN-DT single-molecule switch.

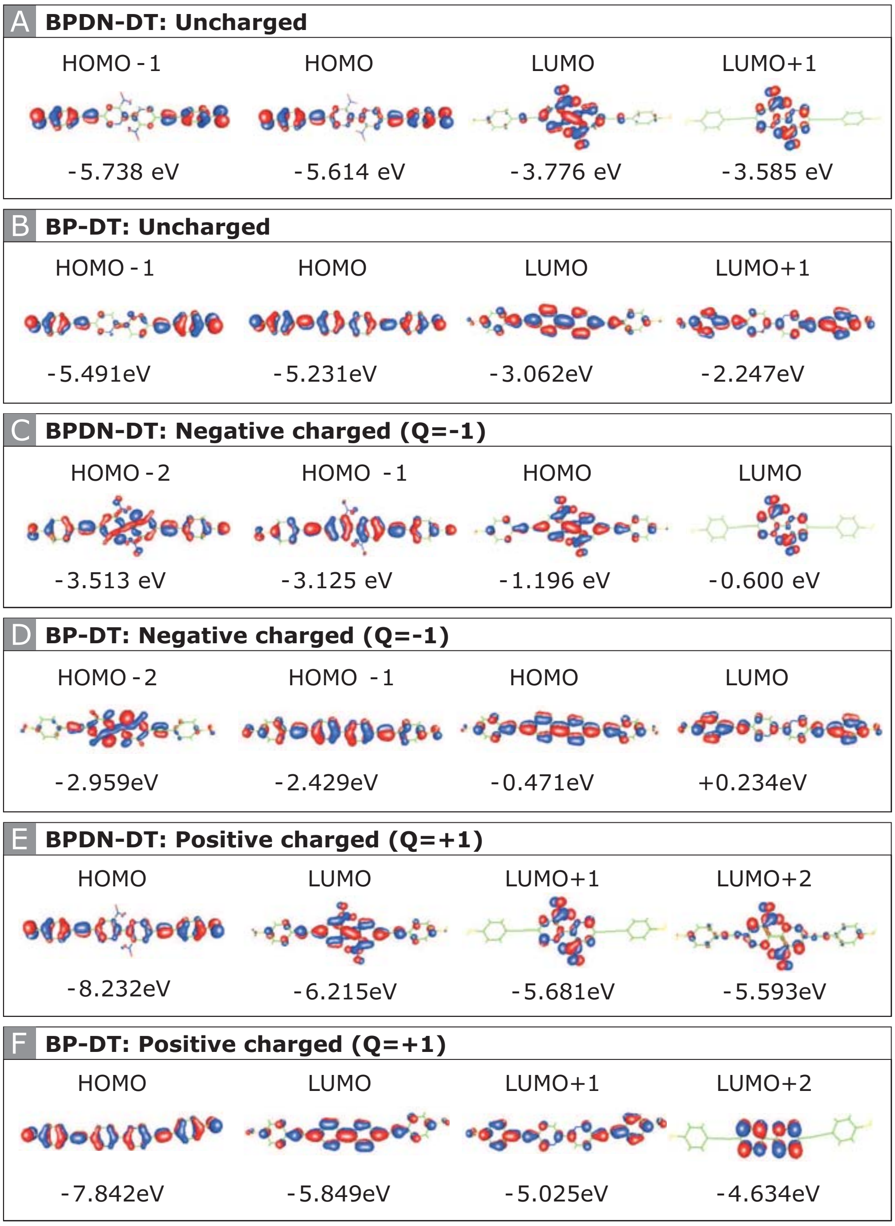
A BPDN-DT: Uncharged
HOMO - 1
HOMO
LUMO
LUMO+1
-5.738 eV
-5.614 eV
-3.776 eV
-3.585 eV
B BP-DT: Uncharged
HOMO - 1
HOMO
LUMO
LUMO+1
-5.491eV
-5.231eV
-3.062eV
-2.247eV
C BPDN-DT: Negative charged (Q=-1)
HOMO - 2
HOMO -1
HOMO
LUMO
-3.513 eV
-3.125 eV
-1.196 eV
-0.600 eV
D BP-DT: Negative charged (Q=-1)
HOMO - 2
HOMO -1
HOMO
LUMO
-2.959eV
-2.429eV
-0.471eV
+0.234eV
E BPDN-DT: Positive charged (Q=+1)
HOMO
LUMO
LUMO+1
LUMO+2
-8.232eV
-6.215eV
-5.681eV
-5.593eV
F BP-DT: Positive charged (Q=+1)
HOMO
LUMO
LUMO+1
LUMO+2
-7.842eV
-5.849eV
-5.025eV
-4.634eV

Figure 7.14: *Density-Functional-Theory (DFT) calculations performed for the BPDN-DT and BP-DT molecules: (A)+(B) Uncharged, (C)+(D) positively charged, and (E)+(F) negatively charged situation. (See text for details.)*

As a real application of a single-molecule device, it will be shown in the next section that the very controlled switching between the two distinct states can be employed for testing memory operation on a single-molecule level.

7.3 Memory Operation

As it was discussed in the last section, the BPDN-DT molecule fulfills all the requirements to be employed as a single-molecule switch: The system can be controlled and reversibly be switched between two distinct and stable states. This very controlled switching mechanism can be employed to store a bit in the molecular system. A prerequisite for storing information is the appearance of a hysteresis in the *I*–*V* signal. The programming principle has been shown in Figure 7.12(C). As shown in the previous section 7.2, the "on" state of the voltage-induced switch persists if the voltage is ramped over the region of bistability sufficiently fast or when positive and negative voltage pulses are applied (see Fig. 7.12).

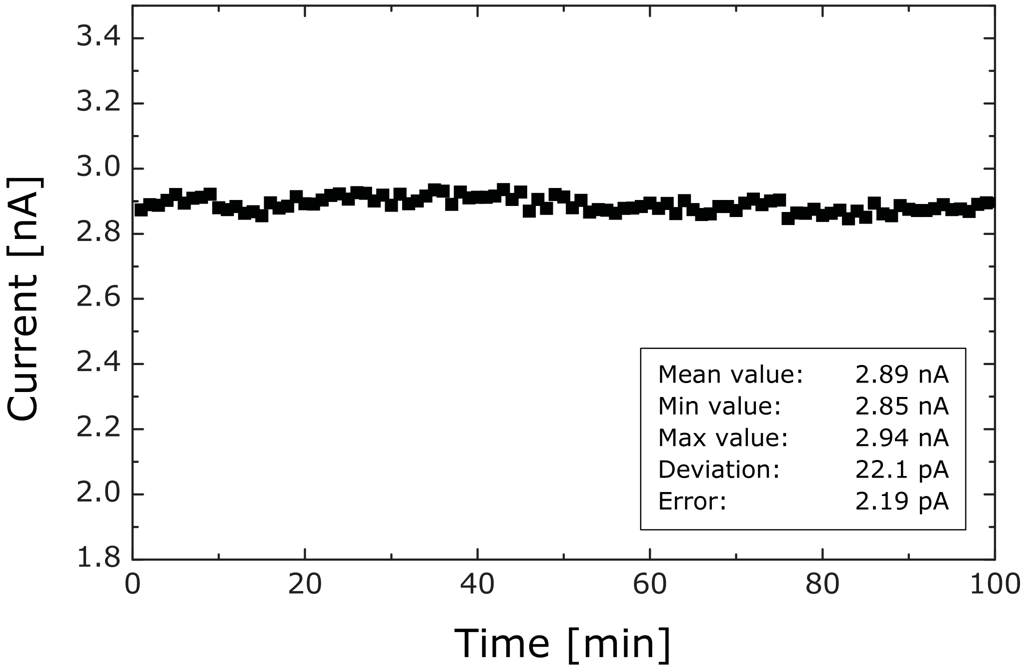

Figure 7.15: *BPDN-DT "on" state stability at 100 K: The current representing the "on" state is measured continuously every minute up to a total recording time of 100 minutes. The current measured represents the "on" state, and is unaffected of the reading voltage at 0.8 V.*

If the programming principle for writing one bit in a memory element is known, then the bit has to be read-out either by not affecting the bit state or by destroying and re-writing the bit. The first type is called "non-destructive read-out". In this section, it will be studied whether the bit state of the BPDN-DT molecule can be probed and whether the read-out erases the bit or not.

As demonstrated in Figure 7.8, the "off" and the "on" state are both unaffected, if the voltage is lower than the critical threshold voltage. The molecule switches only to the other state, if the voltage exceeds the corresponding threshold voltage.

In order to test the non-volatility of the memory, i.e. the stability of the "on" state, successive read pulses at 0.8 V were applied. Figure 7.15 shows the stability of the current of the Au–BPDN-DT–Au junction measured at a voltage of 0.8 V as a function of time at 100 K. The voltage was continuously applied and the current was measured every 60 s. The current signal stays constant at about 2.9 nA for the entire time measured of 100 min. This demonstrates a remarkable stability of the "on" state of the BPDN-DT.

This nondestructive reading makes it possible to use this single-molecule system as a memory element. As mentioned above, voltage pulses exceeding the threshold voltages can be applied to switch the system between the two discrete states in a very controlled and reversible manner. A pulse pattern consisting of write (+1.6 V, 50 ms length) and erase (–1.6 V, 50 ms length) pulses with intermediate readings (+1.1 V, 3 s duration) was applied to the metal–single-molecule–metal system to demonstrate its memory operation (Figure 7.16(A)). The inset of Figure 7.16(B) shows the *I*–*V* curve for the specific sample used for this measurement. The slight difference in the hysteresis compared to the above-described data shows the typical variation in single-molecule junctions which occurs due to microscopic changes in the molecule-metal coupling. In this configuration, the reading voltage at +1.1 V is farther separated from the critical switching range (+1.3 to +1.4 V).

The current through the molecule was directly probed and the data shown in Figure 7.16(B) is raw data without any further signal processing. During the reading times of 3 seconds, the current signals were constant and no decay of the two states was observed. Even when using continuous reading times of up to 30 s, the signal decreased only by 5%. The currents measured for the "off" state vary between 0.05 and 0.13 nA, those for the "on" state between 0.9 and 3.6 nA, yielding a bit separation ($I_{\text{on}}/I_{\text{off}}$) ranging between 7 and 70. The variation in the "on" state current can be explained by the steep increase in the I–V signal around +1.1 V (inset of Figure 7.16(B)). Furthermore, periodic reading of a stored bit (i.e. no voltage applied between readings) established that this single-molecule memory is nonvolatile over a measurement time of several minutes (e.g. 100 min in Figure 7.15) at 100 K (see Fig. 7.15).

The voltage-induced switching behavior of BPDN-DT has already been discussed in the previous section. For memory operation it is not only required to switch back and forth in a controlled manner, but, but also to be able to read out the bit state of the memory. This was shown in Figure 7.15 where the "on" state did not decay over a long time of several minutes. In Figure 7.16 it was further demonstrated that the BPDN-DT molecule can be switched back and forth in response to a voltage pulse and that the bit state of the system can be written and erased for many cycles. These measurements have therefore demonstrated that the BPDN-DT molecule can be employed as a single-molecule memory element.

7.4 Conclusions

In this chapter, it has been demonstrated that molecules can have an intramolecular functionality. In particular, it has been shown that the SB diode molecule reveals a temperature-independent current rectification, and that the BPDN-DT exhibits a voltage-induced switching behavior. Since at low temperatures ($T = 100$ K), stochastic switching is absent, and because the reference molecule, the BP-DT, without functionality did not switch in response to the voltage pulse, it could be concluded that the switching has doubtlessly a molecular origin.

By direct comparison, it has been revealed that the switching is due to the functional nitro groups. The dynamic investigations showed a bistable behavior for the two distinct states. An excellent control over the switching was achieved and since the molecular system offers sufficient stability to non-destructively probe and thereby read out the bit state, memory operation could be demonstrated.

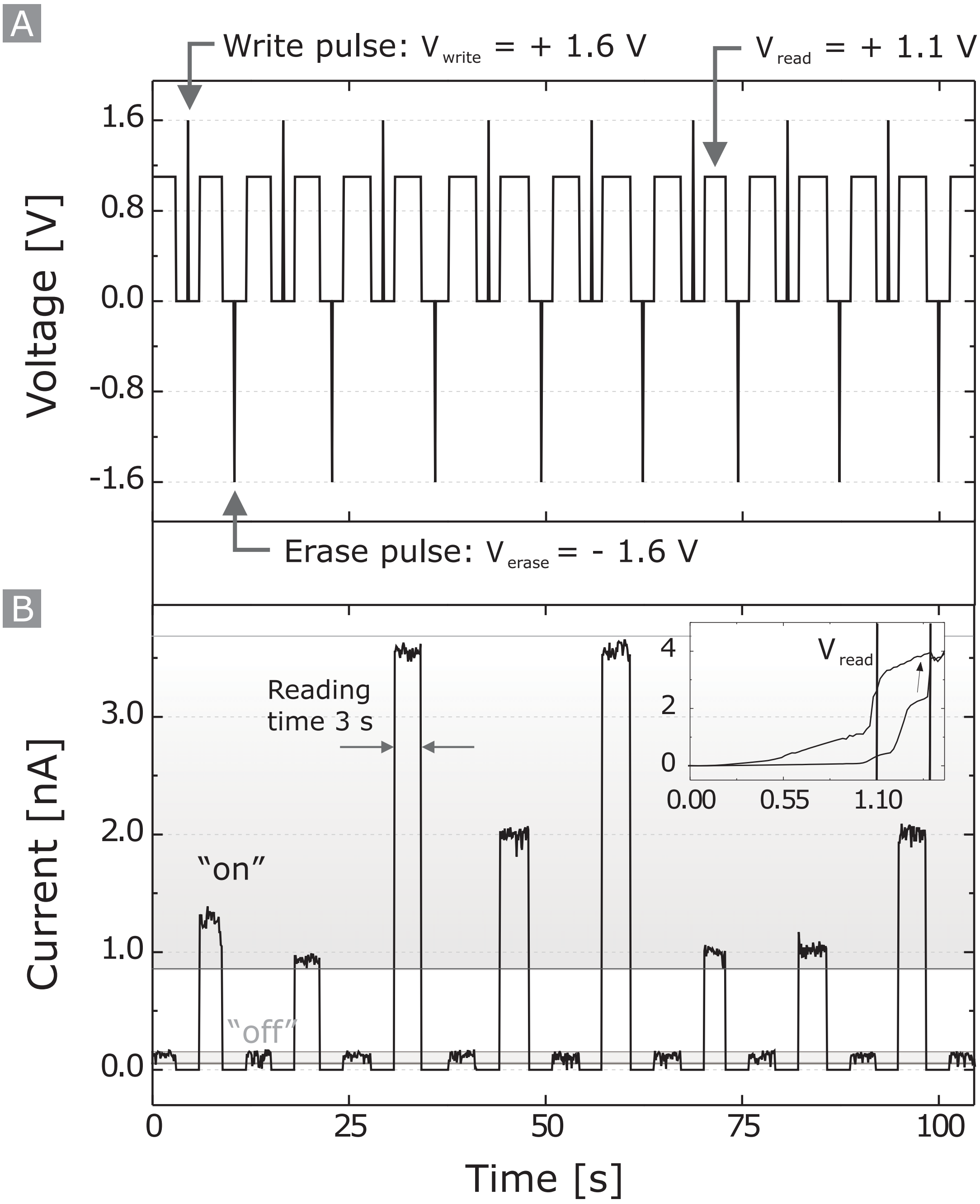

Figure 7.16: *Memory operation of the BPDN-DT system: (A) Write, read and erase pulse pattern applied. (B) Resulting switching between "off" and "on" state:* I_{off} *varies between 0.05 and 0.13 nA,* I_{on} *between 0.9 and 3.6 nA. Reading times of 3 s display excellent signal stability. The inset shows the corresponding I–V curve, indicating switching at 1.4 V and reading at 1.1 V (black lines).*

References

[1] N. Agraït, A. L. Yeyati, and J. M. van Ruitenbeek. Quantum properties of atomic-sized conductors. *Phys. Reports*, 377:81, 2003.

[2] N. Ashcroft and N. Mermin. *Solid State Physics*. Saunders College, 1976.

[3] S. J. Bae, C. R. Lee, I. S. Choi, C. S. Hwang, M. S. Gong, K. Kim, and S. W. Joo. Adsorption of 4-biphenylisocyanide on gold and silver nanoparticle surfaces: Surface-enhanced Raman scattering study. *J. Phys. Chem. B*, 106(28):7076–7080, 2002.

[4] G. Binnig, H. Rohrer, Ch. Gerber, and E. Weiber. *Phys. Rev. Lett.*, 50:120, 1982.

[5] A. S. Blum, J. G. Kushmerick, D. P. Long, C. H. Patterson, J. C. Yang, J. C. Henderson, Y. X. Yao, J. M. Tour, R. Shashidhar, and B. R. Ratna. Molecularly inherent voltage-controlled conductance switching. *Nature Materials*, 4(2):167–172, 2005.

[6] G. Breit. *Theory of Rensonance Reactions*. Springer, 1959.

[7] G. Breit and E. Wigner. Capture of slow neutrons. *Phys. Rev.*, 49:519, 1936.

[8] J. Chen, L. C. Calvet, M. A. Reed, D. W. Carr, D. S. Grubisha, and D. W. Bennett. Electronic transport through metal–1,4-phenylene diisocyanide–metal junctions. *Chem. Phys. Lett.*, 313:741–748, 1999.

[9] J. Chen, M. A. Reed, A. M. Rawlett, and J. M. Tour. Large on-off ratios and negative differential resistance in a molecular electronic device. *Science*, 286(5444):1550–1552, 1999.

[10] J. Chen, W. Wang, M. A. Reed, A. M. Rawlett, D. W. Price, and J. M. Tour. Room-temperature negative differential resistance in nanoscale molecular junctions. *Appl. Phys. Lett.*, 77(8):1224–1226, 2000.

[11] Y. Chen, G. Y. Jung, D. A. A. Ohlberg, X. M. Li, D. R. Stewart, J. O. Jeppesen, K. A. Nielsen, J. F. Stoddart, and R. S. Williams. Nanoscale molecular-switch crossbar circuits. *Nanotech.*, 14(4):462–468, 2003.

[12] C. P. Collier, E. W. Wong, M. Belohradsky, F. M. Raymo, J. F. Stoddart, P. J. Kuekes, R. S. Williams, and J. R. Heath. Electronically configurable molecular-based logic gates. *Science*, 285(5426):391–394, 1999.

[13] J. C. Cuevas, A. L. Yeyati, and A. Martín Rodero. Microscopic origin of conducting channels in metallic atomic-sized contacts. *Phys. Rev. Lett.*, 80:1066–1069, 1998.

[14] S. Datta. *Electronic Transport in Mesoscopic Systems*. Cambridge University Press, United Kingdom, 1995.

[15] S. Datta, W. Tian, S. Hong, R. Reifenberger, J. I. Henderson, and C. P. Kubiak. Current-voltage characteristics of self-assembled monolayers by scanning tunneling microscopy. *Phys. Rev. Lett.*, 79(13):2530–2533, 1997.

[16] M. di Leo. *Stromfluss durch organische Moleküle: Herstellung und Charakterisierung von Einzelmolekülkontakten*. PhD thesis, Fachhochschule München, 2002.

[17] M. di Ventra, S. T. Pantelides, and N. D. Lang. The benzene molecules as a molecular resonant-tunneling transistor. *Appl. Phys. Lett.*, 76(23):3446–3450, 2000.

[18] Z. J. Donhauser, B. A. Mantooth, K. F. Kelly, L. A. Bumm, J. D. Monnell, J. J. Stapleton, D. W. Price, A. M. Rawlett, D. L. Allara, J. M. Tour, and P. S. Weiss. Conductance switching in single molecules through conformational changes. *Science*, 292(5525):2303–2307, 2001.

[19] C. J. F. Dupraz, U. Beierlein, and J. P. Kotthaus. Low temperature conductance measurements of self-assembled monolayers of 1,4-phenylene diisocyanide. *Chem. Phys. Chem.*, 4(11):1247–1252, 2003.

[20] U. Dürig, O. Züger, and D. W. Pohl. Observation of metallic adhesion using the scanning tunneling microscope. *Phys. Rev. Lett.*, 65:349–352, 1990.

[21] M. Elbing, R. Ochs, M. Koentopp, M. Fischer, C. von Hänisch, F. Weigend, F. Evers, H. B. Weber, and M. Mayor. A single-molecule diode. *PNAS*, 102:8815–8820, 2005.

[22] E. G. Emberly and G. Kirczenow. Models of electron transport through organic molecular monolayers self-assembled on nanoscale metallic contacts. *Phys. Rev. B*, 64:235412–1–235412–8, 2001.

[23] A. K. Flatt, S. M. Dirk, J. C. Henderson, D. E. Shen, J. Su, M. A. Reed, and J. M. Tour. Synthesis and testing of new end-functionalized oligomers for molecular electronics. *Tetrahedron*, 59:8555–8570, 2003.

[24] M. Fujihira, K. Nishiyama, and H. Yamada. *Thin Solid Films*, 132:77–82, 1985.

[25] M. Galperin, M. A. Ratner, and A. Nitzan. Hysteresis, switching, and negative differential resistance in molecular junctions: A polaron model. *Nano Letters*, 5(1):125–130, 2005.

[26] J. K. Gimzewski and R. Möller. Transition from the tunneling regime to point contact studied using scanning tunneling microscopy. *Physica B*, 36:1284–1287, 1987.

[27] H. Gronbeck, A. Curioni, and W. Andreoni. Thiols and disulfides on the au(111) surface: The headgroup-gold interaction. *J. Am. Chem. Soc.*, 122(16):3839–3842, 2000.

[28] S. Hong, R. Reifenberger, W. Tian, S. Datta, J. I. Henderson, and C. P. Kubiak. Molecular conductance spectroscopy of conjugated, phenyl-based molecules on Au(111): the effect of end groups on molecular conduction. *Superlattices and Microstructures*, 28(4):289–303, 2000.

[29] Å. Johansson and S. Stafström. Interactions between molecular wires and a gold surface. *Chem. Phys. Lett.*, 322(5):301–306, 2000.

[30] Z. K. Keane, J. W. Ciszek, J. M. Tour, and D. Natelson. Three-terminal devices to examine single-molecule conductance switching. *Nano Lett.*, 6:1518–1521, 2006.

[31] Plenum Press New York, B, Kramer, editor. *Resistance fluctuations in small samples: Be carful when playing with Ohm's Law*. S. Washburn, 1991.

[32] J. M. Krans, J. M. van Ruitenbeek, V. V. Fisun, I. K. Yanson, and L. J. de Jongh. *Nature*, 375:767, 1995.

[33] S. Kubatkin, A. Danilov, M. Hjort, J. Cornil, J. L. Bredas, N. Stuhr-Hansen, P. Hedegard, and T. Bjornholm. Single-electron transistor of a single organic molecule with access to several redox states. *Nature*, 425(6959):698–701, 2003.

[34] S. Kubatkin, A. Danilov, M. Hjort, J. Cornil, J. L. Bredas, N. Stuhr-Hansen, P. Hedegard, and T. Bjornholm. Single electron transistor with a single conjugated molecule. *Curr. Appl. Phys.*, 4(5):554–558, 2004.

[35] P. J. Kuekes, D. R. Stewart, and R. S. Williams. The crossbar latch: Logic value storage, restoration, and inversion in crossbar circuits. *J. Appl. Phys.*, 97(3):034301, 2005.

[36] H. Kuhn and D. Möbius. *Angew. Chem.*, 83:672–676, 1971.

[37] H. Kuhn and D. Möbius. *Angew. Chem. Int. Ed. Engl.*, 10:460–464, 1971.

[38] R. Landauer. *IBM J. Res. Develop.*, 1:223, 1957.

[39] N. D. Lang and Ph. Avouris. Electrical conductance of individual molecules. *Phys. Rev. B*, 64:12532–1–125323–7, 2001.

[40] C. N. Lau, D. R. Stewart, R. S. Williams, and M. Bockrath. Direct observation of nanoscale switching centers in metal/molecule/metal structures. *Nano Lett.*, 4(4):569–572, 2004.

[41] J.-O. Lee, G. Lientschnig, F. Wiertz, M. Struijk, R. A. J. Janssen, R. Egberink, D. N. Reinhoudt, P. Hadley, and C. Dekker. Absence of strong gate effects in electrical measurements on phenylene-based conjugated molecules. *Nano Lett.*, 3(2):113–117, 2003.

[42] J. Liao, L. Bernard, M. Langer, C. Schönenberger, and M. Calame. Reversible formation of molecular junctions in 2d nanparticle arrays. *Adv. Mat.*, 18:2444–2447, 2006.

[43] D. R. Lide. *Handbook of Chemistry and Physics*. CRC Press, New York, 1997.

[44] M. Magoga and Ch. Joachim. Conductance and transparence of long molecular wires. *Phys. Rev. B*, 56(8):4722–4729, 1997.

[45] M. Mahadevan and R. M. Bradley. Simulations and theory of electromigration-induced slit formation in unpassivated single-crystal metal lines. *Phys. Rev. B*, 59:11037–11046, 1999.

[46] R. M. Metzger. Unimolecular electrical rectifiers. *Chem. Rev.*, 103:3803–3834, 2003.

[47] R. M. Metzger, B. Chen, U. Höpfner, M. V. Lakshmikantham, D. Vuillaume, T. Kawai, X. Wu, H. Tachibana, T. V. Hughes, H. Sakurai, J. W. Baldwin, Ch. Hosch, M. P. Cava, L. Brehmer, and G. J. Ashwell. Unimolecular electrical rectification in hexadecylquinolinium tricyanoquinodimethanide. *J. Am. Chem. Soc.*, 119:10455–10466, 1997.

[48] R. M. Metzger and C. A. Panetta. *J. Chim. Phys.*, 85:1125–1134, 1988.

[49] J. Mizobata, A. Fujii, S. Kurokawa, and A. Sakai. High-bias conductance of atom-sized Al contacts. *Phys. Rev. B*, 68:155428–155425, 2003.

[50] G. M. Morales, P. Jiang, S. Yuan, Y. Lee, A. Sanchez, W. You, and L. Yu. Inversion of the rectifying effect in diblock molecular diodes by protonation. *J. Am. Chem. Soc.*, 127:10456–10456, 2005.

[51] J. Moreland and J. W. Elkin. Electron tunneling experiments using Nb-Sn "break" junctions. *J. Appl. Phys.*, 58:3888–3895, 1985.

[52] C. J. Muller, J. M. van Ruitenbeek, and L. J. de Jongh. Experimental observation of the transition from weak link to tunnel junction. *Physica C*, 191:485–504, 1992.

[53] M.-K. Ng, D. C. Lee, and L. Yu. Molecular diodes based on conjugated diblock co-oligomers. *J. Am. Chem. Soc.*, 124:11862–11863, 2002.

[54] M.-K. Ng and L. Yu. Synthesis of amphiphilic conjugated diblock oligomers as molecular diodes. *Angew. Chem. Int. Ed.*, 41:3598–3601, 2002.

[55] A. Nitzan and M. A. Ratner. Electron transport in molecular wire junctions. *Science*, 300:1384–1389, 2003.

[56] G. S. Ohm. *Die galvanische Kette, mathematisch bearbeitet*. Sänidg, Wiesbaden, 1827.

[57] H. Ohnishi, Y. Kondo, and K. Takayanagi. Quantized conductance through individual rows of suspended gold atoms. *Nature*, 395:780–783, 1998.

[58] H. Park, A. K. L. Lim, A. P. Alivisatos, J. Park, and P. L. McEuen. Fabrication of metallic electrodes with nanometer separation by electromigration. *Appl. Phys. Lett.*, 75:301–303, 1999.

[59] M. Paulsson, F. Zahid, and S. Datta. *Nanoscience, Engineering and Technology Handbook*. CRC Press, New York, 2003.

[60] G. K. Ramachandran, T. J. Hopson, A. M. Rawlett, L. A. Nagahara, A. Primak, and S. M. Lindsay. A bond-fluctuation mechanism for stochastic switching in wired molecules. *Science*, 300(5624):1413–1416, 2003.

[61] M. A. Ratner and A. Aviram. Molecular rectifiers. *Chem. Phys. Lett.*, 29:277–283, 1974.

[62] M. A. Reed, J. Chen, A. M. Rawlett, D. W. Price, and J. M. Tour. Molecular random access memory cell. *Appl. Phys. Lett.*, 78(23):3735–3737, 2001.

[63] M. A. Reed, C. Zhou, C. J. Muller, T. P. Burgin, and J. M. Tour. Conductance of a molecular junction. *Science*, 278(5336):252–254, 1997.

[64] J. Repp, G. Meyer, S. Paavilainen, F. E. Olsson, and M. Persson. Imaging bond formation between a gold atom and pentacene on an insulating surface. *Science*, 312:1196–1199, 2006.

[65] M. P. Samanta, W. Tian, S. Datta, J. I. Henderson, and C. P. Kubiak. Electronic conduction through organic molecules. *Phys. Rev. B.*, 53(12):R7626, 1996.

[66] E. Scheer, N. Agraït, J. C. Cuevas, A. L. Yeyati, B. Ludoph, A. Martín Rodero, G. R. Bollinger, J. M. van Ruitenbeek, and C. Urbina. The signature of chemical valence in the electrical conduction through a single-atom contact. *Nature*, 394:154–157, 1998.

[67] E. Scheer, P. Joyez, E. Esteve, C. Urbina, and M. H. Devoret. Conduction channel transmissions of atomic-size aluminum contacts. *Phys. Rev. Lett.*, 78:3535, 1997.

[68] J. M. Seminario, A. G. Zacarias, and J. M. Tour. Molecular alligator clips for single-molecule electronics studies of group 16 and isonitriles interfaced with Au contacts. *J. Am. Chem. Soc.*, 121:411–416, 1999.

[69] V. S. Yu. A possible method for studying Fermi surfaces. *Sov. Phys.-JETP*, 21:655–656, 1965.

[70] J. G. Simmons. Generalized formula for the electric tunnel effect between similar electrods separated by a thin insulating film. *J. Appl. Phys.*, 34:1793–1799, 1963.

[71] R. H. M. Smit, Y. Noat, C. Untiedt, N. D. Lang, M. C. van Hemert, and J. M. van Ruitenbeek. Measurement of the conductance of a hydrogen molecule. *Nature*, 419:906–909, 2002.

[72] M. R. Sørensen, M. R. Brandbyge, and K. W. Jacobsen. Mechanical deformation of atomic-scale metallic contacts: Structure and mechanisms. *Phys. Rev. B*, 57:3283, 1998.

[73] D. R. Stewart, D. A. A. Ohlberg, P. A. Beck, Y. Chen, R. S. Williams, J. O. Jeppesen, K. A. Nielsen, and J. F. Stoddart. Molecule-independent electrical switching in Pt/organic monolayer/Ti devices. *Nano Lett.*, 4(1):133–136, 2004.

[74] K. Stokbro, J. Taylor, M. Brandbyge, J. L. Mozos, and P. Ordejón. Theoretical study of the nonlinear conductance of di-thiol benzene coupled to Au(111) surfaces via thiol and thiolate bonds. *Comput. Mat. Sci.*, 27:151–160, 2003.

[75] S. A. Swanson, R. McClain, K. S. Lovejoy, N. B. Alamdari, J. S. Hamilton, and J. C. Scott. Self-assembled diisocyanide monolayer films on gold and palladium. *Langmuir*, 21(11):5034–5039, 2005.

[76] S. M. Sze. *Physics of Semiconductor Devices*. John Wiley & Sons, New York, 1981.

[77] A. Ulman. Formation and structure of self-assembled monolayers. *Chem. Rev.*, 95:1533–1564, 1996.

[78] J. M. van Ruitenbeek, A. Alvarez, I. Pieyro, C. Grahmann, P. Joyez, M. H. Devoret, D. Esteve, and C. Urbina. Adjustable nanofabricated atomic size contacts. *Rev. Sci. Instrum.*, 67:108, 1996.

[79] B. J. van Wees, H. van Houten, C. W. J. Beenakker, J. G. Williamson, L. P. Kouwenhoven, D. van der Marel, and C. T. Foxon. Quantized conductance of point contacts in a two-dimensional electron gas. *Phys. Rev. Lett.*, 60(9):848–850, 1988.

[80] B. J. van Wees, H. van Houten, C. W. J. Beenakker, J. G. Williamson, L. P. Kouwenhoven, D. van der Marel, and C. T. Foxon. Quantized conductance of point contacts in a two-dimensional electron gas. *Phys. Rev. B*, 6043(9):848–85012431, 1991.

[81] L. Venkataraman, J. E. Klare, I. W. Tam, C. Nuckolls, M. S. Hybertsen, and M. L. Steigerwald. Single-molecule circuits with well-defined molecular conductance. *Nano Lett.*, 6(3):458–462, 2006.

[82] S. A. G. Vrouwe, E. van der Giessen, S. J. van der Molen, D. Dulic, M. L. Trouwborst, and B. J. van Wees. Mechanics of lithographically defined break junctions. *Phys. Rev. B*, 71:35313, 2005.

[83] M. Warlimont. *Handbook of Condensed Matter and Materials Data*. Springer, 2005.

[84] H. B. Weber, J. Reichert, F. Weigend, F. Ochs, D. Beckmann, M. Mayor, R. Ahlrichs, and H. v. Löhneysen. Electronic transport through single conjugated molecules. *Chem. Phys.*, 281:113–125, 2002.

[85] D. A. Wharam, T. J. Thornton, R. Newbury, M. Pepper, H. Ahmed, J. E. F. Frost, D. G. Hasko, D. C. Peacock, and G. A. C. Ritchie, D. A. Jones. *J. Phys. C*, 21:L209, 1988.

[86] X. Y. Xiao, B. Q. Xu, and N. J. Tao. Measurement of single molecule conductance: Benzenedithiol and benzenedimethanethiol. *Nano Letters*, 4(2):267–271, 2004.

[87] B. Xu and N. J. Tao. Measurement of single-molecule resistance by repeated formation of molecular junctions. *Science*, 301:1221–1223, 2003.

[88] S. N. Yaliraki, A. E. Roitberg, C. Gonzalez, V. Mujica, and M. A. Ratner. The injecting energy at molecule/metal interfaces: Implications for conductance of molecular junctions from an *ab initio* molecular description. *J. Chem. Phys.*, 111:6997, 1999.

[89] A. I. Yanson, G. Rubio Bollinger, H. E. Van den Brom, N. Agrat, and J. M. van Ruitenbeek. Formation and manipulation of a metallic wire of single gold atoms. *Nature*, 395:783, 1998.

[90] C. Zhou, M. R. Deshpande, M. A. Reed, L. Jones, and J. M. Tour. Nanoscale metal/self-assembled monolayer/metal heterostructures. *Appl. Phys. Lett.*, 71:611–613, 1997.

List of Figures

1.1 Three different types of transport regimes in a mesoscopic, quasi-1D conductor: (A) Diffusive transport due to scattering occurring within the transport channel. (B) Ballistic transport without scattering due to the absence of scattering centers within the channel. (C) Ballistic transport through a Quantum Point Contact (QPC). In QPCs, the width, w, and the length, l, are both smaller than the characteristic length scale, e.g. the elastic mean free path, L_{mf}. 3

1.2 A conductor consisting of a coherent scatterer (S) connected via two ballistic leads to a left and a right reservoir of electrons. The lead direction is labelled x. 5

1.3 First experimental observations of conductance quantization: (A) 2D electron gas in a GaAs–AlGaAs heterojunction (reproduced from [82]). (B) Na-Na break-junction (reproduced from [34]). The channel separation of the transverse modes is different due to different Fermi wavelengths in semiconductors and metals: The distinct steps are smeared-out in (A) when the thermal energy becomes comparable to the mode separation, whereas in (B), conductance quantization can even be observed at room temperature. 8

1.4 (A) Schematic illustration of a molecule connected to two electrodes. (B) Energetic situation under a small bias V. Inherent hopping process (red) versus coherent quantum tunnelling process (blue). 11

1.5 (A) Simple one-level model of a molecule represented by one molecular orbital with hopping rates $\Gamma_l/\hbar$ and $\Gamma_r/\hbar$ to left and right electrodes. (B) Corresponding I–V and G_{Diff}–V data without broadening, and (C) with broadening of the molecular level due to coupling. 12

1.6 (A) Molecular structure of Benzene (C_6H_6) in different representations. Kekulé and organic chemistry notation, simplified non-resonant and resonant structure, as well as the shell model. (B) The linear combination of the atomic orbitals define the molecular orbitals (reproduced from Blacklight Power Inc., www.blacklightpower.com). (C) Delocalized π orbitals illustrated with the electrostatic potential surface (gray color-code). 18

1.7 Schematic Illustration of (A) elastic electron tunnelling, and (B) inelastic electron tunnelling. An Additional inelastic channel gives rise to (C) two kinks in the I–V, (D) two steps in the G_{Diff}–V, and (E) two peaks in the dG_{Diff}/dV–V plot. 22

2.1 Schematic illustration of various selected experimental approaches used for contacting molecules: The upper row shows approaches with a fixed gap. (A) Self-assembled monolayer (SAM) and Nanopore architectures, (B) magnetic bead junction, and (C) electromigration techniques. The lower row shows techniques which offer a tunable gap: (D) STM/AFM technique allowing for direct or indirect (via Au cluster) contact to the molecules embedded in a supporting insulating SAM of other molecules. (E) Crossed-wire junction where one wire is covered with a SAM whereas the other one is deflected by the Lorentz force in a magnetic field $\vec{B}$ by passing a deflection current through the wire. (F) Mercury drop technique making use of the high surface tension of Mercury without formation of a meniscus creating therefore a defined contact area. 25

2.2 (A) TEM image of a Au bridge consisting of 4 Au atoms between a STM tip and the surface consisting of 4 Au atoms (reproduced from [58]). (B) Calculation of an atomic contact formation using a STM (reproduced from [73]). 27

2.3 Principle of operation of a MCBJ: (A) A freestanding metal bridge with a central lateral constriction is fabricated on top of a flexible substrate and mounted into a three-point bending mechanism. (B) The bending force applied to the bottom of the substrate introduces surface extension which finally breaks the metal bridge at its smallest constriction, creating two separated electrodes which can be controlled thereafter with picometer accuracy in both the opening and closing direction. 30

2.4 (A) Schematic top and side view of the mounting of a MCBJ as used in the pioneering work by Muller et al. and van Ruitenbeek et al., displaying the notched wire, four fixed counter supports, drops of epoxy adhesive and the stacked piezo element. (B) Top view of a manually notched Au wire. The substrate is 4.5 mm wide and the wire has a diameter of 0.1 mm. The inset shows an enlargement of the wire with the notch between the two drops of epoxy (*s* is approximately 1 mm). On each side of the notch, four wires make contact to the sample wire using silver paint. Reproduced from [Agrait2003]. . 31

2.5 Electron-beam lithography process steps used for the fabrication of the small metal bridge on a MCBJ sample: (A) Exposure of a double layer resist system to an electron beam, creating an undercut due to different molecular weights. (B) Evaporation of Au after development. The structure is uncovered in a lift-off step (C) removing the PMMA and the excess material. (D) Reactive ion etching is used to partially remove the PI and in order to achieve a freestanding, cantilevered bridge. 34

2.6 (A) Sample design for a 100 mm × 100 mm plate containing 40 samples, and (B) a processed sample plate. The samples are laser-cut and still kept into the embedding frame via pull linkage. The inset shows a SEM picture of the freestanding metal bridge. 35

2.7 (A) Computer-Aided Design (CAD) graphic of the sample holder developed. (B) A picture showing various details of the sample holder. 35

2.8 Illustration of the technical realization of the sample holder: A stable fixation of the sample in the three-point bending mechanism is achieved by using bolts with flanges. The additional lower bolts support the back-bending of the sample in case the bending exceeded the elastic range of the metal substrate. Stable electrical contact to the sample is ensured using spring-loaded contacts. 37

2.9 (A) Overview of the entire setup: UHV chamber on the left hand side, rack with instruments on the right hand side. (B) The picture shows the two MCBJ systems of the setup. The left one is equipped with a He flow cryostat enabling temperature-dependent measurements, the right one is restricted to room temperature measurements. 39

2.10 Temperature measured in the pushing-rod (y-axis) versus temperature measured in the He cryostat (x-axis, set point). Before (black curve) and after improvement (gray curve) of the thermal contact between cooling finger of the He cryostat and the sample holder. The temperature of the sample reaches finally 6.5 K, instead of 47 K before improvement. 40

2.11 A) DC measurement type, B) Differential AC resistance measurement by analog superposition of the DC working voltage to an AC amplitude. C) The cabling of the DUT to the instruments using a switch box. Signal and ground are guided and switched separately. This enables *in-situ* changing the different instruments without affecting the molecular junction. 41

3.1 Temperature dependence of the resistance of the Au bridge and the connector lines, measured under a small bias of 5 mV in the temperature range between 300 K and 25 K. An expected almost linear decrease of the resistance with lowering temperature is observed. The extrapolated offset at low temperatures indicates scattering at defect and impurity locations within the amorphous evaporated film. 45

3.2 Initial breaking of a junction during simultaneous measurement of its electrical resistance (bias of 5 mV applied). The initial resistance of approximately 150 Ω increases first almost linearly to 250 Ω (for pushing-rod positions smaller than 1200°), then in irregular steps. This behavior is due to the transition from bulk properties to smaller, microscopic dimensions. Finally, the breaking of the Au–Au QPC at a resistance of approximately 12.9 k Ω at pushing-rod position 2300°, indicates the transition from direct contact to tunneling (blue arrow). 47

3.3 (A) Ideal tunneling barrier with a constant barrier height, and (B) a generalized tunneling barrier. 50

3.4 Tunneling resistance measured at 30 K with small bias of 10 mV applied during simultaneous closing of the junction. The closing direction is from left to right. The resistance decays exponentially and suddenly drops to a closed metal-metal QPC ("jump-to-contact") with a resistance of $R_0 = 1/G_0$. This value is maintained upon further closing. 51

3.5 Tunneling resistance measured at a bias of 10 mV applied for times up to 1500 s (25 min). The electrode motion was stopped at a distance that the tunneling resistance yields a value of approximately 15 MΩ, far away from "jumping-to-contact". 54

3.6 Statistical distribution of the tunneling signal recorded in Fig. 3.5. The distribution reveals a sharp peak at 15.8 MΩ with very low fluctuations, indicating a very constant gap distance. 55

3.7 The electrode distance correction is adjusted manually by moving the pushing-rod upon cooling in order to maintain a constant tunneling resistance of approximately 1 MΩ. The correction values follow an almost linear behavior for high temperatures (S_{HT} for T > 200 K) and change the slope for low temperatures (S_{LT} for T < 200 K). At lower temperatures than 100 K, the system reacts too fast to be able to manually adjust the gap distance over the mechanics. This is due to the low thermal capacitance. 56

3.8 Conductance measured during opening at 300 K, 250 K and 150 K of a Au-Au contact. The signal shows distinct steps, close to integer values of G_0. 58

3.9 (A) Repeated breaking and closing of the junction under a small bias of 5 mV. (B)-(E) Pronounced steps close to multiple integer values of G_0 appear in the conductance versus distance plot, indicating formation of atomic-sized electrode tips. 61

3.10 Temperature dependence of the hysteresis occurring between opening and closing positions. The opening positions remain almost constant whereas the closing positions are shifting. The hysteresis increases with decreasing temperatures. This is due to a decreasing surface mobility of the Au atoms which needs to be compensated by a larger mechanical movement in order to close the junction again. 63

4.1 Closing of a junction with molecules applied under a small bias of 2 mV (closing from left to right): (A) Starting from an open junction with TΩ resistance, a sudden drop in resistance over three orders of magnitude is observed at pushing-rod position 2462°. (B) During further closing, the signal is maintained and its trace forms a stable plateau approximately (42 ± 5) pm long. (C) The resistance drops again over two orders of magnitude at pushing-rod position 2452°, and values below the inverse of the conductance quantum ($R_0 = 1/G_0 = 12.9$ kΩ) are measured, indicating a closed metal–metal contact. The gray curve shows the closing behavior prior to the application of molecules. 69

4.2 Ideal and more realistic illustration of a simple molecular junction. The phenyl-1,4-dithiol molecule (PDT) can bond on different sites to the metal, providing a different work function. Moreover, the geometrical shapes of the two electrodes can differ on the microscopic level, causing a different voltage drop across the molecule. 71

4.3 Illustration of the different situations assumed in the junction: Distance variation from (A) an open junction with molecules attached so far only to one electrode, to (B) a metal–molecule–metal contact, and (C) a closed metal–metal contact. Corresponding *I*–*V* measurements (experimental data) reveal (A) a noisy signal in the sub-pA range, (B) stable *I*–*V* curves with features characteristic of the particular metal–molecule–metal system under investigation (currents typically in the nA range), and (C) an ohmic behavior with currents in the μA range. 72

4.4 (A) 1500 *I*–*V* curves acquired at 300 K for 4,4"-Bis(acetylthiol)-2,2',5',2"-tetramethyl-[1,1';4',1"] terphenyl (TPDT-DM) using the statistical measurement approach. (B) Current spectrum extracted at ±0.4 V displaying three sets of curves: (C) distance-dependent exponential curves indicating tunneling (S1) - the arrow indicates decreasing electrode distance. (D) Two sets (S2 and S3) containing a few curves with stochastic switching between the two distinct curves. The two envelopes according to the fluctuations in the dataset (A) are drawn in the background in light gray. 75

5.1 -NC and -SH coupled single- and double-phenyl-ring systems with their corresponding energy diagrams: (A) 1,4-phenyl-dithiol (PDT), (B) 4,4'-Bis(acetylthio)-biphenyl-dithiol (BPDT), (V) 1,4-phenyl-diisocyanide (PDI), and (D) 4,4'-biphenyl-diisocyanide (BPDI) 81

5.2 Current–voltage, *I*–*V*, and differential conductance–voltage, G_{Diff}–*V*, characteristics of phenyl-1,4-dithiol (PDT) measured at (A) 250 K and (B) 50 K. The conductance gap, $2{\cdot}\Delta_{\mathrm{cond}}$, decreases from 0.9 V at 250 K to 0.6 V at 50 K. At 50 K, an instability occurs for voltages larger than 0.6 V. This feature is inherent to the molecular system and cannot be attributed to the noise of the setup. 84

5.3 Resistance histograms of 100 closing and opening cycles: (A) In the absence of molecules, and (B) the presence of PDT molecules (the gray dotted line in (B) represents approximately the envelope of the data in (A)). The measurements were taken at 300 K under constant bias (5 mV). The inset shows one representative contacting curve with a plateau length of only (6 ± 2) pm. . . . 85

5.4 Transport properties of PDI: Several I–V and G_{Diff}–V sweeps taken at 50 K. The conductance gap $2{\cdot}\Delta_{cond}$ is around 0.4 V, slightly smaller than in case of PDT. No instability is observed for voltages above ± 0.6 V, in contrast to the thiol coupled PDT. 88

5.5 Comparison of I–V and G_{Diff}–V data, measured for PDI and PDT at 50 K. . 90

5.6 Experimental G–V data for PDI and PDT, fitted to a Lorentzian distribution using equation (5.2). The parameters achieved are given in the inset. 93

5.7 Transport behavior for BPDT and BPDI: I–V and G–V sweeps taken at 50 K. In agreement with the measurements on PDT and PDI, the CN-coupled BPDI reveals a lower onset in current than the BPDT. 95

5.8 (A) Temperature-dependence of the transport properties of BPDI: Decreasing conductance gap with increasing molecular signature. (B) Low temperature (8 K) measurements for the same molecule revealing a rich conductance spectra. 96

6.1 Molecular structures of PDT, **2**, **3** and **4**. The acetyl protection groups (-$COCH_3$) were already removed upon coupling to the metal. The length of the molecules increases from 0.846 nm for the PDT, to 2.189 nm for the molecule **4**.101

6.2 Transport properties of the oligophenylenes, PDT (**1**), **2**, **3** and **4**. The double-sweep I–V characteristics were taken at 50 K. The curves drawn are restricted to their stable and reproducible voltage window. The data represents the statistically most probably curves found within a huge data set, measured on more than 50 samples. The arrows indicate the locations of the first peak, defining the conductance gap. 103

6.3 Increasing values of the conductance gap with increasing number of phenyl rings (left axis). The experimental data is based on several samples measured (error bars). The length of the molecules increases linearly with the number of phenyl rings (right axis). 105

7.1 Molecular diode as proposed by A. Aviram and M. Ratner [63]: (A) Molecular structure consisting of a donor and an acceptor part, spaced via an insulating bridge. (B) Zero bias energy diagram. (C) Forward and (D) reversed bias situation giving rise to different current flow in the two directions. 110

7.2 Molecular structure of the SB diode molecule coupled symmetrically to Au electrodes over thiol linkers. The asymmetric cyanoethyl and trimethylsilylethyl thiol protecting groups are already deprotected, and thus not drawn. 112

7.3 I–V characteristics of the SB-diode molecule taken at 300 K. The inset shows the rectification ratio of approximately 10 at 1.2 V. The onset in current is around + 1.0 V. 113

7.4 The I–V characteristics show the transport properties of the SB-diode molecule taken at various temperatures. The rectification behavior is maintained upon temperature changes. The current onset is shifted from + 1.0 V towards + 1.2 V with decreasing temperature. 114

7.5 Subsequently measured I–V sweeps (raw data) for the SB-diode in a larger voltage window from −1.8 V to +1.8 V. The high-field conditions lead to irreversible changes of the molecular junction destroying first the rectification behavior (2nd and 3rd sweep), and finally the molecular junction itself (4th sweep), forming a closed Au–Au junction. 115

7.6 Molecular structures of the two molecules under investigation: (A) BPDN-DT and (B) BP-DT. Charge-carrier transport characteristics of single BPDN-DT (blue) and BP-DT (red) molecules acquired at 100 K: (C) Statistically representative I–V curves (double sweep) based on several hundreds of sweeps acquired. An approximately six times higher current is observed for the BP-DT molecule compared to the BPDN-DT molecule (all raw data). A reversible hysteresis in the BPDN-DT signal is highlighted with gray rings. (D) G_{diff}–V data reveals a similar conductance gap for both molecules of approximately 1.0 V. Black arrows indicate the discontinuity in the BPDN-DT curve. 119

7.7 Switching behavior measured at room temperature: The Au–single-BPDN-DT–Au system switches at slightly higher voltages compared to 100 K at 1.3 V to a higher conductive state. The sweep from higher voltages to zero volt shows an additional shift and again a hysteresis. 120

7.8 Stepwise increase of the maximum voltage of the I–V double sweep of the Au–single-BPDN-DT–Au system. The system switches if 0.9 V are approached. The initial "off" state is no longer accessible when the voltage has exceeded the positive voltage threshold and the system stays in the "on" state even after decreasing the maximum voltage again. The gray curve shows the switching sweep displayed in (C) again for the guidance in (D)-(E). 122

7.9 Several repeated switching cycles of the BPDN-DT: If the voltage applied to the Au–single-BPDN-DT–Au junction exceeds a certain positive threshold value ($V_{\text{Switch,pos}}$), the system switches from the initial "off" state to the "on" state. This state is maintained when operating only at voltages above $V_{\text{Switch,neg}}$. A negative voltage sweep or a pulse below the negative threshold value ($V_{\text{Switch,neg}}$) resets the molecule again to the initial "off" state. 123

7.10 The intersection of the two current traces on the positive and negative voltage axis, measured at 100 K. 124

7.11 Dynamics of the switching mechanism: (A) Upon increasing the current measurement integration time significantly ($t_{int,long} = 320$ ms per data point), the current signal becomes bistable for increasing voltages within a certain range, finally switching to the "on" state for higher voltages. (B) When lowering the voltage with $t_{int,long}$, fluctuations can be observed in a certain voltage range, after which the "on" state finally relaxes into the "off" state for $V < V_{\text{Switch}}$. (C) For short integration time ($t_{int,short} = 0.64$ ms per data point) a sudden switching to a high conductive "on" state occurs. The system maintains the "on" state even upon decreasing the voltage. The gray area represents the region of V_{Switch}. (D) Schematic illustration of the switching response for slow and fast voltage sweeps. 126

7.12 Schematic of the switching behavior: (A) Sweeping the voltage slowly, the system switches after passing a bistable region to the "on" state. However, for voltages below the bistable region, the "off" state relaxes. Only by using fast integration times (B), a hysteresis is observed. Instead of sweeps, voltage pulses can be applied instead (C) to control and detect the state of the molecular system. 129

7.13 Density Functional Theory (DFT) calculations performed for the BPDN-DT and BP-DT molecules: Molecular structures show (A)+(B) the uncharged, (C)+(D) the positively charged, and (E)+(F) negatively charged molecules. The BPDN-DT shows a tilting between the two pyridil units of approximately 60°, which is only slightly affected by the positive or negative charging. BP-DT reveals always a planar structure which is not affected by the charging. 130

7.14 Density-Functional-Theory (DFT) calculations performed for the BPDN-DT and BP-DT molecules: (A)+(B) Uncharged, (C)+(D) positively charged, and (E)+(F) negatively charged situation. (See text for details.) 132

7.15 BPDN-DT "on" state stability at 100 K: The current representing the "on" state is measured continuously every minute up to a total recording time of 100 minutes. The current measured represents the "on" state, and is unaffected of the reading voltage at 0.8 V. 133

7.16 Memory operation of the BPDN-DT system: (A) Write, read and erase pulse pattern applied. (B) Resulting switching between "off" and "on" state: I_{off} varies between 0.05 and 0.13 nA, I_{on} between 0.9 and 3.6 nA. Reading times of 3 s display excellent signal stability. The inset shows the corresponding I–V curve, indicating switching at 1.4 V and reading at 1.1 V (black lines). 137

A.1 Overview on the molecules which were characterized in this thesis: A) Phenyl-based, thiol-terminated molecules. B) Phenyl-based, cyano-terminated molecules. C) Diode molecule D) Voltage-induced switching molecules. 163

List of Tables

1.1 Length scales ranging from objects much larger than 1 μm down to sub-nm with corresponding transport mechanisms and theoretical frameworks. 4

1.2 Different charge-carrier transport properties for the three distinct regimes of coupling. 16

5.1 Fitting results of the width of the peak, Γ, in the experimental data of PDT and PDI, according to a Breit-Wigner distribution. Also given are the conductance values of the first peak in resonance, the level positions, ϵ, and the resulting conductance gap, Δ_{cond}. 91

5.2 Density Functional Theory (DFT) calculations performed for PDT and PDI, reproduced from Lang *et al.* [18; 41]. 94

6.1 Low bias resistances of PDT, molecules **2**, **3**, and **4** determined statistically by histograms over 100 opening and closing cycles under a fixed small bias. 104

6.2 Overview on the length of the oligophenylenes investigated. PDT reveals a sulphur-sulphur distance below 1 nm, whereas the four rings in **4** yield a sulphur-sulphur distance of almost 2 nm. 106

Appendix A

Molecules

Molecule	Name	Institutes
PDT	Phenyl-1,4-Dithiol	FZK
BPDT	4,4'-biphenyl-dithiol	FZK
2	4,4'-Bis(acetylthio)-2,2'-dimethyl-biphenyl-dithiol	FZK
3	4,4'-Bis(acetylthio)-2,2'-dimethyl-terphenyl-dithiol	FZK
4	4,4'-Bis(acetylthio)-2,2'-dimethyl-quaterphenyl-dithiol	FZK
PDI	phenyl-1,4-diisocyanide	Sigma-Aldrich
BPDI	4,4'-biphenyl-diisocyanide	IBM YKT
TPDI	4,4'-terphenyl-diisocyanide	IBM YKT
SB-Diode	-	UC
BP-DT	Bipyridil oligo-phenylene-ethynylene-dithiol	RU
BPDN-DT	Bipyridil oligo-phenylene-ethynylene-dithiol	RU

Institutes

FZK	Research Center Karlsruhe	Dr. Marcel Mayor
IBM YKT	IBM T. J. Watson Research Center, Yorktown Heights	Dr. Ali Afzali-Ardakani
UC	University of Chicago	Prof. Dr. Luping Yu
RU	Rice University, Houston, Texas	Prof. Dr. James Tour

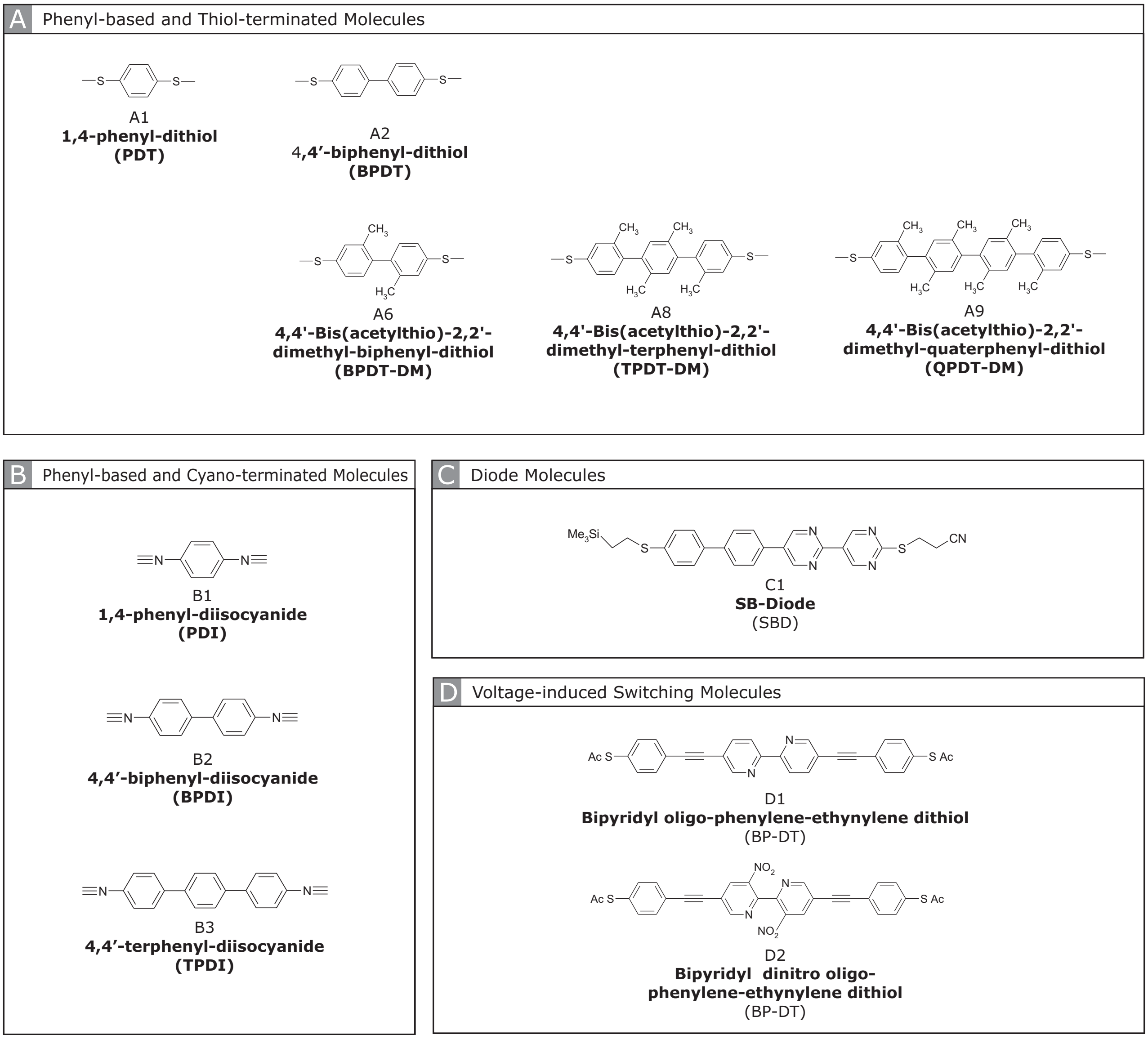

A Phenyl-based and Thiol-terminated Molecules

A1
1,4-phenyl-dithiol
(PDT)

A2
4,4’-biphenyl-dithiol
(BPDT)

A6
4,4'-Bis(acetylthio)-2,2'-
dimethyl-biphenyl-dithiol
(BPDT-DM)

A8
4,4'-Bis(acetylthio)-2,2'-
dimethyl-terphenyl-dithiol
(TPDT-DM)

A9
4,4'-Bis(acetylthio)-2,2'-
dimethyl-quaterphenyl-dithiol
(QPDT-DM)

B Phenyl-based and Cyano-terminated Molecules

B1
1,4-phenyl-diisocyanide
(PDI)

B2
4,4’-biphenyl-diisocyanide
(BPDI)

B3
4,4’-terphenyl-diisocyanide
(TPDI)

C Diode Molecules

C1
SB-Diode
(SBD)

D Voltage-induced Switching Molecules

D1
Bipyridyl oligo-phenylene-ethynylene dithiol
(BP-DT)

D2
Bipyridyl dinitro oligo-
phenylene-ethynylene dithiol
(BP-DT)

Figure A.1: *Overview on the molecules which were characterized in this thesis: A) Phenyl-based, thiol-terminated molecules. B) Phenyl-based, cyano-terminated molecules. C) Diode molecule D) Voltage-induced switching molecules.*

Appendix B

List of Publications

Articles

- E. Lörtscher, H. B. Weber, and H. Riel. *Statistical Approach to Investigating Transport through Single Molecules.* **Phys. Rev. Lett.**, Vol. 98, 176807-1–4 (2007).

- E. Lörtscher, J. W. Ciszek, J. M. Tour, and H. Riel. *Reversible and Controllable Switching of a Single-Molecule Junction.* **Small**, Vol. 2, 973–977 (2006).

- E. Lörtscher, J. W. Ciszek, J. M. Tour, and H. Riel. *A Single-Molecule Switch and Memory Element.* **Journal of Physics**, Vol. 61, 987–991 (2006).

- E. Lörtscher, and H. Riel. *Single-Molecule Switch and Memory Element.* **European Research Consortium for Informatics and Mathematics (ERCIM)**, No. 67, 50–51 (2006).

- O. Hayden, M. T. Björk, H. Schmid, H. Riel, U. Drechsler, S. F. Karg, E. Lörtscher, W. Riess. *Fully Depleted Nanowire Field-Effect Transistor in Inversion Mode.* **Small**, Vol. 3, 230–234 (2006).

- E. Lörtscher, M. Elbing, M. Tschudy, C. von Hänisch, H. B. Weber, M. Mayor, and H. Riel. *Length-dependent Transport in Molecular Rods with Reduced π-conjugation.* Submitted (2007).

- E. Lörtscher, Marcel Mayor, Charles Rettner, and Heike Riel. *Transport Studies through Thiol- and Isocyanide-Coupled Metal–Single-Molecule–Metal Junctions.* tba (2007).
- M. Ruben, A. Landa, M. Mayor, H. Görls, E. Lörtscher, H. Riel, H. B. Weber, A. Arnold, F. Evers. *Electrical Transport through a Single Ruthenium(II) bis-Terpyridyl Complex.* tba (2007).
- M. Röösli, M. Lörtscher, M. Egger, D. Pfluger, N. Schreier E. Lörtscher, P. Locher, A. Spoerri, Ch. Minder. *Leukaemia, Brain Tumours and Exposure to Extremely Low Frequency Magnetic Fields: Cohort Study of Swiss Railway Employees.* **Occupational and Environmental Medicine**, doi:10.1136/oem.2006.030270, May (2007).
- M. Röösli, M. Lörtscher, M. Egger, D. Pfluger, N. Schreier E. Lörtscher, P. Locher, A. Spoerri, Ch. Minder. *Mortality from Neurodegenerative Disease and Exposure to Extremely Low-Frequency Magnetic Fields: 31 Years of Observations on Swiss Railway Employees.* **Neuroepidemiology**, Vol. 28, No. 4 (2007).
- M. Lörtscher, E. Lörtscher. *Niederfrequente elektromagnetische Felder in Führerständen von Triebfahrzeugen der SBB* . **Elektrische Bahnen**, Vol. 8–9 (2004).

Oral Presentations

- E. Lörtscher, C. J. Cho, H. Riel. *Single-Molecule Transport Studies.* **The 9th European Conference on Molecular Electronics (ECME)**, Metz (2007) (invited).
- E. Lörtscher, H. Riel. *Introduction to Molecular Electronics: Single-Molecule Transport Studies.* **Summerschool of the Marie Curie Network of Excellence BIMORE**, San Bendetto del Tronto (2007) (invited).
- E. Lörtscher. *Charge Transport Measurements through Single Molecules.* **Annual Meeting of the Swiss Physical Society (SPS)**, Zurich (2007) (invited).
- E. Lörtscher, J. W. Ciszek, J. M. Tour, and H. Riel. *A Statistical Approach for Electrical Transport Investigations through Single Molecules.* **Material Research Society (MRS) Spring Meeting**, San Francisco (2006) (invited).

- E. Lörtscher, J. W. Ciszek, J. M. Tour, and H. Riel. *A Statistical Approach for Electrical Transport Investigations through Single Molecules*. **ICN+T**, Basel (2006).
- E. Lörtscher, H. B. Weber, and H. Riel. *A Statistical Approach for Electrical Transport Investigations through Single Molecules*. **Transport through Single Molecules**, Leiden (2005).

Poster Presentations

- E. Lörtscher, J. W. Ciszek, J. M. Tour, and H. Riel. *A Single-Molecule Switch and Memory Element*. **Trends in Nanoscience**, Klosters Irsee (2007).
- E. Lörtscher, J. W. Ciszek, J. M. Tour, and H. Riel. *A Single-Molecule Switch and Memory Element.*. **Wilhelm and Else Heräus Seminar about Quantum Transport at the Molecular Scale**, Bad Honnef (2006).
- E. Lörtscher, H. B. Weber, and H. Riel. *A Statistical Approach for Electrical Transport Investigations through Single Molecules.*. **Transport through Single Molecules**, Leiden (2005).
- E. Lörtscher, H. B. Weber, and H. Riel. *A Statistical Approach for Electrical Transport Investigations through Single Molecules*. **NNCR Annual Meeting**, Gwatt (2005).
- E. Lörtscher, H. B. Weber, and H. Riel. *A Statistical Approach for Electrical Transport Investigations through Single Molecules*. **3rd European Conference on Organic Electronics and Related Phenomena (ECOER)**, Wintherthur (2005).

Appendix C

Acknowledgments

It is a pleasure for me to express my gratitude to the many people who have contributed to this work in the past three years. Without their help and support, it would not have been possible.

My sincere thanks are given to Prof. Dr. Christian Schönenberger for the confidence in my work as an external PhD student and for the interesting discussions during the meetings at IBM, the University of Basel, and at conferences. Moreover, I thank Prof. Dr. Jan van Ruitenbeek. It is a great honor to have one of the pioneers in Molecular Electronics and of the mechanically controllable break-junction technique as a referee.

It was a wonderful opportunity and a great pleasure to work at the IBM Zurich Research Laboratory in a familiar environment together with experts in the various fields and diverse in culture. I profited enormously from the wide range of knowledge in the Science & Technology Department. Therefore, I thank the people who made this happen. My warmest thanks go to my manager and tutor Dr. habil. Walter Riess. His expertise and many ideas created a very motivating and stimulating atmosphere. The same warmest thanks go to Dr. Heike Riel, my supervisor and second team player in the impressive molecular electronics subgroup. It was always a pleasure to discuss the experimental results. I appreciated her profound knowledge that goes far beyond the field of Molecular Electronics. Her guidance and support helped tremendously in accomplishing my work.

Moreover, I wish to acknowledge the excellent support from the entire “Nanoscale Devices and Nanoscale Structures” group. I hope that the helpful and companionate atmosphere will be maintained much longer. First of all, I acknowledge Dr. Siegfried Karg for many helpful discussions and critical questions. Meinrad Tschudy helped me with various technical solutions, always realized in the quickest time and with the highest perfection. Ute Drechsler provided a great support in all processing steps. I was lucky to get access to the cleanroom facilities.

Simon Scherrer, Hans-Peter Ott, Kurt Waser, Hans-Ruedi Steinauer, Martin Witzig, and Urs Bapst from the model and electronic shop helped me with the realization of the three-point bending mechanism and many other tools. The last but not least thanks for the people of the IBM Zurich Laboratory, go to Dr. Paul F. Seidler, the head of the Science & Technology Department.

Moreover, I am grateful to Prof. Dr. Heiko B. Weber for many discussions concerning Molecular Electronics. In the starting phase of this project, when he was with IBM as a visiting scientist, he gave us the right ideas for what is necessary and what needs to be done in this relatively young field of research.

Molecular Electronics would not exist without the contributions from the chemists. Many groups provided me with beautiful molecules: Prof. Dr. Marcel Mayor who made many compounds together with Dr. Mark Elbing. The switching molecules were synthesized by Prof. Dr. James Tour and Dr. Jake W. Ciszek. Dr. Cherie Kagan and Dr. Ali Afzali-Ardakani provided the isocyanide-coupled molecules. I would also like to thank to those chemists whose molecules unfortunately did not find a place in this thesis: Prof. Dr. Peter Belser and Dr. Vijay Iyer from the University of Fribourg, and Dr. Mario Ruben from the University of Strassbourg.

I further appreciated the support and help for electron-beam writing from various sites. In the starting phase, Daniel Secker and Michel Bergler-di Leo structured many samples using their e-beam tool in Karlsruhe. Dr. Charles Rettner made the step to an almost “mass production” possible with his knowledge and the Leica tool. These e-beam samples would still be kept within a useless plate of metal without the help of Paul Fischbacher from Digipack.

Most recently, within the last months of my thesis work, a collaboration with the theory group at the Institute of Nanotechnology at the Research Center Karlsruhe was established. I thank Dr. Ferdinand Evers and Dr. Velimir Meded for sharing their DFT results and theoretical concepts.

I deeply thank my parents without: their continuous support throughout my studies this work would not have been possible. Most of all, I thank my girlfriend, Eliane, for her enormous patience and for more than I can express.

Appendix D

Abbreviations

Symbols

A	Device area [m^2]
$\mathring{A}$	Ångstrom (1 $\mathring{A} \equiv 10^{-10}$ m)
E_F	Fermi energy [eV]
G	Conductance [S]
G_{Diff}	Differential conductance [S]
G_S	Sharvin conductance [S]
h	Pushing-rod travel [m]
$\hbar$	Planck's constant [eV$\cdot$ s]
I	Current [A]
l	Length [m]
L	Distance between the supporting bolts in the MCBJ geometry [m]
L_φ	Phase-coherence length [m]
L_{dB}	De Brogli wavelength [m]

L_{mf}	Mean-free path [m]
nm	Nanometer (1 $nm \equiv 10^{-9}$ m)
p	Pressure [bar]
pm	Picometer (1 $pm \equiv 10^{-12}$ m)
V	Voltage [V]
Q	Charge [e]
r	Transmission ratio in the MCBJ geometry
s	Cantilevered distance of the MCBJ bridge [m]
Δ_{Mode}	Mode separation [eV]
Γ	Level broadening [eV]

Devices and Methods

AC	Alternating current
AFM	Atomic Force Microscope
DC	Direct current
DFT	Density Functional Theory
DOS	Density of states
DUT	Device under test
GPIB	General Purpose Interface/Instrumentation Bus
HOMO	Highest occupied molecular orbital
IETS	Inelastic Electron Tunneling Spectroscopy
IR	Infrared (Light)
LabView	Laboratory Virtual Instrumentation Engineering Workbench
LUMO	Lowest unoccupied molecular orbital
MCBJ	Mechanically controllable break-junction
NEGF	Non-Equilibrium Green's Function
QPC	Quantum Point Contact
RIE	Reactive Ion Etching
SAM	Self-assembled Monolayer
STM	Scanning Tunneling Microscope
SMU	Source Measure Unit
TEM	Transmission Electron Microscope

UHV	Ultra-high vacuum
UV	Ultraviolet (light/radiation)

Materials

2	4,4-Bis(acetylthio)-2,2-dimethyl-biphenyl
3	" Terphenyl-dithiol"
4	" Quaterphenyl-Dithiol"
Au	Gold
BDT	Phenyl-1,4-dithiol
BDPI	4,4-Bis(diisocyano)-2,2-biphenyl
BeCu	Berillium-Copper
BPDT	4,4-Bis(acetylthio)-2,2-biphenyl
IP	Isopropanol
MIBK	Isobutylmethylketone
Na	Sodium
PDI	Phenyl-1,4-diisocyanide
PDMS	Polydimethylsiloxane
PhBr	Phosphorous bronze
PI	Polyimide
PMMA	Polymethylmethacrylate
Pt	Platinum
Si_3N_4	Silicon-Nitrite
Ti	Titanium

Appendix E

Curriculum Vitae

Personal Data

Name : Emanuel Marc Lörtscher

Date of Birth : September 21, 1976

Place of Birth : Wimmis (BE)

Nationality : Swiss

Professional Development

01/07 - present **Post-Doctoral researcher**, Science and Technology Department,

IBM Zurich Research Laboratory, Rüschlikon, Switzerland.

Project Topic: Molecular-Scale Electronics and Strain in Nanostructures.

11/06	**PhD thesis**, *Summa cum laude*, University of Basel (Prof. Dr. Ch. Schönenberger). *Title*: ”Charge-Carrier Transport Measurements through Single Molecules”.
01/04 - 10/06	**PhD work**, Science and Technology Department, IBM Zurich Research Laboratory, Rüschlikon, Switzerland (Dr. H. Riel, Dr. habil. W. Riess). *Project topic*: Molecular-Scale Electronics.
03/03	**Diploma degree in physics**, Dipl.-Phys. ETHZ, received from the Swiss Federal Institute of Technology, Zurich (ETHZ).
10/02 - 02/03	**Diploma thesis**, Science and Technology Department, IBM Zurich Research Laboratory, Rüschlikon, Switzerland (Dr. H. Riel, Dr. habil. W. Riess). *Title*: ”Absolute Quantum Efficiency of Photoluminescence of Thin Organic Layers and Magnetic Field Effects of Organic Light-Emitting Devices”.
06/02 - 7/02	**Semester work**, Institute for Quantum Electronics, Swiss Federal Institute of Technology Zurich (ETHZ) (Prof. Dr. P. Günter). *Title*: ”Charge Transport Studies in Organic-Field-Effect Transistors”.
01/98 - 12/00	**Practical training** (Anfängerpraktikum und Vorgerücktenpraktikum), Physics Department, Swiss Federal Institute of Technology, Zurich (ETHZ).

Work Experience

2003	Magnetic-field studies in Swiss Railways, joint collaboration with the Swiss Federal Office for Transport (BAV) and the Swiss Federal Office of Public Health (BAG).
2002	Development of database applications and HTML programming for various customers.
1998 - 2002	IT coordinator at PAX, Schweizerische Lebensversicherungs-Gesellschaft, Zurich.
1997 - 1998	Internship at PAX, Schweizerische Lebensversicherungs-Gesellschaft, Zurich.
1993 - 1996	Internship at Engineering-Organization-Traction (ENOTRAC) AG, Uetendorf.

General Education

10/97 - 03/03	Physics studies at the Swiss Federal Institute of Technology Zurich (ETHZ).
1992 - 1997	Matura Type C (Math and Science), Urdorf.
1990 - 1992	Sekundarschule, Bonstetten.
1984 - 1990	Primarschule, Wettswil.

Awards

2007 IBM Outstanding Technical Achievement Award (Science and Base Technology).

”Reversible and Controllable Switching of a Single-Molecule Junction”.

2007 Swiss Physical Society 2007 Award for Applied Physics (”Oerlikon Prize”)

2006 IBM Research Division Technical Accomplishment (Science and Base Technology).

”Reversible and Controllable Switching of a Single-Molecule Junction”.

Ich erkläre hiermit, dass ich die vorliegende Arbeit selbständig verfasst und nur die angegebenen Quellen und Hilfsmittel verwendet habe.

Rüschlikon, 15. Oktober 2006

ISBN 978-3-86727-380-0